Fundamental Non-Equilibrium Experiments Relevant to Low Earth Orbit Return Missions



Alex B. Glenn

Supervisor: Prof. M. McGilvray
Dr. P. L. Collen

Department of Engineering Science
University of Oxford

This dissertation is submitted for the degree of
Doctor of Philosophy

Wadham College June 2025

Acknowledgements

First, thank you to my supervisor, Matthew McGilvray, without whom I would have not had the opportunity to work on such awesome projects. Thank you for setting ambitious goals, your uncanny ability to tell if data is rubbish straight away, for having faith that I can deliver on demanding tasks and for turning up to the late night and weekend sessions. You've helped me to become a much more confident researcher and engineer. I've come a long way since the Chai Lattes.

Thank you also to Peter Collen – for taking me under your wing from day one, teaching me how to do shock tube experiments, for always being a pleasure to talk to, and of course for sticking around as my secondary supervisor (when you probably wanted a well-deserved break from shock tubes). I'm sorry for all my annoying questions in the beginning. You went to great efforts to explain and teach me about all things shock tubes and radiation, and I am so very grateful.

None of this work would have been possible without the immense efforts and teamwork of the Oxford Hypersonics Group. In particular, I'd like to thank Tristan Crumpton – for going above and beyond in the 2023 AST campaign, always bringing some class into the control room and for making what was supposed to be a stressful year actually really quite enjoyable. I'll be sure to put some of the Scottish slang I've learnt to use! Chris Hambidge – for keeping the group afloat and for all the extra efforts you make to ensure the success of mine and every other project in the group. Joe Steer, Maïlys Buquet and Justin Clarke – thank you for staying positive and for your relentless support of trips to Jericho coffee traders. In particular: Joe – from breaking records, gluing windows, obscene doses of gasket stripper and vacuum putty, and the pure elation from the moment we got the FOSTERS box to work – it really has been a rollercoaster, thanks for being such a good campaign buddy and friend; Maïlys – thank you for maintaining high spirits, enabling my JCT visits (by possibly being the only person to exceed it), for generally making the lab a more fun place and for all the hard work you put in during the VUV campaign; Justin – thank you for the considerable hours you've spent at my computer getting "numerical things" to work, for the insightful conversations about shock tubes and for all the laughs we've had along the way – you've been a tremendous help. Andy Hyslop – thanks for being a great desk

buddy and then house mate, for listening to me talk about the tunnel nearly every night and of course for introducing me to the cinnamon socials at Ole and Steen. What a game changer! Tobias Hermann – thank you for your supervision over the first couple of years and for the continued interesting discussions and encyclopaedic knowledge about radiation and optics. Jack 'JAQUIRI' Hillyer – the extra work you've done for the benefit of the wider group is colossal. Thank you for being on call for the occasional DAQUIRI hiccup and hopefully for the last time – Morning! Aaron Kennedy – Thank you for putting in the late night sessions with me early on to get AST operational. And finally, thank you to the wider group of 'lackies' – Josh, Anthony, Wes, Nemi and Conor – for putting in some hard shifts to get AST clean and ready for the next shot. To all those mentioned and the remainder of the hypersonics group, the last five[1] years have been a huge pleasure – thank you all for making them so enjoyable!

The work for this thesis could not have been carried out without the significant amount of administrative, technical and I.T. support. Special thanks go to Anna, Alex, Kathryn, Anna, Harry, Leo, Dave, Duncan, "Bill and Hal", Jason, Greg, Craig and Roger. Thank you for your immense competence and for always delivering, even though our requests would traditionally be last minute and urgent. This work would have been no where near as successful without the efforts from all of you, and I am eternally grateful.

I've had the privilege of collaborating with various members of external organisations and institutions. In particular, I'd like to thank Brett Cruden and Aaron Brandis at NASA Ames – for the loan of UV spectrometry equipment during the first AST campaign in my early stages, and for the continued support and constructive conversations regarding the intricacies of shock tube experiments, optics calibrations and the NEQAIR code. Additionally, I'd like to acknowledge Christophe Laux and Carolyn Jacobs, at CentraleSupélec and the University of Queensland, for their assistance in comparison of shock tube radiance data to that from plasma torches. Tamara Sopek – thank you for all your help with the first AST campaign and for helping me learn what a shock wave actually is.

To my old housemates – Kate, Kay, Alice and Aaron – somehow we got through those crazy lockdown couple of years and kept each other sane. Thank you for all the wholesome moments, the dinner parties and let's not forget the drama. Those times are warmly remembered.

To my mates back home – thank you for putting up with my flaky attendance to socials over the last couple of years, for only ever being a phone call away and for your support and encouragement. I can't wait for us all to hang out again!

[1] but if anyone asks, four

I owe a lot to my parents - for the unconditional support in this and all other endeavours I've attempted. There's been a number of difficult and unconventional challenges over the last few years. Whether you've supported the idea or not, you've both always supported me and been there in my moments of need. Even if that's meant flying half way around the world! Thank you for everything. It also wouldn't be right to not thank Lottie, who kept us all in check for so long and reminded us of the important things. She is very missed.

And, of course – last but by no means least – Alice. Beginning to date someone as they enter the early stages of (what turned out to be) a nine-month shock tube campaign must have been very confusing and frustrating at times. Thank you for being understanding and supportive, during both the experiments and write up phase. For giving me a tactful but firm nudge to stay on track when I needed it, for always having faith that I could finish this DPhil, and for giving me a future to look forward to. We've both achieved so much in the last year and I can't wait to see what the future holds. Keep slaying!

List of Publications

First-authored unpublished and unsubmitted draft papers re-formatted into chapters in this integrated thesis, intended for later journal submissions:

1. Glenn, A. B., Crumpton, T. J., Collen, P. L., and McGilvray, M., "Investigation into Equilibrium Radiance Offset in Air Shock Tube Tests"

2. Glenn, A. B., Clarke, J., Collen, P. L., Di Mare, L., and McGilvray, M., "Development and Validation of a Constrained Spectral Fitting Routine"

3. Glenn, A. B., Clarke, J., Collen, P. L., Di Mare, L., and McGilvray, M., "Thermochemical Characterisation of Shock-Heated Pure Nitrogen"

4. Glenn, A. B., Clarke, J., Collen, P. L., Di Mare, L., and McGilvray, M., "Thermochemical Characterisation of Shock-Heated Synthetic Air"

First-authored conference papers and presentations relevant to this thesis but not included herein:

1. Glenn, A. B., Collen, P. L., and McGilvray, M., "Experimental Non-Equilibrium Radiation Measurements for Low-Earth Orbit Return," *AIAA SCITECH 2022 Forum, 2022, p. 2154.*

2. Glenn, A., Collen, P., Jacobs, C., Laux, C., and McGilvray, M., "Comparison of Equilibrium Radiation Between Shock Tube and Plasma Torch Spectroscopy for Atmospheric Pressure Air," 2022. *9th International Workshop on Radiation of High Temperature Gases for Space Missions*

3. Glenn, A. B., Collen, P., and McGilvray, M., "Radiation Measurements of Shockwaves in Synthetic Air and Pure Nitrogen," *AIAA SCITECH 2024 Forum, 2024, p. 0226.*

4. Glenn, A. B., Clarke, J., Collen, P. L., Di Mare, L., and McGilvray, M., "Thermochemical Characterisation of Shock-Heated Flows", 2024. *10th International Workshop on Radiation of High Temperature Gases for Space Missions*

Co-authored papers during the tenure of the author's DPhil candidacy (not included herein):

1. Satchell, M., Glenn, A., Collen, P., Penty-Garaets, R., McGilvray, M., and di Mare, L., "An Analytical Method of Evaluating Nonuniformities in Shock Tube Flows. Part 2: Application," 2021.

2. McGilvray, M., Collen, P., Doherty, L., Steer, J., Leader, J., Glenn, A., and Hambidge, C., “The Oxford T6 Stalker tunnel: performance, upgrades and new modes of operation,” 2022.

3. Hermann, T., Collen, P., Glenn, A., Sopek, T., McGilvray, M., and Di Mare, L., “Emission spectroscopy of low density air shock tube flows above 10 km/s,” 2022. *9th International Workshop on Radiation of High Temperature Gases for Space Missions*

4. Buquet, M., Glenn, A., Collen, P., Williams, B., McGlivray, M., and Hermann, T., “Design of a Spatially Resolved VUV Spectroscopy System for Shock Tube Flows,” 2022. *9th International Workshop on Radiation of High Temperature Gases for Space Missions*

5. Collen, P. L., Glenn, A. B., Doherty, L. J., and McGilvray, M., “Absolute Measurements of Air Shock-Layer Radiation in the T6 Aluminium Shock Tube,” *Journal of Thermophysics and Heat Transfer*, 2023, pp. 1–14.

6. Clarke, J., Glenn, A., McGilvray, M., and di Mare, L., “Numerical Simulation of a Shock Tube in Thermochemical Non-Equilibrium,” *AIAA SCITECH 2023 Forum, 2023, p. 1797.*

7. Steer, J., Collen, P. L., Glenn, A. B., Hambidge, C., Doherty, L. J., McGilvray, M., Loehle, S., and Walpot, L, "Shock radiation tests for ice giant entry probes including CH4 in the T6 free-piston driven wind tunnel," *AIAA SCITECH 2023 Forum, p. 1729.*

8. Steer, J., Collen, P. L., Glenn, A. B., Sopek, T., Hambidge, C., Doherty, L. J., McGilvray, M., Loehle, S., and Walpot, L., "Experimental study of a galileo subscale model at ice giant entry conditions in the T6 free-piston driven wind tunnel," *AIAA SciTech 2023 Forum, page 1339.*

9. Clarke, J., Glenn, A. B., Di Mare, L., and McGilvray, M., “Numerical Simulations of Carbon Contaminants in T6 Shock Tube Tests,” *AIAA SCITECH 2024 Forum, 2024, p. 0868.*

10. McGilvray, M., McIntyre, T. J., Glenn, A., and Morgan, R. G., “Shock-Tube Measurements of Radiation for Titan Atmospheric Entry,” *Journal of Thermophysics and Heat Transfer, 2024, pp. 1–8.*

11. Steer, J., Collen, P., Glenn, A., Hambidge, C., Doherty, L. J., McGilvray, M., Sopek, T., Loehle, S., and Walpot, L, "Commissioning of upgrades to T6 to study giant planet entry," *Journal of Spacecraft and Rockets*, pages 1–18.

12. Sopek, T., Glenn, A., Clarke, J., di Mare, L., Collen, P., and McGilvray, M., "Radiative heat transfer measurements of Titan atmospheric entry in a shock tube," *Journal of Thermophysics and Heat Transfer, 2024, pages 1–23.*

13. Crumpton, T. J., Steer, J., Clarke, J., Glenn, A. B., Collen, P.L., McGilvray, M., "Analysis of Mars Entry Shock Wave Radiance in the T6 Stalker Hypersonic Wind Tunnel," *AIAA SCITECH 2024 Forum, 2024, p. 0861.*

14. Buquet, M., Glenn, A., Williams, B., McGlivray, M., and Hermann, T., "Vacuum Ultraviolet Emission Spectroscopy in Shock Tube Flows," 2024. *10th International Workshop on Radiation of High Temperature Gases for Space Missions*

15. Buquet, M., Glenn, A., Le Page, L. M., Williams, B., Ewart, P., McGlivray, M., and Hermann, T., "Ultraviolet Laser Absorption Spectroscopy in Shock Tube Flows," 2024. *10th International Workshop on Radiation of High Temperature Gases for Space Missions*

Abstract

This thesis details the work undertaken to characterise the non-equilibrium thermochemical state evolution through a high-enthalpy flow, representative of the stagnation line ahead of a vehicle during re-entry from Low Earth Orbit. The motivation for this work is to enhance future vehicle designs by improving understanding of vehicle observability, radiative and convective heat loads, and the onset of free electron production to avoid communications blackout. Additionally, it links to aerothermodynamic coupling phenomena, which may impact the forces imposed on the vehicle surface and consequently its trajectory.

Fundamental experiments were conducted in the University of Oxford's T6 Stalker Tunnel: a high-enthalpy, transient facility designed to replicate the high-temperature, hypersonic flow conditions experienced during atmospheric re-entry. In these experiments, the Aluminium Shock Tube (AST) mode was employed to generate a normal shock wave that travels through a controlled test gas. This process compresses, accelerates, and excites the gas molecules, initiating vibrational excitation, dissociation, ionisation, and radiation emission - all key phenomena observed within the shock layer of a hypersonic vehicle.

A newly developed dual channel optical emission spectroscopy arrangement was used to acquire spatially and spectrally resolved absolute radiance measurements of the thermochemically relaxing test slugs, providing a spatial field of view of 90 mm and covering a spectral range from 200 to 850 nm. The observed spectral features reveal the excited energy states of atoms and molecules in the flow, while the simultaneous spatial resolution provides insight into how these states evolve through the shock layer. Together, the spatio-spectrally resolved images encode valuable information about the thermochemical evolution occurring in the test slug.

Before analysing the non-equilibrium region, this thesis addresses discrepancies observed in equilibrium spectral radiance measurements from previous low-speed air campaigns conducted in both T6 and NASA's Electric Arc Shock Tube (EAST). While the measurements between these facilities have been consistent with one another, they exhibit a significant background offset compared to the equilibrium radiance levels predicted by NASA's CEA and NEQAIR codes. Resolving this discrepancy is an important prerequisite before carrying out any analysis of the non-equilibrium region. A reduction in spectrometer slit widths

significantly improved agreement between experiment and numerical predictions above $\sim$600 nm, removing practically all background offset, while remaining offsets below 400 nm are characterised as a function of test condition. In particular, the NO bands from 200 to $\sim$280 nm, which emit the most intense radiation levels, show improvement at lower pressures at the compromise of increased contaminant mole fractions. Numerical predictions in this region are also shown to be the most sensitive to the radiation model selected. A downstream plasma cleaner was also trialled on the final 2 m of the AST to test if improved cleaning of tube walls may reduce residual contaminant levels in the test slug or influence the observed background levels, however the results were inconclusive against leak rate and had no bearing on the remaining offset around the NO bands.

Following from this, a novel spectral fitting routine was developed, which ensures conservation of mass, momentum, energy and charge, to convert the spatio-spectral radiance data into temperature and number density profiles through a thermochemically relaxing test slug. The method uses a two-temperature model and assumes Boltzmann distributions throughout. Validations are performed by a series of artificial radiance datasets with incorporation of experimental artefacts. The conservation criteria are shown to significantly improve the species number density predictions, while vibrational temperature is accurately extracted with and without the conservation constraints. Rotational temperatures show reasonable trends though display high uncertainty levels, as predicted by a Monte Carlo analysis. Despite only being able to extract information from species which emit detectable radiation in the observed wavelength regions, the methodology accurately characterises important parameters within a thermochemically evolving test slug, and demonstrates its use as a powerful tool to determine measurements of value in future shock tube campaigns.

Finally, the new T6 AST low-speed pure nitrogen and synthetic air datasets are summarised and conditions are selected for analysis by the new spectral fitting routine. The pure nitrogen tests provide an initial simplified mixture with reduced complexity of energy exchange interactions. N_2, N_2^+ and N are extracted in shocks from 6.2 to 7.4 km/s and comparisons performed against EAST data. Results show the extent of N_2 dissociation is strongly affected by shock speed over this relatively narrow region, as well as the shock trajectory down the tube. Lastly, N_2, N_2^+, NO, N and O are extracted for a 7.3 km/s test case in synthetic air. Results are normalised by time since processed by the shock and nominal post-shock pressure, to produce profiles that show close agreement between both T6 and EAST data, and are directly representative of thermochemical state evolution occurring from the bow shock to the boundary layer edge of an entry vehicle.

Table of contents

List of Publications **v**

List of figures **xv**

List of tables **xxix**

1 Introduction **1**
1.1 Research Motivation 1
1.2 Thesis Aims 7
1.3 Thesis Structure 8

2 Literature Review **11**
2.1 Facilities 12
2.1.1 Continuous Facilities 13
2.1.2 Impulse Facilities 18
2.2 Operational Shock Tubes 23
2.2.1 Electric Arc Shock Tube 23
2.2.2 X2 Non-Reflected Shock Tube 29
2.2.3 Hyper-Velocity Shock Tube 31
2.2.4 Detonation-Driven Double-Diaphragm Shock Tube 32
2.2.5 European Shock Tube for High-Enthalpy Research 33
2.2.6 Stanford University Reflected Shock Tube 33
2.3 Radiative Transport Solvers 35
2.4 Past Attempts to Characterise Shock Layers via Emission Spectroscopy . . 36
2.4.1 Optical Emission Spectroscopy 37
2.4.2 Equilibrium Discrepancy 39
2.4.3 Evaluating Rates Against Radiance Profiles 46
2.4.4 Spectral Fitting in Pure Nitrogen 48
2.4.5 Spectral Fitting in Air 51

2.5 Summary 54

3 Experimental Method 55
3.1 The Oxford T6 Stalker Tunnel 55
3.2 The Free-Piston Driver 56
3.3 T6 Shock Tube Modes 59
3.4 Aluminium Shock Tube Mode 60
3.4.1 Principle of Operation 60
3.4.2 Facility Instrumentation 62
3.4.3 Auxiliary Infrastructure and Shot Procedure 65
3.4.4 Inconsistencies of Stagnation Line Analogy 66
3.5 Telecentric Optical Emission Spectroscopy 69
3.5.1 Physical Setup 69
3.5.2 Advantage of a Telecentric System 73
3.5.3 Intensified Cameras 76
3.5.4 Camera Triggering 76
3.6 Calibrations 77
3.6.1 Wavelength Calibrations 78
3.6.2 Instrument Line Shape 79
3.6.3 Spatial Calibrations 80
3.6.4 Spatial Resolution Function 81
3.6.5 Intensity Calibrations 83
3.7 Example Calibrated Data 88
3.8 Uncertainties 90

4 Investigation into Equilibrium Radiance Offset in Air Shock Tube Tests 92
4.1 Introduction 93
4.2 Experimental Campaign 95
4.2.1 Condition Map 95
4.2.2 Calibrated Radiance Data 97
4.3 Hydrodynamic Investigation 99
4.4 Contamination Investigation 100
4.4.1 Contaminant Gauging 101
4.4.2 Leak Rates and Manual Cleaning 102
4.4.3 Plasma Cleaning 104
4.4.4 Excess Free Electrons 106
4.5 Optical Setup and Processing 107

4.5.1 Spectrometer Slit Width . . . 107
4.5.2 Telecentric vs Telescopic . . . 109
4.5.3 In-Test Stray Light Measurements . . . 109
4.6 Radiative Modelling . . . 112
4.7 Condition Dependencies . . . 113
4.7.1 Pressure . . . 113
4.7.2 Shock Speed . . . 115
4.8 Summary of Improvements . . . 116
4.9 Conclusion . . . 118

5 Development and Validation of a Constrained Spectral Fitting Routine 120
5.1 Introduction . . . 121
5.2 Methodology . . . 123
5.2.1 Underlying Physics and Shock Tube Analogy . . . 123
5.2.2 Constrained Spectral Fitting Routine . . . 124
5.3 Validation . . . 129
5.3.1 Validation Procedure Against NESS-NEQAIR . . . 129
5.3.2 Constrained vs Unconstrained . . . 131
5.3.3 Contaminants . . . 134
5.3.4 Spatial Convolutions . . . 137
5.3.5 Adding Electron Number Density Information . . . 141
5.4 Real shock tube data: EAST-62-40 . . . 142
5.5 Conclusion . . . 147

6 Thermochemical Characterisation of Shock-Heated Pure Nitrogen 149
6.1 Introduction . . . 150
6.2 Experimental Campaign . . . 152
6.2.1 The Oxford T6 Stalker Tunnel in Aluminium Shock Tube Mode . . . 152
6.2.2 Test Summary . . . 153
6.2.3 Conditions Selected for Spectral Fitting . . . 155
6.2.4 The Effect of Pressure . . . 157
6.3 Constrained Spectral Fitting . . . 158
6.3.1 Methodology . . . 158
6.3.2 Spectral Information . . . 159
6.4 Results . . . 163
6.4.1 Vibrational Temperature (T_{ve}) . . . 163
6.4.2 Species number densities . . . 164

6.4.3 Physical properties . . . 167
6.4.4 Comparison Against Park 2T . . . 168
6.4.5 Comparison Against EAST . . . 169
6.5 Conclusion . . . 173

7 Thermochemical Characterisation of Shock-Heated Synthetic Air 175
7.1 Introduction . . . 176
7.2 Test Summary . . . 177
7.3 Radiance Data . . . 178
7.4 Spectral Fitting of T6 AST Data . . . 182
7.4.1 Methodology . . . 182
7.4.2 Selected Condition . . . 182
7.4.3 Results . . . 185
7.5 Comparison to EAST . . . 191
7.6 Comparison to 2T Model . . . 194
7.7 Conclusion . . . 196

8 Conclusions and Recommendations 198
8.1 Conclusions and Contributions . . . 198
8.1.1 Conclusions . . . 198
8.2 Recommendations For Future Work . . . 202

References 206

Appendix A Supplementary Work During Development of Constrained Spectral Fitting Routine 221
A.1 Spectral Fits of Constrained Spectral Routine for Initial NESS-NEQAIR Data 222
A.2 Contaminant Species Studies . . . 223
A.2.1 No contaminants . . . 223
A.2.2 CN only . . . 226
A.2.3 CN, C_2, C, H_2, H . . . 229
A.3 Spatial Smearing Study Full Results . . . 232
A.4 Reduced Gate Width . . . 234
A.5 Artificial Noise . . . 238
A.6 Spatial Averaging . . . 241
A.7 Boundary Layer Mass Loss . . . 243
A.8 Diffusion . . . 246

A.9 Experimental Artefacts Combined 248
A.10 Further Application of Constrained Methodology 251
A.10.1 Including T_{tr} and E^{-} 252
A.10.2 Effect of higher and lower resolution spectral data 254
A.11 Radiation Model Dependency 257

Appendix B Supplementary Content for Spectral Fitting of Pure Nitrogen Tests 259
B.1 CEA-NEQAIR Spectral Radiance Comparisons 259
B.2 Spatial Resolution Functions 261

Appendix C Supplementary Content for Spectral Fitting of Synthetic Air Tests 264
C.1 Synthetic Air Validation 264
C.2 CEA-NEQAIR Spectral Radiance Comparisons 267
C.3 Spatial Resolution Functions 268

List of figures

1.1 Summary of annual global launch attempts over the last five years. Adapted from [164]. Suborbital launches are not included. 3
1.2 Velocity-altitude map with superimposed regions of vibrational excitation, dissociation and ionisation. Taken from Anderson [1]. 4
1.3 Illustration of the evolving thermochemical state through a hypersonic vehicle shock layer. Not to scale. 5
1.4 Predictions of stagnation point convective and radiative heating for different vehicle nose radii during Earth entry, from the relations of Brandis and Johnston [20]. 6

2.1 Summary of selected mission trajectories and approximate ground test capabilities. Taken from Collen [32]. 13
2.2 Inductively Coupled Plasma torch illustrations. Both taken from the work of Casses et al. [27]. 14
2.3 Illustration and results of studying recombining non-equilibrium phenomena in air. Both taken from Tibère-Inglesse and Cruden [187]. 16
2.4 Illustrations of the PWK1 Plasma Wind Tunnel facility. 17
2.5 Schematic and t-x diagram of RST operation. Separation between shock wave and contact surface is exaggerated for clarity. Taken from Hornung Han [87]. 19
2.6 Schematic and t-x diagram of a free-piston driven ExT. Taken from Gildfind et al. [66]. 21
2.7 The Electric Arc Shock Tube (EAST) facility at NASA Ames. 24
2.8 Trend of atomic carbon and hydrogen line emissions as EAST upgrades are implemented, taken from Cruden et al. [39]. All shots performed with a pressure of 26.6 Pa (0.2 Torr) and a nominal shock speed of 10 km/s. Data are presented as relative measurements, with integrated line intensity normalised against the background radiance. 26

2.9 Effect of oxygen plasma cleaning on CN impurity levels in UV emission spectra for 10 km/s and 0.2 Torr test cases in air. High resolution spectra enable the different spectral features to be distinguished. CN is shown to reduce drastically after the driven tube section has been plasma cleaned. . . 27
2.10 Illustration of test slug emerging from the end of the X2 tube, into the test section. Associated optics included have been condensed down to a single lens. Not to scale. Taken from McGilvray et al. [119]. 30
2.11 Schematic of the free-piston double-diaphragm HVST facility. Taken from Yamada et al. [197]. 31
2.12 Illustration of the double diaphragm facility and spectral radiance measurement system. Taken from Tang et al. [180]. 32
2.13 CAD overview of the ESTHER facility. Taken from Ferreira and da Silva [60]. 33
2.14 Illustration of reflected shock tube stagnation region and associated ultraviolet laser optics. Taken from Streicher et al. [175]. 34
2.15 Single frame colour exposure of flow over a Galileo probe during expansion tube tests in the T6 Stalker tunnel. Taken from Steer et al. [171]. 38
2.16 Boltzmann plots attained from oxygen and nitrogen transitions in PWT re-entry experiments. Taken from Hermann et al. [79]. 39
2.17 Area plot of CEA equilibrium mole fraction predictions across a range of temperatures in 1 bar air. 40
2.18 Spatial and spectral radiance profiles for T6s198 (6.65 km/s, 213.9 Pa synthetic air) from the ultraviolet and visible/near-infrared spectral channels. Equilibrium spectra extracted are compared against CEA-NEQAIR, with main molecular and atomic features labelled. Adapted from Glenn et al. [69]. 41
2.19 Comparison of equilibrium spectra at 6 km/s and 2.0 Torr obtained from EAST and T6 facilities. Equilibrium predictions are shown from CEA and NEQAIR v15.3 with alternative photorecombination models. Plots taken from Cruden [42]. 42
2.20 Comparison of EAST ultraviolet spectrum to CEA-NEQAIR with and without O_2 photorecombination at 4 km/s and 10 Torr. 43
2.21 Comparison of high-resolution equilibrium spectra from ICP torch measurements and SPECAIR for an air plasma in a state of local thermodynamic equilibrium at $\sim$7500 K. The x-axis is wavelength in units of nanometres. Taken from Laux et al. [102]. 44

2.22 Comparison of SPECAIR and NEQAIR ultraviolet spectra for a ∼7000 K plasma. Shaded regions are calculated from the plasma temperature profile uncertainty limits. Taken from Glenn et al. [67]. 45
2.23 Comparison between experimental N_2/CH_4 spectrum and SPECAIR prediction at the exit of an ICP torch with local thermodynamic equilibrium temperature of ∼6750 K. Taken from Merhaben et al. [125]. 45
2.24 Comparison of one-dimensional post-shot analysis code results fed into NEQAIR for T6s164 with a 9.59 km/s shock in 0.1 Torr air (close to a benchmark EAST test case). Taken from Clarke et al. [30]. 47
2.25 Assessment of the spectral distribution averaged over ± 1 mm of peak radiance for 7.3 km/s test slugs in 33.3 Pa synthetic air from T6 AST, compared to NESS simulations including a 0.08% C_2 mole fraction. Plots taken from Clarke et al. [31]. Experimental data is from the work of this thesis, and analysed by spectral fitting in Chapter 7. 48
2.26 Comparison of the experimental spectrum from the supposed equilibrium region of the EAST-62-40 test slug against CEA and spectral fitting results for different spectral channels. The shot condition is at 6.88 km/s in 0.2 Torr pure nitrogen. Taken from Tibère-Inglesse and Cruden [187]. 49
2.27 Rotational and vibrational temperature profiles obtained by fitting the spatially resolved spectra for the Red and Blue cameras. For shot EAST-62-40 at 6.88 km/s in 0.2 Torr pure nitrogen. Taken from Tibère-Inglesse and Cruden [187]. 50
2.28 Time-resolved rotational and vibrational temperatures of N_2 (C) and N_2^+ fitted from pure nitrogen experimental spectra at 6.6 km/s and 200 Pa. Taken from Tang et al. [180]. 51
2.29 NO and OH A-state vibrational temperatures in the post-shock relaxation region, against results from a thermochemical model. Taken from Sharma et al. [155]. 52
2.30 Experimental temperatures compared with a computation by a zero-dimensional state-to-state model and a two-temperature LAURA simulation. T_{frozen} = 8267 K and $T_{equilibrium}$ = 4179 K. Shock location is set at x = 0 mm. Taken from Yanes and Austin [199]. 53

3.1 Diagram showing different T6 facility modes, taken from Collen [32]. . . . 56

3.2 Summary of primary shock speed performance from different driver technologies, including the free-piston driver (FPD). P_4/P_1 represents the driver:shock tube pressure ratio at the moment of diaphragm burst. Taken from Bakos and Erdos [3]. 57
3.3 Earth entry trajectories alongside T6 shock tube conditions achieved and performance limit predictions of each ST mode. Adapted from Collen [32]. 59
3.4 Radiation emission from a test slug traversing across AST window during a shot. 60
3.5 Section view of T6 Stalker tunnel in AST mode from above. Taken from Glenn et al. [69]. 60
3.6 Illustration of the analogy between a hypersonic vehicle stagnation line and a shock tube experiment. Not to scale. A relaxing radiance profile is included to aid the illustration. 61
3.7 Image of AST Pitot rake, looking into dump tank. 63
3.8 Engineering drawing of the T6 AST, with STS and Pitot rake measurement locations shown. The main drawing scale is 50:1. All dimensions are in millimetres. Taken from Collen [32]. 64
3.9 Individual slices of test gas processed by a decelerating shock. Colouring at each STS represents the decreasing entropy of sequential slices, which together constitute the final gradient in the resulting test slug. Taken from Satchell et al. [153]. 67
3.10 Plot to illustrate the differences in post-shock axial velocity, owed to differences in particle time of flight, between an entry vehicle stagnation line and a shock tube. Post-shock axial velocity in the shock frame of reference ($U_{2,S}$) is plotted against post-shock distance (X_S), for a shock travelling at U_S. . . 69
3.11 The Vis/NIR (upper) and UV/Vis (lower) telecentric OES systems capturing radiation from a shock layer traversing across the windows. Not to scale. Longpass filters in the UV/Vis setup are only necessary when viewing above 400 nm. 70
3.12 Illustration of ray paths for fully telescopic and fully telecentric optical systems. Mirrors are simplified down to the relevant focusing mirrors. A<B & A<C for telescopic (illustrating increased OSF further from centre of FOV), while A=B=C for telecentric (since OSF is independent of location in FOV). f denotes the focal length of the respective telecentric focusing mirrors. 73

3.13 OSF's plotted as a function of distance from FOV centre for both blue and red OES systems. These have been derived by numerical ray tracing. The width of the OSF increases by ~50% from the centre to the FOV limit. This demonstrates the optical systems are not perfectly telecentric. 74
3.14 Comparison of OSF's for the new blue and red OES systems against previous telescopic setups used in prior T6 AST campaigns. Ray traces are performed 30 mm downstream from the FOV centre, where the shock is typically located during camera gating. 75
3.15 Example ILS broadening functions for both (a) Blue and (b) Red optical setups, fitted with a square root Voigt function. Measured line shapes were acquired using a 150 G/mm grating and slit width set to 10μm for both spectrometers. Corresponding Gaussian and Lorentzian FWHM's are: 1 nm and 0.0001 nm respectively for the blue; 0.6 nm and 0.00005 nm for the red. 80
3.16 Image of (a) the diffused light leaving the calibration plate positioned exactly on tunnel centreline and (b) the consequent 2D image attained (bottom) and summed spatial profile of peaks (top) to perform a spatial calibration. . . . 81
3.17 T6s492 total SRF's and constituent components. 82
3.18 Diagram of OES system calibration process above 300 nm. Taken from Collen [32] 84
3.19 Diagram of additional steps required to calibrate the Blue OES system below 300 nm. The plot key is identical to Fig. 3.18. Taken from Collen [32]. . . . 85
3.20 Images of the Integrating Sphere and Deuterium Lamp positioned during the intensity calibration of the blue spectral channel. The pedestal and mounts were each designed to ensure the centre of each light source was level with the tube centreline. 86
3.21 Calibrated spatio-spectral radiance data for T6s492 (6.65km/s, 90 Pa fill in pure nitrogen). Horizontal green lines indicate spatial region averaged over to generate spectral radiance plot. Vertical green lines indicate wavelength region integrated over to generate spatial radiance profile. The yellow shaded region indicates a region purposely blocked for an alternative stray light extraction studied in Chapter 4. 89
3.22 Typical uncertainty spectral dependence from both spectral channels, in the equilibrium and non-equilibrium region, for the image acquisition and calibration process discussed in this chapter. Extracted from Collen [32] . . 91

4.1 Experimental equilibrium spectral radiance in synthetic air captured in previous (a) T6 AST [69] and (b) EAST [45] campaigns. CEA-NEQAIR results in synthetic air have been convolved with appropriate instrument line shapes for comparisons. 94
4.2 Condition map of synthetic air and pure nitrogen shots from the recent T6 AST low-speed campaign. Shots from the original AST low-speed campaign are also included. 96
4.3 Example shock speed profile typical of the nominal 7.1 km/s, 175 Pa, 1 bar post-shock condition targetted in the first stage of the campaign. Note that the shock trajectory is only shown for the AST section (after the conical expansion). 96
4.4 Calibrated spatio-spectral radiance data for T6s459 (6.72km/s, 175 Pa fill in synthetic air). Horizontal lines indicate spatial region averaged over to generate spectral radiance plot. Vertical lines indicate wavelength region integrated over to generate spatial radiance profile. CEA-NEQAIR spectral radiance prediction in synthetic air provided for comparison (in pink). . . . 98
4.5 Experimental ultraviolet radiance profile from T6s198 (6.55 km/s in 213.9 Pa synthetic air) compared to CEA-NEQAIR and LASTA-NEQAIR predictions. Adapted from Glenn et al. [69]. 99
4.6 Spectral fit profiles and associated individual contributions over 335 to 395 nm for tests summarised in Table 4.5. CEA-NEQAIR predictions are also shown for comparison. 103
4.7 Implementation of GV10x 300W Downstream Asher from ibss Group, Inc. to the final 2 m section of AST on both (a) upstream and (b) downstream ends. 105
4.8 Low and high resolution ultraviolet spectra after plasma cleaning the final 2 m section of AST. Spectral fitting is used to provide estimates of CN contributions, as listed in Table 4.6. 106
4.9 Equilibrium spectra from T6s465 and T6s464 (both at 7 km/s, 175 Pa, 101.2 kPa post-shock) with CEA-NEQAIR predictions for different N bound-free background levels. 107
4.10 Comparison of measured equilibrium spectral radiance normalised by CEA-NEQAIR predictions. (a) Data from 6.5–7.4 km/s with 40–50 kPa post-shock pressures, using telecentric OES. (b) Comparison of telecentric vs. telescopic OES at 7.1 km/s, 100 kPa. "Narrow" slits are 10μm, and "wide" slits are 170μm (Blue) and 100μm (Red). 108

4.11 Image of window holders installed into AST test section. Black surfaces are flush with tube inner wall to remove reflections in opposing spectral images. 110
4.12 Comparison of stray light levels taken pre- and post-shock and the resulting equilibrium spectra. Performed to the ultraviolet spectral channel of T6s481 (5.7 km/s, 261.1 Pa fill in synthetic air, 99.7 kPa post-shock). 111
4.13 Equilibrium ultraviolet spectral radiance of T6s481 (5.7 km/s, 261.1 Pa fill in synthetic air, 99.7 kPa post-shock). CEA simulation results were fed into NEQAIR and SPECAIR radiation codes. Attempts in NEQAIR using new O_2 photodissociation modelling [42] and increasing N bound-free emission are included. Dashed lines show cumulative radiance profiles on the right hand y-axis. 113
4.14 Radiance profiles of lowest pressure synthetic air test: T6s491 (7.25 km/s, 18 Pa fill, 11.2 kPa post-shock). The relaxation profile displays a plateau at the end of the observable test slug, indicating valid thermochemical equilibrium data for the shot with longest relaxation time. 114
4.15 Plots to assess the effect of post-shock pressure on remaining discrepancies in synthetic air ultraviolet equilibrium spectra, for shocks from 7 to 7.4 km/s. 115
4.16 Equilibrium spectral radiance deviations from CEA-NEQAIR predictions for synthetic air shots of similar post-shock pressure and different shock speeds. 116
4.17 Example of experimental equilibrium spectra in close agreement with CEA-NEQAIR predictions for synthetic air test T6s483 (8.0 km/s, 33.0 Pa fill, 23.4 kPa post-shock pressure). 117
4.18 Example of experimental equilibrium spectra in close agreement with CEA-NEQAIR predictions for pure nitrogen test T6s477 (7.4 km/s, 73 Pa fill, 41.7 kPa post-shock pressure). 117

5.1 Flow diagram of the constrained spectral fitting routine. The SRF scaling is explained in Section 5.3.4 126
5.2 Steps to generate artificial NESS-NEQAIR spectra of T6s492 (6.65 km/s in 90 Pa pure nitrogen): (a) and (b) are produced by NESS and fed into NEQAIR to make (c) and (d); averaging over chosen spatial region, as shown by green lines, produces spectra as shown in (e) and (f). 130
5.3 Comparison of T_{tr} and T_{ve} attained from constrained and unconstrained spectral fitting against the original NESS profiles. 131
5.4 Comparison of species number densities attained by constrained and unconstrained spectral fitting against the original NESS profiles. 132

5.5 Post-shock physical properties corresponding to the temperature and species number density profiles attained by constrained and unconstrained spectral fitting. . . . 133
5.6 Simulations of equilibrium spectral radiance for T6s492 (6.65 km/s, 90 Pa fill in pure nitrogen) with and without contaminants. . . . 134
5.7 Results from spectrally fitting a contaminated NESS-NEQAIR simulation of T6s492. Contaminant species included in the spectral fitting routine (in addition to N_2, N_2^+, N, N^+ and E^-) are labelled. . . . 136
5.8 Spatial and spectral profiles before and after applying spatial convolutions, immediately behind the shock. Blue and Red radiance profiles are based on NESS simulations of T6s492. Convolutions in each channel are performed with the corresponding SRF functions. . . . 138
5.9 Plots to illustrate the generation of the SRF weighting profile and positioning against artificially convolved NESS-NEQAIR radiance profiles. . . . 139
5.10 Standard and weighted spectral fit results against the convolved NESS-NEQAIR simulated data averaged over the first 0.3 mm behind the shock for portions of the UV spectrum. . . . 140
5.11 T_{ve} and N_2^+ extracted by spectrally fitting convolved data with and without the SRF weighting correction. . . . 141
5.12 Results from including electron number densities into the constrained spectral fitting routine. . . . 142
5.13 Shock speed profile for EAST-62-40 in 26.6 Pa pure nitrogen. . . . 143
5.14 Vibrational temperature profiles extracted for EAST-62-40 via alternate spectral fitting methodologies. . . . 144
5.15 Number density profiles attained from constrained spectral fitting of EAST-62-40 with and without shock deceleration effects. . . . 145
5.16 Constrained spectral fit results of EAST-62-40 by fitting with and without the effects of shock deceleration. . . . 146

6.1 The T6 Aluminium Shock Tube, connected to the secondary driver (left) and dump tank (right). Taken from Glenn et al. [69]. . . . 152
6.2 Map of pure nitrogen conditions from recent T6 AST campaign. The tests for which spectral fitting have been performed in this paper have been highlighted. Adapted from Glenn et al. [68]. . . . 153
6.3 Shock speed and radiance profiles of the T6 tests selected for spectral fitting in this paper. Shock profiles are only plotted for the AST section of T6 . . . 155

6.4 Spectra for T6 AST pure nitrogen tests selected for spectral fitting, from the end of each test slug. 156
6.5 Spectra for T6 AST pure nitrogen tests selected for spectral fitting, taken over the peak 2 mm region. 157
6.6 Radiance profiles of T6 AST tests with similar shock speeds (as listed in Table 6.1) normalised by respective post-shock pressures, to emphasise the extended relaxation in lower pressure tests. Static pressure traces from the penultimate STS before camera gating are also provided. 158
6.7 CEA-NEQAIR v15.1 simulation results for T6s492 (6.65 km/s at window, 89.95 Pa fill pressure, ∼41.5kPa post-shock pressure) in pure nitrogen with 0.05% CO_2 mole fraction. Individual species and molecular bands are plotted separately within subplots. N+ and other N2 bands have been ignored since they are negligible in comparison. Spectra have been convolved with ILS of the experimental data. 161
6.8 Spectral fit results for nominal T6s492, through different stages of the excited test slug. Results are exemplary of typical spectral fit agreements. 162
6.9 Vibe-electronic temperature profiles extracted by constrained spectral fitting for the selected pure nitrogen shots. Dashed lines show CEA predictions. . 164
6.10 Mole fraction profiles extracted by constrained spectral fitting for the selected pure nitrogen shots. Dashed lines show CEA predictions. 165
6.11 Post-shock physical properties corresponding to the spectral fitting results of the selected pure nitrogen tests. 167
6.12 Comparison of profiles extracted for T6s492 against the predictions of NESS 1D solver using Park 2T model and Park rates. 168
6.13 Shock speed profiles of T6s492 and EAST-62-40 relative to optical access location. 169
6.14 Comparison of T6s492 and EAST-62-40 outputs from constrained spectral fitting. x-axes have been normalised by multiplying the time post-shock by the nominal post-shock pressures listed in Table 6.5. 171
6.15 Comparison of T6s492 and EAST-62-40 outputs from constrained spectral fitting. x-axes have been normalised by multiplying the time post-shock by the local densities inferred by the spectral fitting routine. 172

7.1 Map of synthetic air conditions from recent T6 AST campaign. Selected tests for spectral fitting, T6s484 and T6s501 of ∼7.3 km/s, 33.3 Pa fill and ∼20 kPa post-shock, have been highlighted. 178

7.2 Calibrated spatio-spectral radiance data for T6s484 (7.3km/s, 33.3 Pa fill in synthetic air). Horizontal green lines indicate spatial region averaged over to generate spectral radiance plot. Vertical green lines indicate wavelength region integrated over to generate spatial radiance profile. The yellow shaded region was purposely blocked in the Blue channel to gauge stray light on the camera sensor array. 179
7.3 Spectra acquired for T6s484 from both ultraviolet and visible/near-infrared spectral channels in different portions of the test slug. 179
7.4 Cumulative radiance trends across shots from new synthetic air dataset. Pressures quoted are nominal post-shock levels, though there are some deviations between tests. 181
7.5 Shock speed and radiance profiles for the selected test cases. Shock profiles are only plotted for the AST section of T6. Radiance profiles are generated by integrating over the spectral regions available for each test and channel. . 184
7.6 Spectral fits achieved towards the end of the test slugs for nominal test case of 7.3 km/s in 33.3 Pa synthetic air. Spectra limits and ILS functions used during fitting are as listed in Tables 7.2 and 7.3. 185
7.7 Spectral fits achieved in the non-equilibrium peak for nominal test case of 7.3 km/s in 33.3 Pa synthetic air. Spectra limits and ILS functions used during fitting are as listed in Tables 7.2 and 7.3. 186
7.8 Comparison of spectral fit outputs for nominal test case of 7.3 km/s in 33.3 Pa synthetic air and $\sim$20 kPa post-shock. Different spectral limits used during fitting for each case are summarised in Table 7.2. NO was not captured in T6s501 and thus not plotted. 188
7.9 Shock speed profile for EAST-59-51. 192
7.10 Comparison of T6s484 and EAST-59-51 outputs from constrained spectral fitting. x-axes have been normalised by multiplying the time post-shock by the nominal post-shock pressures. 193
7.11 Comparison of profiles extracted for T6s484(B) against the predictions of NESS 1D solver using Park 2T model and modified Cruden rates. 194
7.12 Comparison of trans-rotational temperatures extracted for T6s484 (B) and T6s501 spectral fitting attempts against predictions of NESS 1D solver using Park 2T model and modified Cruden rates. 195

A.1 Spectral fit results in different portions of the test slug for first run of the constrained spectral fitting routine in Section 5.3.2. The blue and red limit lines indicate the wavelength regions where spectral fitting was performed. Final results are plotted from the VUV through to the NIR to serve as predictions in these areas, from the temperatures and number densities arrived at. 222
A.2 T_{tr} and T_{ve} extracted by spectrally fitting contaminated NESS-NEQAIR radiance, without including any contaminants in the fitting of both constrained and unconstrained attempts. 223
A.3 Number densities of the 5 species of interest, extracted by spectrally fitting contaminated NESS-NEQAIR radiance, without including any contaminants in the fitting of both constrained and unconstrained attempts. 224
A.4 Post-shock physical properties corresponding to the temperature and species number density profiles attained by constrained and unconstrained attempts, without including any contaminants in the spectral fitting. 225
A.5 T_{tr} and T_{ve} extracted by spectrally fitting contaminated NESS-NEQAIR radiance and including CN in the routine. 226
A.6 Number densities extracted by spectrally fitting contaminated NESS-NEQAIR radiance and including CN in the routine. 227
A.7 Spectral fit results from equilibrium, relaxation and peak non-equilibrium portions of the contaminated test slug, implementing N_2, N, N_2^+, N^+, CN and E^- species in the fitting routine. Blue and red limit lines indicate the wavelength regions where the spectral fit was performed. 228
A.8 T_{tr} and T_{ve} extracted by spectrally fitting contaminated NESS-NEQAIR radiance, from adding CN, C_2, C, H_2 and H to the routines. 229
A.9 Number density profiles for species of interest extracted by spectrally fitting contaminated NESS-NEQAIR radiance, from adding CN, C_2, C, H_2 and H to the routine. 230
A.10 Number density profiles for contaminant species extracted by spectrally fitting contaminated NESS-NEQAIR radiance, from adding CN, C_2, C, H_2 and H to the routine. 231
A.11 Post-shock physical properties corresponding to spectral fitting results of convolved data with and without the SRF weighting correction, as considered in Section 5.3.4. 232
A.12 Results of spectrally fitting convolved data with and without the SRF weighting correction for parameters not shown in Section 5.3.4. 233

A.13 Comparison of SRF profiles for different camera gate widths for Blue and Red channels. 234
A.14 Half gate width: T_{tr} and T_{ve} extracted from spectrally fitting artificial data convolved with half the true gating time. 235
A.15 Zero gate width: T_{tr} and T_{ve} extracted from spectrally fitting artificial data convolved with SRF containing no gating contribution. 235
A.16 Half gate width: Number densities extracted from spectrally fitting artificial data convolved with half the true gating time. 236
A.17 Zero gate width: Number densities extracted from spectrally fitting artificial data convolved with SRF containing no gating contribution. 237
A.18 T_{tr} and T_{ve} extracted by spectrally fitting against noisy NESS-NEQAIR artificial spectra, plotted with the original NESS outputs and CEA equilibrium prediction for comparison. 238
A.19 Spectral fit profiles in (a) equilibrium (b) relaxation and (c) immediate post-shock portions of the test slug, plotted against original NESS-NEQAIR spectral radiance traces with random noise superimposed. The noise level is representative of that in typical shot data. 239
A.20 Species number density profiles extracted by spectrally fitting against noisy NESS-NEQAIR artificial spectra, plotted with the original NESS outputs and CEA equilibrium prediction for comparison. 240
A.21 Radiance profile integrated over 290-520 nm, from the NESS-NEQAIR simulation of T6s492 (6.65 km/s, 90 Pa in pure nitrogen). Shaded regions illustrate the portions of the test slug averaged spatially to generate spectra, which are defined at the mid-point of each region as indicated by black crosses. An inset plot shows the later portions of the test slug, where radiance is much lower in magnitude than immediately behind the shock. 241
A.22 Species number density profiles extracted by fitting against average spectra, produced from different portions of the first 110 mm from the NESS-NEQAIR simulation. Original NESS outputs and CEA equilibrium predictions are plotted for comparison. 242
A.23 T_{tr} and T_{ve} extracted by fitting against average spectra, produced from different portions of the first 110 mm from the NESS-NEQAIR simulation. Original NESS outputs and CEA equilibrium predictions are plotted for comparison. 243
A.24 Plots of constraints defined from NESS and results of the constrained spectral fitting routine. 244

A.25 T_{tr} and T_{ve} attained against the original NESS profiles after spectrally fitting by constraining with the NESS static pressure trace. 244
A.26 Species number densities attained against the original NESS profiles after spectrally fitting by constraining with the NESS static pressure trace. 245
A.27 T_{tr} and T_{ve} from spectrally fitting NESS-NEQAIR radiance data with diffusion effects included. 246
A.28 Species number density profiles from spectrally fitting NESS-NEQAIR radiance data with diffusion effects included. 247
A.29 T_{tr} and T_{ve} attained from constrained and unconstrained fitting of artificial data with multiple experimental artefacts included. 248
A.30 Number density profiles attained from constrained and unconstrained fitting of artificial data with multiple experimental artefacts included. 250
A.31 Post-shock physical properties corresponding to the constrained unconstrained spectral fits of artificial data with multiple experimental artefacts included. 251
A.32 Results from performing constrained spectral fitting routine on initial NESS-NEQAIR data based on T6s492 (from Section 5.3.2) with the inclusion of T_{tr} data for one run, and T_{tr} and E^- for another. 253
A.33 Examples of the artificial T6s492 NESS-NEQAIR spectral radiance traces from Section 5.3.2 with: (a) increased wavelength range; (b) high resolution ultraviolet data (equivalent to resolution of real high res. data); and (c) even higher resolution ultraviolet data (double that of real high resolution data). . 254
A.34 Results from applying constrained spectral fitting routine to artificial NESS-NEQAIR data with different spectral resolutions and wavelength regions. Results have been normalised against the NESS output values. A logarithmic x axis is used to aid readability of results near the shock front. 256
A.35 Spectral radiance predictions from a NESS simulation of 7.3 km/s 33.3 Pa synthetic air test case, with version 15.3 of NEQAIR at different points through the predicted test slug. Both Boltzmann and non-Boltzmann QSS model results are shown for comparison. 257

B.1 T6s477 measured equilibrium spectral radiance traces compared to CEA-NEQAIR predictions convolved with experiment ILS. 260
B.2 T6s482 measured equilibrium spectral radiance traces compared to CEA-NEQAIR predictions convolved with experiment ILS. 260
B.3 T6s492 measured equilibrium spectral radiance traces compared to CEA-NEQAIR predictions convolved with experiment ILS. 261

B.4 EAST-62-40 measured equilibrium spectral radiance traces compared to CEA-NEQAIR predictions convolved with experiment ILS. 261
B.5 T6s477 total SRF's and constituent components. 262
B.6 T6s482 total SRF's and constituent components. 262
B.7 T6s492 total SRF's and constituent components. 263
B.8 EAST-62-40 total SRF's and constituent components. 263

C.1 Validation of constrained spectral fitting routine for NESS-NEQAIR artificial radiance data at 7.3 km/s in 33.3 Pa synthetic air. Selected parameters showed close agreement to original NESS results. 265
C.2 Spectral fit results in different portions of the test slug against the NESS-NEQAIR generated spectra for 7.3 km/s shock in 33.3 Pa synthetic air. Emission data from NESS-NEQAIR was only provided in the plotted spectral regions. 266
C.3 T6s484 measured equilibrium spectral radiance traces compared to CEA-NEQAIR predictions convolved with experiment ILS. 267
C.4 T6s501 measured equilibrium spectral radiance traces compared to CEA-NEQAIR predictions convolved with experiment ILS. 268
C.5 EAST-59-51 measured equilibrium spectral radiance traces compared to CEA-NEQAIR predictions convolved with experiment ILS. 268
C.6 T6s484 total SRF's and constituent components. 269
C.7 T6s501 total SRF's and constituent components. 269
C.8 EAST-59-51 SRF's. 270

List of tables

2.1 Comparison of different operation modes of the Oxford T6 Stalker Tunnel. . 18

3.1 T6 driver conditions used in the works of this thesis. Diaphragms are made of aluminium (Al) or stainless steel (S.S.) depending on selected condition. 58
3.2 Optical components used in the blue and red telecentric OES setups. 72

4.1 Summary of test gas transitions observed in the new T6 AST low-speed synthetic air dataset, over the UV/Vis and Vis/NIR wavelength regions. . . 98
4.2 Summary of contaminant transitions observed in the new T6 AST low-speed dataset, over the UV/Vis and Vis/NIR wavelength regions. 100
4.3 Summary of condition parameters for selected tests, split into high resolution ultraviolet spectra (top) and low resolution spectra (bottom). 101
4.4 Summary of temperatures and number densities extracted by spectral fitting of the ultraviolet spectra for tests studied in this paper. CEA predictions are provided for comparison. Results are split into high resolution spectra (top) and low resolution spectra (bottom) as provided in Table 4.3. Uncertainties are extracted from a Monte Carlo analysis. 102
4.5 Comparison of repeat shots T6s461 and T6s462 in 175 Pa synthetic air. CN radical radiance contributions and number densities are as extracted from spectral fits. 104
4.6 Summary of shots to assess effect of plasma cleaning. Shock speeds quoted are at the window, all conducted in a 175 Pa test gas. Leak rate is measured once the facility is re-assembled and pumped down to ultimate pressure. . . 105

5.1 Summary of inputs and outputs of the constrained spectral fitting routine. . 124

6.1 Selected T6 test conditions to perform spectral fitting (top). Plus similar low and high pressure tests (bottom). 154

6.2 ILS FWHM's used for spectral fitting of T6 data, fitted to the square root of a Voigt function. The same slit functions apply to all three T6 tests selected. 154
6.3 Summary of molecular transitions observed in selected pure nitrogen test cases. The energy of the upper level of each species is given relative to their ground states. CN is included due to the presence of carbon contamination. 159
6.4 List of atomic nitrogen lines observed in Vis/NIR of selected tests. 160
6.5 Selected T6 and EAST test conditions for analysis. Wavelength ranges used for spectral fitting are listed. Shock speeds quoted are as measured at windows. 169
6.6 ILS FWHM's used for spectral fitting of selected tests, fitted to the square root of a Voigt function. 170

7.1 Summary of synthetic air and contaminant spectral features observed in the selected tests, over the UV/Vis and Vis/NIR wavelength regions. 180
7.2 Selected T6 tests for spectral fitting analysis. Wavelength ranges used for spectral fitting are listed. T6s484 trialled spectral fitting over two UV regions to assess the effect of uncertainties around radiative modelling of NO in the lower wavelengths. 183
7.3 ILS FWHM's used for spectral fitting, applied to the square root of a Voigt function. 183

Chapter 1

Introduction

> Let's think the unthinkable, let's do the undoable. Let us prepare to grapple with the ineffable itself, and see if we may not eff it after all.
>
> Douglas Adams

1.1 Research Motivation

The exploration of space has long been a measure of a nation's technological advancements and a demonstration of their scientific prowess, calling upon a broad range of subjects and disciplines. The achievements of various space missions through history serve as accolades to the scientists and engineers of the time. These include, though are not limited to: the Apollo 11 moon landing in 1969 [130]; the launch of the Hubble space telescope in 1990 [133]; the start of the International Space Station (ISS) assembly in 1998 [136]; and the successful landing of Spirit (2004) [137], Opportunity (2004) [137] and Curiosity (2012) [138] rovers on Mars, to search for signs of water and microbial life. Each mission has expanded humanity's reach into the final frontier of space, with future planned missions aiming to extend this further. Artemis II is scheduled for late 2025, as the first crewed mission of the Orion spacecraft to carry astronauts around the moon and back [134]. This is in preparation for future lunar landings. The European Space Agency's (ESA) Jupiter Icy Moons Explorer, "JUICE", was launched in 2023 with a trajectory set to arrive at Jupiter in 2031, and has the objective of making detailed observations of Jupiter and three of its large ocean-bearing moons - Ganymede, Callisto and Europa [58]. NASA are undertaking work to send a rotorcraft "Dragonfly" to Saturn's moon Titan, with launch and arrival scheduled for

2028 and 2034 respectively [165]. Additionally, NASA is advancing a range of technologies in the effort to send astronauts to Mars as early as the 2030s [132]. Further afield, work is underway to understand the aerothermal environment of proposed ice giant entry missions to Uranus and Neptune [57] in the outer limits of our solar system.

Closer to home, the space industry is evolving. The year 2020 marked the first commercial crewed space flight, with Space X's Crew Dragon capsule successfully carrying astronauts to the ISS. This is a product of the huge rise of private companies in the space sector and what seems to be the "dawn of a new era in commercial space exploration". Transformation in the space sector has been marked by significant innovations and contributions from private entities, such as Space X [167], Blue Origin [9] and Rocket Lab [6] - developing reusable rocket technologies and drastically reducing launch costs (under NASA's Commercial Crew Program [135]) in the pursuit of making space exploration a more financially viable endeavour. These private companies have transitioned from supporting roles to leading major space initiatives. This shift has introduced competition, which in turn accelerated technological advancements and has ultimately expanded access to space. In March 2024 alone, Space X successfully launched twelve Falcon 9 two-stage rockets [8], including three launches within 20 hours, demonstrating the operational efficiency and capacity of the modern day. The Falcon 9 is commonly used for deploying satellites into Low Earth Orbit (LEO), and often involves the return and landing of the first stage for re-use [166]. Additionally, it's been used to launch the aforementioned Space X Dragon capsule [165], into a LEO to convene with the ISS. The frequency of LEO missions has increased exponentially, since even the start of the century. In 2007, nearly 50 years after the initial space race of the 1960s, the number of catalogued objects in LEO reached the 10,000 mark. This is equivalent to almost 200 objects a year. Only 15 years later, in late 2021, the 20,000 mark was crossed - equivalent to more than 650 objects per year over that time [183]. Figure 1.1 shows how the number of attempted space launches worldwide has increased over the last five years, reaching a total of 223 attempts in 2023. Around 80% of which targeted a LEO, driven largely by the deployment of satellite constellations such as Space X's Starlink [164].

It is therefore apparent that, although missions to other planets in the solar system and beyond may be exciting excursions into the unknown and monumental feats of engineering, it is actually the Low Earth Orbit mission which is by far the most frequent and still the most profitable to the emerging private space entities. Additionally, LEO missions play important roles in the military and defence sectors to bolster national security, primarily in surveillance and rapid response. Missile early-warning systems are an example of this. The precision and timeliness of data acquired during such missions is important for informed decision making in dynamic security environments. Furthermore, the most advanced hypersonic technologies

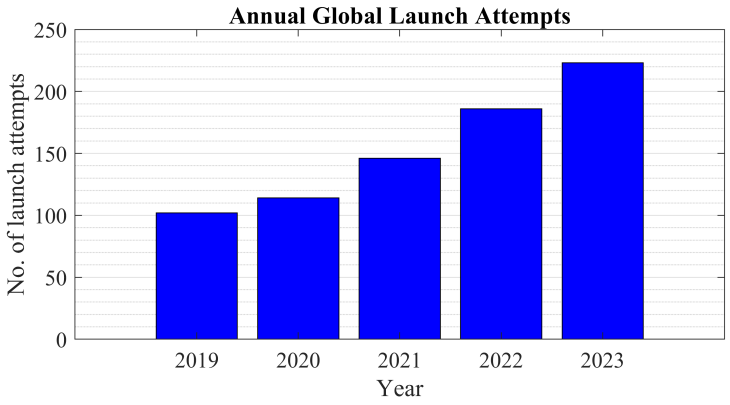


Fig. 1.1 Summary of annual global launch attempts over the last five years. Adapted from [164]. Suborbital launches are not included.

are necessary to provide a rapid response to potential security threats. Continued research to improve hypersonic vehicle design is thus of paramount importance.

A critical aspect of many of these LEO missions is the safe return of astronauts, payloads and rocket infrastructure back to Earth. This return journey involves an extreme heating environment which must be endured for the vast majority of the trajectory. Figure 1.2 plots typical return trajectories of the space shuttle (a historic example of a LEO return vehicle) in relation to the onset of various high-temperature gas effects. It's evident that vibrational excitation and dissociation of molecular N_2 and O_2 species plays a dominant role for most of the journey. These processes arise due to the bow shock ahead of the entry vehicle, as it penetrates through the Earth's atmosphere a number of times faster than the local speed of sound of the quiescent gas. The shock provides a mechanism to convert the kinetic energy of the vehicle into the internal energy of the gas molecules, which almost instantaneously attain excited energy states as a result. In an attempt to release this energy and reach a new state of equilibrium, the molecules undergo various thermochemical reactions as they progress through the shock layer towards the surface of the vehicle. This includes collisional processes such as vibrational excitation, dissociation and ionisation, along with radiation emission as a means to drop between discrete energy states via the release of a photon. These processes have been illustrated in Fig. 1.3.

The high-temperature, thermochemically transitioning, environment can yield both significant convective and radiative heat fluxes towards the vehicle surface. Just before the turn of the century, Gnoffo [70] indicated that the ability to predict the aerothermodynamic heating environment, of trajectories achieved even 30 years prior, was still lacking. More recently, the work of Brandis and Johnston [20] (2014) developed on the stagnation point heat flux relations of Sutton and Graves Jr [177] (1971) for convective heating, and similarly on the

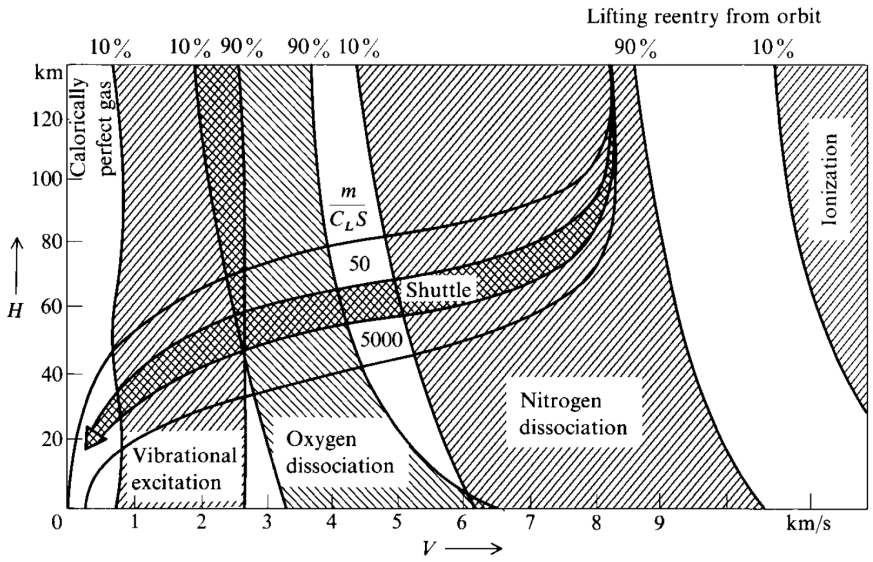


Fig. 1.2 Velocity-altitude map with superimposed regions of vibrational excitation, dissociation and ionisation. Taken from Anderson [1].

Tauber and Sutton [182] (1991) relations for radiative heating. These have been applied in Fig. 1.4 to predict both heat fluxes for a range of Earth entry velocities, densities and vehicle nose radii. It's apparent that for LEO return missions, peaking at velocities around 8 km/s, that convective heating dominates over the radiative heating to the vehicle. However, the radiative heating contribution increases more rapidly as both vehicle size and velocity increase.

The degree of thermochemical non-equilibrium at the boundary layer edge is also an important factor. Timescales of the thermal relaxation and chemical reactions relative to particle times of flight through the shock layer determine the reach of the non-equilibrium phenomena towards the vehicle surface. This can have a significant influence on shock wave/boundary layer interactions and ultimately the heat flux experienced by a vehicle, as shown by Jiang et al. [95]. It's therefore desirable to characterise the thermochemical state of the gas through this region, to improve entry vehicle design for future missions. Though the high-temperature gas effects can be detrimental to the vehicle, the radiation emission provides a means to perform non-intrusive optical spectroscopy measurements, which have proved invaluable for assessing the thermochemical state of high enthalpy flows [1].

There are other reasons, beyond heating, to motivate characterisation of the thermochemical state through a LEO return vehicle's shock layer. In the post-shock region, the gas undergoes a phase change to become a partially ionised plasma, due to the presence of free

[1]Various examples of spectrally resolved radiation measurements performed in the effort to study planet entry flow environments are given in the literature review in Chapter 2.

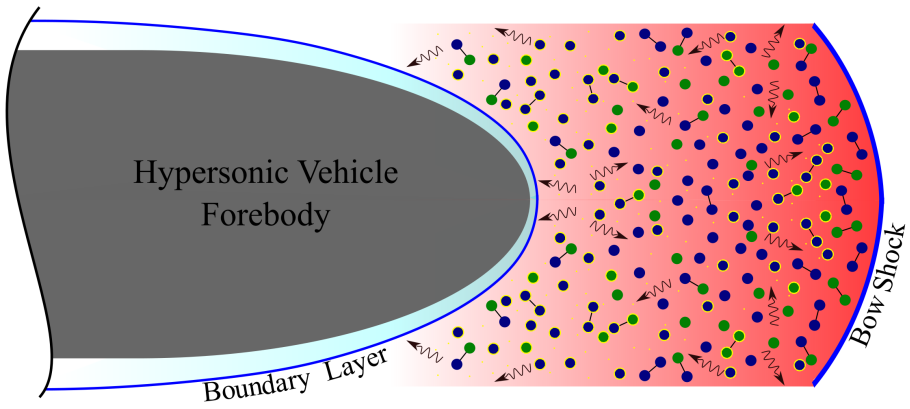
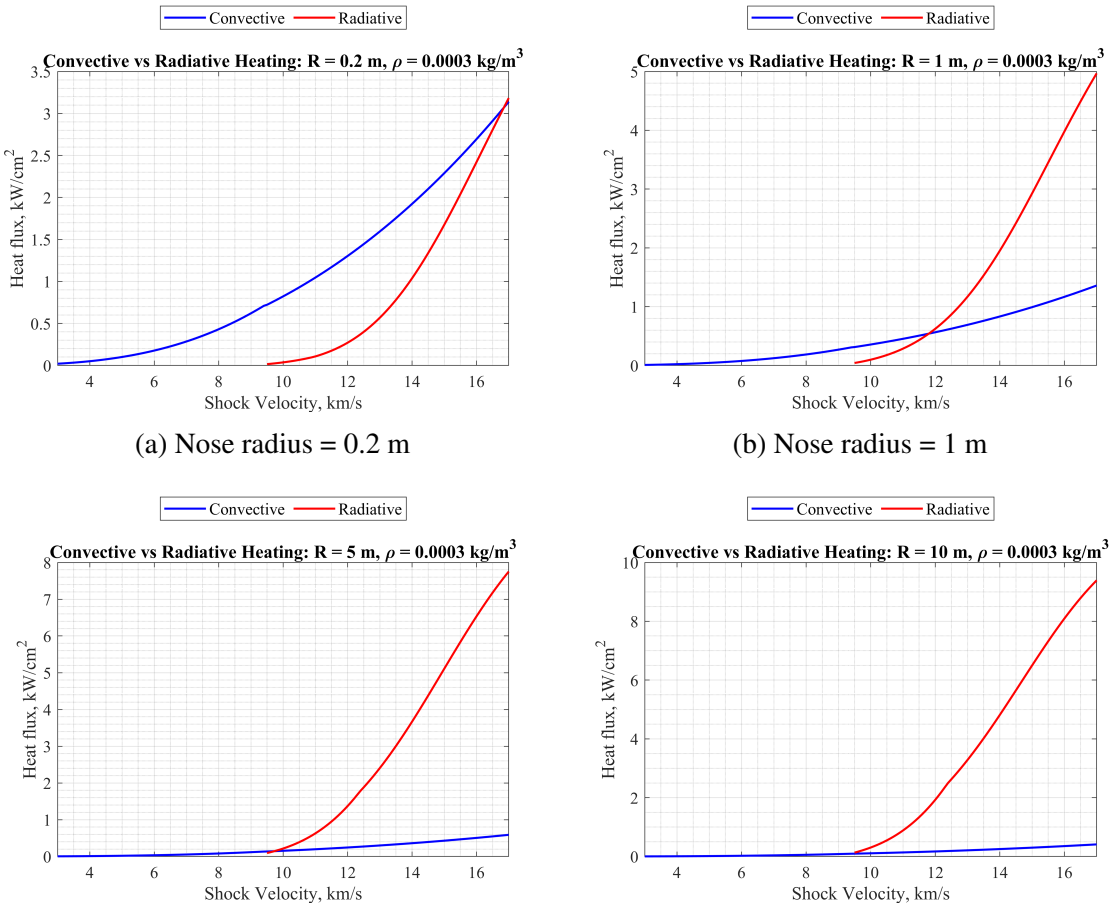


Fig. 1.3 Illustration of the evolving thermochemical state through a hypersonic vehicle shock layer. Not to scale.

electrons resulting from ionisation reactions. These free electrons can cause communications blackout during the entry mission, by absorption of radio frequency signals. Understanding the onset of this phenomenon is important for appropriate placement and design of future vehicle antennas. Another motivation for thermochemical characterisation is the radiation emission itself may create visibility issues, both from the vehicle and on the ground. Additionally, aerothermodynamic coupling effects may influence the forces experienced on the vehicle surface. The high temperatures can therefore augment the stress and loading of the vehicle, as well as the trajectory. And finally, as has been referred to, the convective heating (as well as the radiative heating) is a strong function of the thermochemical state through the shock layer.

The work of this thesis contributes towards the characterisation of the thermochemical state through the shock layer of LEO return vehicles. Specifically, along the stagnation line, from the shock front to the boundary layer edge. Experiments have been performed in the Oxford T6 Stalker Tunnel while operating in Aluminium Shock Tube mode to recreate the high-enthalpy flows at ground level. Spectrally and spatially resolved measurements of absolute radiance were taken and converted to temperature and species number density information through the artificial shock layer. A more detailed summary of relevant past works in this area and of the methodology used in this thesis is provided in the following chapters. The results of this work may be used to improve the design of future LEO return vehicles, by providing new data and analyses to more accurately describe the thermochemical state along their stagnation line, which can ultimately enhance vehicle safety and efficiency.



(a) Nose radius = 0.2 m

(b) Nose radius = 1 m

(c) Nose radius = 5 m

(d) Nose radius = 10 m

Fig. 1.4 Predictions of stagnation point convective and radiative heating for different vehicle nose radii during Earth entry, from the relations of Brandis and Johnston [20].

1.2 Thesis Aims

The ultimate aim of this thesis is to acquire reliable temperature and species number density information, relevant to the stagnation line ahead of a vehicle during LEO return missions. This is achieved through a sequence of contributions as summarised below:

1. **Reduce the discrepancies of shock tube equilibrium radiance measurements against numerical predictions.**

   As will be shown in the literature review, early attempts to capture shock tube spectral radiance data at speeds from ~4 to ~8 km/s has shown notable discrepancies in the equilibrium region to the predictions of NASA's equilibrium and radiative transport codes [2]. It's necessary to remove, or at least understand, these discrepancies before a reliable analysis of the non-equilibrium region can be made. The final thermochemical equilibrium state is the most certain of those attained during the post-shock relaxation phase. Agreement here therefore represents agreement of the experimental data and calibration methodology to the radiation transport calculations and models used. Clarity here is an important step before introducing the additional complication of chemical kinetics, which become relevant when considering the non-equilibrium region.

2. **Develop a means to convert radiance through the shock layer into temperature and species number density profiles that obey conservation of mass, momentum and energy.**

   Spatially and spectrally resolved radiance behind normal shock waves has been measured during the works of this thesis. However, since the radiative heating component is mostly negligible at LEO return conditions, this is more importantly a means to infer the species number densities through the shock layer and the distribution of their energy states (which corresponds to their temperature on a macroscopic level). A new constrained spectral fitting routine is developed, calling upon the University of Oxford's in-house thermochemical property and transport library, "OCEAN", and NASA's radiative transport and spectra program, "NEQAIR", to generate solutions that obey conservation of mass, momentum and energy. This is a novel approach compared to all prior works. The methodology is first validated against a series of numerically generated artificial data, incorporating various experimental artefacts, and then applied to radiance data captured in NASA's Electric Arc Shock Tube (EAST) facility. Comparisons are made against results from prior spectral fitting attempts.

[2] These are called "Chemical Equilibrium with Applications" (CEA) and "Nonequilibrium Radiative Transport and Spectra Program" (NEQAIR) respectively, and will be reviewed in more detail in Chapter 2.

3. **Analysis of pure nitrogen non-equilibrium data.**

   Pure nitrogen provides a simplified test mixture with 5 species (N_2, N_2^+, N, N^+, E^-) and four reaction mechanisms, to perform a more fundamental study compared to tests in air. Conditions from both the T6 Aluminium Shock Tube and NASA's EAST facility are analysed using the aforementioned constrained spectral fitting routine. This provides data for isolated nitrogen systems and tests the constrained routine for a simplified gas mixture. Valuable information is extracted to determine the extent of thermal and chemical non-equilibrium phenomena through pure nitrogen shock layers at speeds relevant to LEO return missions. Effects of shock speed and pressure on the thermochemical relaxation are also discussed.

4. **Analysis of synthetic air non-equilibrium data.**

   The next progression in complexity is to introduce oxygen species to the test mixture, bringing the experiment one step closer to the true flight case. A 7.3 km/s test performed in the T6 Aluminium Shock Tube with a synthetic air (20.9% O2/ 79.1% N2) test gas is analysed using the constrained spectral fitting routine, and a similar EAST condition is selected for comparison. Temperatures and number density profiles are extracted through the high-enthalpy test slug. Results provide valuable information of the thermochemical state evolution directly relatable to the vehicle stagnation line, minus the boundary layer, catalytic wall and ablation effects.

1.3 Thesis Structure

Each of the aims listed in the previous section form an independent chapter of this thesis. Chapters 4 to 7 are re-formatted from stand-alone draft papers intended for future journal publications, to comprise the main content of this integrated thesis. A summary of the remaining chapters is given below:

1. **Chapter 2 - Literature Review:** This chapter provides a summary of various other works relating to the study of non-equilibrium thermochemistry encountered during Earth entry missions. This includes studies performed in both continuous and other impulse facilities around the world, and a review of the operation and typical experiments conducted in each. Gaps in the literature and unresolved discrepancies are highlighted to provide a justification of the path taken for the remainder of this thesis.

2. **Chapter 3 - Experimental Method:** The aim of this chapter is to give the reader a full understanding of how calibrated spatio-spectral radiance data is acquired from the T6

Aluminium Shock Tube. This includes the design, instrumentation and operation of the facility. It also provides details of new telecentric optical systems, designed specifically for the study of LEO return non-equilibrium radiation in the facility. Finally, an overview of the steps to calibrate spatio-spectral emission data is provided.

3. **Chapter 4 - Investigation into Equilibrium Radiance Offset in Air Shock Tube Tests:** This chapter investigates how equilibrium spectral radiance captured in a shock tube may deviate from numerical predictions, particularly focusing on experimental considerations for conditions at LEO return entry speeds. This includes adjusting optical setup parameters, testing alternative radiation models and trials of plasma cleaning the downstream end of the AST. Significant improvements are made above $\sim$600 nm, though discrepancies from the NO bands remain at 200 to 280 nm, which are characterised as a function of shock speed and post-shock pressure.

4. **Chapter 5 - Development and Validation of a Constrained Spectral Fitting Routine:** After improving agreement between shock tube equilibrium spectra and numerical predictions, attention turns to the non-equilibrium region. This chapter develops and validates a constrained spectral fitting routine, to extract temperatures and species number densities, from spectrally and spatially resolved radiance measurements of shock-heated flows. The routine is novel to all prior spectral fitting attempts since results satisfy conservation of mass, momentum and energy through the shocked gas, though are limited to a 2T model and Boltzmann distributions are assumed. The study demonstrates the enhanced accuracy and robustness of spectrally fitted results by implementing the conservation constraints. The ability of the constrained routine to deal with various experimental artefacts, and still characterise the parameters of interest accurately, is also evaluated. Furthermore, it's demonstrated the constrained routine has applicability beyond the confines of the current datasets and can be used as a tool to identify additional measurements that should be made in future shock tube experiments, to improve overall characterisation of thermochemically relaxing high-enthalpy flows. Finally, the constrained routine is applied to pure nitrogen radiance data from NASA's EAST facility, for which results from prior unconstrained spectral fitting attempts exist for comparison.

5. **Chapter 6 - Thermochemical Characterisation of Shock-Heated Pure Nitrogen:** In this chapter, pure nitrogen test cases from the T6 Aluminium Shock Tube LEO return campaign are selected for thermochemical characterisation. The constrained spectral fitting routine is applied, to extract temperatures and species number densities through the relaxing test slugs. The extent of both thermal and chemical non-equilibrium are

evaluated over shock speeds from 6.2 to 7.4 km/s. Data from EAST with a comparable shock velocity is also included in the analysis. Results suggest certain reactions may not reach completion in the observable test slugs, nor within the predictions of well-established thermochemical models.

6. **Chapter 7 - Thermochemical Characterisation of Shock-Heated Synthetic Air:** This chapter extends the thermochemical characterisation process by applying the constrained spectral fitting routine to synthetic air data captured in both T6 Aluminium Shock Tube and EAST facilities. Temperatures and number densities extracted are close representations of the thermochemical state evolution experienced along the stagnation line of an entry vehicle, from the bow shock to the boundary layer edge.

7. **Chapter 8 - Conclusions and Recommendations:** Finally, this chapter summarises the key results from the work undertaken in this thesis and recommends areas to improve in further works.

Chapter 2

Literature Review

> Thermodynamics is a funny subject. The first time you go through it, you don't understand it at all. The second time you go through it, you think you understand it, except for one or two small points. The third time you go through it, you know you don't understand it, but by that time you are so used to it, it doesn't bother you any more.
>
> Arnold Sommerfeld

The first chapter established the importance of thermochemical characterisation in the shock layer ahead of vehicles during Low Earth Orbit (LEO) return missions. This chapter now provides a summary of previous works that have contributed to this goal, identifying key gaps in the literature to guide the path taken for the remainder of this thesis.

The review begins by examining ground test facilities capable of replicating high-enthalpy conditions, with a particular focus on existing shock tube facilities. Additionally, it includes a review of numerical tools relevant to shock layer radiation studies, providing the reader with a foundational understanding of the facilities and computational methods referenced in later sections.

Next, emphasis is placed on recent studies involving spectrally resolved radiation measurements and the extraction of information from non-equilibrium flows. This overview informs the reader of the current state of research, setting the stage for the following chapters, which build upon these works.

2.1 Facilities

To study the high-enthalpy non-equilibrium phenomena experienced ahead of a hypersonic vehicle, the first step is to create a means of producing such a flow. Performing measurements during an actual flight test is the ultimate way of achieving this, since the flow-field is by definition 100% representative of the true flight case. However, these are extortionately expensive and therefore only carried out very sporadically. Flight test programs of note over the past half a century relevant to the study of radiation (that have been discussed in the literature) include FIRE II by Richardson [151], BSUV2 by Erdman et al. [56] and Orion by Cruden and Brandis [47]. In addition to the expense, strict limits are placed on the installable instrumentation due to the payload requirements of a given mission. On top of this, there are limited bandwidths to transmit data acquired during the flight test. The instrumentation and associated components therefore likely need to survive the entire flight trajectory, so the full dataset may be attained. An alternative way to acquire true flight data is to perform airborne measurements some distance from an entry vehicle during it's descent. This approach was taken by Zander et al. [200] in 2020, to perform spectrally resolved measurements of the Hayabusa2 capsule during its re-entry into Earth's atmosphere. Though spatial resolution was prohibited due to the distances involved, they successfully capture many spectral features from around 600 to 1000 nm, including atomic nitrogen, oxygen and hydrogen transitions.

Finally, a multitude of complex and coupled phenomena lead to the heat fluxes and forces experienced by the vehicle. This incudes the rates of thermochemical relaxation (and thus the reach of non-equilibrium phenomena towards the surface) which can augment heat flux and interfere with the boundary layer [95]. Following from this, the prediction of boundary layer transition (BLT) is also an important factor to determine the distribution of heat flux experienced by entry vehicles or hypersonic propulsion systems. The works of Malik et al. [114], Jewell [93] and Ward et al. [191] are just a few examples of efforts to understand BLT from the literature. Additionally, catalytic and ablative processes at the surface can augment the heat flux, introduce carbon species into the flow and change the surface roughness of the vehicle, as shown in works of Hollis [83]. Attempts to characterise each of these phenomena and interpret their contribution to the overall heat load in the post-flight analysis have been made by Cruden et al. [48], and Boyd and Jenniskens [12]. These efforts demonstrate the significant difficulties involved with such an analysis and raise a strong case for the isolation of phenomena so they may be independently studied. This is achieved with ground test facilities. Here, the difficulties encountered when trying to recreate a full hypersonic flow-field become advantageous to provide simplified datasets. Additionally, this enables experiments to be performed much more frequently, at a fraction of the cost and implement much more instrumentation and diagnostics. Many forms of facilities are

available and may be categorised into various subsets, some of which have been summarised generally in Fig. 2.1 against selected mission trajectories. Due to the context of this work, only facilities capable of producing high enough enthalpies to facilitate optical emission studies are discussed in this section. Descriptions of both continuous and transient facilities are provided, along with their advantages, disadvantages and some examples of previous experiments they have performed. Knowledge of these facilities is a prerequisite to inform the reader before delving into the studies of non-equilibrium phenomena and thermochemical characterisation that have been conducted in them.

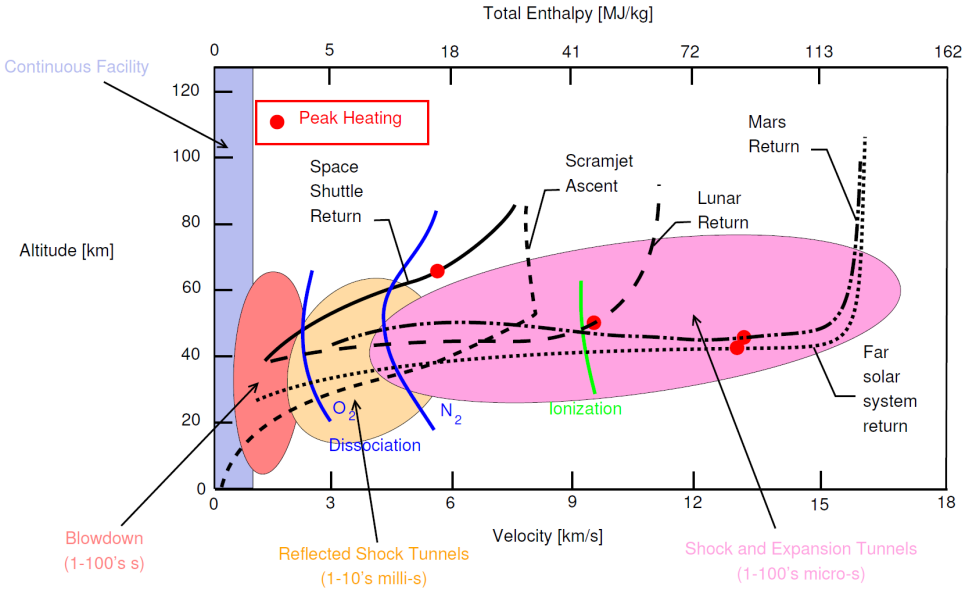


Fig. 2.1 Summary of selected mission trajectories and approximate ground test capabilities. Taken from Collen [32].

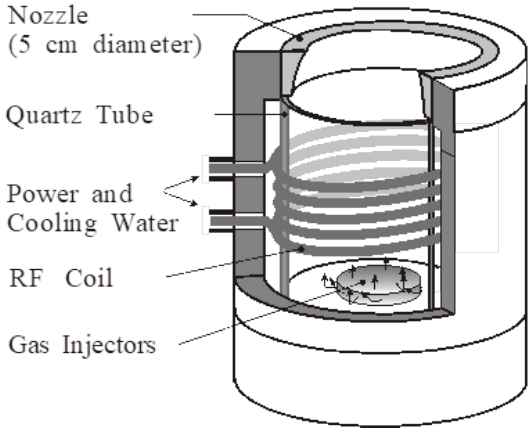
2.1.1 Continuous Facilities

As can be seen in Fig. 2.1, continuous facilities are generally not able to reproduce the aerodynamic aspect of the hypersonic flight environment. This is due to the immense power requirements needed to generate such high velocity flows, along with the high temperature gas effects associated with them. Facility power requirements could easily be hundreds of megawatts or even gigawatts, depending on the entry mission to be replicated. Huge difficulties arise relating to the heat transfer to tunnel components and even a capable power source. It quickly becomes evident that to operate a high-enthalpy experiment continuously, there must be a sacrifice in the Mach number and/or total pressure of the flow. Despite this, many studies have successfully been performed in continuous facilities, to inform of the

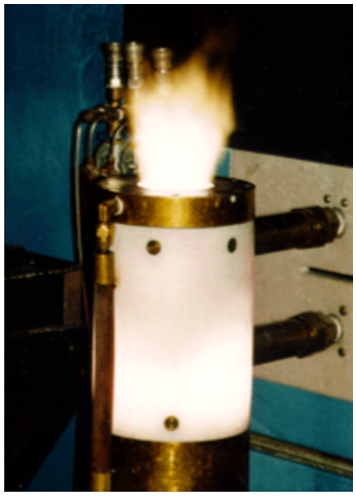
thermochemical state in shock layers and update radiative transport codes. One primary advantage common to all continuous facilities in the context of radiation measurements is long exposure times. This allows accumulation of signal and thus improves the signal-to-noise ratio (S:N) of spectra acquired even at high resolutions, enabling clear distinction of many molecular bands and atomic transitions. A brief review of two continuous facilities that have contributed strongly to the literature around shock layer radiation is now given.

Inductively Coupled Plasma Torch

The Inductively Coupled Plasma (ICP) Torch was first proposed by Reed [150] and is illustrated in Fig. 2.2. Fundamentally, gas is injected into a volume wherein a magnetic field rapidly oscillates to generate free electrons. These then collide with heavier particles to cause further ionisation, as well as raising their temperature, until enough electrons have been produced for the plasma to become self-sustaining. This form of continuous operation is highly advantageous over other continuous facilities (such as Plasma Wind Tunnels) since no metallic components come into contact with the flow, thus prohibiting many contaminants from entering the test gas. Casses et al. [27] demonstrate alternative axial and swirl injector geometries may be used to help stabilise the flow in different periods of the start-up and operation phases.



(a) ICP torch head schematic.



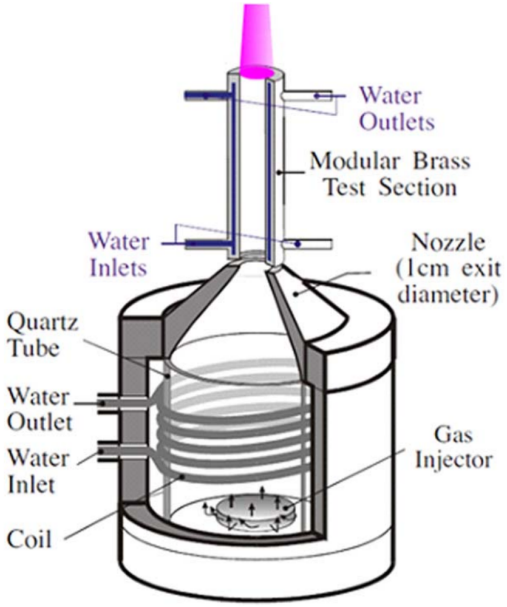
(b) ICP torch in operation.

Fig. 2.2 Inductively Coupled Plasma torch illustrations. Both taken from the work of Casses et al. [27].

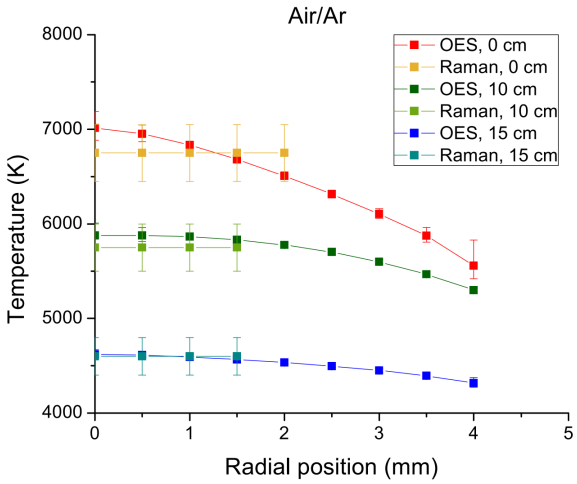
ICP torches are renowned for producing a well-controlled environment and are able to generate plasma in a state of local thermodynamic equilibrium, as validated in the comprehensive works of Laux [101]. The facilities used in research settings typically have nozzle diameters of around 50 mm and so create a relatively small plasma jet, which is often measured $\sim$16 mm from the nozzle exit where laminar flow is present. Axisymmetry is assumed to allow an Abel inversion in order to characterise the radial distribution of the thermodynamic state through the plasma, as shown by Laux [101]. Although flows up to 1 km/s have been achieved in the works of Tibère-Inglesse et al. [188], the velocities are usually in the subsonic regime due to high static enthalpies and the power limits already discussed. Additionally, the ICP torch exhausts to atmospheric air, thus limiting the total pressure at which experiments may be performed. It's because of these characteristics that, apart from a few ablation studies (as shown in the works of MacDonald et al. [112] and Löhle et al. [108]) ICP torches have traditionally been used solely to perform reliable high-resolution spectral measurements of equilibrium plasma.

The work of Laux [101] is often referenced in the context of atmospheric entry studies, which includes a detailed and extensive characterisation of the thermochemical state of an air plasma. Results from this study were used to update the NEQAIR2 radiation code from the ultraviolet to the near-infrared wavelength regions. Since then, studies have expanded from this to capture spectral radiance for a range of atmospheres and wider wavelength regions. Vacher et al. [190] have attained measurements for Titan's atmosphere, while McGuire et al. [122, 123] have extended datasets into the VUV for both air and Mars atmospheres. Additionally, more fundamental studies have been carried out in simplified gas mixtures of pure nitrogen by Yalin et al. [195].

Although ICP torch plasmas do not produce the thermochemical evolution experienced behind a shock front, non-equilibrium phenomena have been investigated for recombining flows. Tibère-Inglesse et al. [188] performed a fundamental study of recombining nitrogen and air plasmas, by attaching a water-cooled tube of varying lengths to the ICP torch exit. Figure 2.3a illustrates the experimental set-up, wile Fig. 2.3b plots temperature profiles extracted from implementing water-cooled tubes of different lengths in air. Since the initial equilibrium state of the plasma leaving the torch exit is well characterised, this set-up provides a reliable means to study the thermochemical processes relevant to the afterbody flow around a hypersonic vehicle.



(a) Illustration of the water-cooled test-section attached to the ICP torch exit for the recombining flow studies by Tibère-Inglesse and Cruden [187]



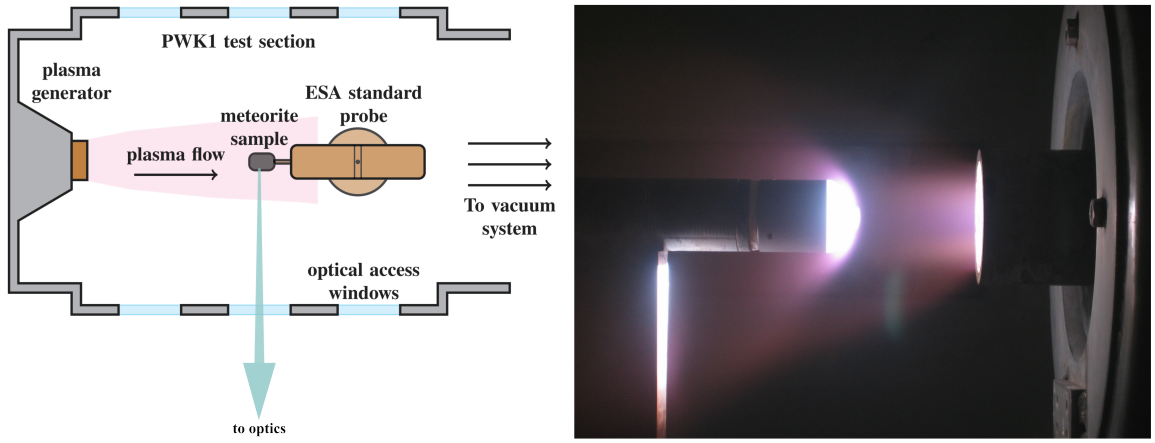
(b) Temperature profiles measured with Raman scattering and Optical Emission Spectroscopy (OES) with water-cooled tubes of 0, 10 and 15 cm in length, for the air/Ar plasma.

Fig. 2.3 Illustration and results of studying recombining non-equilibrium phenomena in air. Both taken from Tibère-Inglesse and Cruden [187].

Plasma Wind Tunnels

The basic principle of a plasma wind tunnel (PWT) is largely similar to that of the ICP Torch, in that energy is imparted to a gas in order to excite the species present before being accelerated through a nozzle. The means of imparting energy to the gas however differs. The most common mechanism involves the discharge of an electrical arc through the flow. A comprehensive review of arc-heated test facilities is provided by Smith et al. [161]. Figure 2.4 provides images of the PWK1 facility, which has produced emission spectra during the ablation of materials to aid in assessment of Thermal Protection System (TPS) performances.

As was the case for the ICP torch, the high static enthalpies require there to be a sacrifice in Mach number from the true flight case, to enable continuous operation of PWT facilities. In most experiments, the flow leaving the nozzle is subsonic. In contrast to the ICP torch, the PWT design can often suffer from contaminants entering the free-stream since the metallic cathode and anode components are in contact with the test gas. Loehle et al. [106] provide a comprehensive summary of the PWT designs available and identify that radio frequency and magnetoplasmadynamic PWT setups produce the least contaminated and highest enthalpy flows. However, these are limited to total pressures from approximately 5 to 10 kPa, which



(a) Schematic of the PWK1 facility, adapted from Ravichandran et al. [148]

(b) Image taken during a PWK1 experiment, taken from Löhle and Reimer [107].

Fig. 2.4 Illustrations of the PWK1 Plasma Wind Tunnel facility.

requires the entire plasma flow and test article be contained within a large vacuum chamber. It's critical the vacuum pumping system can remove the mass flow from the plasma in order to maintain continuous operation.

Historically, the development of PWT's has been to study stagnation-point heat fluxes, though this has since expanded to ablation studies and various optical techniques to inform of the thermochemical state of the flow. The low free-stream Mach number from the PWT prevents the initial non-equilibrium region of the shock layer from being studied, however Hermann et al. [79] demonstrated there to be a significant degree of non-equilibrium phenomena and non-Boltzmann internal energy distributions in the plasma free-stream. Additionally, unsteadiness was observed in the flow due to the arc-attachment process. Despite this, work by Hermann et al. [81] later showed that conditions close to equilibrium may be achieved at low total pressures. This validates the PWT facility as a viable means to study shock layer radiation away from the initial post-shock relaxation processes, and furthermore provides an alternative to impulse facilities which would typically struggle to achieve sufficient test times or camera signals at such low pressure conditions. Since the PWT is run continuously, and thus allows much longer camera exposure times, this provides a clear advantage to establish the PWT as a valuable source of data in the context of radiation studies at these low pressure conditions.

Finally, thanks to the long run times, PWT's are able to produce realistic heat fluxes, to model wall temperatures and boundary layers. This allows them to create some of the coupled radiation effects close to the vehicle surface. It's particularly advantageous for the study of surface heating from radiation in the vacuum ultraviolet (VUV) region. This is

the greatest source of radiative heat flux for many Earth entry missions, though also of the highest uncertainties due to difficulties in its measurements and thus limited datasets. The VUV radiation is absorbed by molecular O_2 in a cooler boundary layer, thus reducing the heat flux experienced by the vehicle or model. By running continuously, a PWT allows realistic boundary layer mole fractions and therefore radiative heat fluxes. Radiative studies from Johnston et al. [97] have also shown the effect of carbonaceous species at the surface and how they may augment the radiative heat flux. It is because of the aforementioned advantages that PWT's are still regarded highly for shock layer radiation studies, which to this day is stimulating the production of new facilities. This is exemplified in the production of the new Osney Plasma Generator 1 (OPG1) facility at the University of Oxford. The development and commissioning of which has been thoroughly documented by Hermann et al. [78] and Chang et al. [28].

2.1.2 Impulse Facilities

It's apparent from the previous section that, although continuous facilities have made valuable contributions to the understanding of shock layer radiation, if the flow velocity is to be matched to the flight case (as well as the high static enthalpies) then the flow environment must be generated transiently. Three primary facility types to achieve this are: Reflected Shock Tunnels (RST); Expansion Tubes/Tunnels (ExT); and Shock Tubes (ST). This section only provides a fundamental explanation on the theory of operation for each type of impulse facility, along with some background of experiments relevant to shock layer radiation studies. The Oxford T6 Stalker Tunnel is able to operate in all of these facility modes, as detailed in the works of Collen [32]. Table 2.1 summarises some of the typical experimental characteristics for each mode, to aid the following discussion. Test time is defined as the time during which a steady condition is achieved in the region of interest. A more detailed account of the T6 Aluminium Shock Tube is provided in Chapter 3, which was the facility mode used to conduct the experiments undertaken for this thesis.

Table 2.1 Comparison of different operation modes of the Oxford T6 Stalker Tunnel.

Facility	**Reflected Shock Tunnel**	**Expansion Tunnel**	**Shock Tube**
Testing type	Subscale model	Subscale model	Shock layer radiation
Test time	1–3 ms	50–500 μs	2–50 μs
Flow core diameter	150–200 mm	50–120 mm	96.3 or 225 mm
Max flow speed	6.5 km/s	12 km/s	18 or 13.4 km/s

Reflected Shock Tunnels

Fundamentally, a RST operates by generating a high-enthalpy stagnation region to feed a converging-diverging nozzle. This then accelerates a flow to usually pass over a sub-scale model, contained within a test section at some level of vacuum pressure to avoid nozzle unstart. Figure 2.5 illustrates these processes. Stagnation of the test gas in RSTs results in the total temperature and pressure being converted into static quantities. Thus, these facilities must endure the severe environment for the test duration. This limits the total enthalpies RSTs can be used up to, to avoid erosion of the nozzle throat and consequent variability in flow conditions. Hornung [85] shows the residual free-stream non-equilibrium effects that may exist in RST facilities as stagnation enthalpy is increased.

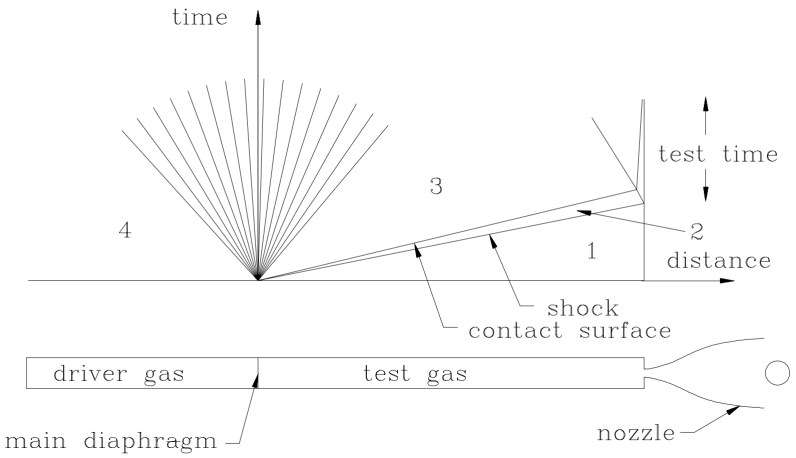


Fig. 2.5 Schematic and t-x diagram of RST operation. Separation between shock wave and contact surface is exaggerated for clarity. Taken from Hornung Han [87].

Despite the enthalpy limitations brought about by the stagnation process, RST facilities have successfully been used for shock layer radiation studies, typically at a reduced Mach number with application of the Mach number independence principle, as shown by Kliche et al. [98]. The RST is applicable to studies of equilibrium heating thanks to its relatively long test time, which allows a full flow-field to be established.

Due to its limitations, RSTs lend themselves to slower and lower pressure test conditions. This has motivated Mars entry studies to be conducted in multiple RST facilities, as is detailed in the works of Wright et al. [193], Hollis and Prabhu [84] and Noeding and Martinez Schramm [140]. Finally, radiation from contaminant species in larger RST facilities has been shown by Cruden et al. [50] to enhance background radiation and consequently introduce discrepancies with heating measurements from other facilities.

Expansion Tunnels/Tubes

Instead of a stagnation region, ExTs use a supersonic unsteady expansion process to raise the total enthalpy of the test gas and produce higher speed flows with less contaminants. Trimpi [189] first proposed the design by equation 2.1, where H is total enthalpy, M the Mach number and h static enthalpy.

$$dH = -(M-1)dh \tag{2.1}$$

The distinction between tunnel and tube is that the former has a nozzle on the end to expand the flow, usually over a scaled model, as was the case for RST. Whereas the latter maintains a constant tube diameter until the flow exits the end of the tube. Without the nozzle, a sub-scale model may still be used, however experiments can also be treated similarly to a shock tube (explained in the next sub-section) in which no model is used and the flow itself is treated as analogous to a vehicle stagnation line.

The unsteady expansion process removes the total enthalpy limit experienced by RSTs and enables the study of conditions up to hyperbolic Earth entry, as shown by Gildfind et al. [66]. Additionally, the ExT test slugs contain the non-equilibrium relaxation phenomena immediately behind the shock front and are therefore a more accurate representation of the shock layer ahead of an entry vehicle. However, Beck and Mackie [7] demonstrate the expansion process to result in thermochemical gradients through the resulting test slug. This can result in a non-equilibrium free-stream flow and raises uncertainties as to the properties of the flow-field by the time it reaches a model, or region of measurement. Furthermore, the benefits of ExTs come at the cost of test time in comparison to RSTs. Figure 2.6 illustrates the operation of a free-piston driven expansion tube.

Scaled models have been tested in a range of test gases for atmospheres relevant to Earth (by Fahy [59]), Venus (by Banerji et al. [4]), Mars and Titan (by Palmer et al. [141]) and Ice Giants (by Steer et al. [173]). These works have often included spectrally resolved radiation measurements. The works by Hermann et al. [80] have even presented spectral measurements in the VUV from super-orbital re-entry experiments in the X2 expansion tunnel facility at the Centre of Hypersonics at the University of Queensland.

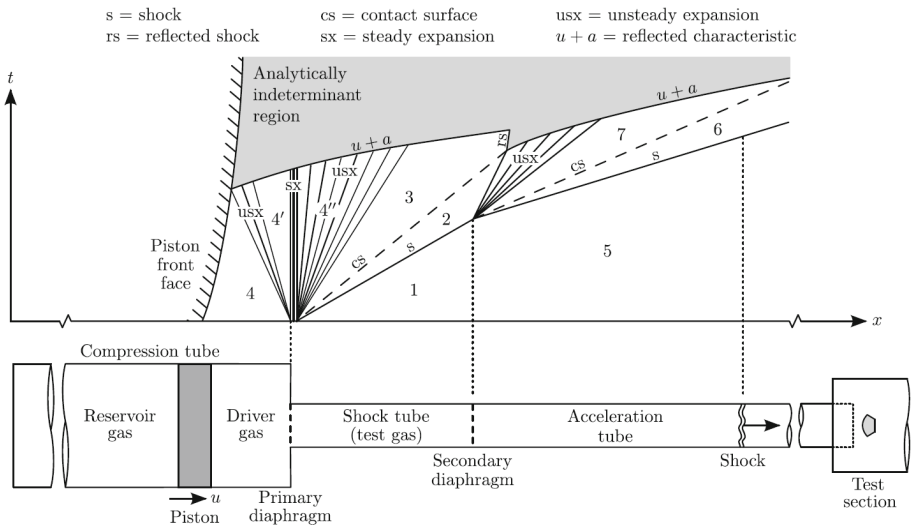


Fig. 2.6 Schematic and t-x diagram of a free-piston driven ExT. Taken from Gildfind et al. [66].

Shock Tubes

In both the previous operation modes, the gas undergoes compression and expansion processes before it reaches the region of interest. Each of these stimulates a series of thermochemical reactions, that take a finite time to run to completion. Thus, the test gas is in an unknown state of thermochemical non-equilibrium before the phenomena of interest begin. This is not analogous to the true flight case and adds uncertainties to the results attained. A shock tube is a simpler mode of operation which enables a more fundamental study, at the compromise of only recreating the stagnation line ahead of a vehicle.

Shock tube experiments involve passing a normal shock through a quiescent test gas of density and composition equivalent to the planet trajectory point of interest. A driver condition is selected such that the speed of the normal shock should match the speed of the vehicle at the chosen trajectory point. This allows an analogy to be made between the flow generated from the normal shock to the contact surface (where test gas meets driver gas) in the shock tube, to the stagnation line ahead of a hypersonic vehicle, from the bow shock front to the boundary layer edge. This is often referred to as the "shock tube - stagnation line analogy" and is illustrated in Fig. 3.6 in Chapter 3. It's emphasised that no model is used in the shock tube experiment and the test slug behind the normal shock is the test subject.

This method of operation removes scaling issues associated with both RST and ExT facilities in the context of radiation studies. In both the previous impulse facility types, neither chemical kinetic rates nor flow-field radiation directly translate from the sub-scale

model to the true flight case [1]. The works of Capra [25] and Morgan et al. [128] show that radiative heat flux through a stream tube scales with the characteristic length, and thus heat flux experienced by the sub-scale model does not directly match to a vehicle during flight. This invalidates the use of binary scaling, where the product of freestream density and the characteristic length is maintained between the model and flight scenarios, which is often used to determine test conditions in ExT facilities. The Goulard number (Γ) is given in Equation 2.2, taken from the works of Goulard [73], where q_R (W/m^2) represents the radiative heat flux, and v_∞ (m/s) and ρ_∞ (kg/m^3) are freestream velocity and density respectively. This provides a means to quantify the severity of radiative scaling issues and radiative coupling with the flow. Leyland et al. [104] predict a Goulard number of 0.01 for Lunar return missions, which corresponds to the threshold defined by Palmer et al. [142] at which radiative coupling effects become important. The value is highly dependent on the composition of the atmosphere in question, which is demonstrated by values up to 0.4 for a 6.4 km/s Titan entry, compared to 0.1 for the $\sim$48 km/s Jupiter entry condition.

$$\Gamma = \frac{2q_R}{\frac{1}{2}\rho_\infty v_\infty^3} \tag{2.2}$$

In addition to radiation, the binary scaling falls apart for chemical kinetics. Hornung et al. [86] and De Crombrugghe et al. [53] show that the final stages of relaxation in the shock layer relies on a number of three-body reactions (as opposed to binary reactions). This is even more important in wake recombination reactions, which are dominated by three-body interactions. These detriments create a strong motivation for an alternative means of generating the full hypersonic flow-field, which does not involve any scaling. Shock tubes offer a relatively straightforward method for achieving this, though the trade-off is the highly transient nature of the experiment.

The full non-equilibrium evolution behind the shock is generated, enabling the study of both non-equilibrium and equilibrium phenomena during a single experiment. This permits very fundamental studies to be performed, with well defined boundary conditions. Unlike the RST and ExT facilities, which involves compression and expansion processes before reaching the test subject, the initial condition of the pre-shocked test gas in a shock tube is well known, and the shock speed by which it is processed can be measured. This greatly reduces uncertainties in the processing and interpretation of experimental data. However, this simplicity prevents the study of many phenomena present around a true flight vehicle - namely oblique shocks and expanding flows. Though, work by Johnston [96] has demonstrated

[1] A rare exception to the model scaling issues is when a full-scale test article may be installed in the test section. This was achieved by Andrianatos et al. [2] for a relatively small Hayabusa forebody in the large X3 expansion tube.

oblique shocks may be studied by generating off-condition shock tube data, to inform about portions of the flow field other than the stagnation line. However, this requires multiple tests to be carried out and introduces shot-to-shot variation uncertainties in the analysis. Finally, shock tube flows are often treated as one-dimensional, which increases simplicity to interpret results and inform computational models. The results can therefore consequently be used to predict the non-equilibrium heating experienced by hypersonic vehicles, as shown by Barnhardt et al. [5].

Two caveats to the shock tube - stagnation line analogy are the shock speed variations, as the normal shock progresses down the shock tube, and the presence of a growing boundary layer along the tube walls behind the shock front. These introduce discrepancies with the vehicle stagnation line flow-field and are discussed in further detail in Chapter 3 in the context of the T6 Aluminium Shock Tube, along with a summary of recent works to understand and correct for these augmentations.

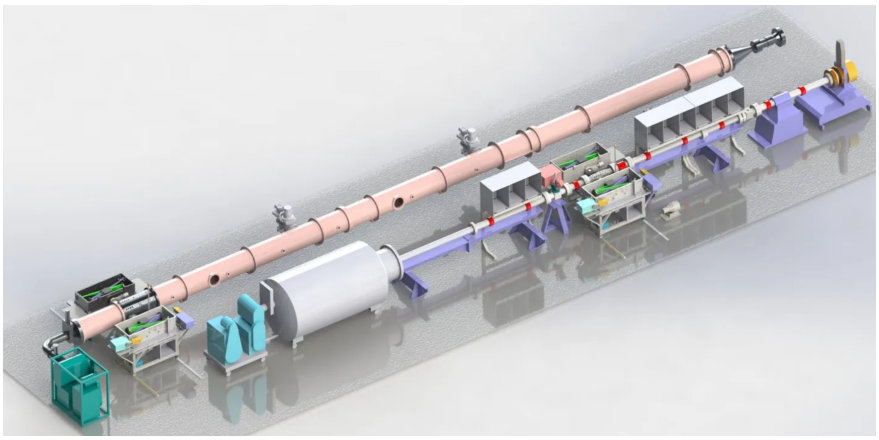
2.2 Operational Shock Tubes

A summary of operational shock tubes from around the world is now given in their own independent section, since they are the primary facility of interest in this thesis. In particular, the source of all data presented and analysed from Chapters 4 to 7 is produced by the T6 Aluminium Shock Tube at the University of Oxford and the Electric Arc Shock Tube at NASA Ames. Chapter 3 provides a comprehensive description of the former, while the latter is reviewed within this section.

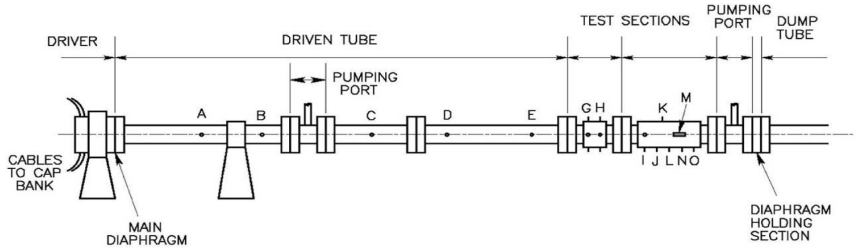
2.2.1 Electric Arc Shock Tube

Most famous of all shock tubes, the Electric Arc Shock Tube (EAST) facility at NASA Ames has reproduced entry vehicle stagnation lines since the 1960s. Data acquired has informed a range of planet entry missions of the expected radiative heating environments. This includes experiments performed in atmospheres for Earth [13, 16], Mars [14] and Titan [17] in works by Brandis et al., as well as Venus [49] and Gas Giants [43] by Cruden et al. Figure 2.7 provides schematics of both small and large diameter shock tubes available and summarises different sections of the EAST facility.

Detailed descriptions of EAST and its operation have been provided in a series of publications over time. The works of Cruden et al. [41, 39] and Greenberg et al. [74] provide comprehensive examples of this, including the most recent upgrades of both the facility and associated optics to perform spectrally and spatially resolved radiation measurements.



(a) Schematic view of EAST, capturing both 101.6 and 609.6 mm shock tubes. Image taken from Cruden [41].



(b) Diagram of EAST identifying different sections of the facility. Taken from Greenberg et al. [74], with "M" indicating the window location where emission spectroscopy measurements are taken.

Fig. 2.7 The Electric Arc Shock Tube (EAST) facility at NASA Ames.

A brief summary of the EAST facility is now given, though the reader is directed to the referenced texts for more detailed accounts.

As the name suggests, the EAST facility utilises a very powerful electric arc driver which has successfully achieved shock velocities of nearly 50 km/s when using hydrogen driver gas, as shown by Sharma and Park [157]. The driver consists of a 1.3 litre conical volume, which is initially filled with hydrogen or helium at pressures from 30 to 200 psi prior to firing a shot. Upon test ignition, a 40 kV, 1.2 MJ capacitor bank is discharged via a metallic filament through the driver volume. The filament vapourises instantaneously and leads to a surge of energy in the driver gas, rapidly raising its temperature and consequently rupturing a diaphragm. This rupture produces a normal shock wave which is forced downstream as the driver gas expands into the driven tube section. The shock continues to travel down the tube, compressing and accelerating test gas until it reaches the main test section. Here, diametrically opposite windows allow radiation from the excited test gas to escape and be captured by designated optical setups.

Though very powerful, the small volume of the driver results in a rapid decay of driver pressure and expansion waves are able to reflect off the driver end to catch up with the normal shock, which causes significant deceleration of the shock. The discharge liner is composed of poly-tetrafluoroethylene (PTFE), formed from both carbon and fluorine atoms, $(CF_2)_n$. Cruden et al. [39] state that approximately 1-2 g of liner material is ablated during each shot, introducing fluorocarbon contaminants into the test flow, which have been identified between 200 to 300 nm in the processed gas behind the shock. Despite these detriments, the EAST facility has successfully produced large amounts of useful data for planet entry missions and informed thermochemistry models based on measurements of the non-equilibrium region immediately behind the shock front. The shock wave is monitored down the tube by a series of "time of arrival sensors" in the form of: pressure sensors (PCB 132A35); fibre optic coupled photodiodes (Hammamatsu H6780-20); or in-house ionisation gauges. Increased frequency of sensors is placed around the windows to increase resolution in this region and help with accurate camera triggering.

The most recent upgrades to the EAST facility are detailed in the works of Cruden et al. [39]. This introduced four simultaneous telecentric emission spectroscopy channels, collectively able to attain spectra from the vacuum ultraviolet (VUV) to the infrared (approximately 120 to 1700 nm). These are housed in bespoke vacuum chambers at pressures on the order of 10^{-3} Pa, to avoid radiation absorption via the O_2 Schumann-Runge bands in the VUV wavelengths, as well as absorption by water vapour and CO_2 in the infrared. The telecentric optical designs also reduce spatial blurring, to improve resolution through the non-equilibrium region of test slugs.

During the same upgrades, contaminant control was improved by implementation of: a more powerful pumping system to evacuate the shock tube test section; a heating blanket to increase the rate of water vapour outgassing from the tunnel walls; and a plasma cleaner to remove remaining hydrocarbon particulates in the recesses of the tube wall after the manual cleaning process. Figure 2.8 tracks the relative carbon and hydrogen contributions via atomic lines at 248 and 656 nm respectively, extracted from tests performed at a condition of 10 km/s in 0.2 Torr air (relevant to peak heating for lunar return). These atomic transitions emit above the molecular background signals, even at the extremely low residual contaminant levels, at such high speeds and thus provide a convenient means to monitor hydrocarbon contamination levels.

Alternatively, the cyano-radical (CN) emits intensely in the ultraviolet wavelengths. The aptly named "CN violet band" is notorious for superimposing over the spectra attained from shock tube emission studies. In the case of air, it superimposes over the N_2^+ first negative bands, as well as atomic N and O transitions which can be distinguished for higher speed

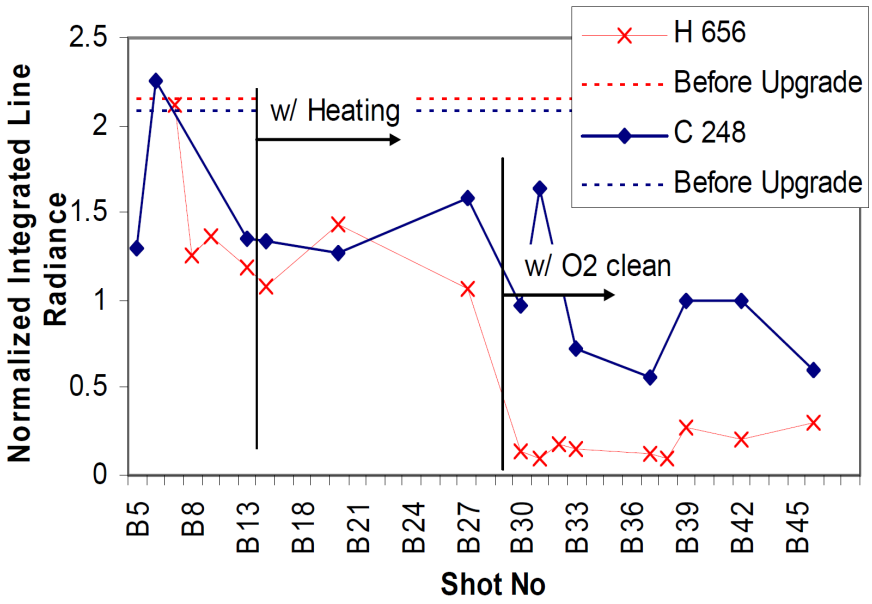


Fig. 2.8 Trend of atomic carbon and hydrogen line emissions as EAST upgrades are implemented, taken from Cruden et al. [39]. All shots performed with a pressure of 26.6 Pa (0.2 Torr) and a nominal shock speed of 10 km/s. Data are presented as relative measurements, with integrated line intensity normalised against the background radiance.

entry cases. High resolution spectra are required to resolve these spectral features. Figure 2.9 repeats the results from the studies of Cruden et al. [39] to evaluate the effectiveness of the plasma cleaner to remove CN from the 10 km/s 0.2 Torr emission spectra. These results show enhanced removal of CN contamination by improved cleaning of the EAST walls, for a peak heating lunar return entry condition. This suggests CN molecules may originate from matter accumulated on the tunnel walls, which are removed by the sudden shock and ingress into the boundary layer of the flow, where their temperature is raised such that they radiate. It's also noted that CN removal was enhanced by plasma cleaning relatively more than C and H atoms, which may indicate the atomic contaminants do not originate from the tube wall as heavily.

To date, no other such study has been performed to evaluate the effect of plasma cleaning shock tube facilities, thus it's unknown whether these results are general or specific to: lunar return entry speeds (which determines the dominant thermochemistry and thus whether molecular CN or atomic C and H production is favoured); arc discharge drivers (which deposit fluorocarbon contaminants down the tube from the discharge liner); or even tube diameter considerations (which determines the relative boundary layer thickness relative to the core flow). Chapter 4 utilises plasma cleaner technology on the T6 Aluminium Shock Tube, which uses an alternate free-piston driver and larger shock tube diameter, at slower

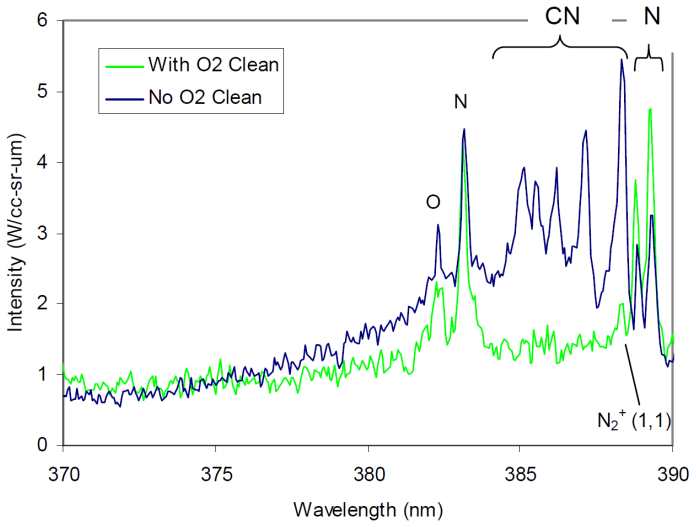


Fig. 2.9 Effect of oxygen plasma cleaning on CN impurity levels in UV emission spectra for 10 km/s and 0.2 Torr test cases in air. High resolution spectra enable the different spectral features to be distinguished. CN is shown to reduce drastically after the driven tube section has been plasma cleaned.

Low Earth Orbit return conditions. This continues the study of CN removal and gives further insight to the origin and removal of shock tube contaminants.

In addition to real stagnation line studies, a series of fundamental studies have also been carried out on the EAST facility. The works of Brandis and Cruden [18, 46] and Tibère-Inglesse and Cruden [187] summarise and analyse a series of pure nitrogen shots (from test series 62) at a range of shock speeds relevant to both lunar and LEO entry missions. Isolation of nitrogen species simplifies the test mixture by reducing the number of possible collision partners and thus the complexity of the energy exchange reactions. This is useful to test thermochemical models and isolate specific reaction mechanisms, before turning to the more complex mixtures of interest for real entry missions. Brandis and Cruden [18] emphasise that by removing oxygen from synthetic air studies, the 11 species and 21 chemical reactions to consider are simplified to only 5 species (N, N^+, N_2, N_2^+, E^-) and 4 reaction mechanisms, summarised as:

$$N_2 + M \longleftrightarrow N + N + M \tag{2.3}$$

$$N + E^- \longleftrightarrow N^+ + E^- + E^- \tag{2.4}$$

$$N + N \longleftrightarrow N_2^+ + E^- \tag{2.5}$$

$$N^+ + N_2 \longleftrightarrow N_2^+ + N \tag{2.6}$$

The pure nitrogen emission spectroscopy data acquired from EAST test series 62 has been used to perform spectral fitting analyses at conditions relevant to both lunar and LEO return entry speeds. The methodology and results of this from previous works will be discussed in more detail in Section 2.4.4 [2].

The EAST facility has two independent driven tubes of 101.6 and 609.6 mm diameters. The former has been used for the vast majority of studies, though the larger diameter counterpart has advantages for the study of lower speed conditions. For optically thin test slugs, signal increases linearly with tube diameter since it corresponds to an increase of the integration path length over which radiation is emitted [3]. Signal at LEO return speeds is typically much less than that encountered in faster entry missions or in alternate atmospheres, and the test slugs produced are close to an optically thin mixture. The use of a larger diameter tube is therefore appealing for the study of LEO return missions.

It was shown by Bogdanoff and Cruden [10] that the compromise of a larger diameter tube is a sacrifice of spatial resolution. This is because for a given solid angle in the emission spectroscopy optics, a larger area is mapped on the closest and furthest limits of the tube wall for a larger diameter tube. This can be reduced by including an aperture in the optical path, though this prevents the intended increase in signal from being realised. The overall effect of the increase in diameter therefore was to limit the maximum achievable shock speed of the facility. Additionally, disturbance of the shocks at very low pressures in the large diameter tube were observed by protuberances at the inner wall. However, more recent attempts by Cruden and Brandis [45] in EAST test series 59 with the larger diameter tube, to study higher-pressure low-speed 7 to 9 km/s entry missions, have proved more successful and compare well against the results of the 101.6 mm tube. The consideration of different diameter tubes is relevant in the present work, since experiments for this thesis were performed in the T6 Aluminium Shock Tube, which has a diameter of 225 mm, more than double that of EAST's. This is important when comparing the spectral radiances from both facilities in later chapters.

The knowledge gained over the extensive emission spectra captured from the EAST facility over the years has lead to a wealth of experience and knowledge in how to perform such measurements during a shock tube experiment optimally. A comprehensive summary is provided by Cruden [41], including a detailed account of the calibration procedure for each

[2] New spectral fitting analyses of pure nitrogen data are also performed in Chapters 5 and 6 of this thesis, building on previous efforts.

[3] The optically thin assumption implies that absorption from within the test gas is negligible. The validity of this assumption is highly dependent on the thermodynamic state of the gas, the intensity of a specific spectral feature and the integration path length.

spectral channel and the characterisation of both spectral and spatial blurring effects. These are termed the "Instrument Line Shape" (ILS) and the "Spatial Resolution Function" (SRF) respectively. The calibration procedures applied to the T6 Aluminium Shock Tube emission spectroscopy systems in this work are summarised in Chapter 3. These draw heavily on the methods of Cruden [41]. Though alternative diagnostic techniques have been implemented on the EAST facility, for example the laser absorption studies by MacDonald et al. [111], the vast majority of campaigns have involved solely emission spectroscopy. Since spectrally resolved emission is also the focus of experiments performed for this thesis, alternative optical diagnostic techniques are only referred to briefly in Section 2.4.1.

Studies based on the emission spectra attained from EAST experiments have contributed to a significant portion of the present knowledge around entry vehicle shock layers and the subsequent radiative heating. Additionally, numerical models based on EAST results have explained discrepancies between true flight data and original predictions, as shown in the works of Cruden et al. [48]. The information attained from these studies has directly contributed to the specification of TPS requirements. However, some discrepancies remain. Most relevant to this thesis, disagreements between experiment and numerical models are observed for tests at speeds below 10 km/s in the equilibrium region. In particular, an under prediction of background radiation has been observed by Cruden and Brandis [45] at speeds from 7 to 9 km/s, and from 3 to 7 km/s by Cruden [42]. The origin of this is still under investigation, though has a wavelength dependence (increasing towards the lower wavelengths near 200 nm) which has been repeated in experiments in the T6 Aluminium Shock Tube, down to shock speeds of 5.5 km/s as shown by Glenn et al. [69]. The discrepancies observed in prior EAST and T6 LEO equilibrium spectra are shown in more detail in Section 2.4.2.

2.2.2 X2 Non-Reflected Shock Tube

As was referred to in Section 2.1.2, the X2 facility at the University of Queensland predominantly operates as an expansion tube. The works of Morgan et al. [129] proposed it be operated as a shock tube in an aptly named "Non-Reflected Shock Tube" configuration. Since the tube does not include windows integrated into the wall, as is the case with EAST and T6 shock tube designs, the test slug was imaged as it exits the end of the 85 mm bore, as shown in Fig. 2.10 [4]. This configuration means radiation does not have to pass through the boundary layer from the tube wall, however this is replaced by the seemingly more complicated combination of a supersonic expansion fan from the tunnel exit walls and the optical line of sight passing through a radially expanding shock.

[4]The first T6 shock tube campaign by Collen et al. [34] also captured radiation emitted from the test slug as it emerged from the tube outlet in 2019, though this has not been repeated since.

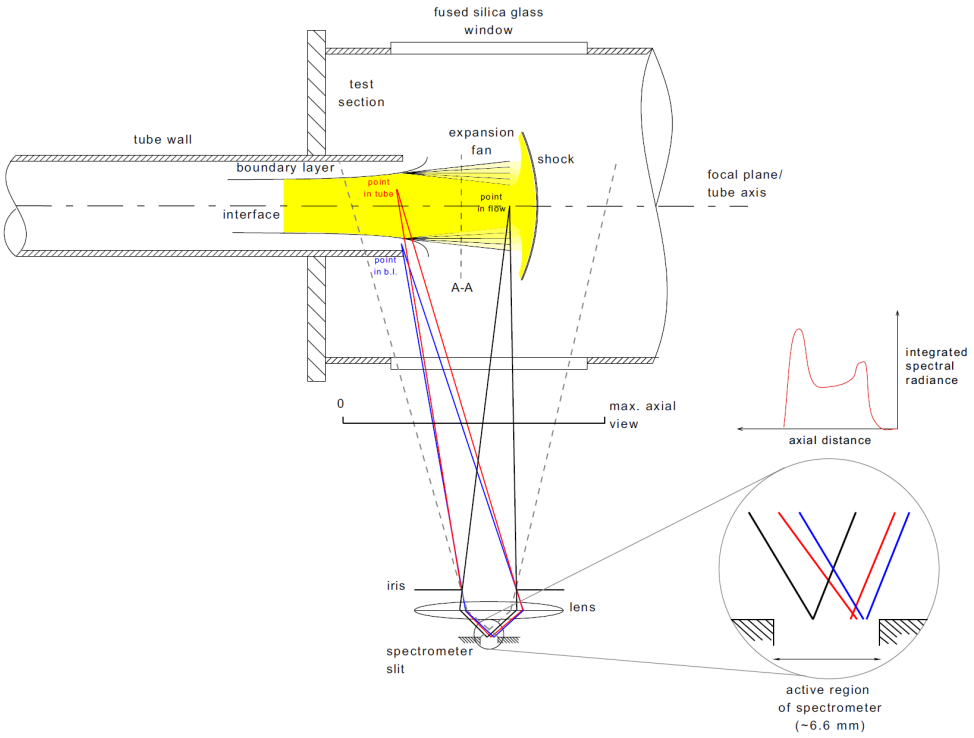


Fig. 2.10 Illustration of test slug emerging from the end of the X2 tube, into the test section. Associated optics included have been condensed down to a single lens. Not to scale. Taken from McGilvray et al. [119].

Despite the unknown consequences of the different measurement location, Brandis et al. [15, 21] first operated the X2 facility in NRST mode for the study of Titan entry conditions, to show close agreement with data attained from the EAST facility. The results of this study were later used to inform collisional radiative models for Titan entry. The works of McGilvray et al. [120, 119] extended the X2 Titan studies to a wider range of conditions and repeated a 8.1 km/s 20 Pa condition to demonstrate the peak radiance diminishes with a highly linear trend as the shock is imaged further from the tube exit. In addition to Titan, a comparison of peak heating lunar return (10 km/s, 0.2 Torr) air data was also made between X2 NRST and EAST by Brandis et al. [13] to show good qualitative agreement between the two datasets. Finally, datasets were extended further into Mars entry studies by McIntyre et al. [124] and even use of a larger 155 mm diameter tube for upper atmosphere Titan entry condition by Jacobs et al. [90]. To date, no report of conditions relevant to LEO return are available in the literature from the X2 NRST facility.

2.2.3 Hyper-Velocity Shock Tube

The Hyper-Velocity Shock Tube (HVST) at the Japanese Aerospace Exploration Agency (JAXA) has not performed experiments for LEO return missions to date. However, it incorporates various alternative approaches to shock tube operation and spectrally resolved measurements and so is briefly included in this review. Commissioning of HVST is detailed in the works of Yamada et al. [197]. Figure 2.11 shows a schematic of the facility. It's apparent that the "low pressure tube" switches from a circular to a square cross-section, which is unusual compared to other shock tube facilities. Additionally, Yamada et al. [198] describes the alternative laser-based high-precision technique to measure shock speed and initiate camera triggering, which is implemented on the facility. Though this method is advanced and extremely precise, it is only performed at the test section. This limits facility analysis, as will be explained in Chapter 3, since the shock speed trajectory determines the enthalpy and thus radiance profiles in the resulting test slug. Furthermore, later work by Takayanagi et al. [179] showed this to be problematic when trying to increase the diaphragm compression ratio and burst pressure to reach higher shock speeds. The limited facility diagnostics prevented a precise diagnosis of the performance losses.

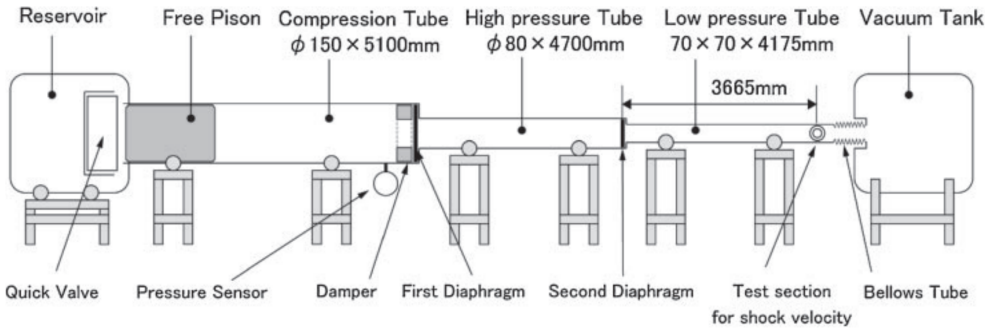


Fig. 2.11 Schematic of the free-piston double-diaphragm HVST facility. Taken from Yamada et al. [197].

The method of radiation measurements also differs from other shock tubes. Takayanagi and Fujita [178] describe the acquisition of spectrally resolved radiation at only a discrete point behind the shock, via a reflective condenser to focus light onto the spectrometer slit. Achieving spatial resolution therefore requires shot repetition with adjustments in the camera trigger delay settings. This introduces shot-to-shot variation uncertainties, which are amplified by the fact shock speed profiles are unknown. Despite the various differences in approach, Fujita et al. [62] show the HVST facility has captured data for Mars entry missions, including in the difficult VUV region, and has shown good agreement to some of EAST's

data. Finally, to date, only measurements at very high speed Earth return conditions have been made in the HVST facility in air by Takayanagi et al. [179].

2.2.4 Detonation-Driven Double-Diaphragm Shock Tube

A detonation-driven double-diaphragm shock tube has been used by Tang et al. [180] at Sichuan University, to study time-resolved ultraviolet spectra in pure nitrogen at LEO return entry speeds. A schematic of the facility is given in Fig. 2.12. The instrumentation resembles similarities to the HVST facility discussed in Section 2.2.3. For example, time of arrival sensors are only positioned just before the test-section, though are in the form of PCB 113B pressure sensors as opposed to a laser. Additionally, the fibre optic spectroscopy system only acquires spectra at one spatial location. Tang et al. [180] therefore attain temporal resolution by repeating shots and adjusting camera triggering delay. This, again, introduces shot-to-shot variation uncertainties, which are not able to be quantified due to the lack of diagnostics along the facility to track the shock trajectory. However, studies of the non-equilibrium region immediately behind the shock should only require velocity information closer to the measurement region. Tang et al. [180] performed spectral fitting to the spectra acquired through the non-equilibrium region of pure nitrogen test slugs at speeds from 6.8 to 9 km/s. The results of this are included in a wider spectral fitting discussion in Section 2.4.4. Despite only performing relative intensity calibrations with a deuterium lamp [5], they manage to temporally resolve rotational and vibrational temperatures which share similarities to the results of Tibère-Inglesse and Cruden [187] in EAST.

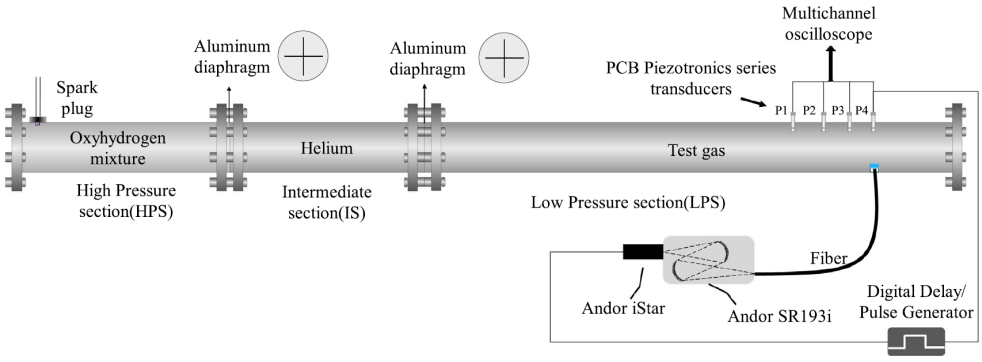


Fig. 2.12 Illustration of the double diaphragm facility and spectral radiance measurement system. Taken from Tang et al. [180].

[5] Absolute intensity calibrations are routinely performed for all experiments and spectral channels in both T6 and EAST facilities. The methodology used in recent T6 Aluminium Shock Tube LEO return studies are detailed in Chapter 3.

2.2.5 European Shock Tube for High-Enthalpy Research

The European Shock Tube for High-Enthalpy Research (ESTHER) facility at the Instituto Superior Técnico is under development to support future planetary exploration missions by the European Space Agency. Early design and performance prediction work is given by Lino da Silva et al. [105]. Figure 2.13 provides a CAD overview of the facility. More recently, Ferreira and da Silva [60] have evaluated the performance of the facility's laser ignition combustion driver for $He:H_2:O_2$ and $N_2:H_2:O_2$ mixtures, successfully characterising compression ratios, acoustic wave formation and flame velocity. Though the facility is yet to perform shock layer radiation experiments, it's predicted to reach shock speeds of at least 10 km/s in air. This, combined with plans to attain spectrally and temporally resolved radiation data using a VUV rated streak camera, will provide another useful reference to compare benchmarks datasets between high-enthalpy impulse facilities.

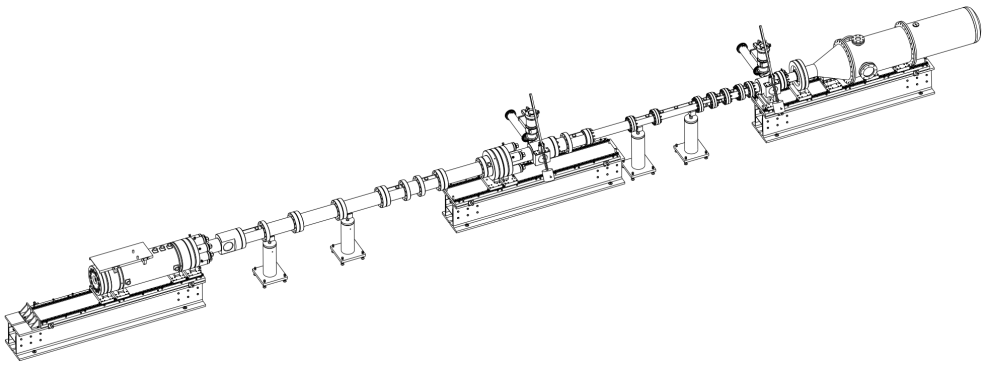


Fig. 2.13 CAD overview of the ESTHER facility. Taken from Ferreira and da Silva [60].

2.2.6 Stanford University Reflected Shock Tube

In addition to shock tubes, reflected shock tubes, where a reflected shock is produced after the incident shock reaches the end wall [6], to produce a high temperature stagnation region, have been used in the context of shock layer radiation studies. Figure 2.14 shows the set-up used in recent experiments in the reflected shock tube at Stanford University. This operation mode is able to generate very high temperatures and pressures in a small, controlled stagnation region, which is typically used for rate coefficient studies. However, the spatial resolution to capture the evolving thermochemical states representative of a shock layer is lost in the reflected shock region, and thus the shock tube - stagnation line analogy no longer applies.

[6] Many of the shock tubes previously discussed have a dump tank at the end, which involves a significant volume increase, so the incident shock may dissipate instead of generating a reflected shock which stagnates the test gas and thus raises the pressures experienced by the facility.

Additionally, the test gas undergoes two rapid heating and compression processes, adding uncertainties and steep transients to the thermochemical states in the resultant test gas.

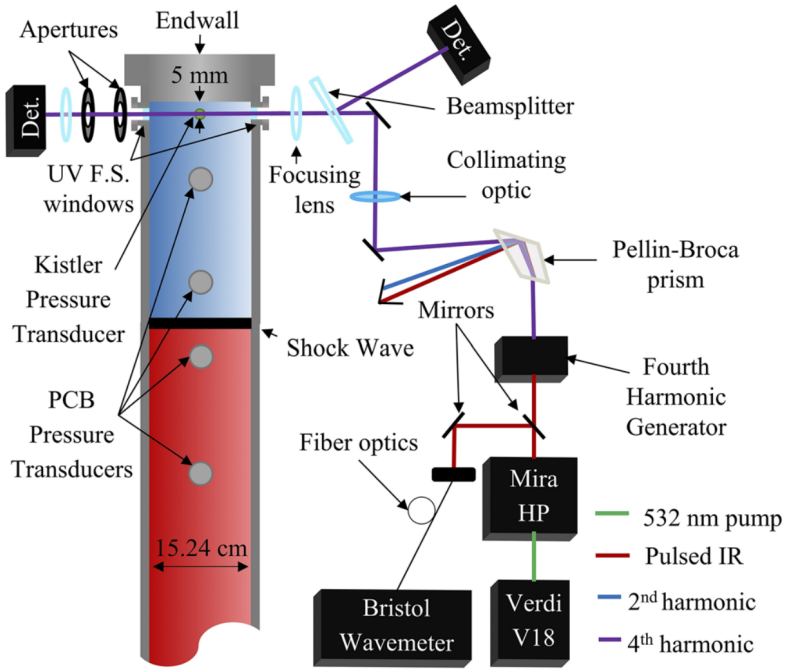


Fig. 2.14 Illustration of reflected shock tube stagnation region and associated ultraviolet laser optics. Taken from Streicher et al. [175].

Works by Bowman and Hanson [11] in 1979 identified the uncertainties around the gas dynamics as one of the major uncertainties in the resultant rate extractions. Later studies by Petersen and Hanson [146] have shown these reflected shock non-idealities are greatest at lower pressure and higher temperature conditions. Despite the drawbacks of a complicated, non-flight representative environment, these facilities have been used to infer valuable reaction rate information and perform state-specific temperature measurements. Recent studies by Streicher et al. [174] inferred NO vibrational temperatures in air, using a sensor method involving three ultraviolet lasers, developing on previous diagnostics of only two (as seen in Streicher et al. [175]). They also present preliminary $O_2 + N_2$ dissociation and $N_2 + O$ Zeldovich reaction rates. Though valuable data is being extracted from these facilities, they are not discussed any further in this thesis, since the conversion of data between incident and reflected shock flow-fields (and extraction of reaction rates) is beyond the scope of the current work.

2.3 Radiative Transport Solvers

A common process in science and engineering is to compare experimental measurements with the numerical predictions from state of the art models, based on the current level of understanding for the phenomena in question. Results from new comparisons may then inform and update new models, and the process continues until satisfactory agreement is achieved for a wide range of scenarios. Radiation is no different. A range of radiative transport solvers have been developed from within multiple research groups, including: NEQAIR (developed within the NASA Ames shock tube radiation group, detailed by Brandis and Cruden [19]); SPECAIR (developed by the CentraleSupélec ICP torch laboratory group, as detailed by Laux et al. [100]); PARADE (developed by the European Space Agency, as detailed by Smith [160]); and SPARK (developed in the Hypersonic Plasmas Laboratory at the University of Lisbon, as detailed by Lopez and Lino Da Silva [109]). The former two are referred to and used in later chapters of this thesis, and so a brief introduction to them both is now given.

NEQAIR: Development of the Non-Equilibrium Air (NEQAIR) radiative transport code began in the 1970s, though was initially called the "HF730" code (as documented by Brandis and Cruden [19]) to then become "NEQAIR" in the 1980s as described in the works of Park [143]. Multiple developments were implemented during the 1990s, which are covered in the works of Whiting et al. [192]. It is also during this time that the plasma torch studies by Laux et al. [102] were incorporated to produce NEQAIR2, significantly improving equilibrium radiance predictions in the ultraviolet to the near-infrared wavelength regions. Efforts have continued in the works of Cruden and Brandis [44, 19] to improve the NEQAIR radiation code from the results of tests conducted over the last decade. It is a well-established and recognised numerical tool in the field of shock layer radiation studies, and has been used to predict the radiative heat fluxes of future planet entry missions.

SPECAIR: The SPECAIR radiation code is an alternative radiative transport model developed by the CentraleSupélec ICP torch laboratory group, originally based on the NEQAIR documented by Park [143]. Laux et al. [100, 102] state the capabilities of modelling 37 molecular transitions from NO, N_2, N_2^+ , O_2, CN, OH, NH, C_2, and CO, as well as atomic lines of N, O, and C. Thus giving capabilities to predict spectral radiance emissions and heat fluxes for a range of planet atmospheres. Section 2.4.2 shows examples of the close agreement SPECAIR simulations have been able to make with spectra acquired from ICP torch experiments.

Although the radiative modelling is not the purpose of this thesis, it is mentioned here due to the frequent reference and use in the following material. These codes do not perform any flow-field or aerodynamic calculations, but rather, can be fed a line of sight (LOS) predicted

from CFD tools to calculate the radiation emission and absorption through the region of interest. Spectrally resolved traces may be generated and convolved with experimental instrument line shapes [7] to provide comparisons against experimental data, or alternatively used to predict the radiative heat flux incident on a vehicle surface for a true flight case.

Each code requires a distribution of energy states to be selected before running a simulation. A Boltzmann distribution may be assumed, where the populations of particles in different energy states have reached a steady distribution, which is a function of the temperature. Conversely, a non-Boltzmann distribution may be defined. This can refer to a much wider range of energy state populations which have not had time to re-distribute into the Boltzmann distribution. These are only typicaly found in the transient non-equilibrium environment following a rapid heating or cooling process, such as those experienced in the compressing and expanding flows around a hypersonic vehicle. The non-Boltzmann population of states in such regions can significantly affect the radiation emission and consequently the heat fluxes produced. Additionally, the use of Quasi-State-Specific (QSS) modelling is often incorporated into non-Boltzmann models. Here, rather than fully resolving each quantum state and how they interact with each other - as is the case in computationally expensive state-to-state modelling - the state-specific populations are treated as "quasi-steady". This is possible since their rates of change may be significantly slower relative to other transient processes occurring simultaneously. This is useful for capturing the nuances of state-specific behaviours without needing to solve the full time-dependent evolution of every state, though is dependent on an approximation. Such models can significantly change the predicted spectral radiation from a flow exhibiting non-Boltzman populations.

2.4 Past Attempts to Characterise Shock Layers via Emission Spectroscopy

Having reviewed high-enthalpy facilities capable of recreating flow conditions relevant to LEO return stagnation lines, along with examples of the studies they have enabled and some of the radiation codes used for comparison, we now turn our attention to the results these facilities have produced in the context of thermochemical state characterisation. The objective of this section is to identify the unexplained discrepancies found in the literature around low-speed air spectrally resolved radiance measurements. This ultimately justifies the work undertaken in the remainder of this thesis. First, a brief overview of optical emission spectroscopy is provided, and why it's a valuable source of information for initial

[7] Characterisation of Instrument Line Shapes is explained in Section 3.6.2.

thermochemical state characterisation attempts. Sections 2.4.2, 2.4.4 and 2.4.5 then provide the motivation for the works of Chapters 4, 6 and 7 respectively. This summary highlights the major developments in the literature, giving readers the necessary background to understand the approach and challenges discussed in the upcoming chapters.

2.4.1 Optical Emission Spectroscopy

The primary instrumentation for the experiments conducted in the T6 Aluminium Shock Tube for this thesis is a dual Optical Emission Spectroscopy (OES) set-up, with two independent channels to cover both ultraviolet and visible to near-infrared wavelength ranges. This set-up provides both spectral and spatial resolution and is reviewed extensively in Chapter 3. Generally, however, many other optical measurement techniques may be performed. A brief discussion of why spectrally resolved emission techniques are historically favoured in the study of shock layer radiation, and indeed used in these works, is given here.

The simplest emission techniques do not provide spectral resolution. These so-called "spectrally-integrated" measurements enable mostly qualitative analysis, providing imagery for flow visualisation as done by Zander et al. [201] and Steer et al. [171]. Figure 2.15 shows an example of this, performed during ice giant entry studies in the T6 Stalker Tunnel while operating in expansion tube mode. Examples of quantitative measurements include shock stand-off measurements by MacLean et al. [113] and test time evaluation work by James et al. [92]. Spectrally integrated measurements can also include the use of photodiodes, to measure the spatial variation in emission behind a shock wave, as performed by Fujita et al. [61]. Optical filters may be used during such measurements to gauge the contributions of different portions of the electromagnetic spectrum to the total radiative heat flux. Photodiodes used in this context should be flush with the facility or model wall, so not to disturb the flow-field and influence the measurement.

By spectrally resolving the radiation emission, analyses may become much more intricate and detailed. The most common technique to achieve this in the context of shock layer radiation studies is OES, which involves a series of lenses or mirrors to create an optical path which focuses and magnifies the radiation onto a spectrometer slit. A diffraction grating and a series of mirrors inside the spectrometer then perform the spectral separation of wavelengths and focus the signal back down onto a camera sensor array. Thorne et al. [186] provide a comprehensive review of the technique, which is renowned for it's relatively easy set-up and therefore common use.

In the context of shock layer radiation studies, the thesis of Laux [101] is frequently referenced as an example of analyses that may be performed with good quality high-resolution spectrally resolved radiation measurements. This included using the relative intensities of

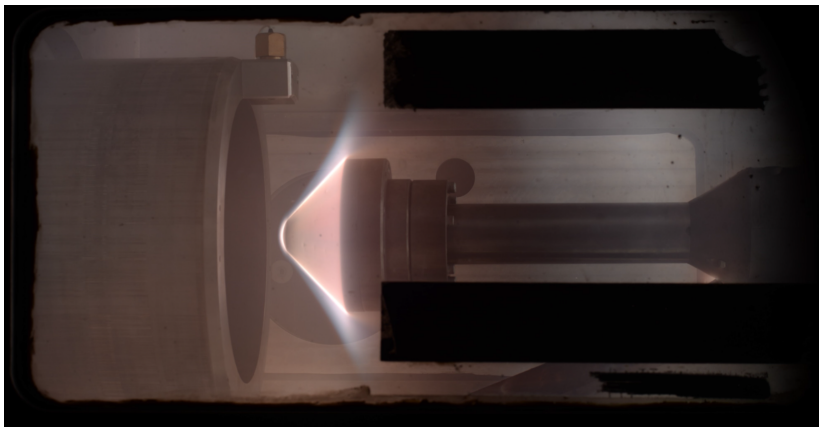


Fig. 2.15 Single frame colour exposure of flow over a Galileo probe during expansion tube tests in the T6 Stalker tunnel. Taken from Steer et al. [171].

molecular and atomic features to extract vibrational and excitation temperatures, taking advantage of the ICP torch plasma being in local thermodynamic equilibrium and use of Boltzmann distributions. Spectral information for a wide range of species can be obtained by capturing the naturally occurring emission from the excited states. In the case of non-equilibrium flows in air or pure nitrogen, many excited atomic states of oxygen and nitrogen atoms can be resolved in the near-infrared wavelengths, as well as ground states in the vacuum ultraviolet and molecular bands in the ultraviolet. Figure 2.16 shows how the excited atomic states may be used on a Boltzmann plot to validate if a Boltzmann distribution is applicable [8]. Combining the spectral resolution with temporal or spatial resolution (as is achieved in the OES set-ups used in EAST, X2 and T6 shock tube radiation studies) allows the evolution of thermochemical states to be evaluated. Recent works have also began the use of spectral fitting techniques, calling on radiative transport codes, to extract temperatures and excited state populations. Previous attempts at this method are shown in more detail in the following discussions of this section, for pure nitrogen and air tests respectively.

In addition to emission techniques, methods which rely on absorption to perform measurements have also been implemented for the study of high-enthalpy flows. One of the most common is tunable diode laser absorption spectroscopy (TDLAS), where a laser's frequency is varied through a test flow over a short wavelength region to scan a small portion of the electromagnetic spectrum at a high resolution. This method has the advantage of allowing access to non-radiating particles in the flow [9] and removes many of the signal

[8] A Boltzmann distribution is confirmed if all points lie on a straight line when using a logarithmic y-axis. Macroscopically, the Boltzmann distribution allows a single value of temperature be defined for the energy mode in question.

[9] Danehy et al. [52] highlight that even at the very high temperatures experienced in a vehicle shock layer, the vast majority of particles remain in the ground state.

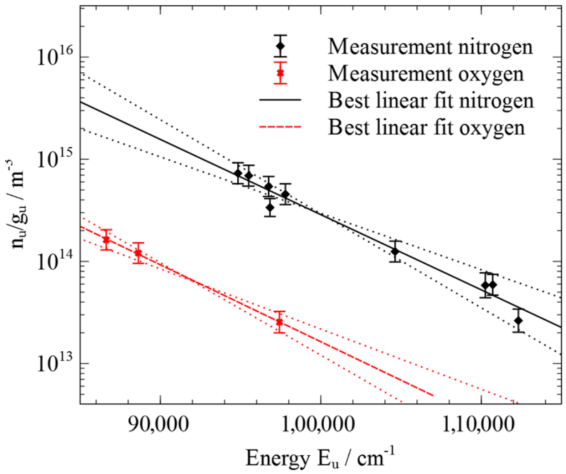


Fig. 2.16 Boltzmann plots attained from oxygen and nitrogen transitions in PWT re-entry experiments. Taken from Hermann et al. [79].

limitations experienced for some species in emission techniques, due to the use of the secondary light source. However, the disadvantage of only accessing very small portions of the electromagnetic spectrum is quite significant for shock tube tests, due to the short test times and relatively long turnarounds in-between experiments. An initial emission study is therefore often necessary to see the broader spectrum and identify potential regions of interest for investigation by laser/absorption techniques. TDLAS has been performed by MacDonald et al. [111] on the EAST facility, to take measurements of CO number densities and translational temperatures in shocked CO and CO_2 test gases.

2.4.2 Equilibrium Discrepancy

The equilibrium thermochemical state is the most certain of all those attained during the post-shock relaxation process. NASA's Chemical Equilibrium with Applications (CEA) solver was developed in the 1960s at the NASA Glenn Research Center [10] to predict chemical equilibrium compositions and properties for a variety of applications in high-enthalpy flows. Figure 2.17 shows how equilibrium mole fractions in air vary as temperature increases to nearly 20,000 K, based on CEA predictions. McBride [115] presents version 2 of the code, which is still frequently used in the context of shock layer radiation studies, to calculate the chemical composition across the LOS through which radiation has travelled during an experiment. This can be fed into one of the radiative transport solvers discussed in Section 2.3 to predict equilibrium spectral radiance traces, providing a means to assess and update radiative transport models, as done in the works of Laux [101].

[10] Then known as the NASA Lewis Research Center.

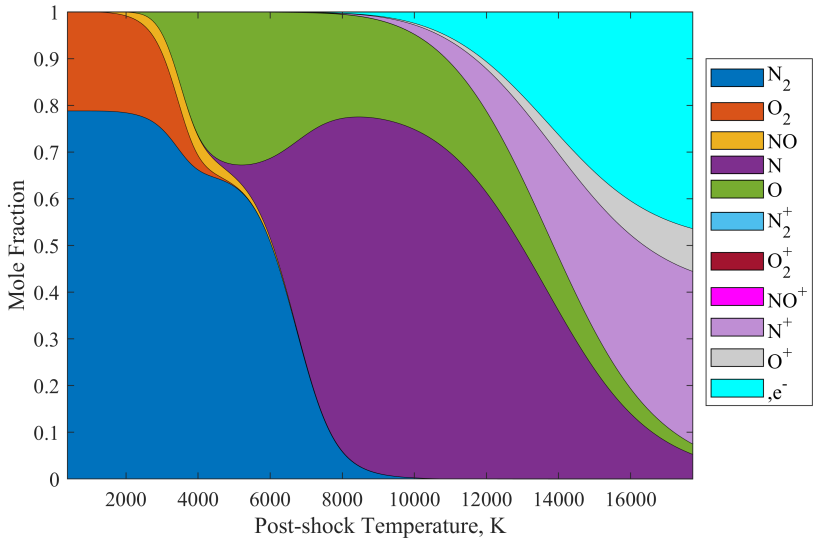


Fig. 2.17 Area plot of CEA equilibrium mole fraction predictions across a range of temperatures in 1 bar air.

Agreement between experiment and numerical predictions across a range of conditions indicates correct modelling of the emission and absorption phenomena. Additionally, comparisons of data from a range of facilities allows evaluation of correct measurement and optical calibration procedures being performed, to generate the experimental profiles. Equilibrium spectra are therefore the starting point of this study, before introducing the additional complication of chemical kinetics, which bring about uncertainties of the thermochemical state (in addition to the radiative modelling uncertainties).

Shock Tube Studies

Glenn et al. [69] took measurements of spectrally resolved radiation behind shocks of 5.5 to 7.2 km/s in synthetic air during a T6 Aluminium Shock Tube campaign in late 2020[11]. The campaign was originally intended for study of the non-equilibrium region and included comparisons of absolute non-equilibrium metrics (as described by Brandis et al. [14]) between experiment and predictions using a two-temperature 11 species air model with Park [145] reaction rates in the POSHAX3 relaxation solver [147]. Despite trialling excitation models from Park [144], Huo et al. [88] and the recent updates from Cruden and Brandis [45] (based on measurements in the EAST facility at 7 to 9 km/s) all attempts of attaining good non-equilibrium comparisons were ultimately hindered by the consistent discrepancies in

[11]This was the first attempt at capturing data relevant to LEO return missions in the T6 facility, over two years prior to the second low-speed air campaign which acquired the datasets used in this thesis.

the equilibrium region. This presented a more fundamental problem that should be solved before attempting further non-equilibrium analyses. Figure 2.18 shows the ultraviolet and visible/near-infrared radiance profiles from Glenn et al. [69] at their nominal 6.55 km/s condition, along with equilibrium spectra plotted against CEA-NEQAIR predictions. The plateau in radiance following the non-equilibrium peak indicates completion of relaxation processes and establishment of thermochemical equilibrium. The spectra shown were thus generated by averaging in this region. It's evident that a continuum background offset is present across all observed regions, though increases towards the lower wavelengths where NO dominates. As can be seen, the measured cumulative radiance in the ultraviolet is nearly three times that predicted by CEA-NEQAIR for T6s198. These continuum offsets were present across all conditions tested in the chosen shock speed range.

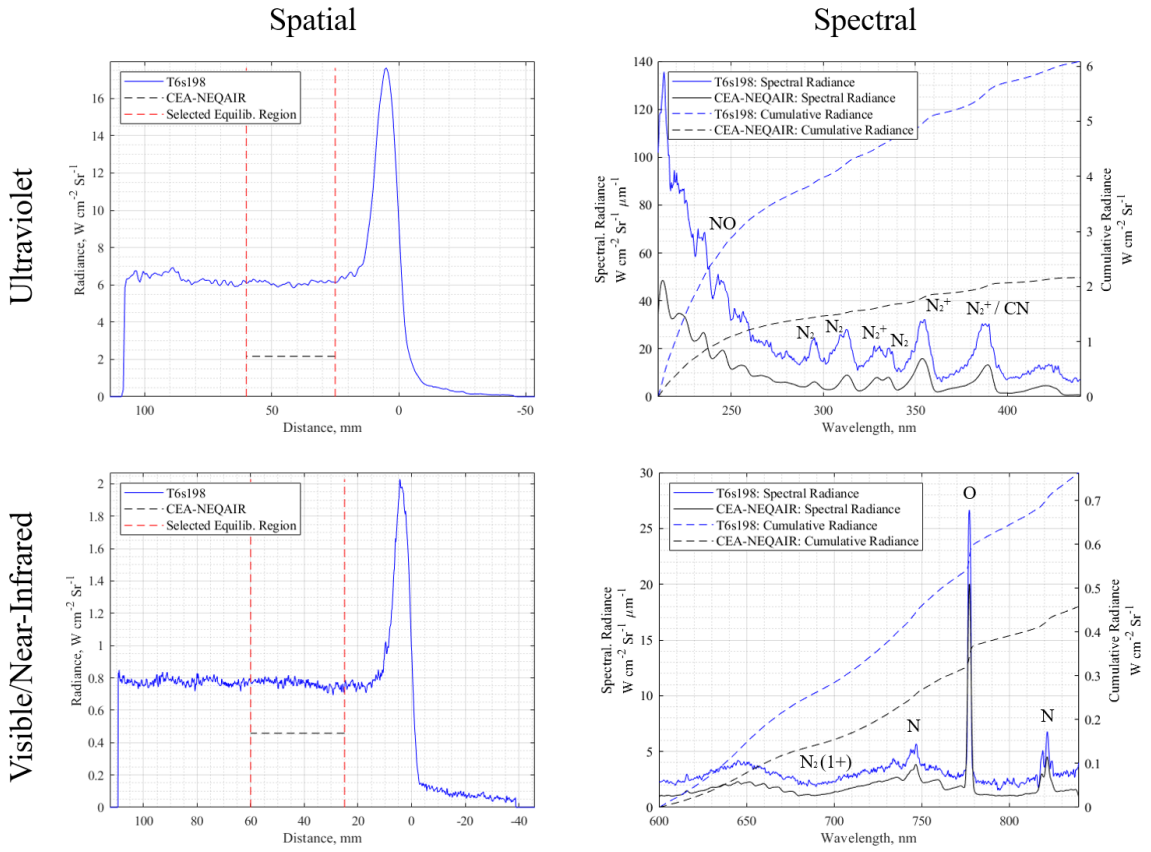
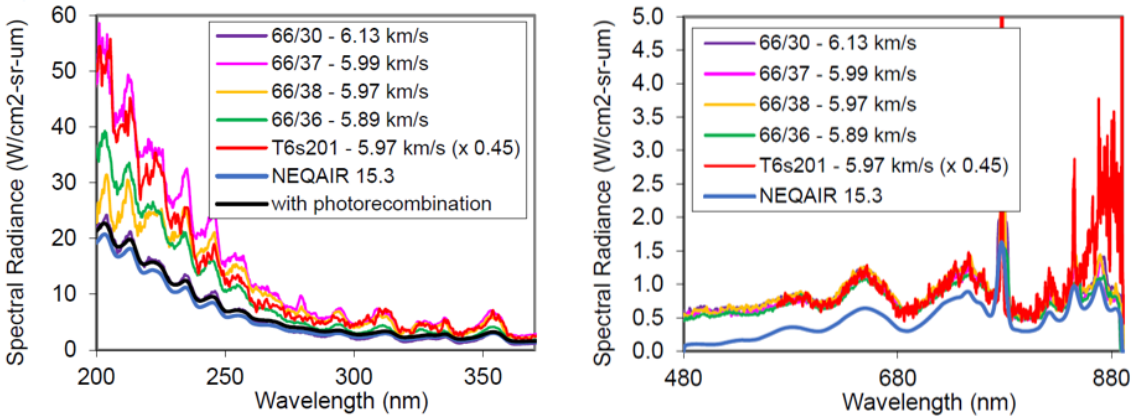


Fig. 2.18 Spatial and spectral radiance profiles for T6s198 (6.65 km/s, 213.9 Pa synthetic air) from the ultraviolet and visible/near-infrared spectral channels. Equilibrium spectra extracted are compared against CEA-NEQAIR, with main molecular and atomic features labelled. Adapted from Glenn et al. [69].

This finding prompted comparison shots to be performed in the EAST facility. Cruden [42] recently analysed a series of air tests at 3 to 7 km/s, including some repeats of low-speed

conditions from the T6 Aluminium Shock Tube. Figure 2.19 compares results from both facilities for a nominal condition of 6 km/s and 2 Torr in air. The T6 data is scaled by the ratio of diameters between the facilities, to enable a like-for-like comparison. This takes advantage of the test conditions being very close to optically thin. A number of repeat tests were conducted on the EAST facility to gauge shot-to-shot variations around the nominal condition and equilibrium simulations performed with the latest NEQAIR v15.3 for comparison. The T6 data aligns closely with the EAST tests, though it's evident that much stronger variation in spectral radiance exists below 300 nm, where NO bands dominate. Additionally, T6 spectral radiance above ~850 nm is the result of noise and thus does not follow the EAST spectral profiles.



(a) Ultraviolet.

(b) Visible/Near-Infrared.

Fig. 2.19 Comparison of equilibrium spectra at 6 km/s and 2.0 Torr obtained from EAST and T6 facilities. Equilibrium predictions are shown from CEA and NEQAIR v15.3 with alternative photorecombination models. Plots taken from Cruden [42].

Figure 2.19 also trials the use of alternative cross-sections for O_2 photodissociation from the PyDiatomic code at the Australian National University [64]. This is to capture photodissociation and photorecombination of O_2 Schumann-Runge ($B^3\Sigma_u^- - X^3\Sigma_g^-$) bands, potentially occurring due to an increased population of higher rotational and vibrational levels at elevated temperatures (as discussed in works of Krish et al. [99] and Bykova and Kuznetsova [23]) which also radiate in this wavelength region. This only showed a small increase in the equilibrium spectral radiance prediction at the 6 km/s test case, as shown in Fig. 2.19, and thus does not explain the remaining discrepancies. However, much better improvements were realised for lower speed and higher pressure cases. Figure 2.20 compares the effect of O_2 photorecombination for a 4 km/s and 10 Torr shot. The contribution of NO at such low speeds is drastically reduced and better agreement from the O_2 photorecombination

modelling can be realised. Chapter 4 applies this new modelling to the lowest speed test case from the new T6 Aluminium Shock Tube campaign, and investigates the effect of various experimental considerations to improve equilibrium agreement at the higher speeds relevant to LEO return.

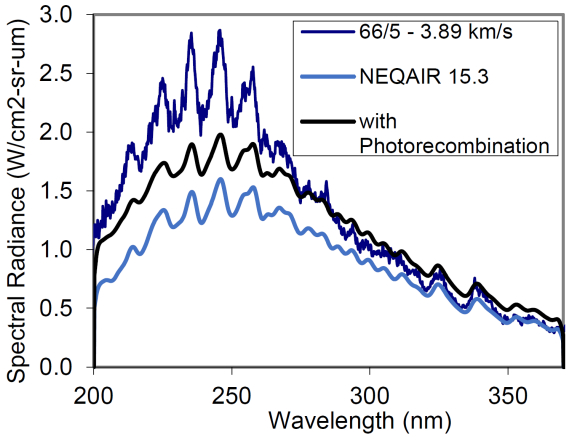


Fig. 2.20 Comparison of EAST ultraviolet spectrum to CEA-NEQAIR with and without O_2 photorecombination at 4 km/s and 10 Torr.

Plasma Torch Studies

As was explained in Section 2.1.1, ICP torches provide a reliable source of equilibrium spectral radiance traces. The works of Laux et al. [102] show exceptional agreement between experimental absolute intensities against the predictions of the SPECAIR radiative transport code. Figure 2.21 shows an extract of this data, though continued close agreement is achieved from $\sim$190 to $\sim$760 nm. The long exposure times on the facility allows high-resolution spectra to be captured and thus distinction of various spectral features. Recent works by McGuire et al. [122] improved agreements between SPECAIR and ICP torch spectra further into the VUV wavelength region, though they highlighted that the data indicates sources of emission are still unaccounted for in the SPECAIR radiation code.

Following from the worse agreement between T6 AST and EAST low-speed data with NEQAIR, Glenn et al. [67] performed a NEQAIR simulation for ICP torch data from CentraleSupélec to evaluate the effect of any radiative modelling differences between the two codes. Figure 2.22 is extracted from this study and demonstrates there are discrepancies in predictions between the two codes, particularly in the lower wavelengths where NO dominates. Interestingly, this is the same region with increased variation between shots from the EAST facility. Though SPECAIR is closer to the measured profile than NEQAIR, it's evident that spectral agreement is not as close as that seen in the prior works of Laux

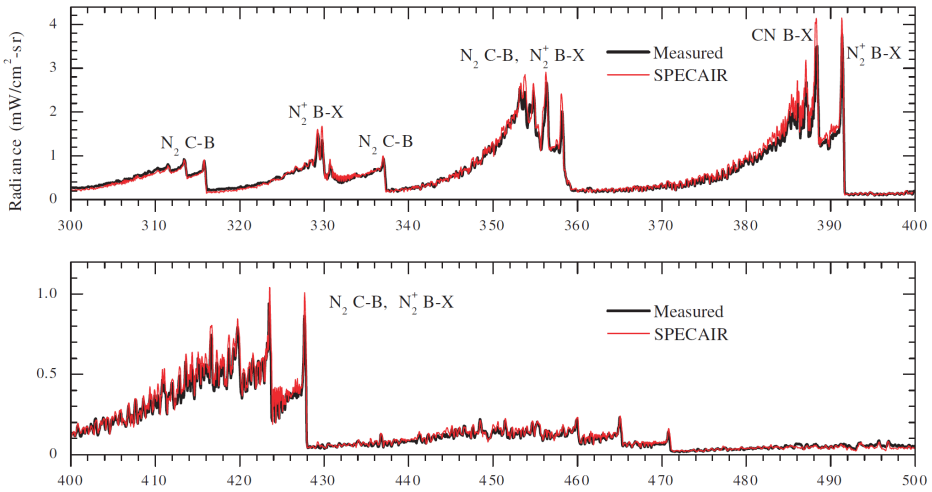


Fig. 2.21 Comparison of high-resolution equilibrium spectra from ICP torch measurements and SPECAIR for an air plasma in a state of local thermodynamic equilibrium at ∼7500 K. The x-axis is wavelength in units of nanometres. Taken from Laux et al. [102].

et al. [102]. Though it's important to note these simulations were performed before the improvements of McGuire et al. [122] and Cruden [42] in the SPECAIR and NEQAIR code respectively. The reader is directed to the references in Section 2.3 for an understanding of the radiative modelling differences between the two codes, since the numerical modelling aspect is not the subject of this thesis. For now, it's just highlighted that NEQAIR has been tailored to the spectra from higher-speed entry conditions in the EAST facility since its initial developments. Whereas SPECAIR has been largely influenced by data from the ICP torch, which is typically limited to enthalpies more appropriate to lower-speed missions. This is an important consideration since spectra at lower speeds are dominated by more molecular species such as NO, N_2 and N_2^+, rather than atomic species which emit strongly for high-speed entry missions. Thus, this comparison tests different portions of the NEQAIR radiative code. Finally, although NEQAIR under predicts the measured ICP torch trace more severely, the total cumulative radiance in the ultraviolet region is out by a factor approximately half that seen in shock tube data. Thus, additional discrepancies still appear to be present in the low-speed shock tube data, compared to the ICP torch.

Finally, it's noted that spectral offsets similar to that seen in the T6 and EAST low-speed air data have appeared in a few recent publications. Figure 2.23 is taken from the recent works of Merhaben et al. [125], which involved characterisation of N_2/CH_4 plasma emissions from the CentraleSupélec ICP torch. Here, SPECAIR predictions were multiplied by a constant factor in order to attain good agreement with experimental data. Furthermore, Thirani et al. [184] normalise spectral traces predicted for NO in the ultraviolet and infrared regions from

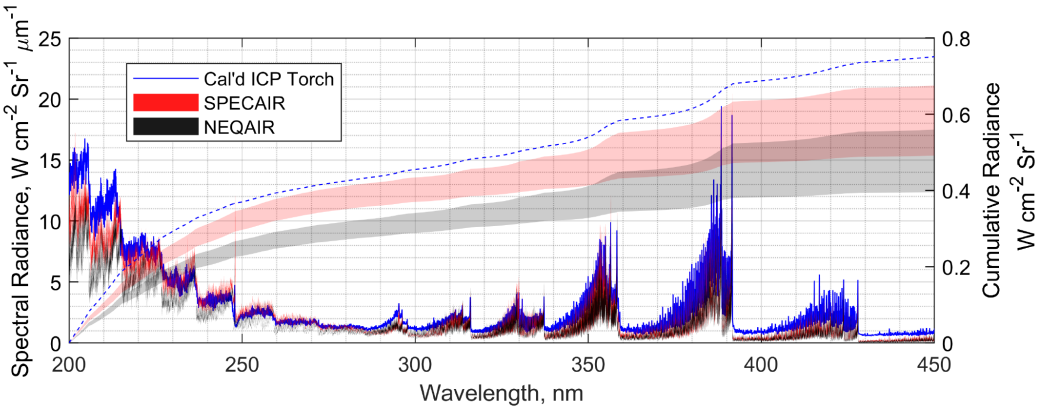


Fig. 2.22 Comparison of SPECAIR and NEQAIR ultraviolet spectra for a ∼7000 K plasma. Shaded regions are calculated from the plasma temperature profile uncertainty limits. Taken from Glenn et al. [67].

Direct Simulation Monte Carlo (DSMC) in order to plot against recent low-speed EAST spectra. This is another example of the difficulties encountered in attaining equilibrium agreement with low-speed air tests, particularly around the wavelengths where NO dominates. These results all point towards a common problem of failure to accurately reproduce the equilibrium spectral radiance traces, particularly in shock tube data with strong NO radiance. This, in combination of the studies of Cruden et al. [39] (reviewed in Section 2.2.1), motivated the work detailed in Chapter 4 of this thesis - to investigate experimental factors within the context of shock tube LEO return experiments that could cause the observed discrepancies. The chapter then goes on to demonstrate low-speed shock tube data in synthetic air and pure nitrogen with improved agreement to CEA-NEQAIR predictions, particularly in the visible to near-infrared wavelengths.

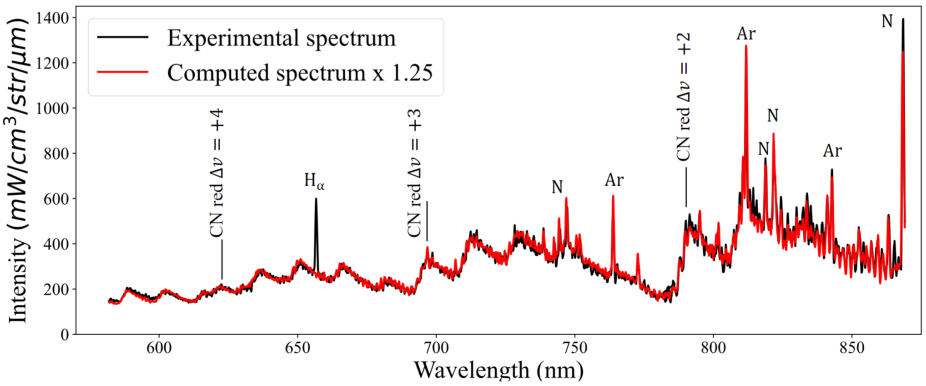


Fig. 2.23 Comparison between experimental N_2/CH_4 spectrum and SPECAIR prediction at the exit of an ICP torch with local thermodynamic equilibrium temperature of ∼6750 K. Taken from Merhaben et al. [125].

2.4.3 Evaluating Rates Against Radiance Profiles

As is explained in Chapter 1, radiative heating during LEO trajectories is mostly negligible and the objective of absolute radiation measurements for such conditions is not to quantify the radiative heat flux, but to understand the thermochemical state evolution through the shock layer. This allows improvements in the rates used by computational models, to subsequently improve the design of future hypersonic vehicles. A number of non-equilibrium solvers have been developed to generate a LOS that can use rates from the literature and produce results to be fed into the aforementioned radiative transport codes discussed in Section 2.3. One such code is the Post-SHock relAXation solver (POSHAX) discussed in the works of Gollan [71] and Potter [147]. This forms part of a compressible flow CFD package developed at the University Of Queensland, detailed in the works of Jacobs et al. [90]. It solves the one-dimensional variations in inviscid flow properties behind a normal shock and has been validated against experimental data by Gollan et al. [72], Capra and Morgan [26] and Lemal et al. [103]. More recently, Clarke et al. [30] have developed a Non-Equilibrium Shock Solver (NESS) at the University of Oxford as an alternative one-dimensional method to calculate the non-equilibrium post-shock properties, that can be applied to shock tube experiments by intrinsically accounting for mass loss to the boundary layer and resolving the shock structure. This has demonstrated the importance of correcting for particle time of flight when comparing shock tube radiance data to that simulated over a blunt body using NASA's Data Parallel Line Relaxation (DPLR) code, to resolve discrepancies originally thought owed to incorrect reaction rates. NASA's DPLR code is a suite of CFD tools for the computation of high-speed flows in chemical and thermal non-equilibrium used to predict the flow-field over 2D and 3D structures (Wright et al. [194]). The thermochemical states encountered in experiments have traditionally been evaluated by adjusting thermochemical rate modelling until good agreement is achieved with the experimental data. One-dimensional results can be fed into the radiative transport codes and convolved with the Spatial Resolution Function (SRF) (as defined by Cruden [41]) of the shock tube radiance measurements, to account for experimental smearing artefacts and allow a like-for-like comparison with the experimental data.

Figure 2.24 shows an example of one-dimensional post-shot analysis tools being used to predict the radiance profiles measured from a high-speed test case. Here, agreement of the radiance predictions to the experimental data indicates correct prediction of the thermochemical state, assuming the radiative modelling is correct. It's noted that the LASTA

simulations [12] were performed with v1.0 of the code which does not account for non-equilibrium thermochemistry and thus did not resolved the peak in radiance immediately behind the shock.

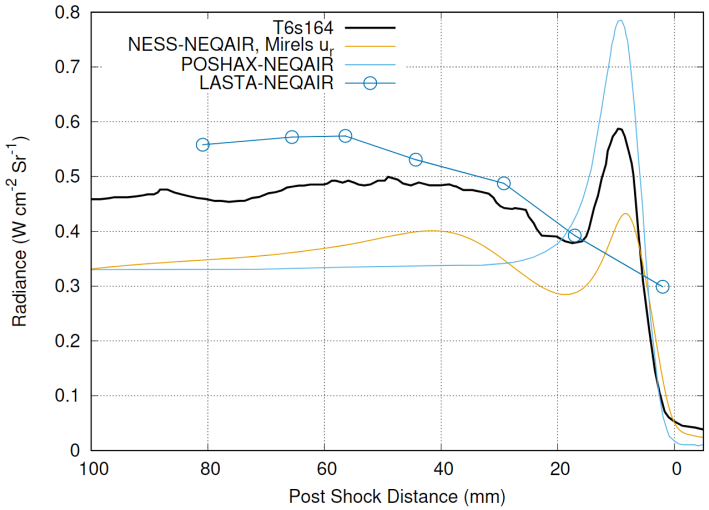
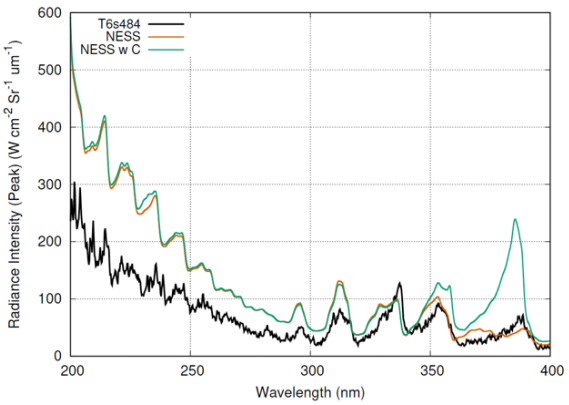


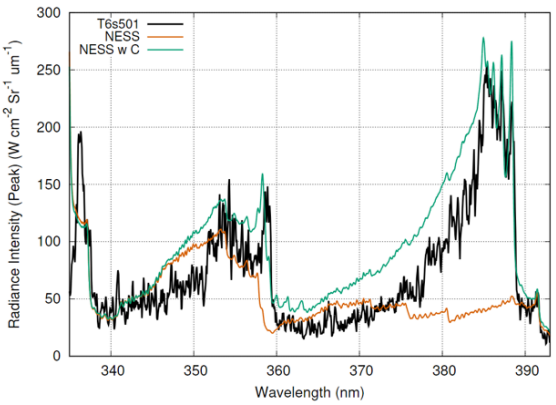
Fig. 2.24 Comparison of one-dimensional post-shot analysis code results fed into NEQAIR for T6s164 with a 9.59 km/s shock in 0.1 Torr air (close to a benchmark EAST test case). Taken from Clarke et al. [30].

Finally, the NESS non-equilibrium solver has been used in recent works of Clarke et al. [31] with NEQAIR to perform spectral comparisons against low-speed synthetic air data acquired from the T6 AST. Figure 2.25 shows examples of spectral comparisons performed in the peak non-equilibrium region of the test slug, for low and high resolution ultraviolet spectra, where C_2 has been doped into the NESS simulation to try to improve agreement with experimental data. The test cases shown, T6s484 and T6s501, were both conducted within the experiments carried out for this thesis and are analysed by a new spectral fitting routine in Chapter 7. For now, the spectral comparisons of Fig. 2.25 provide a reference for the non-equilibrium spectral agreements achieved by using the traditional method of feeding shock solver results into a radiative transport solver.

[12]The LAgrange Shock Tube Analysis (LASTA) code has been developed at the University of Oxford to enable the effect of shock speed variations to be accounted for in the post-shot analysis and is discussed in more detail in later chapters.



(a) Radiance profile from 200 nm to 400 nm for T6s484.



(b) Radiance profile from 335 nm to 393 nm for T6s501.

Fig. 2.25 Assessment of the spectral distribution averaged over $\pm$ 1 mm of peak radiance for 7.3 km/s test slugs in 33.3 Pa synthetic air from T6 AST, compared to NESS simulations including a 0.08% C_2 mole fraction. Plots taken from Clarke et al. [31]. Experimental data is from the work of this thesis, and analysed by spectral fitting in Chapter 7.

2.4.4 Spectral Fitting in Pure Nitrogen

An alternative to the method of modelling the flow-field and adjusting thermochemical rates until close agreement between radiance profiles is attained, is to use the spectrally resolved radiance traces to directly infer temperatures and population densities. This is the approach taken by the method of spectral fitting. Both NEQAIR and SPECAIR radiation codes have such capabilities, in which temperatures and state populations are optimised to attain a spectral profile which closely matches the experimental data. The temperatures and densities that achieve the final fit thus define the thermochemical state which generated the observed spectrum. This approaches the problem from the opposite angle to that discussed in Section 2.4.3, though the results still rely on the underlying assumptions that the radiation models are correct. When spatial (or temporal) resolution is also achieved, as in the case of shock tube data, spectra from different portions of the test slug may be spectrally fit to extract information of the thermochemical state evolution through the test slug. Shock tubes provide a simple application of this technique since the flow at a given cross-section is treated as homogeneous (according to current standard practice).

Cruden and Brandis [46] applied the NEQAIR spectral fitting program to pure nitrogen EAST data at 10.3 km/s to determine the number densities of electronic states responsible for radiation, along with temperatures, as a function of position behind the shock. They trialled both Boltzmann and non-Boltzmann distributions, achieving close fits in the UV and visible spectra, respectively. Inclusion of contaminants such as C, H, and CN improved the

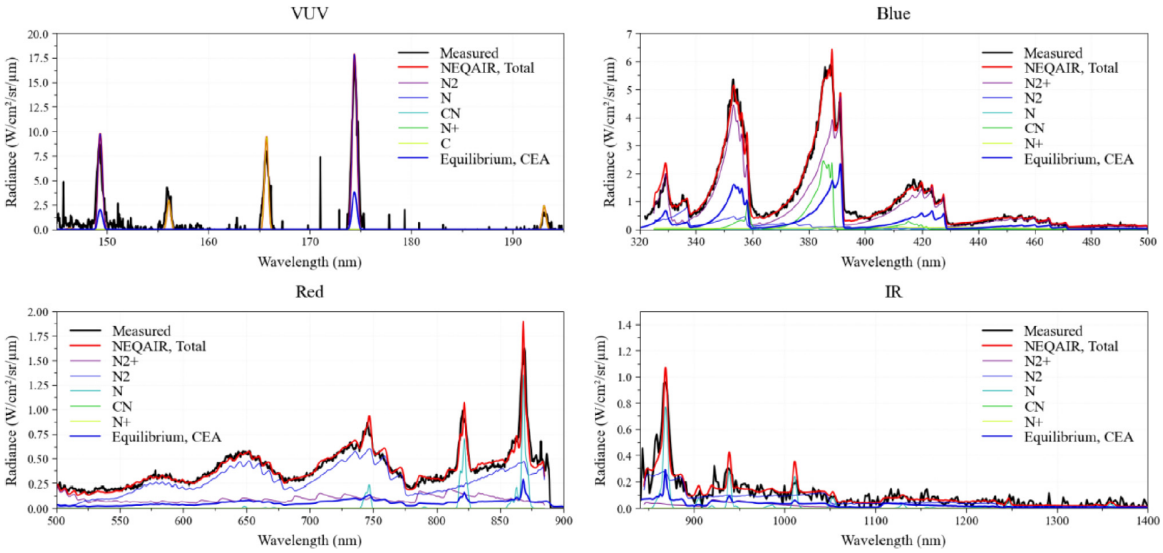


Fig. 2.26 Comparison of the experimental spectrum from the supposed equilibrium region of the EAST-62-40 test slug against CEA and spectral fitting results for different spectral channels. The shot condition is at 6.88 km/s in 0.2 Torr pure nitrogen. Taken from Tibère-Inglesse and Cruden [187].

spectral fits. They also inferred that electron density should be about twice the equilibrium predictions based on an analysis of the continuum magnitude. Tibère-Inglesse and Cruden [187] performed a similar study on slower-speed 7 km/s pure nitrogen cases from the same EAST dataset, where molecular species contributed more to the observed spectral radiance. Examples of the close agreement achieved by spectral fits in different wavelength regions can be seen in Fig. 2.26, along with the individual species contributions. These results are from EAST-62-40 test case at 6.88 km/s in 0.2 Torr pure nitrogen, which is further analysed in Chapters 5 and 6 of this thesis. They suggested that thermal and possibly chemical equilibrium might not be reached as far back as 50 mm/80 μs from the shock front. A two-temperature analysis revealed differences between rotational temperatures of various species and between rotational and vibrational temperatures of a single species in the non-equilibrium region. Results from different cameras (and thus wavelength regions) showed some discrepancies. These can be seen in Fig. 2.27. Interestingly, they highlight that only one temperature profile is presented for each camera as the assumption on the distribution (Boltzmann or non-Boltzmann) had no significant influence on the resulting temperatures.

More recently, similar low speed pure nitrogen experiments have been performed by Tang et al. [180] in the detonation-driven double-diaphragm shock tube discussed in Section 2.2.4. They performed spectral fits in the ultraviolet wavelength regions of pure nitrogen shocks from 6.6 to 9 km/s, using the SPECAIR spectral fitting software and assumed Boltzmann

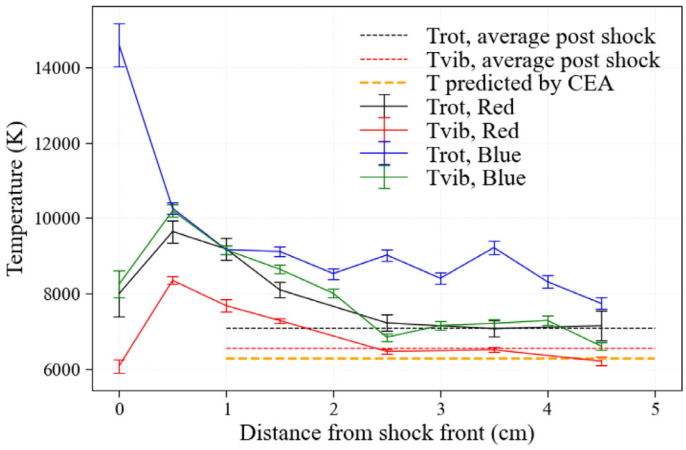


Fig. 2.27 Rotational and vibrational temperature profiles obtained by fitting the spatially resolved spectra for the Red and Blue cameras. For shot EAST-62-40 at 6.88 km/s in 0.2 Torr pure nitrogen. Taken from Tibère-Inglesse and Cruden [187].

distributions. Despite performing only relative intensity calibrations, rather than absolute, they were able to resolve similar trends in the resultant temperature profiles to that seen in the EAST-62-40 data for a slightly lower shock speed of 6.6 km/s and higher fill pressure of 200 Pa. Results for which are plotted in Fig. 2.28. In both cases the N_2^+ (B) band (which dominates large portions of the "Blue" spectral channel defined by EAST) rotational temperature exceeds the vibrational temperature and both of N_2 (C) temperatures by at least 3000 K immediately behind the shock front. This result agrees with similar pure nitrogen studies carried out by Sharma and Gillespie [156] over 30 years prior.

These studies demonstrate that spectral fitting of individual species or spectral bands can be an effective method for differentiating their temperatures from the global test slug. However, these previous analyses have made no effort to ensure conservation of mass, momentum or energy in their results, which therefore may not be physically possible. The work detailed in Chapter 5 does just that, but simplifies the test slug to a global two-temperature model and expands to perform the spectral fitting over as many wavelength regions as possible. By constraining the thermochemical states characterised through the test slug to those that obey the fundamental laws of thermodynamics, the myriad of possible spectral fits is thus limited to those which are at least physically possible. Additionally, by limiting to a two-temperature model, results may be compared to the results of well-established thermochemical models, such as Park [144, 145].

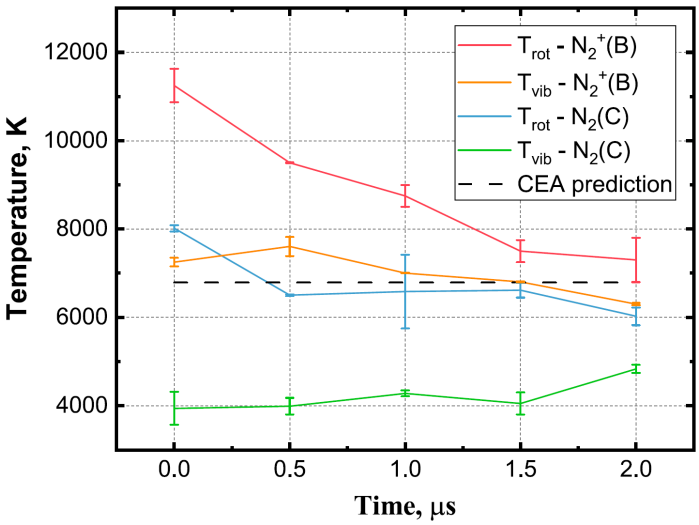


Fig. 2.28 Time-resolved rotational and vibrational temperatures of N_2 (C) and N_2^+ fitted from pure nitrogen experimental spectra at 6.6 km/s and 200 Pa. Taken from Tang et al. [180].

2.4.5 Spectral Fitting in Air

It's apparent from reading through literature that fewer spectral fitting studies have been performed with data from air experiments, within the context of shock layer radiation studies and enthalpies relevant to LEO return missions. The aforementioned non-equilibrium recombination studies performed by Tibère-Inglesse et al. [188] refer to the use of an "optimization algorithm" within the SPECAIR radiation code to minimise the difference between computed and experimental spectra. They use "overpopulation factors" to improve agreement with the N_2 second positive band in the ultraviolet. Though it's concluded during this study that the air/Ar mixture remained in a state of chemical equilibrium, in contrast to the N_2/Ar mixture which was found to be in a state of chemical non-equilibrium at the cooling tube exit.

Sharma et al. [155] used spectral fitting techniques to investigate the vibrational temperature of NO and OH radicals in the non-equilibrium relaxation region behind a stationary shock wave in air at Mach 7.42 free-stream. The LIFBASE spectral fitting software [110] yielded vibrational temperature profiles for OH, though an in-house algorithm was developed for NO to account for higher vibrational and rotational levels, to avoid extremely large temperature estimates. Results showed that NO vibrational temperatures were significantly higher than OH, as repeated in Fig. 2.29, suggesting significant thermal non-equilibrium within the first 5 mm of post-shock air flow.

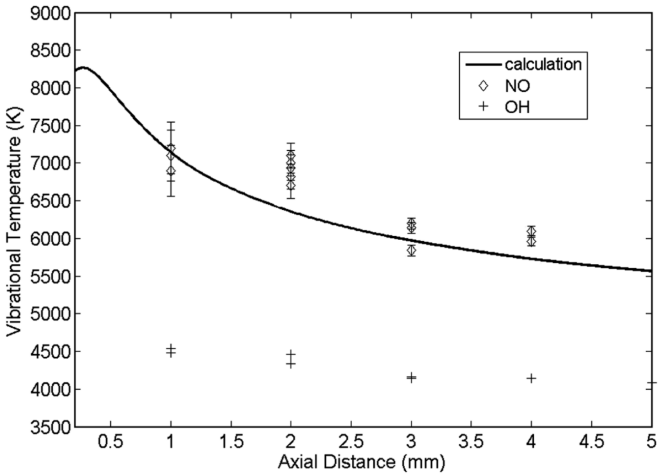


Fig. 2.29 NO and OH A-state vibrational temperatures in the post-shock relaxation region, against results from a thermochemical model. Taken from Sharma et al. [155].

More recently, Yanes and Austin [199] performed a similar analysis, measuring the NO excitation temperatures from spatially resolved emission spectra along the stagnation line ahead of a circular cylinder in a Mach 7.19 free-stream. Spectral fitting was again performed using an in-house code similar to that by Sharma et al. [155]. Two-temperature fits of the experimental spectra show that vibrational and rotational temperatures of the electronically excited NO are in thermal non-equilibrium until approximately 35% of the stand-off distance. Figure 2.30 repeats these results, with comparisons against a zero-dimensional state-to-state (referred to as "STS") model and a two-temperature LAURA simulation [13]. Additionally, they show estimates of the vibrational temperature suggest formation of NO in a non-Boltzmann distribution via the second Zeldovich reaction.

Both these studies were carried out for conditions significantly slower than the Mach $\sim$20 conditions of interest for LEO return missions, which will additionally contain larger number densities of other species due to enhanced O_2 and N_2 dissociation and subsequent ionisation reactions. Stark broadening studies have been performed in air by Cruden [40] and Laux et al. [102] for spectrally resolved radiance data from EAST and ICP torch facilities respectively, at higher enthalpy conditions to extract electron number density information. However, this has only been performed successfully in shock tube experiments for shock speeds above $\sim$9 km/s to date, and leaves many other important species unaccounted for. Thus, there is a gap in the literature to provide reliable thermochemical state information for air at LEO return speeds. It's also emphasised again, that the aforementioned studies did

[13]LAURA is a structured, multi-block, computational aerothermodynamic simulation code developed at the NASA Langley Research Center (see Thompson et al. [185]).

not check fundamental conservation laws were obeyed through their shock layers, further consolidating the novelty and value of the the approach taken in later chapters of this thesis.

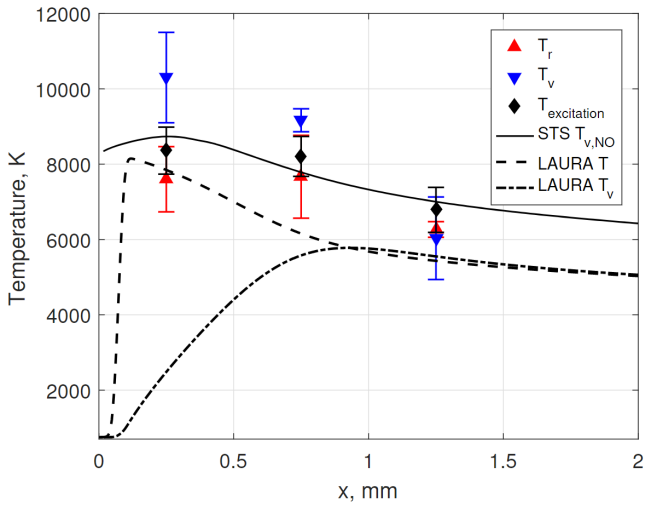


Fig. 2.30 Experimental temperatures compared with a computation by a zero-dimensional state-to-state model and a two-temperature LAURA simulation. T_{frozen} = 8267 K and $T_{equilibrium}$ = 4179 K. Shock location is set at x = 0 mm. Taken from Yanes and Austin [199].

2.5 Summary

This section has reviewed the facilities that may be used to create high-enthalpy flows at ground level and discussed many of the relevant works undertaken to characterise thermo-chemical states in such environments. A series of shock tube facilities from around the world have been described along with brief explanations of their nuances in operation and optical diagnostics. Particular emphasis was placed on the Electric Arc Shock Tube at NASA Ames, since two of its test cases are included in the analyses of later chapters. Additionally, much of the methodology and OES calibration procedures used in this thesis draws heavily from the knowledge gained by those operating and analysing data from EAST.

A review of results from previous LEO return studies have identified clear gaps in the literature to go after. First, there is an unresolved continuum background offset observed across all spectral wavelengths from previous EAST and T6 low-speed equilibrium data. Improvements here are necessary before reliable non-equilibrium analyses can be performed. With that, the method of spectral fitting shows promise to characterise the hypersonic vehicle stagnation line, and can utilise the ample available OES data acquired from EAST and T6 facilities. Though it's identified that previous shock tube spectral fitting analyses do not ensure the conservation of mass, momentum and energy laws are obeyed in the thermochemical state evolution outputs. Additionally, there's little evidence in the literature of performing such analyses in air mixtures for the Mach numbers and enthalpies relevant to LEO return missions. This provides strong motivation for the experiments undertaken in this work and the development of the constrained spectral fitting methodology.

Chapter 3

Experimental Method

> In theory, there is no difference between theory and practice. But in practice, there is.
>
> Yogi Berra

This chapter provides a brief overview of the Oxford T6 Stalker Tunnel capabilities and delves into the details of Aluminium Shock Tube design, instrumentation and experimental procedures. New telecentric optics designed for the study of LEO stagnation lines are described, along with the calibration procedure to ultimately attain spatially and spectrally resolved absolute radiance measurements. This chapter is intended to give the reader a full picture of how the calibrated data is generated, which is then referred to and analysed in the following chapters.

3.1 The Oxford T6 Stalker Tunnel

The Oxford T6 Stalker Tunnel is a high-enthalpy transient multi-mode ground test facility for aerothermodynamics research. It is the first European facility of its kind, capable of reproducing flight enthalpies from 2.7 to 115.0 $MJkg^{-1}$, corresponding to Mach 7 flight and proposed hypervelocity super-orbital Mars Sample Return missions. A comprehensive review of the facility, its commissioning and initial data acquisition have been given in numerous works of Collen et al. [33, 35, 34, 37]. Sequential upgrades to the facility are then summarised in the works of McGilvray et al. [116] and Steer et al. [171], enabling T6 to perform tests on flammable gas mixtures and thus permit the study of Ice Giant entry missions, which have been achieved up to 20 km/s. Figure 3.1 illustrates the four facility

modes, all sharing the same free-piston driver. A general overview of the operation of Reflected Shock Tunnels, Expansion Tunnels/Tubes and Shock Tubes has been provided in Section 2.1.2 of this thesis. Although T6 is capable of operating in all of these facility modes, only the Aluminium Shock Tube mode of operation was used to conduct the experiments carried out for this thesis, and thus is the subject of this chapter.

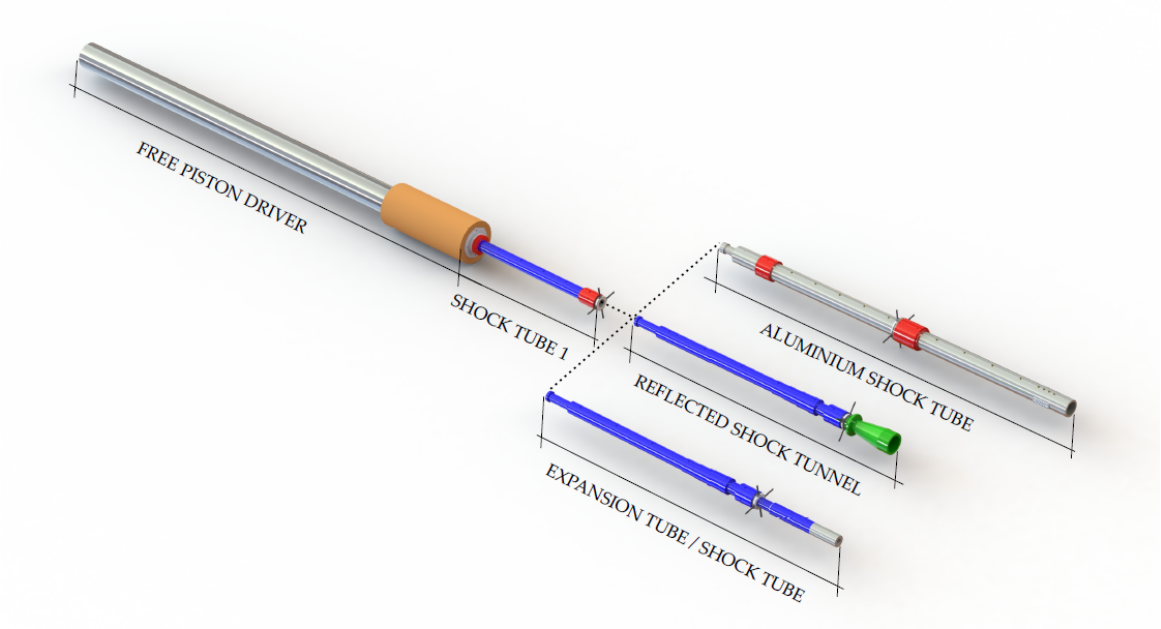


Fig. 3.1 Diagram showing different T6 facility modes, taken from Collen [32].

3.2 The Free-Piston Driver

The first challenge of recreating hypersonic flight conditions is a sufficient power source, such that the total enthalpy and Mach number can be met. Stalker [169] demonstrates that the test section power level is, to a good approximation, the product of the flow kinetic energy per unit area and the mass flow to yield, as described by equation 3.1. Where ρ_∞, A_∞ and V are the test section density, cross-sectional area and velocity respectively.

$$W = \frac{1}{2}\rho_\infty A_\infty V^3 \tag{3.1}$$

For the Low Earth Orbit (LEO) return missions of interest in these works, the T6 Aluminium Shock Tube would require around 200 MW of power to maintain steady operation. Fundamentally therefore, if both enthalpy and velocity are to be matched to the flight case, the conditions must be generated transiently. Continuous operation of high-enthalpy facilities

can only be run at the expense of a subsonic (or sometimes supersonic) flow field [1]. Impulse drivers are an alternative means to produce enough energy over a short duration, to match both the total enthalpy and hypersonic flow field, at the compromise of a finite test time.

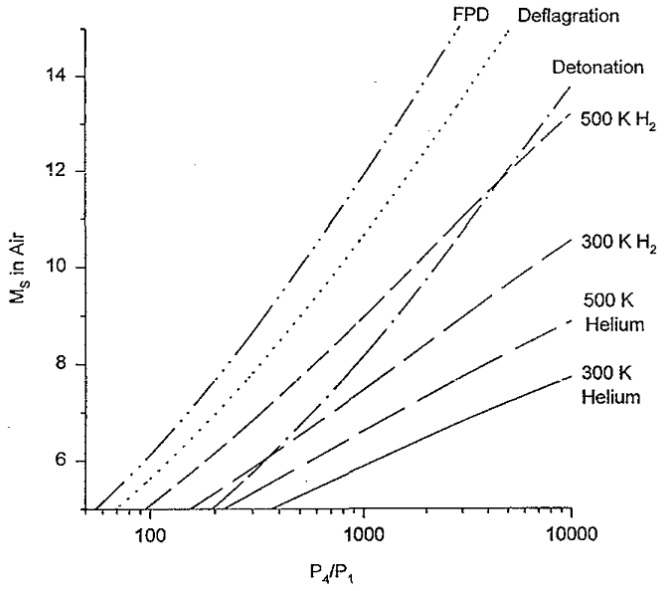


Fig. 3.2 Summary of primary shock speed performance from different driver technologies, including the free-piston driver (FPD). P_4/P_1 represents the driver:shock tube pressure ratio at the moment of diaphragm burst. Taken from Bakos and Erdos [3].

Various driver technologies have been proposed - Fig. 3.2 compares the performance of a few of these. In all cases, the strongest driver parameter to achieve the fastest shock speeds (and thus total enthalpies) is sound speed, followed by pressure. Thus, the operating principle of all designs is to supply a low molecular weight gas at an elevated temperature and pressure. The arc driver design provides the highest absolute performance, via the rapid discharge of an electrical current through a filament, but struggles to maintain steady flow properties. This is implemented on the Electric Arc Shock Tube (EAST) facility at NASA Ames and has generated shock speeds of up to 46 km/s by Sharma and Park [157, 158] The free-piston design offers the next best performance of the remaining driver technologies, as shown in Fig. 3.2. Though has drawbacks in the form of its mechanical complexity, initial costs and perhaps most of all the knowledge required to develop safe driver conditions. The piston is used to polytropically compress the driver gas, rapidly increasing the temperature and pressure until diaphragm rupture. The continued motion of the piston after rupture maintains a steady driver condition, delaying the generation of expansion waves and thus

[1] Continuous facilities are discussed in more detail in the Literature Review, along with their limitations and relevant works.

shock deceleration. The driver gas also cushions the piston, decelerating it to a "soft" landing before reaching the nylon buffers at the end of the compression tube. Tanno et al. [181] term this as "tuned operation" and it is imperative to ensure safe operation of the facility. Details on the development and commissioning of T6 driver conditions can be found in the works of Subiah et al. [176] and Collen et al. [35].

The free-piston design was conceived and put into practice on a reflected shock tunnel in 1959 by Prof. Raymond Stalker. Facilities using this driver technology are often referred to as Stalker tunnels due to this heritage. The T6 driver was originally designed and developed for the T3 facility at the Australian National University in 1968, as the first large scale Stalker tunnel. A review by Morgan [127] shows it was used extensively in the 1970s and 80s for fundamental studies of high enthalpy flow phenomena. After being decommissioned in the early 2000s, the compression and driver tube assembly was bought by McGilvray et al. [117] at the University of Oxford in 2014 for use on T6. To date, driver conditions with burst pressure up to 46.2 MPa have been commissioned, using a piston of either 35.8 kg or 89 kg.

Table 3.1 summarises the three driver conditions that were used for the shock tube tests conducted during the works of this thesis. All conditions make use of the lightweight piston and use a 76.2 mm orifice plate. The compression ratio from the piston stroke is 60:1. Different helium:argon ratios were used to achieve the desired shock speed for each given test case. The fast polytropic compression from the piston rapidly raises the temperature of the driver gas, enabling burst pressures significantly above that from the compression ratio alone. Diaphragms made from sheets of stainless steel (S.S.) and aluminium (Al) with specified scoring depths are used to control the burst pressure. Scoring also helps to maintain a consistent diaphragm opening pattern and reduces the diaphragm shrapnel pieces sent down the tube. The heavier piston is designed for driver conditions intended for Reflected Shock Tunnel operation mode, and thus was not utilised for the shock tubes tests referred to herein.

Table 3.1 T6 driver conditions used in the works of this thesis. Diaphragms are made of aluminium (Al) or stainless steel (S.S.) depending on selected condition.

Condition	**Reservoir Pressure, kPa**	**Compression Tube, Pa**	**Rupture Pressure, MPa**	**Diaphragm thickness × score depth**	**Main Driver Gas**
Low	730	10,500	9.8	3mm Al. × 0.3mm	Argon
Medium	2100	32,200	29.6	1.5mm S.S. × 0.35mm	Helium
High	2600	35,000	46.2	2mm S.S. × 0.4mm	Helium

3.3 T6 Shock Tube Modes

The T6 Stalker Tunnel is capable of operating in two different shock tube modes: Aluminium Shock Tube (AST) and Steel Shock Tube (SST). These differ primarily by their diameter. The SST maintains a constant diameter of 96.3 mm throughout, from the point of diaphragm rupture to the exit into the dump tank. AST has a conical expansion region taking the diameter to 225 mm, to increase the integration path length for optically thin emission studies. This is at the expense of a reduction in performance, limiting the maximum achievable shock speed. Both operation modes have been used to study the stagnation lines relevant to entry vehicles for a number of different planet atmospheres, including Earth [37, 69], Mars [51], Titan[162] and Ice Giant [172, 173] entry missions. Figure 3.3 plots the trajectories of past and proposed Earth return missions, along with the conditions achieved in each mode. Since the works of this thesis focus on conditions relevant to Low Earth Orbit (LEO) return missions, the AST mode is most appropriate to improve signal-to-noise (S:N) for relatively optically thin test cases and was thus used for the experiments discussed herein.

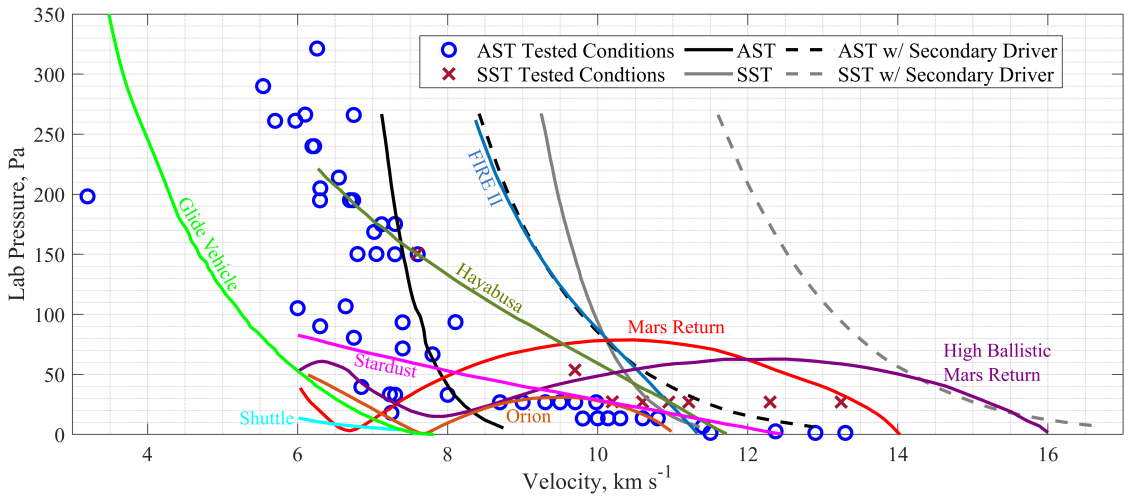


Fig. 3.3 Earth entry trajectories alongside T6 shock tube conditions achieved and performance limit predictions of each ST mode. Adapted from Collen [32].

Figure 3.4 shows an excited test gas traversing past the T6 Aluminium Shock Tube window during a shot. As the normal shock progresses down the tube, it may traverse across various other instrumentation taking measurements of pressure, heat flux, radiation, charge, etc. The temporally resolved results from which can also be used to calculate shock speed. These, along with accurate measurements of test gas fill pressure and composition, provide some of the key advantages of shock tube experiments over other impulse facilities (as discussed in Section 2.1.2) and contribute strongly to the applicability of T6 AST to

the fundamental study of radiation and non-equilibrium phenomena, as is carried out in the following chapters of this thesis. The remainder of this chapter explains the AST mode of operation in greater detail, as well as the associated telecentric optical emission spectroscopy diagnostics used to capture spatially and spectrally resolved radiance images.

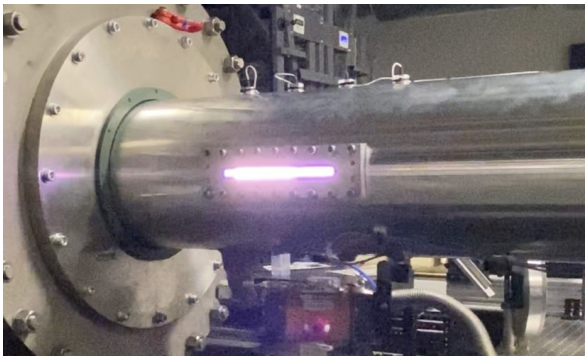


Fig. 3.4 Radiation emission from a test slug traversing across AST window during a shot.

3.4 Aluminium Shock Tube Mode

3.4.1 Principle of Operation

As discussed, the AST mode of operation enables T6 to reproduce the stagnation line ahead of a hypersonic vehicle, up to the boundary layer edge. This allows radiation measurements to be taken from the excited test gas, at matched total enthalpy and velocity to the true flight case. Results can be studied without any scaling considerations, as would be the case for the flow over a subscale model. A cross-section view of the T6 AST facility is given in Fig. 3.5.

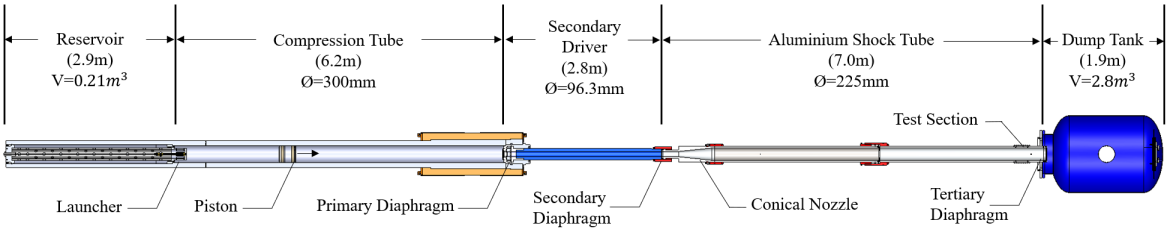


Fig. 3.5 Section view of T6 Stalker tunnel in AST mode from above. Taken from Glenn et al. [69].

A free-piston driver is used to polytropically compress a helium-argon mixture in the compression tube until rupture of the primary diaphragm, generating a shock wave which then travels downstream. Prior to this rupture, the AST section has been filled with a test

gas relevant for the planet entry condition of interest. The normal shock wave progresses through the test gas, compressing and accelerating the gas to travel downstream. The flow between the normal shock and contact discontinuity (separating the test gas and expanding driver gas) is treated as analogous to the stagnation streamline ahead of a hypersonic vehicle. This is illustrated in Fig. 3.6 and is applied from the bow shock ahead of the entry vehicle to the boundary layer edge [2]. The shock tube is filled with the equivalent composition and density to the desired planet atmosphere and altitude, and a driver condition selected to produce a normal shock travelling at the same speed as the vehicle for the chosen trajectory point. This imitates the thermochemical evolution through the entire test slug, equivalent to the vehicle shock layer stagnation line, including the non-equilibrium and relaxation processes. After primary diaphragm rupture, the continued piston motion acts to delay expansion wave generation and propagation, helping to postpone shock deceleration. The driver gas expanding out into the driven section cushions the piston to allow for a "soft" landing at the end of the compression tube. An optional secondary driver between the driver and AST can be filled with helium, through use of a secondary diaphragm, to reach faster shock speeds (as shown by Gildfind et al. [65]). In cases when it is not needed, there is no secondary diaphragm and the secondary driver is filled with the test gas.

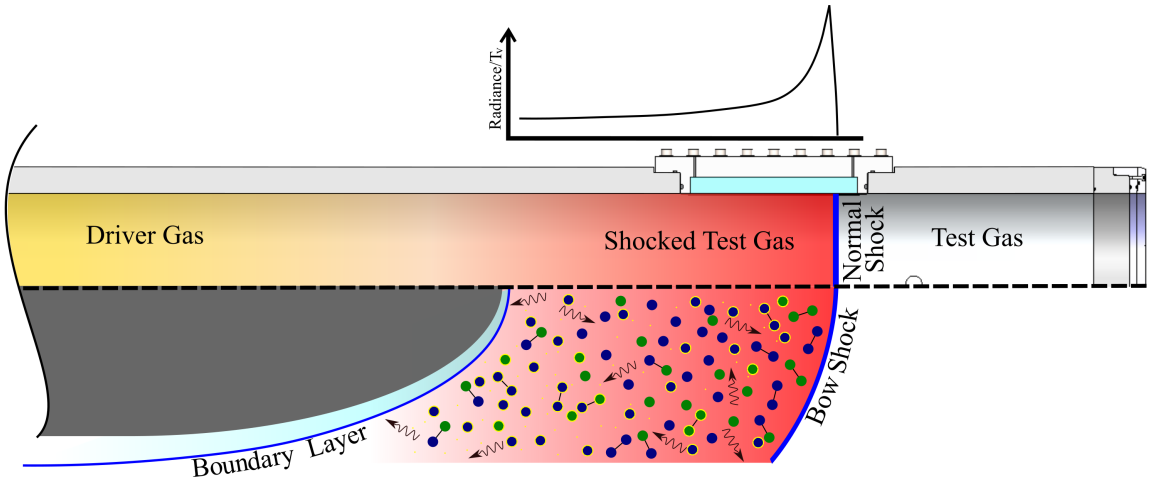


Fig. 3.6 Illustration of the analogy between a hypersonic vehicle stagnation line and a shock tube experiment. Not to scale. A relaxing radiance profile is included to aid the illustration.

The design of the AST lends itself to low-speed shock layer radiation studies. The 225 mm diameter tube provides a large integration path-length for optically thin radiation, which increases S:N, whilst reduced boundary layer effects result in less shock deceleration and longer test gas slugs (as detailed in the works of Mirels [126]). For reference, predicted

[2] It's emphasised that the shock tube flow is 1D and thus replicates only the stagnation line, rather than other regions of flow around the vehicle, which may have notable transverse components.

boundary layer thicknesses along the tube's inner wall, at the field of view limit, range from approximately 0.6 to 2.0 mm for shots considered in this thesis. These values correspond to high- and low-pressure tests with post-shock pressures of 100 kPa and 10 kPa, respectively, based on Mirels calculations. However, the flow is often treated as 1D along the tube axis, thus assuming uniform core flow properties across the entire tube diameter.

3.4.2 Facility Instrumentation

Shock speed measurements along the length of the tube are necessary to characterise facility performance and provide one of the boundary conditions of the shock tube experiment. It determines the enthalpy and entropy imparted to each slice of test gas along the length of the tube. Thus, it's measurement and uncertainty are important considerations for the analysis of radiation measurements. The effects of shock speed variation are discussed in more detail in Section 3.4.4.

Shock Timing Stations (STS's) are flush-mounted in the tube wall along the length of the secondary driver and AST section, to track the shock from its pressure rise as it progresses down the tube. In total, 17 PCB Piezotronics series 113B piezoelectric transducers were used along the facility - four 113B26's in the secondary driver and 13 113B27's in the AST section (with nominal sensitivities of 1.45 $VMPa^{-1}$ and 7.25 $VMPa^{-1}$ respectively). Each are quoted to have rise times less than 1 μs. The overall uncertainty of static pressure measurements is estimated to be 7%, based on the works of Hayne [77] for similar experiments on the X2 facility. This information is used to generate the shock speed profile of the normal shock, by performing distance over time calculations between adjacent STS's. Uncertainties are calculated using the methodology of James et al. [91].

Figure 3.7 shows the Pitot rake which is installed 112.5 mm (i.e. one radius) from the tube outlet to allow assessment of test time and flow uniformity, both radially and axially. To maximise the tube length in the constraints of the room (and maximise test time) AST is inserted directly into the dump tank. A cantilevered mounting arm therefore extends downstream inside the dump tank to hold the rake. The design is asymmetric with respect to the AST bore, covering only the bottom half of the AST outlet flow, with 6 probes each spaced 20 mm apart. The top probe aligns with the tunnel centreline. Since the Pitot rake probes face into the flow directly, bow shocks form ahead of the probes and create a high temperature and pressure environment. This justifies the alternate PCB 113B24 transducers with lower sensitivity (0.73 $VMPa^{-1}$) but higher pressure rating compared to the 113B27's used as STS's. Additionally, swirl-caps act as a protective metal shroud around the PCB sensors to prevent direct impact of particles onto the transducer, as designed by McGilvray et al. [118] to reduce the magnitude and period of Helmholtz resonance (pressure fluctuations)

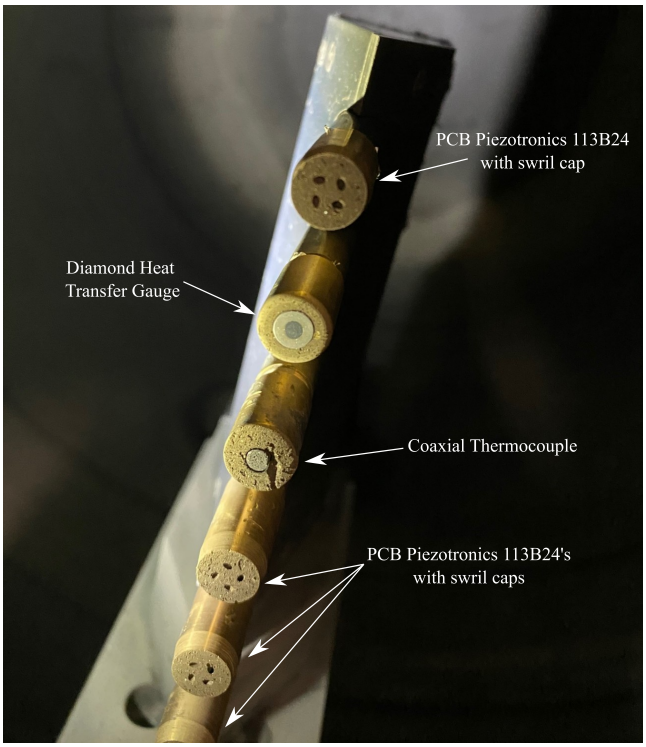


Fig. 3.7 Image of AST Pitot rake, looking into dump tank.

present in prior pitot shield-cap designs by Neely and Stalker [139]. Again, Pitot pressure measurement uncertainty is estimated to be 7% based on the works of Hayne [77]. Alternate transducers may be included in the Pitot rake to provide measurements of other parameters. Figure 3.7 includes a coaxial thermocouple and Diamond Heat Transfer Gauge (as designed by Geraets et al. [63]) to provide measurements of heat flux on the representative stagnation line. Early attempts at measuring electron temperature and number densities have also been conducted through the use of Langmuir probes mounted into the rake, based on the works of Dunn and Lordi [54, 55]. Damage seen on the sensor faces in Fig. 3.7 is exemplary of the harsh nature of the testing environment generated in the AST.

Engineering drawings are provided in Fig. 3.8 to give the exact locations of STS's and Pitot probes, taken from the work of Collen [32]. Closer spacing of the STS's around the window provides measurements of greater resolution, however the uncertainty of the shock speed in this region increases since the errors from sensor placement and shock time arrival are proportionally larger than the distance between sensors. Dimensions of the conical nozzle section are also provided. Both the STS and Pitot pressure sensors are amplified by three 8-channel rack mounted PCB Piezotronics 483C05 signal conditioners, all set with a gain of 1. The amplified signals are then sent to two National Instruments PXIe-6368 multifunction DAQ cards, installed in a National Instruments PXIe-1092 chassis.

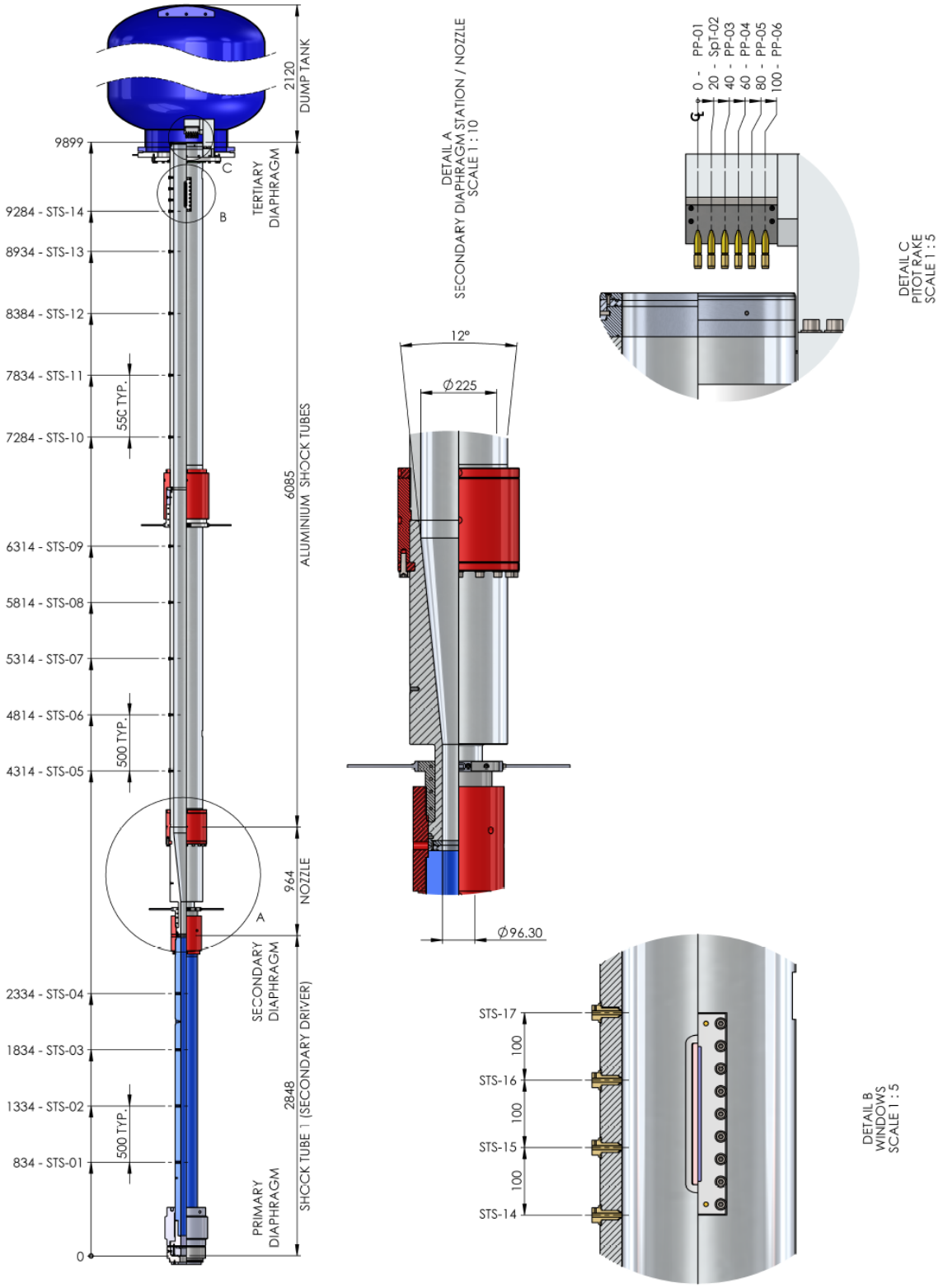


Fig. 3.8 Engineering drawing of the T6 AST, with STS and Pitot rake measurement locations shown. The main drawing scale is 50:1. All dimensions are in millimetres. Taken from Collen [32].

3.4.3 Auxiliary Infrastructure and Shot Procedure

Two more boundary conditions of shock tube experiments are the test gas initial fill pressure and composition. The facility therefore requires the means to accurately create and measure the artificial atmosphere prior to firing the shot. Significant pumping power is consequently necessary to expel the ambient air from the test and driver volumes. Additionally, the leak rate of ambient air into the facility should be minimised by establishing good sealing at the facility interfaces and pipework. It's these parameters which determine the ultimate pump down vacuum pressure achievable and therefore the residual level of contaminant room air left in the tube before filling with the desired test gas. The time taken to reach the ultimate pump down pressure is also a function of carbon dioxide and water vapour molecules outgassing from the tunnel walls. This is a statistical phenomenon at very low pressures, dependent on the likeliness of a molecule to eventually take a trajectory leading it to the vacuum port and out of the facility. The likeliness of this (and thus the time required to reach ultimate pressure) can be improved by larger vacuum ports and a more powerful pumping system, to remove the molecules more effectively. A brief summary of the steps to prepare for AST experiments is given below, along with details of the auxiliary equipment involved. The general principle will be similar to many other high-enthalpy impulse facilities, though is written specifically to the operation of AST.

First, the Aluminium Shock Tube, Secondary Driver (if secondary diaphragm installed), Dump Tank, Compression Tube and Piston Space (pipework keeping the piston onto the launcher prior to shot) must be evacuated. The optional tertiary diaphragm between the AST and Dump Tank was typically not installed for the tests discussed herein (unless explicitly specified in later chapters) to help minimise leak rate. When combined, the Dump Tank increases the volume of the test gas by $\sim$10 times. This reduces the rate of pressure increase, for a given mass flux of ambient air into the facility, by the same factor. Therefore making it much easier for the operator to stay on the intended condition and reduces contaminants in the test gas, at the expense of faster test gas consumption. The same principles apply to the driver, where leaks into the Helium/Argon mixture can be detrimental to the performance of the facility. A large Busch COBRA DS 2000 vacuum pump is connected to the Dump Tank and does most of the heavy lifting to evacuate the AST and Dump Tank test volume. Simultaneously, an Edwards E2M18 rotary vane pump is used to pump down the compression tube. The piston space pipework must be evacuated before bringing down the compression tube, to avoid the the piston pre-launching. This is achieved over a few seconds with another Edwards E2M18 rotary vane pump. Typically, the large Busch pump can bring the shock tube and Dump Tank volume to a pressure of less than 1 Pa. However, after reaching a pressure on the order of $\sim$500 Pa, an Edwards EXT-75DX turbomolecular pump is used (in series

with an Edwards nXDS10i dry scroll pump and parallel to the large Busch pump) to reach pressures on the order of 0.01 Pa in AST. Almost all the experiments discussed in this thesis were carried out in "straight-through" mode, in which there is no secondary diaphragm and the secondary driver forms a single volume with the AST and Dump Tank. In cases when a Mylar secondary diaphragm is used, another Edwards nXDS10i dry scroll pump is used to evacuate the secondary diaphragm section. Care has to be taken during this to maintain a small pressure differential either side of the thin diaphragm, to avoid it bursting during the pump down. The leak rate of the test volume was routinely measured after pumping down for several hours and was typically of an order of 1 mPa s^{-1}.

After successfully pumping down all sections of the facility, the filling and firing procedure was as follows: first, the compression tube was filled with the desired Helium/Argon composition, to the pressure of the chosen driver condition. If in use, the secondary driver was then filled, followed by the high pressure reservoir. A 1000 Torr Inficon CDG-025D gauge is used to measure the fill pressure, typically around 10 kPa. The large Busch and Edwards turbomolecular pumps have access to the AST volume during this process, to maintain the ultimate vacuum pressure. These are then isolated and the test volume is filled with the desired test gas. For tests in this work, pre-prepared gas cylinder mixtures of synthetic air (20.9% O_2/79.1% N_2) and pure nitrogen were used. This saves the time of creating the gas mixtures in-situ in the tube, whilst ambient air leaks into the facility and high-pressure reservoir gas is in the lab area. Additionally, it ensures a consistent composition between tests. The synthetic air was acquired from Air Products with a purity of 99.9999% . While the pure nitrogen was from BOC with a 99.999% purity level. The pressure in the test volume was read by a 5 Torr Inficon CDG-025D gauge mounted onto the Dump Tank. The given accuracy of which is 0.2% of the reading. After achieving the desired fill pressure, the gauge is closed off and the facility is fired. This sequence of events was chosen to minimise the time for ambient air to leak into the facility and preserve purity of the test gas. The time between filling and firing was typically 30 seconds to a minute.

3.4.4 Inconsistencies of Stagnation Line Analogy

The analogy of a shock tube experiment to a planet entry vehicle stagnation line has been mentioned a few times. Figure 3.6 illustrates how the flow between the normal shock and contact surface of a shock tube experiment is akin to the flow between the bow shock and boundary layer edge on a hypersonic vehicle's stagnation line. The two scenarios share the same thermochemical excitation and relaxation processes progressing through the gas, or partially ionised plasma. Therefore, if the composition and density of the desired planet entry trajectory point can be matched in the initial shock tube fill condition, and a shock

wave generated to travel at the speed of the entry vehicle at that point - then the post-shock flow is, in theory, analogous to the stagnation line of the vehicle in terms of enthalpy and hypersonic flow field. This is the basic principle of the shock tube analogy. However, it has been demonstrated in recent literature that there are discrepancies between the two scenarios.

The first discrepancy originates from the variations in shock speed during a shock tube experiment, as it progresses down to the measurement region. It has been well documented in works of Satchel et al. [153, 152], Collen et al. [38] and Steer et al. [170] that shock speed variations directly lead to entropy and thermochemical gradients in the resulting test slug, which in turn influences the radiance measurements. The LAgrange Shock Tube Analysis (LASTA) code developed at the University of Oxford enables the shock speed variation to be accounted for in the post-shot analysis and numerical comparisons. Of note, Collen et al. [38] resolve historic discrepancies between EAST equilibrium data and numerical predictions by accounting for the shock deceleration effects. This is owed to each slice of gas along the tube being processed by a different strength shock, and therefore assigned a different enthalpy and entropy. These enthalpy and entropy gradients endure the boundary layer mass extraction and duration of the test. Since the thermochemical equilibrium state of each slice is dependent of the static enthalpy increase imparted to the particles, the thermochemical state through the test slug also varies, despite each slice having attained its own equilibrium state. And finally, the varying thermochemical states generate different radiative transport properties through a line of sight, which can be identified by spectrally resolved radiation measurements. This combined with spatial or temporal resolution allows the transitions in thermochemical state to be verified. Shock speed variation effects are illustrated in Fig. 3.9.

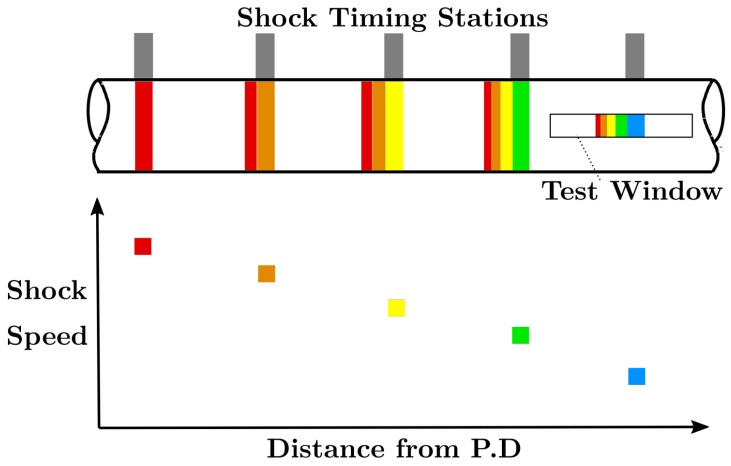


Fig. 3.9 Individual slices of test gas processed by a decelerating shock. Colouring at each STS represents the decreasing entropy of sequential slices, which together constitute the final gradient in the resulting test slug. Taken from Satchell et al. [153].

The other important discrepancy between a shock tube experiment and a vehicle stagnation line is the difference in particle times of flight (ToF), owed to the growing boundary layer around the circumference of a shock tube inner wall. When plotted against time, the progress of thermochemical relaxation for a shock tube experiment is truly analogous to the flight case. However, the particle trajectories differ as mass is extracted from the core flow of the test gas by the boundary layer. The post-shock velocity profiles for the two scenarios are plotted in Fig. 3.10 in the shock frame of reference, including profiles both at and before the Mirels limit [126] for a shock tube. In this shock frame of reference, the particles decelerate as they approach either the contact surface or vehicle, however the trajectories taken differ. The shock tube boundary layer initially causes enhanced deceleration as particles are almost immediately extracted by the growing boundary layer, however this rate diminishes closer to the contact surface. Clarke et al. [29] demonstrate that a spatial transformation is therefore required when comparing spatial profiles of any parameter, between the two scenarios - producing Eq. 3.2 where Δ_b is the blunt body shock stand-off distance, x_b is the post-shock distance in metres, δ_m is the maximal Mirels test slug length and x_m is again the post-shock distance in metres. Use of this correction in the works of Clarke et al. [30] has drastically reduced differences between shock tube experimental data and simulations in NASA's Data Parallel Line Relaxation (DPLR) code [131, 194] over a blunt body - resolving discrepancies originally thought owed to incorrect reaction rates. Additionally, Eq. 3.3, is required when comparing spatially resolved data of two shock tubes with different diameters. Alternatively, knowledge of the post-shock velocity profile allows spatially resolved data to be transformed onto a time axis, which is common to all shock tube diameters and flight scenarios. Note that a considered shock tube test may or may not be at the Mirels limit, depending on the condition considered and the shock tube length:area ratio. In cases where it is not, the test time is increasing due to the shock travelling faster than the contact surface. This leaves the particles with some velocity at the contact surface, in the shock frame of reference.

$$\Delta_b \ln\left(1-\frac{x_b}{\Delta_b}\right) = 2\delta_m\left(\ln\left(1-\left(\frac{x_m}{\delta_m}\right)^{0.5}\right)+\left(\frac{x_m}{\delta_m}\right)^{0.5}\right) \tag{3.2}$$

$$\begin{aligned}\delta_{m,1}&\left(\ln\left(1-\left(\frac{x_{m,1}}{\delta_{m,1}}\right)^{0.5}\right)+\left(\frac{x_{m,1}}{\delta_{m,1}}\right)^{0.5}\right)\\ &= \delta_{m,2}\left(\ln\left(1-\left(\frac{x_{m,2}}{\delta_{m,2}}\right)^{0.5}\right)+\left(\frac{x_{m,2}}{\delta_{m,2}}\right)^{0.5}\right)\end{aligned} \tag{3.3}$$

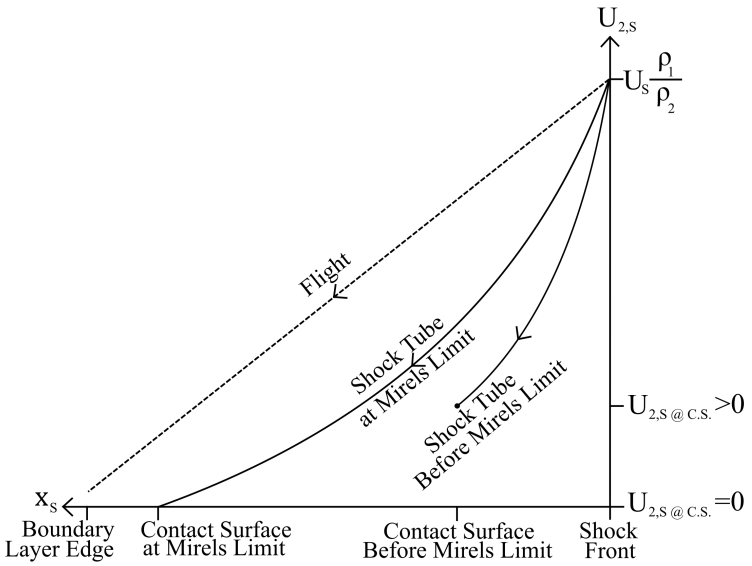


Fig. 3.10 Plot to illustrate the differences in post-shock axial velocity, owed to differences in particle time of flight, between an entry vehicle stagnation line and a shock tube. Post-shock axial velocity in the shock frame of reference ($U_{2,S}$) is plotted against post-shock distance (X_S), for a shock travelling at U_S.

3.5 Telecentric Optical Emission Spectroscopy

3.5.1 Physical Setup

Primary analysis of the shocked gas is performed in the downstream section at the AST windows via two Optical Emission Spectroscopy (OES) setups, which are illustrated in Fig. 3.11. These systems provide both spatial and spectral resolution, enabling the spectra to be captured as a function of post-shock distance. Fundamentally, the spectra will change along the spatial axis due to the evolution of the thermochemical state through the test slug. The spectra at each location can be used to infer the temperatures and number densities of the excited species. The reader is directed to Thorne et al. [186] for a more comprehensive explanation of the operating principles and applications of this instrumentation, and to Herzberg and Spinks [82] for a detailed introduction to the atomic spectra and atomic structure relationships.

Radiation emitted from the test gas escapes through two diametrically opposite windows along the tube axis. These are located 9.3 m from the primary diaphragm. As illustrated in Fig. 3.11, radiation exits from both windows to then follow a designated optical path formed by a series of mirrors, and is finally focused back down onto a spectrometer slit. Each path is tailored for a specific wavelength region: a "blue side" is used to capture ultraviolet/visible

(UV/Vis) wavelengths; and a "red side" for visible/near infrared (Vis/NIR). Over the range of test cases considered in this thesis, the blue side was used to observe wavelengths from 200 up to 520 nm, whereas the red side captured from 430 up to 850 nm. The optical paths are directed and focused by mirrors, as opposed to lenses, since this avoids the issues of chromatic aberrations for the study of broad wavelength regions. Table 3.2 provides a summary of all the components constituting each optical path of the telecentric setups. The apertures of the windows to allow radiation to escape are 10 mm vertically and 190 mm and 200 mm axially for the blue and red systems respectively. Differences in length are owed to the available optical material ingot sizes at the time. STS's near the windows are more closely spaced to provide higher resolution velocity measurements.

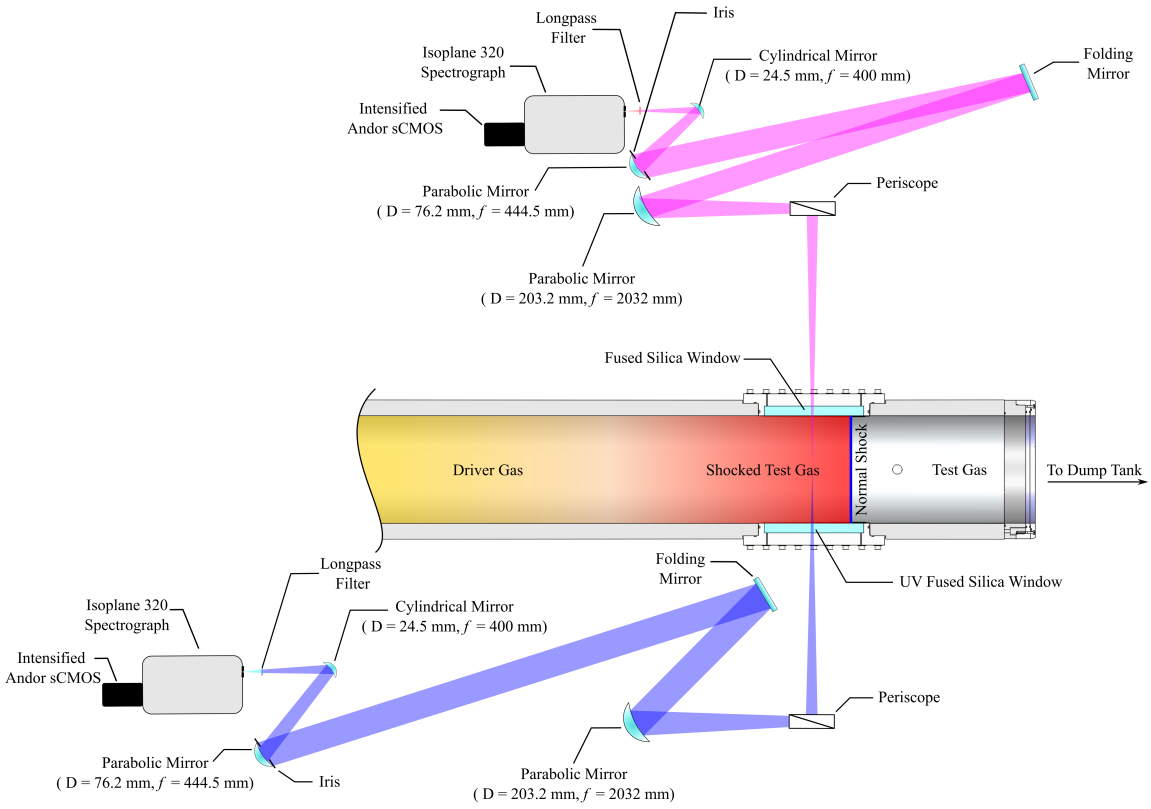


Fig. 3.11 The Vis/NIR (upper) and UV/Vis (lower) telecentric OES systems capturing radiation from a shock layer traversing across the windows. Not to scale. Longpass filters in the UV/Vis setup are only necessary when viewing above 400 nm.

Once radiation along the length of the window is focused onto the spectrometer slit; it is spectrally separated by a diffraction grating while retaining its spatial profile along the tube axis. The wavelength dispersed image then falls on the camera sensor at the spectrometer outlet to finally capture the spatially and spectrally resolved image. Exposure times of

0.5µs were typically used for both spectral channels in this work unless stated otherwise, to minimise smearing due to shock motion while maintaining sufficient S:N. This is especially important when analysing the transitory non-equilibrium region and given that smearing due to shock motion is often the largest component of the Spatial Resolution Function (SRF) as defined by Cruden [41]. Both sides use intensified Andor iStar sCMOS cameras: a Gen 2 W-AGT photocathode and P46 phosphor intensifier on the red camera; and a Gen 2 WE-AGT photocathode and P43 phosphor intensifier on the blue. These are each mounted onto Princeton Instruments Isoplane-320 spectrographs, with internal mirrors and grating coated accordingly to the wavelength regions. Low resolution 150 G/mm gratings with blaze wavelengths of 300 and 500 nm were used for the blue and red setups respectively, to provide access to a broad range of spectral features. Additionally, a 600 G/mm grating in the blue can be swapped in, enabling higher resolution spectra to be attained. This is useful for distinguishing the N_2^+ first negative band from the CN violet contamination, for example, as will be seen in later chapters. The fundamental design and components of both blue and red telecentric setups is the same, with differences in mirror positions owing to different spatial constraints on each side of T6.

Table 3.2 Optical components used in the blue and red telecentric OES setups.

No. in Sequence	Description	
	Blue	**Red**
1	UV Fused Silica window	Fused silica window
2	200mm x 25mm flat mirror made to order by McPherson with Al+MgF_2 coating	200mm x 50mm flat mirror made by Tempotec with a protected silver coating
3	Same as above	285mm x 50mm flat mirror made by Tempotec with a protected silver coating
4	Edmund optics #32-076-000 f/10, 203.2mm diameter parabolic mirror. w/ Teledyne H1900 MgF_2 coating	Same as Blue except coated w/ Teledyne H4000 protected silver coating
5	200mm diameter flat mirror made to order by McPherson with Al+MgF_2 coating	200mm x 60mm flat mirror made by Tempotec with a protected silver coating
6	Edmund optics #32-064-000, f/5.8, 76.2mm diameter parabolic mirror. w/ Teledyne H1900 MgF_2 coating	Same as Blue except coated w/ Teledyne H4000 protected silver coating
7	Thorlabs CCM254-400-UC-SP 1" cylindrical mirror coated w/ Teledyne H1900 MgF_2	Same as Blue except w/ Thorlabs protected silver coating
8	(Optional) Edmund Optics #18-793 Hoya UV28N 280nm longpass filter	Thorlabs FEL0550 550nm or FELH0400 400nm longpass filter

3.5.2 Advantage of a Telecentric System

Figure 3.12 illustrates the ray paths for two extremes of a fully telescopic and a fully telecentric optical system. Each are focused on the tube centreline and map light onto the camera sensor, at a location dependent on where the photon originates along the tunnel axis. Different colour rays show how radiation is directed when emitted from the principal axis, compared to the upstream and downstream FOV limits. Dimensions A, B and C indicate size of the optical blurring component at these respectively. They are derived from the upstream and downstream limits of where the rays intersect the near or far tube inner wall. The length of these is indicative of the "Optical Smear Function" (OSF) - the optical component of the SRF, as described by Cruden [41]. In the case a of telescopic system, the OSF increases as you move away from the centre of the optics FOV. This is shown by A<B and A<C in the top diagram of Fig. 3.12. Conversely, a perfectly telecentric setup maintains a constant OSF regardless of the location in the FOV, at the sacrifice of depth of field information.

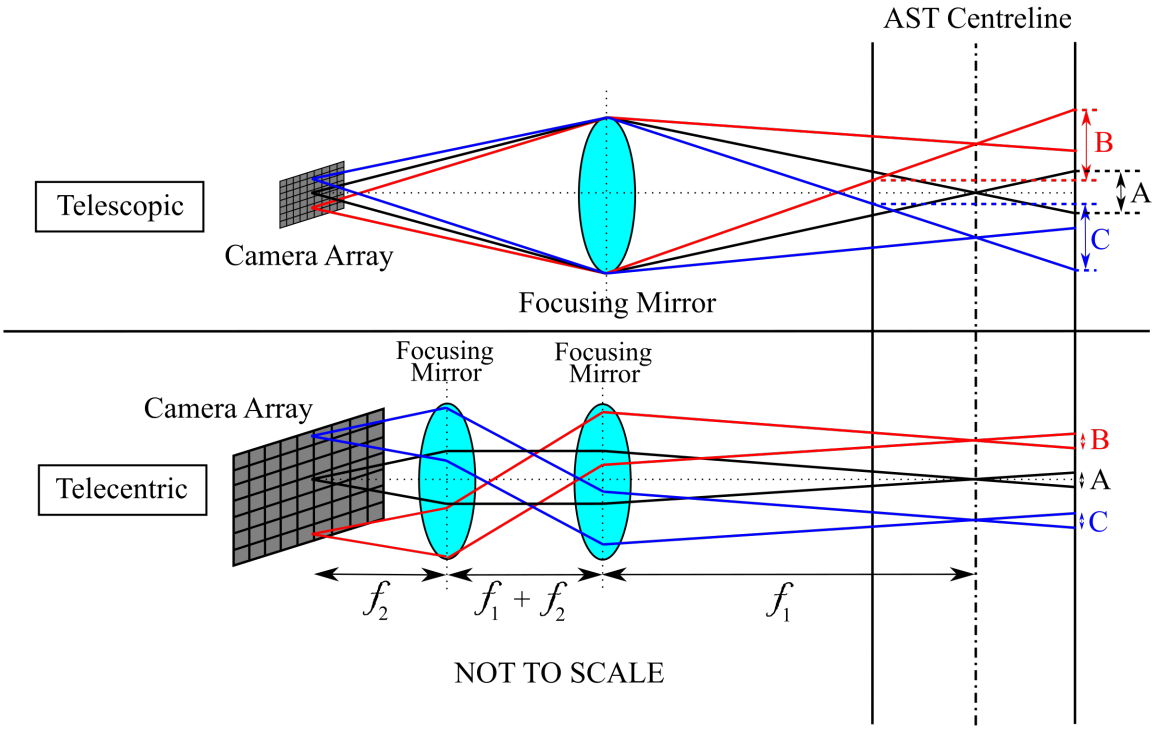
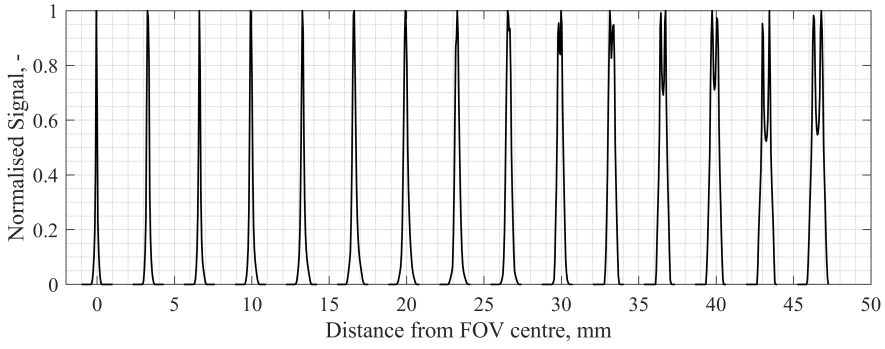
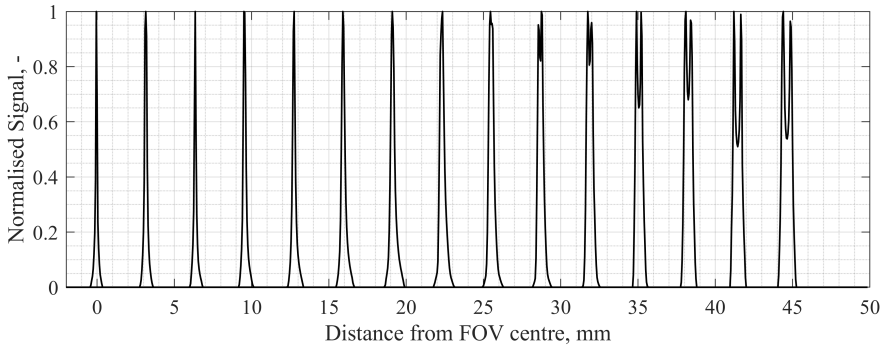


Fig. 3.12 Illustration of ray paths for fully telescopic and fully telecentric optical systems. Mirrors are simplified down to the relevant focusing mirrors. A<B & A<C for telescopic (illustrating increased OSF further from centre of FOV), while A=B=C for telecentric (since OSF is independent of location in FOV). f denotes the focal length of the respective telecentric focusing mirrors.

In reality, an optical system may not be fully telescopic or telecentric. The works of Greenberg et al. [74] and Cruden [41] detail the design and characterisation of OES systems used on the EAST facility and show how an optical system may be somewhere between the two. Figure 3.13 plots the variation in OSF of the blue and red OES systems (used to capture data analysed in this thesis) as a function of distance along the AST axis. The degree of "telecentricity" achieved can be evaluated by how much the OSF broadens towards the FOV limits. For both spectral channels, the OSF function base increases by ~50%, indicating they are not perfectly telecentric.



(a) Blue



(b) Red

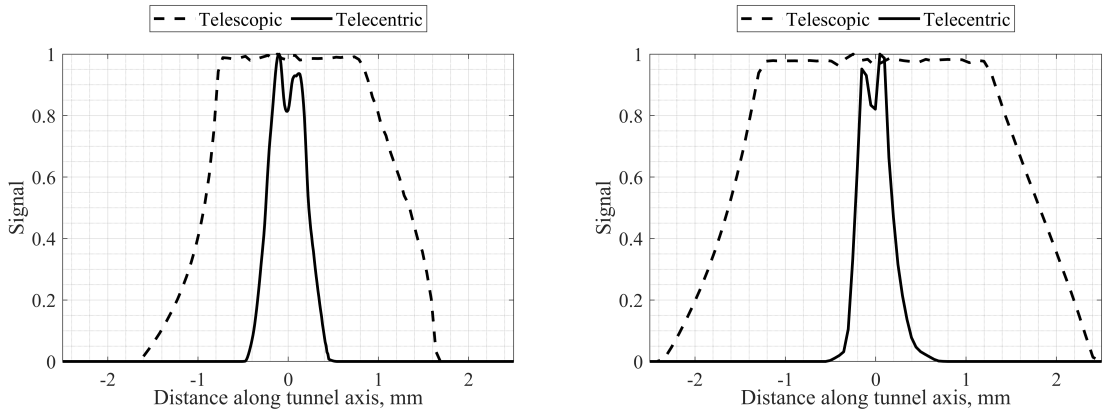
Fig. 3.13 OSF's plotted as a function of distance from FOV centre for both blue and red OES systems. These have been derived by numerical ray tracing. The width of the OSF increases by ~50% from the centre to the FOV limit. This demonstrates the optical systems are not perfectly telecentric.

A double-peak artefact appears in both spectral channels towards the FOV limits. Investigation suggests it arises from introducing the second focusing mirror and cylindrical mirror[3]. Both these optical components are required to transition to a telecentric system. The cylindrical mirror helps to focus rays both horizontally and vertically at the same optical path

[3]Note the double-peak has not been observed in ray tracing of previous telescopic systems using the same methods, indicating it is not a numerical artefact.

position - without which no image plane exists for OSF characterisation. Consequently, their individual effects cannot be isolated. However, since the shock is typically imaged before the artefact emerges, its impact on the resolution of the immediate non-equilibrium test gas is minimal (and negligible compared to shock motion). Additionally, as it is characterised in the OSF, a component of the SRF, it will be accounted for in numerical comparisons.

The telecentric OES's were newly developed for the considered experiments, to reduce the increase in OSF from the optical centreline, since the shock is imaged typically ~20 mm from the FOV limit (to observe as much post-shock relaxation as possible). Telescopic OES setups have been used in all previous T6 AST radiation campaigns to date, including the works of Collen et al. [37], Glenn et al. [69], Sopek et al. [162] and Crumpton et al.[51]. Additionally, the new optics were designed to zoom in further spatially than the previous setups, such that the non-equilibrium region may be magnified. This will be advantageous to capture the thermochemical state evolution through the post-shock relaxation phase in later chapters. It does however require compromise of the FOV compared to prior telescopic setups, due to the finite size of the Andor camera sCMOS arrays. The nominal de-magnification factor of both the red and blue telecentric OES's is 6.5, corresponding to a 90 mm FOV along the AST axis. Figure 3.14 illustrates the improvement in OSF from the new telecentric setups compared to the prior telescopic systems, which has again been derived from numerical ray tracing of the entire optical paths. Approaching telecentric also eases comparisons to numerical predictions, since the resultant SRF remains more constant with location in the FOV. Performing a convolution by a function varying with respect to location becomes much more complex, and is often simplified by using the function at the shock location.



(a) Blue (b) Red

Fig. 3.14 Comparison of OSF's for the new blue and red OES systems against previous telescopic setups used in prior T6 AST campaigns. Ray traces are performed 30 mm downstream from the FOV centre, where the shock is typically located during camera gating.

3.5.3 Intensified Cameras

Each sCMOS camera has a 2560 x 2160 pixel array, used to resolve spectrally and spatially on each axis respectively. However, the intensifier has a resolution of only 1280 x 1080 pixels. Though this is detrimental to image resolution, it does allow 2x2 binning, in which the sensor readout is down-sampled by summing the signal on a square of 2x2 pixels. This improves the S:N by the factor given by Eq. 3.4, where N_{px} is the number of pixels binned and S_{sig} and S_n are the signal and noise counts on one pixel respectively. This assumes the noise on each pixel is statistically independent and is performed within the Andor camera software, allowing the images to be saved as 32-bit, thus maintaining the dynamic range of the image.

$$\mathrm{S:N} = \sqrt{N_{px}}\frac{S_{sig}}{S_n} \tag{3.4}$$

3.5.4 Camera Triggering

The shock tube mode of operation imposes stringent requirements on the triggering of the intensified Andor sCMOS cameras, to capture radiation emitted for the brief period when the shock passes the windows. For example, a shock travelling at 7 km s^{-1} (typical of a LEO return mission) is equivalent to 7 mm μs^{-1}. The shock would therefore traverse the 200 mm long window in less than 30 µs. On top of this, placement of the shock approximately three-quarters across the image FOV is required to capture sufficient pre-shock signal, resolve the entire non-equilibrium peak and see the post-shock relaxation process (ideally to equilibrium). Typically therefore, for the 90 mm FOV of the telecentric OES systems used in these works, there's approximately a 15 mm region where the shock is to be captured. This gives a $\pm$ 1 µs margin for error from the triggering system. Additionally, the methodology needs to account for the shot-to-shot variation and predict when the shock will be at the desired location in real time, during the experiment. Furthermore, it usually takes the most part of a day to prepare for a shot, with the efforts of several people. Thus, it is crucial the method is reliable to avoid failed shots and wasted efforts.

A Fast Oscillator Shock Timer Enabling Repeatable Spectroscopy (FOSTERS) trigger box was designed in the prior works of Collen [32]. This is based on the time of flight box design by Jacobs [89]. It uses a Microchip Technology PIC16F1769 microcontroller to monitor the signal from two selected STS's upstream of the window. The second of these STS's is equidistant from both the first STS monitored by FOSTERS and the window centre. The sudden voltage jump from the pressure rise as the shock passes an STS is recognised and starts the internal 8MHz clock. The time taken for the shock to pass the second STS

monitored by FOSTERS is recorded. Assuming a constant shock speed, the shock should be at the centre of the window when the recorded time is elapsed again. A trigger is therefore sent to the Andor cameras at this time. The FOSTERS box allows precise positioning of the shock by implementing positive or negative delays (in increments of 62.5 ns) as well as adjustment of the STS voltage threshold to suit the test in question. Typically, faster and lower pressure test cases are trickier to trigger correctly, since the shock moves further in each FOSTERS time step, for the former. Whilst lower voltage thresholds are required for lower pressures, which increases the likeliness of a pre-trigger from a spurious voltage source. Arming of the FOSTERS box and cameras is left to just a few seconds before firing the shot to minimise the opportunity of this happening. The FOSTERS box is also capable of sending a pre-trigger signal, immediately as the shock is detected at the first monitored STS. This is needed for the fast gating of the Andor cameras. Additionally, the final output trigger sent to the cameras is also sent to the DAQ, so the triggering of the cameras can be seen on the same time axis as the shock trajectory information from the STS's. This is useful if the shock was not captured in the FOV at all, enabling the experimenter to realise if the triggering was too soon or too late.

The use of a simple delay generator, of which the standard DAQ software and infrastructure is capable of, is not suitable since the absolute time to trigger the cameras relative to the STS rise times is not known prior to firing the shot - it must be calculated live. The time constraints of the calculation prevent many higher level software programs from being chosen in this application. Even in the case of the microcontroller, the only mathematical operation that can be performed within the time constraints is a multiplication by two, which can be completed in a single clock. Using this technique, the shock location was typically repeatable within 5 mm for the shock speeds considered in these works.

3.6 Calibrations

Calibrations must be performed along each of the three axes that compose the shot images of radiating test gas, these are: space; wavelength; intensity. The first two are necessary to map the placement of each pixel on the camera sensor arrays to the spatial and spectral locations. While the intensity calibration is required to convert the measurement of counts acquired at each pixel into units of absolute spectral radiance ($W\,\mathrm{cm}^{-2}\,\mathrm{sr}^{-1}\,\mu\mathrm{m}^{-1}$). The procedure given in this section is largely based on that documented by Cruden [41], as used on the EAST facility at NASA Ames and has also been described comprehensively with reference to application in T6 AST in the work of Collen [32]. The content provided in this section is therefore a summary of the key points from these works, to provide a coherent

and complete picture of how the calibrated spectrally and spatially resolved shot images are generated. The reader is directed to the referenced works for more detailed accounts of the calibration process. Intensity calibrations are performed as standard before every shot. Wavelength calibrations are needed when a new grating, slit width or centre wavelength is used. And spatial calibrations were typically also performed before every shot as a quick means to check mirrors had not been knocked during the cleaning process between shots [4].

3.6.1 Wavelength Calibrations

Before carrying out a test on the T6 AST, the spectral features of interest will be identified. This will determine the grating density and orientation in each IsoPlane spectrometer, to give the desired spectral resolution and centre wavelength. It is then necessary to translate the resulting spectral axis onto the horizontal axis of the camera array, so that spectral features in the shot image can be correctly identified [5]. This is achieved with a Princeton Instruments IntelliCal® Hg/Ne–Ar lamp, positioned approximately 100 mm in front and normal to the spectrometer slit [6]. The Intellical is a light source with distinct spectral features of known wavelengths, which when resolved along the horizontal axis of the camera array, can be used to interpolate the wavelength at each pixel column. This process is performed in an interactive MATLAB routine, allowing the user to manually identify the captured atomic transitions and assign the correct wavelength values. Since the spectral region is roughly known, this is usually a simple process. Filters are removed between the Intellical and the spectrometer slit, so that higher order diffractions of each line may also be identified and thus increase the resolution of features selected. A linear interpolation is then applied to assign a wavelength to all pixels. The gradient of pixels/nm was typically very consistent between all features, demonstrating minimal non-linear effects along the spectral axis. Spectral features of the Intellical are assigned from the NIST-traceable calibration standard for the lamp.

[4] Cleaning of the facility between shots is important to minimise contaminant species present on the walls, which gradually build up with shots over time. Details and analysis are provided in Chapter 4.

[5] It is also important for the subsequent calibration surface generation, to ensure the standard calibration data from the calibration lamps is applied correctly.

[6] This positioning is used to ensure all light lands on the spectrometer mirrors to minimise the stray light inside. This helps to reduce the background signal of the wavelength calibration image. Although it's not important for the wavelength calibration process (since only position, not magnitude is used) it is helpful to extract the Instrument Line Shape, as seen in Section 3.6.2.

3.6.2 Instrument Line Shape

Quantum physics dictates that each atomic or molecular energy transition resulting in the emission of a photon, can only occur between two distinct energy levels. Thus, the energy, and therefore wavelength, of each photon only exists at discrete values. Various physical mechanisms of broadening can occur to these discrete lines in a high temperature environment (as is comprehensively covered in the thesis of Laux [101]) to generate predictable line shapes. These are owed to the environment generated in the test itself. However, the measuring instrument also introduces a broadening mechanism. This must be measured and characterised, before using it to convolve with predictions of radiative solvers such as NEQAIR, thus enabling like-for-like comparisons with the experimental data.

When extracting the Instrument Line Shape (ILS) there is a choice of using the exact raw measured profile of a single atomic transition (from one of the transitions in the Intellical wavelength calibration image), or alternatively applying a fit to said function. In the works of this thesis, the square root of a Voigt function was used to provide a decent fit of the measured ILS, as defined by Equations 3.5 to 3.8. Where x here is the wavelength axis, the Gaussian full width at half maximum (FWHM) = $\sigma \times 2\sqrt{2ln(2)}$, Lorentzian FWHM is $2 \times \gamma$ and μ is the wavelength of the spectral feature of interest. All sharing common units of nanometres. Typically, the raw measured profile is the preferred convolution function to apply to numerical data, since it is exactly the broadening function generated by the instrumentation (which isn't necessarily symmetric like the fitted versions will be). However, the square root of Voigt can also be defined in NEQAIR, which can perform the spectral convolution in-house. This removes a step to generate artificial spectra and also speeds up the process considerably, which is beneficial when thousands of iterations need to be produced back-to-back during a spectral fitting routine [7]. Thus, in these works, the raw measured line shape has been used for comparisons between experimental and numerical equilibrium spectra, and the square root of Voigt function has been used during the spectral fitting routines. Figure 3.15 shows a comparison of the measured and fitted line shapes for both blue and red OES systems, using the 150 G/mm gratings and 10 μm slits in both spectrometers, typical for the broad range images taken and analysed in the following chapters. Use of a high resolution grating will make these line shapes narrower to enable better resolution of overlapping spectral features, but reduces the range of wavelengths captured in a single image.

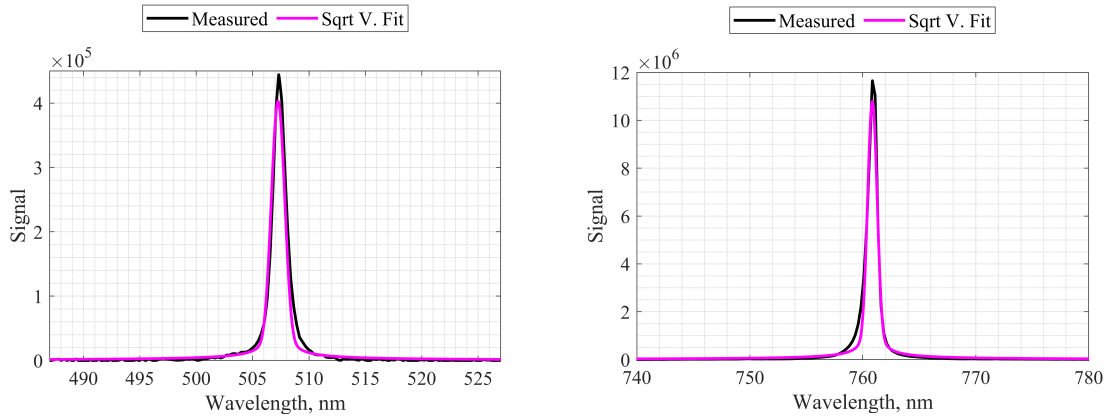
[7] Chapter 5 gives an in-depth explanation and validation of a new spectral fitting methodology which is then applied in Chapters 6 and 7.

$$Gauss(x;\sigma) = \frac{1}{\sigma\sqrt{2\pi}} e^{-\frac{(x-\mu)^2}{2\sigma^2}} \tag{3.5}$$

$$Lorentz(x;\gamma) = \frac{\gamma}{\pi((\gamma-\mu)^2+x^2)} \tag{3.6}$$

$$Voigt(x;\sigma,\gamma) = \int_{-\infty}^{\infty} Lorentz(x;\gamma)Gauss(x-x';\sigma)\,dx' \tag{3.7}$$

$$ILS(x;\sigma,\gamma) = [Voigt(x;\sigma,\gamma)]^{1/2} \tag{3.8}$$



(a) Blue (b) Red

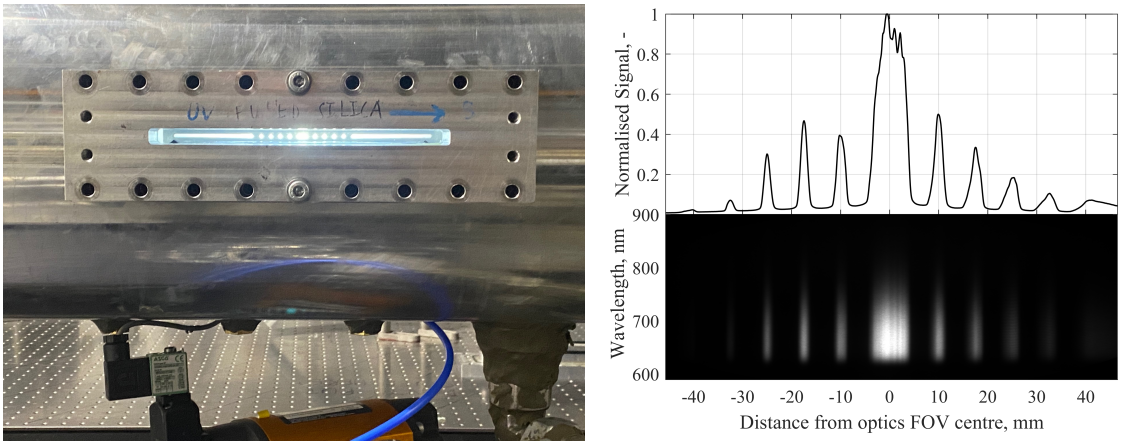
Fig. 3.15 Example ILS broadening functions for both (a) Blue and (b) Red optical setups, fitted with a square root Voigt function. Measured line shapes were acquired using a 150 G/mm grating and slit width set to 10µm for both spectrometers. Corresponding Gaussian and Lorentzian FWHM's are: 1 nm and 0.0001 nm respectively for the blue; 0.6 nm and 0.00005 nm for the red.

3.6.3 Spatial Calibrations

Fundamentally, the spatial calibration process is necessary to map the AST centreline axis onto the vertical axis of the Andor camera sCMOS array. This is achieved by positioning a series of light sources at known locations along the tunnel axis, to then capture and assign them to a camera pixel row. The process is analogous to the wavelength calibration procedure, but on the perpendicular axis. Again, an interactive MATLAB routine is used to assign the measured peak locations to the pixel rows, and then perform a linear interpolation to allocate a spatial location to all pixels, relative to the FOV centre. To achieve this, a calibration plate

is installed from the opposite window, designed to position holes of known locations exactly along the tube centreline. The axial hole locations were machined to a tolerance of ±0.1 mm. An LED light source is placed behind the plate and directed towards it. A diffuser removes some of the directionality of the light source, to give a more uniform distribution across the FOV. Figure 3.16 provides images of the light leaving the calibration plate and out the AST window, as well as the image and spatial profile it produces along the vertical axis of the camera sensor array.

This process was also found to be useful as a means to quickly assess and improve the quality of alignment of the optics. Since the series of holes and slots originating from the tube centreline could be focused back down to a crisp image of dots on-and-off along the spectrometer slit. Additionally, it is a useful means for determining the extent of the actual FOV and magnification achieved. By carrying out this procedure on both spectral channels, the Blue and Red OES systems were referenced to the same datum. Axial coordinates between the two systems therefore correspond to one another.



(a) Light produced.

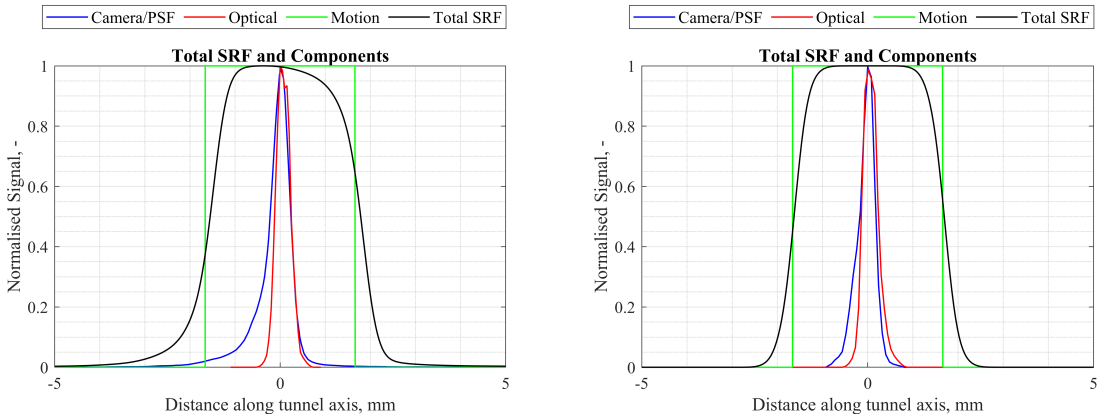
(b) Image captured.

Fig. 3.16 Image of (a) the diffused light leaving the calibration plate positioned exactly on tunnel centreline and (b) the consequent 2D image attained (bottom) and summed spatial profile of peaks (top) to perform a spatial calibration.

3.6.4 Spatial Resolution Function

Similar to the ILS function defined for the spectral axis, there is a so-called "Spatial Resolution Function" (SRF) used to convolve numerical data along the spatial axis. Cruden [41] explains this is made up of three components. First, the broadening caused by charge sharing between adjacent pixels of the sCMOS arrays is extracted by experimentally measuring the Point Spread Function (PSF) as described by Zong et al. [202]. This can be fit with a

symmetric function such as the square root of a Voigt function, as was demonstrated for the ILS. The PSF is measured by placing a pinhole in font of a light source on the tube centreline, perpendicular to the window. The pinhole size is selected such that, after being de-magnified by the optics, it is focused down to an area smaller than one pixel of the sCMOS array. Thus any blurring is due to charge bleeding between the pixels. The second component is the OSF, which has been described and characterised by numerical ray tracing as shown in Fig. 3.13 and Fig. 3.14 in Section 3.5.2. Finally, the smearing due to shock motion during the camera gating time must be accounted for. This is modelled as a square wave of width equal to the distance of shock travel during the camera gating time. Cruden [41] demonstrates that the square pulse approximation is less valid as exposure time is decreased, and so the gating function of the camera should be measured to account for the rise profile as the intensifier fully "opens". The Andor iStar sCMOS cameras are quoted to have a rise time less than 35 ns when the pre-trigger is used. This was deemed to be sufficiently small with respect to the gating time (typically 0.5µs) for the square pulse approximation to be valid. Since shock speed at the window varies shot-to-shot, the shock motion component is unique to each shot [8]. The final SRF function is attained by convolving all three of these components. Figure 3.17 shows the Blue and Red SRF's for T6s492. This corresponds to a pure nitrogen test case referred to and analysed in Chapters 5 and 6.



(a) Blue (b) Red

Fig. 3.17 T6s492 total SRF's and constituent components.

[8] Generally speaking, the smearing due to shock motion is also unique to each spectral channel for a given shot, since different gating times may be used.

3.6.5 Intensity Calibrations

The final step of the calibration process is the intensity calibration, which fundamentally is necessary to convert the counts acquired at each pixel of the Andor sCMOS array to the units of absolute spectral radiance ($W\,\mathrm{cm}^{-2}\,\mathrm{sr}^{-1}\,\mu\mathrm{m}^{-1}$). This is achieved by taking images of a calibrated light source (of known spectral radiance) and measuring the counts at each pixel. This information can be used to create a "calibration surface" of dimensions equal to the sCMOS array and in units of $\mathrm{Counts}/(\mathrm{s}.W\,\mathrm{cm}^{-2}\,\mathrm{sr}^{-1}\,\mu\mathrm{m}^{-1})$. Once a shot image is acquired, the counts may then be converted to absolute spectral radiance by a simple division operation, as shown in Equation 3.9.

$$\frac{\text{Calibrated Shot Image}}{(\mathrm{W\ cm^{-2}\,sr^{-1}}\,\mu\mathrm{m}^{-1})} = \frac{\text{Raw Shot Image}\left(\frac{\text{Counts}}{\text{s}}\right)}{\text{Calibration Surface}\left(\frac{\text{Counts}}{\text{s}\cdot\mathrm{W\ cm^{-2}\,sr^{-1}}\,\mu\mathrm{m}^{-1}}\right)} \tag{3.9}$$

This is the top-level description of the intensity calibration procedure, though there are various intricacies and artefacts to be dealt with during the calibration surface generation. These are explained in the series of steps summarised below. Figures 3.18 and 3.19 have been extracted from the work of Collen [32] to provide a visual representation of the process. The reader is directed to this text if a more detailed description of the methodology is required [9]. A summary of the key points is provided here, to give a complete and coherent account of how calibrated spectral radiance data is attained, without rehashing all the information that has been comprehensively covered in past works. A uniformly radiating Bentham Instruments SRS8 quartz-tungsten-halogen integrating sphere was used to produce a full-field calibration at wavelengths above 300 nm for both the Vis/NIR and UV/Vis optical paths. In addition, a McPherson Model 634 VUV deuterium lamp was used to calibrate the UV/Vis wavelengths below 300 nm. These intensity calibrations were performed as standard procedure before every test. The following steps are numbered according to the diagrams of Fig.'s 3.18 and 3.19.

Step 1: The Integrating Sphere (IS) is positioned on the opposite side of the tube to the OES system to be calibrated, as shown in Fig. 3.20a, and is level with the tube centreline [10]. The aperture is directed perpendicular to the tube axis, such that emitted radiation escapes through the opposite window and lands on the first periscope mirror of the OES system to be calibrated. A spatio-spectrally resolved image from the IS is taken on the Andor sCMOS

[9] Additionally, the reader is directed to the work of Cruden [41] where calibrations performed on the EAST facility are explained. It is upon this work which the T6 AST methodology is based.

[10] Ideally, the aperture would be positioned on the tube centreline, however this is not possible once the AST is installed onto the facility. Tests were done before installation to confirm negligible difference in images acquired from the IS positioned on the tube centreline, compared to a positioning one AST outer radius from the centreline.

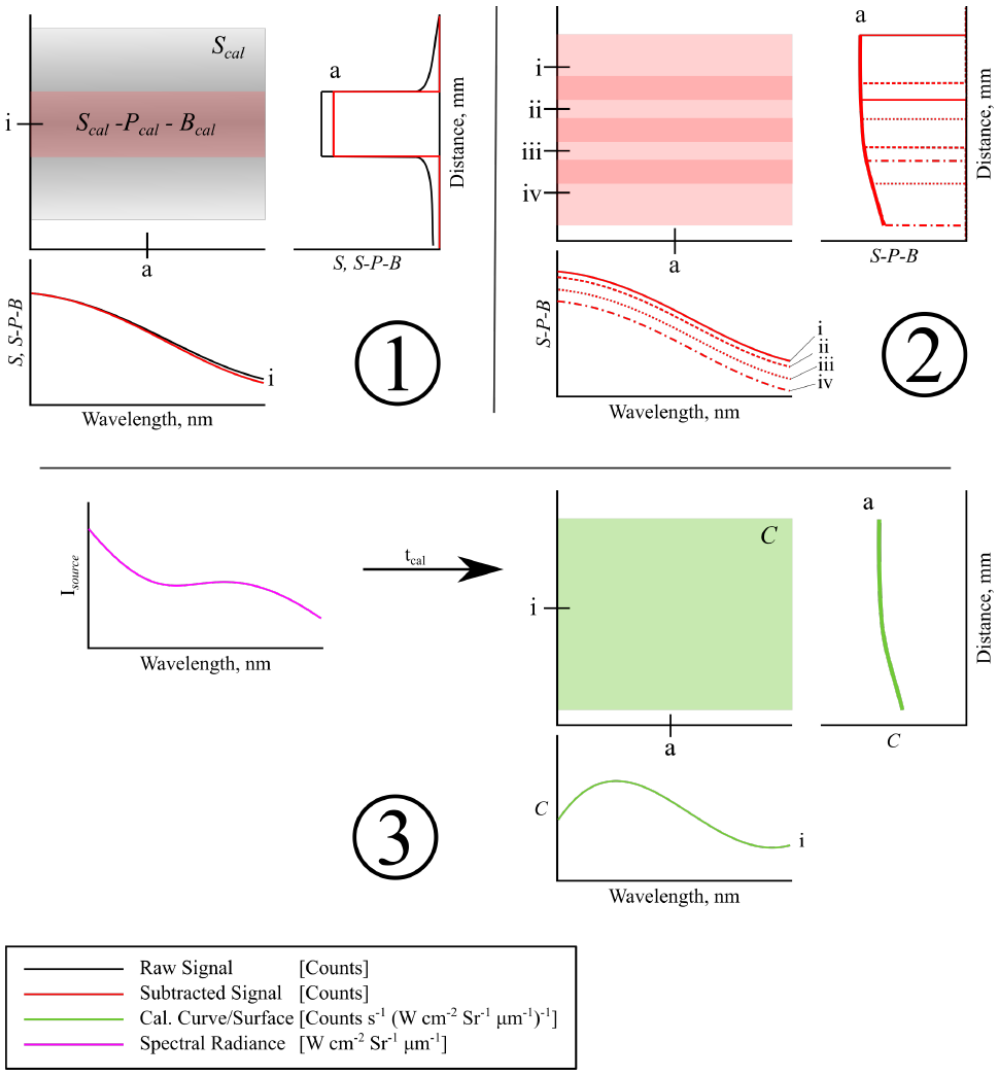


Fig. 3.18 Diagram of OES system calibration process above 300 nm. Taken from Collen [32]

array. Since the outlet diameter (50 mm) is less than the FOV (90 mm), the captured signal fills only a portion of the observed spatial region. The IS is therefore translated along the tube axis and multiple overlapping images are acquired to cover the entire camera sensor. The initial raw image (S_{cal}) (denoted by the grey region of Fig. 3.18) consists of: the desired signal from the IS; scattered light from the broadband source (referred to as the "pedestal" and denoted P_{cal} in Fig. 3.18); and background thermal camera noise (denoted as B_{cal}). The background is determined by imaging with the IS turned off and the resulting image subtracted from the raw image. To remove the pedestal, the method of Cruden [41] is applied. This involves identifying the IS edges and zeroing intensity away from the source location. The pedestal values at the edges are linearly interpolated across the illuminated region and subtracted from the raw image. This process is repeated for each pixel column to account

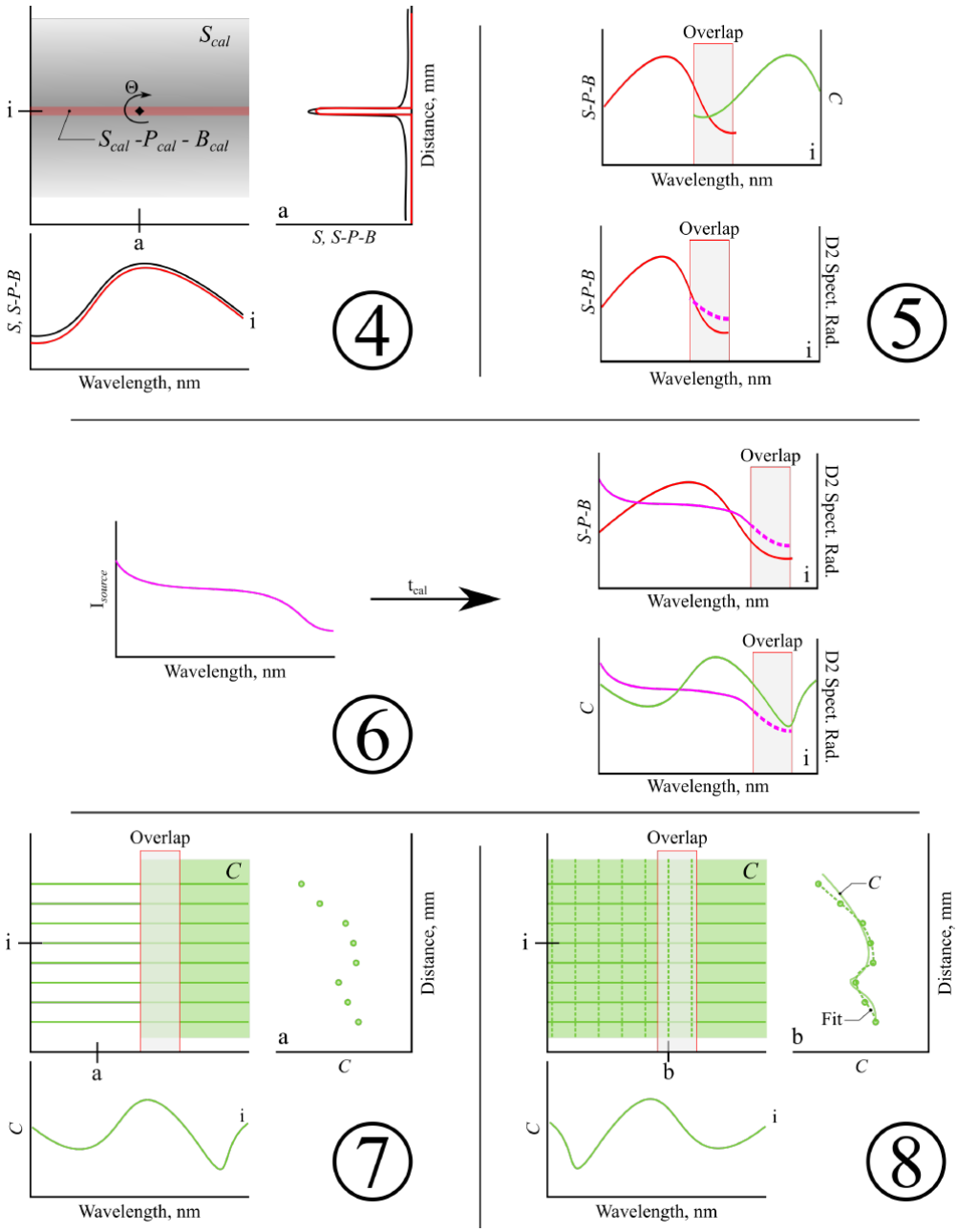
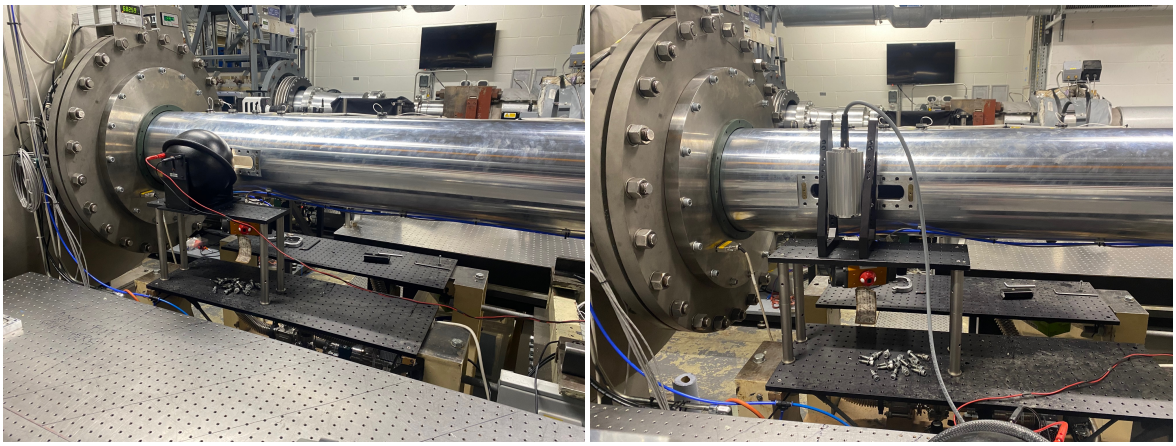


Fig. 3.19 Diagram of additional steps required to calibrate the Blue OES system below 300 nm. The plot key is identical to Fig. 3.18. Taken from Collen [32].

for any spectral dependency. The resulting image, shown in red, ideally forms close to a square-pulse profile through the spatial cross-sections. This process is repeated for each IS calibration image.

Step 2: After removing the background signal and stray light from each IS calibration image, they are stitched together to form a continuous surface across the entire sCMOS array.



(a) Integrating Sphere (b) Deuterium Lamp

Fig. 3.20 Images of the Integrating Sphere and Deuterium Lamp positioned during the intensity calibration of the blue spectral channel. The pedestal and mounts were each designed to ensure the centre of each light source was level with the tube centreline.

An acceptable core region of each IS calibration image is chosen (deemed to be free of edge blurring effects), which are then combined by averaging in the regions of overlap. If step 1 has been done well, this usually results in a seamless transition between the individual images, with no steps or gaps in the calibration surface, which would in turn put artificial features into the calibrated data. Vignetting effects often result in a gradual decrease in signal towards the spatial limits of the sCMOS arrays. Units of the surface created at this stage is still counts.

Step 3: The next step is a unit conversion of the generated surface. The spectral radiance calibration standard, as provided by Bentham Instruments, is linearly interpolated to the spectral axis of the sCMOS array. Each pixel row (representing a spatial location) is then divided by this calibration standard, to give a surface now in units of Counts$/(W\,\mathrm{cm}^{-2}\,\mathrm{sr}^{-1}\,\mu\mathrm{m}^{-1})$. Finally, each pixel is divided by the calibration exposure time [11]. For OES systems only looking above 300 nm, this is the final step and produces the desired calibration surface in units of Counts$/\mathrm{s}.(W\,\mathrm{cm}^{-2}\,\mathrm{sr}^{-1}\,\mu\mathrm{m}^{-1})$.

Step 3.1: An optional additional step, not depicted in Fig. 3.18, is to remove the dark corners of the sCMOS array (as done by Cruden [41]) originating from the camera intensifier being smaller than the sensor. A noise threshold is defined, slightly above the values at these corners, and all values below which are set to infinity. This is done so that, when the final calibration process is performed (as defined in Equation 3.9) these corner regions will become zero, as opposed to some large non-zero values. This step was carried out on all

[11] All IS calibration images are acquired using the same exposure time.

calibration surfaces generated for shots considered in this thesis, unless the OES system looked below 300 nm, then the calibration process continues onto step 4.

Step 4: When the blue OES system is looking at wavelengths below 300 nm, the Deuterium (D2) Lamp must be used to generate the portion of calibration surface below 300 nm. However, the D2 lamp is not capable of performing a full-field calibration like the IS, which introduces a couple of complexities to the process. The first is due to the outlet diameter of the source being close to 1 mm, resulting in a light source which under fills the OES system optics and spectrometer slit [12]. The second consequence due to the small aperture of the source is that, capturing overlapping images (as was the case for IS calibration images) is extremely impractical. An alternative method of only imaging at distinct locations and interpolating the spectral profiles across the sCMOS spatial rows is therefore performed. These are summarised in the following steps. However, the first step of the D2 calibration process is to capture the images and perform the background and stray light subtractions, analogously to that for the IS (and illustrated in Fig. 3.19). Different exposure times are used for the D2 images, compared to IS ones. Typically 6 to 9 D2 images were acquired for the blue telecentric OES system, corresponding to 10 to 15 mm spacing of D2 images.

Step 5: Each of the D2 images must be calibrated by the calibration surface generated at the end of step 3 (denoted as C in Fig. 3.19 for a single D2 spectral cross-section at spatial row i). The IS calibration standard goes down to 300 nm, and the D2 lamp standard goes up to 410 nm. Thus, there is a region of overlap, even if the signal levels are dropping for both near the limits of their range. An overlap region of 350 to 390 nm was typically used for the data in this thesis, where both calibration lamps exhibit sufficient signal to work with. The D2 lamp cross-section is thus calibrated via this small range, using the division process of Equation 3.9. This is illustrated by the dashed magenta line in Fig. 3.19. The process is carried out for each D2 image.

Step 6: As was the case with the Bentham Instruments IS, McPherson provide a calibration standard for the D2 lamp. The resulting calibrated spectral radiance acquired in the overlap region of step 5 is used as a reference to scale this standard calibration curve by a single factor. In order to avoid artefacts of the instrument resolution (and since the D2 lamp is not a full-field source), the calibrated D2 lamp cross-section is summed over the spatial axis. A best fit of the McPherson calibration standard is then made to this resulting calibrated D2 cross-section in the region of overlap, essentially giving the calibrated spectral profile of the D2 lamp at the considered location (in units of $W\,\mathrm{cm}^{-2}\,\mathrm{sr}^{-1}\,\mu\mathrm{m}^{-1}$). The scaling process is illustrated by the upper right plot of stage 6 in Fig 3.19. The measured D2 lamp

[12] In contrast to the radiation captured as a shock traverses the window, which will fill the optics and spectrometer slit.

counts can then be divided by this spectral trace to generate the portion of the calibration surface to be used at the single considered location (depicted by the lower right plot of stage 6). This process is repeated for each D2 lamp image, to produce a series of "calibration cross-sections" across the full wavelength range projected onto the sCMOS array.

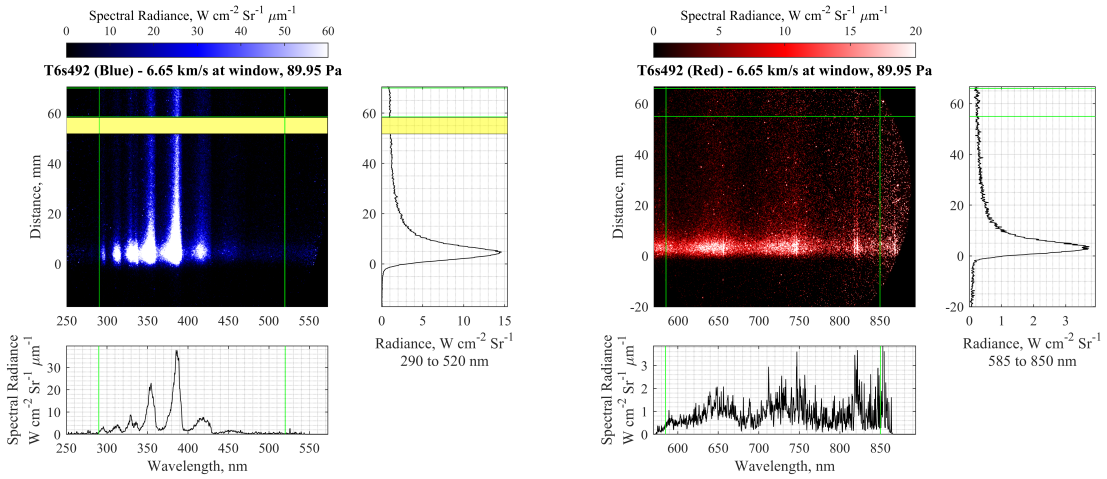
Step 7: The D2-IS calibration cross-sections are illustrated in step 7 of Fig. 3.19 as horizontal green lines. The IS full-field calibration surface '*C*' generated from steps 1 to 3, is depicted as the lighter green surface (starting from 300 nm upwards). Hence, the calibration surface is only known at a few discrete pixel rows of the sCMOS array below 300 nm. This is seen easily in the top right plot of step 7, representing a spatial cross-section at '*a*' on the wavelength axis, through the lower wavelengths. The next objective therefore is to perform an interpolation to assign the calibration surface values at all remaining spatial locations, at these lower wavelengths. There are multiple options to achieve this: Cruden and Brandis [44] takes advantage of the spatial profile known from the prior full-field calibration surface and fits it to the lower wavelength regions; Collen [32] applies a fifth-order polynomial fit between the D2 lamp image locations, which was found to also capture the observed spatial profile accurately. Both methods have been used to generate calibration surfaces for shots in this thesis, and differences between the calibrated data from each deemed negligible. It was noticed however, that the former is often more robust when one of the D2 cross-sections doesn't quite follow the spatial trend (i.e. one of the dots is far to the left or right in the top right plot of step 7). This very occasionally occurred and could be owed to the actual acquisition of the image and incorrect software settings, or the stray light or background removal step not performed quite correctly, etc. In these cases, the process was either started again with that point removed, or the Cruden method was applied if a good fit was still achieved.

Step 8: After interpolating the D2 cross-section across the lower wavelengths, the final calibration surface for the blue OES system is created. This is shown by the green shaded region in step 8 of Fig. 3.19. The quality of the fit can be assessed by comparing the spatial profiles of the original D2-IS cross-section points against the full-field spatial profile. This is shown at cross-section '*b*' in step 8.

3.7 Example Calibrated Data

After the steps in Section 3.6.5 have been carried out, a calibration surface will be ready for a given spectral channel. All that's left, is to take a "shot image" of the shock as it traverses the windows. A shot background image is also taken, with the same gating time and is subtracted from the shot image. Then, just as was the case for calibration intensity images,

the stray light is removed by extracting the magnitude of counts acquired in pixel locations corresponding to a region where no radiation is emitted. For the shot image, this is achieved by fitting a third order polynomial spline function across the spectral profile of the pre-signal ahead of the shock, as described by Cruden [41]. This is assumed to be constant spatially and thus subtracted at all spatial rows of the camera array image. The fitting is necessary in order to remove noise from the profile, which may add spurious spectral features to the data when subtracted. Finally, the shot image is then divided by the calibration surface to convert the shot image pixel counts to units of absolute spectral radiance $(W\,\mathrm{cm}^{-2}\,\mathrm{sr}^{-1}\,\mu\mathrm{m}^{-1})$. Examples of calibrated 2D spatio-spectral shot radiance images, acquired from the blue and red telecentric OES systems using the low resolution gratings, are shown in Fig. 3.21. These correspond to the T6s492 pure nitrogen condition. The shock was travelling at 6.65 km s^{-1} through a test gas at 90 Pa. Molecular N_2 second positive and N_2^+ first negative bands dominate in the UV/Vis region, while the Vis/NIR contains a background N_2 first positive band superimposed with atomic N transitions. More details of spectral features in both pure nitrogen and synthetic air test gases are given in later chapters. The spatial coordinates in both the blue and red images have been normalised so the shock front is at 0 mm and the positive values indicate the post-shock direction. Correspondence between the two spectral channels is still maintained.



(a) T6s492 UV/Vis

(b) T6s492 Vis/NIR

Fig. 3.21 Calibrated spatio-spectral radiance data for T6s492 (6.65km/s, 90 Pa fill in pure nitrogen). Horizontal green lines indicate spatial region averaged over to generate spectral radiance plot. Vertical green lines indicate wavelength region integrated over to generate spatial radiance profile. The yellow shaded region indicates a region purposely blocked for an alternative stray light extraction studied in Chapter 4.

Equilibrium spectral radiance traces are plotted below the 2D radiance maps, by averaging over regions furthest from the shock front and closest to thermochemical equilibrium, as indicated by the green horizontal lines. Spatially resolved radiance traces are acquired by integrating across the wavelengths between the vertical green lines, and are plotted to the right of the 2D radiance maps. The non-equilibrium peak can be seen in both spectral channels immediately behind the shock, followed by a relaxation region, as the thermochemical state approaches a new equilibrium. Data at a range of pressures is analysed in the following chapters, since at lower pressures the frequency of particle collisions is reduced and the non-equilibrium relaxation phenomena therefore occur over a larger spatial region. This helps to improve the spatial resolution and aids characterisation of the relaxation process, though reduces the S:N for a given shock speed. Thus, a balance is to be struck for the LEO return speeds investigated in the works of this thesis, where signal is smaller than many other common conditions. The radiance profiles in Figure 3.21 can be seen to just reach a steady plateau within the telecentric optics FOV, which is ideal for characterising the entire thermochemical relaxation process. Though a lower pressure condition would allow higher resolution measurements but may not equilibrate in the FOV, for example. After completing the calibration process, the next step is data analysis. The ultimate goal of the spatio-spectral radiance images in this thesis is to convert the spectral traces into temperature and number density profiles through post-shock test gas, including the non-equilibrium relaxation process. This is performed by a constrained spectral fitting routine. The methodology and validation are given in Chapter 5, to then apply it to pure nitrogen and synthetic air test cases in Chapters 6 and 7 respectively. Before this, a discussion of the discrepancies between measured equilibrium spectral radiance and numerical predictions is provided in Chapter 4.

3.8 Uncertainties

Finally, an example of typical spectral radiance uncertainties from the image acquisition and calibration procedure discussed, is briefly given. Figure 3.22 plots the equilibrium and non-equilibrium spectral radiance uncertainty profiles taken from the work of Collen [32], for a comparable condition to those considered in this thesis and using the same calibration methodology. This is the result of a perturbation analysis and similar trends were shown across all tests analysed by this method. The plot has been replicated here purely to inform the reader, though they are directed to the works of Collen for a more detailed review of the perturbation uncertainty analysis.

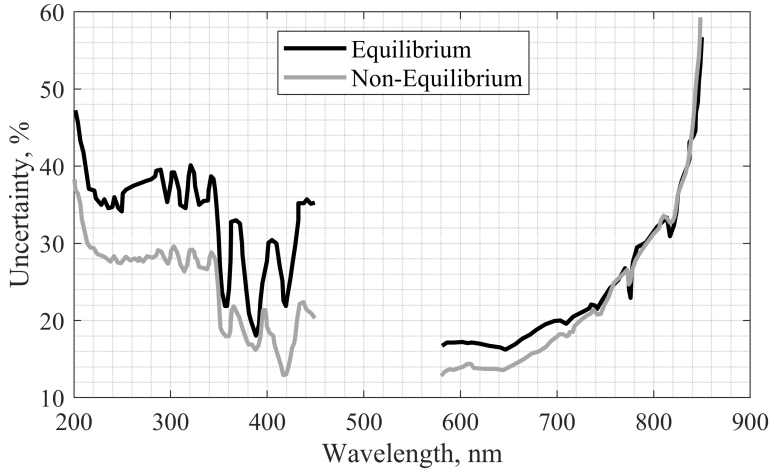


Fig. 3.22 Typical uncertainty spectral dependence from both spectral channels, in the equilibrium and non-equilibrium region, for the image acquisition and calibration process discussed in this chapter. Extracted from Collen [32]

Chapter 4

Investigation into Equilibrium Radiance Offset in Air Shock Tube Tests

Well, we have to do something.

Peter Collen

Preamble

The first research aim of this thesis is to further understand and reduce the discrepancies between measured shock tube equilibrium radiance and numerical predictions. These have been clearly demonstrated in previous test campaigns at Low Earth Orbit return speeds in both the T6 Aluminium Shock Tube and Electric Arc Shock Tube facilities[1]. This work investigates how the observed experimental offsets may be reduced, to pave the way for new reliable datasets that can be used for thermochemical characterisation studies in the later chapters. It includes the consideration of facility cleaning procedures, optical setup parameters and trials different radiation models.

This chapter is a draft of work intended for future journal publication, which has been reformatted and adapted for inclusion in this thesis. A statement of authorship is provided at the end of the chapter, while references are contained within the main body of references at the end of the thesis. This chapter stands independently, with no supplementary content in the Appendix.

[1] And have been discussed in Chapter 2 of this thesis.

4.1 Introduction

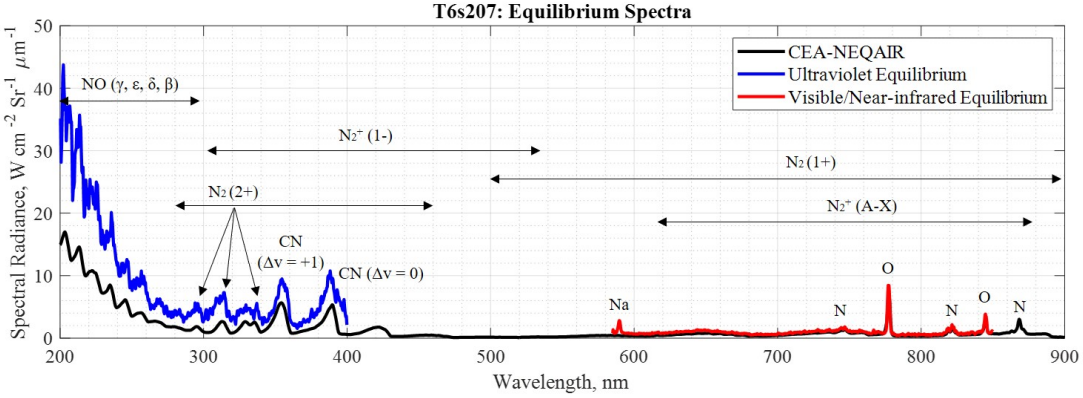
Shock tubes are a type of ground test facility capable of recreating the high-enthalpy stagnation lines ahead of planet entry vehicles. They enable a transient study of the thermochemical evolution behind a normal shock. The shock raises the internal energy of molecules within a chosen test gas, stimulating vibrational excitation, dissociation, ionisation and photon emission processes. This is necessary for the test gas to reach a new equilibrium state and occurs over a finite time period. The rates of the associated thermal relaxation and chemical reactions, relative to the time of flight of the particles, determines the spatial extent of thermochemical non-equilibrium. Recreating these conditions at ground level enables this extreme flow environment to be studied with a range of diagnostics.

Optical emission spectroscopy (OES) is the primary diagnostic in shock tube facilities for measuring radiation. This provides both spatial and spectral resolution of the radiance profile from the test slug as it traverses across the optics field of view. Previous telescopic OES arrangements used on the Oxford T6 Stalker Tunnel are detailed in the prior works of Collen et al. [32], while the more recently developed telecentric systems have been discussed in Chapter 3. When operating in Aluminium Shock Tube (AST) mode, T6 is able to replicate benchmark results from the Electric Arc Shock Tube (EAST) at NASA Ames [39, 41]. Cross-facility comparisons of air radiance measured in both facilities have shown close agreement for shock speeds at 7.7 to 10 km/s [37], as well as lower speed cases from 6 to 7 km/s [42]. Additionally, comparable contaminant radiance levels are seen in both facilities [68].

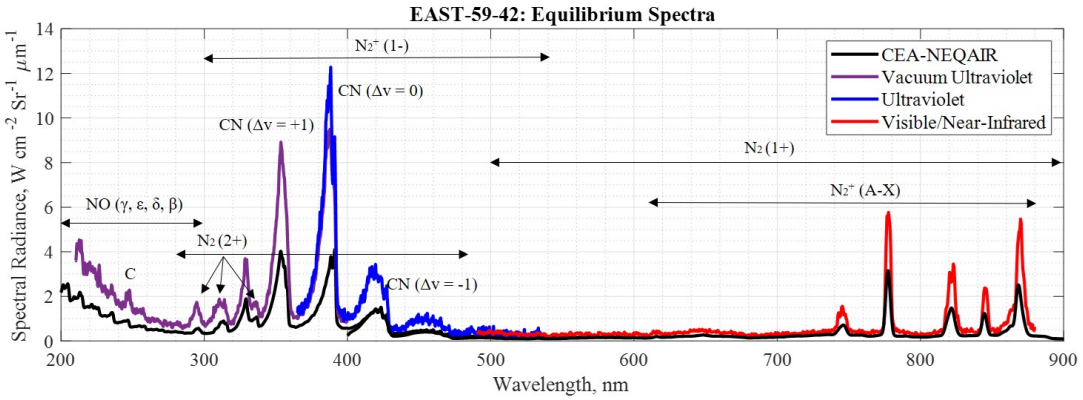
New low-speed air datasets from both T6 AST and EAST facilities have been published in recent literature. In 2017, Cruden and Brandis [45] reported new parameters for the rate chemistry and non-Boltzmann modelling from air test data at 7 to 9 km/s in the EAST facility. They highlight that molecular NO, N_2 and N_2^+ produce a large percentage of the radiation in the ultraviolet wavelengths. The range of available Low Earth Orbit (LEO) shock tube radiance data has since been extended further down to speeds of 5.5 km/s by Glenn et al. [69] in the T6 AST in 2022. Despite efforts to analyse the non-equilibrium region, they identified that all results were ultimately hindered by the presence of an offset between the measured and predicted equilibrium spectral radiance. This has since been replicated in the EAST facility at conditions from 3 to 7 km/s by Cruden [42].

Figure 4.1 demonstrates this continuum offset for both T6 AST and EAST equilibrium spectral radiance measurements. Equilibrium predictions are generated by NASA's Chemical Equilibrium with Applications (CEA) solver [115], to predict the chemical equilibrium composition of the post-shock test slug. The resulting thermochemical state is fed into NEQAIR as a line of sight across the diameter of the tube, thus assuming a homogeneous

core flow. Equilibrium spectra from both facilities display radiation from contaminant species (such as the cyano radical, CN) and an increased divergence towards lower wavelengths, where NO dominates. Discrepancies of the magnitude displayed in Fig. 4.1 have not been reproduced in comparisons against Inductively Coupled Plasma (ICP) torch spectra and CEA-SPECAIR simulations, nor do they exist for all test gases. This observation warrants a more detailed investigation into the shock tube air tests, to identify the origins of the discrepancies and improve upon them where possible. This is the fundamental objective of the current paper.



(a) T6s207: 6.64 km/s, 107 Pa fill



(b) EAST-59-42: 8.09km/s, 40 Pa fill

Fig. 4.1 Experimental equilibrium spectral radiance in synthetic air captured in previous (a) T6 AST [69] and (b) EAST [45] campaigns. CEA-NEQAIR results in synthetic air have been convolved with appropriate instrument line shapes for comparisons.

Section 4.2 provides an overview of the test conditions achieved in the T6 Aluminium Shock Tube at LEO return speeds, along with the relevant emitting species of interest. Hydrodynamic effects through the test slug are briefly discussed in Section 4.3, validating the use of CEA to predict equilibrium compositions behind the shock fronts. The effect of

facility leaks and plasma cleaning of the AST walls is shown in Section 4.4, followed by an investigation into the optical setup, with a focus on the effect of reducing the spectrometer slit widths in Section 4.5. A series of alternative radiation models are trialled in Section 4.6, and the condition dependency of remaining ultraviolet equilibrium offsets shown in Section 4.7. Finally, examples of the new improved agreements between synthetic and pure nitrogen equilibrium spectra to CEA-NEQAIR predictions are provided in Section 4.8. This work ultimately provides a new low-speed dataset of synthetic air and pure nitrogen shots, with reliable equilibrium spectral radiance measurements, enabling future studies to investigate the additional complication of chemical kinetics (in the non-equilibrium region) with more certainty.

4.2 Experimental Campaign

The T6 Stalker tunnel (T6) is a multi-mode high-enthalpy transient ground test facility at the University of Oxford. The Aluminium Shock Tube (AST) mode of operation enables reproduction of the stagnation line ahead of a hypersonic vehicle, up to the boundary layer edge. Comprehensive descriptions of the facility, its operation and the telecentric Optical Emission Spectroscopy (OES) diagnostics have been given in Chapter 3.

4.2.1 Condition Map

A campaign to study low-speed synthetic air test slugs was conducted in the T6 AST during 2023. Figure 4.2 summarises the conditions achieved, along with their key motives. Early stages of the campaign involved repeating a series of tests at $\sim$7.1 km/s in 175 Pa of a synthetic air (20.9% O_2/ 79.1% N_2) test gas, while trialling different cleaning methods and spectral settings. A large portion of the data discussed in this paper is from these tests. An example shock speed profile for this condition is provided in Fig. 4.3. The latter phase of the campaign broadened the experimental scope, encompassing a wider range of shock velocities and pressures. These tests provide conditions with varying total enthalpies and relaxation rates, facilitating a deeper study of non-equilibrium phenomena. These will be used briefly in this paper, though only in the context of their equilibrium radiance. The conditions also extended into simplified pure nitrogen mixtures. While this paper focuses on the equilibrium results from tests in both phases of the campaign, future publications will delve into the thermochemical characterisation through the non-equilibrium regions.

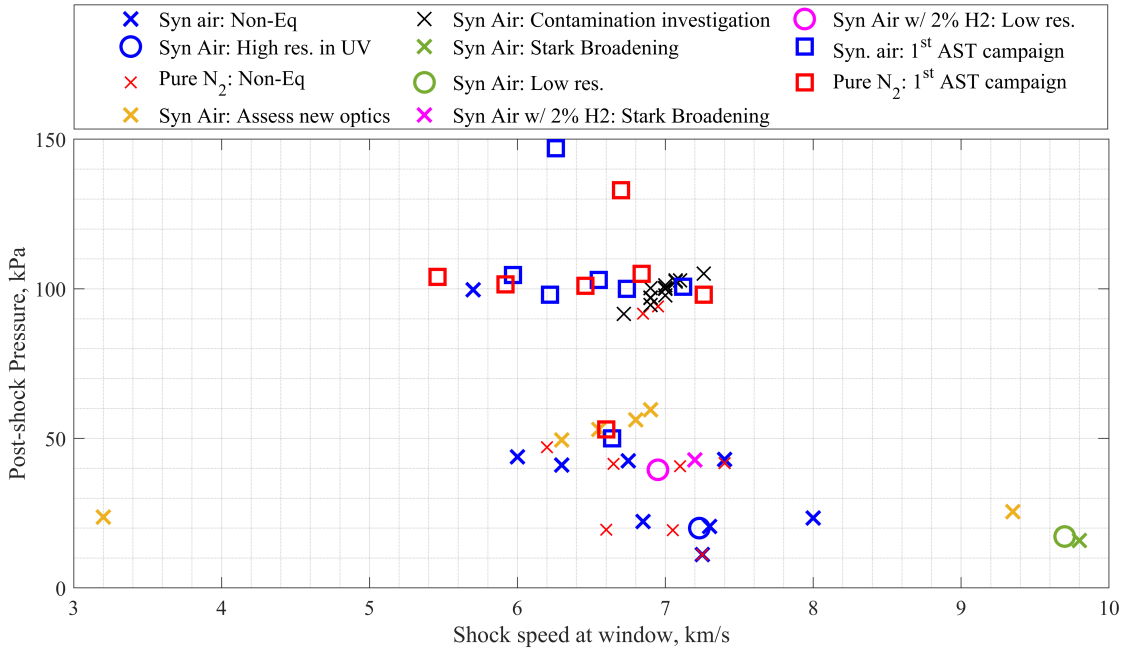


Fig. 4.2 Condition map of synthetic air and pure nitrogen shots from the recent T6 AST low-speed campaign. Shots from the original AST low-speed campaign are also included.

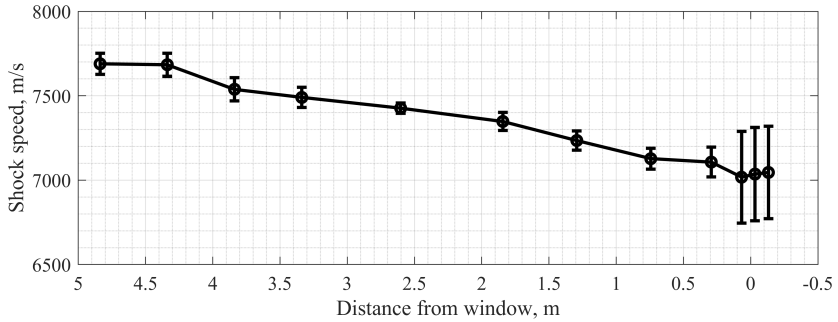
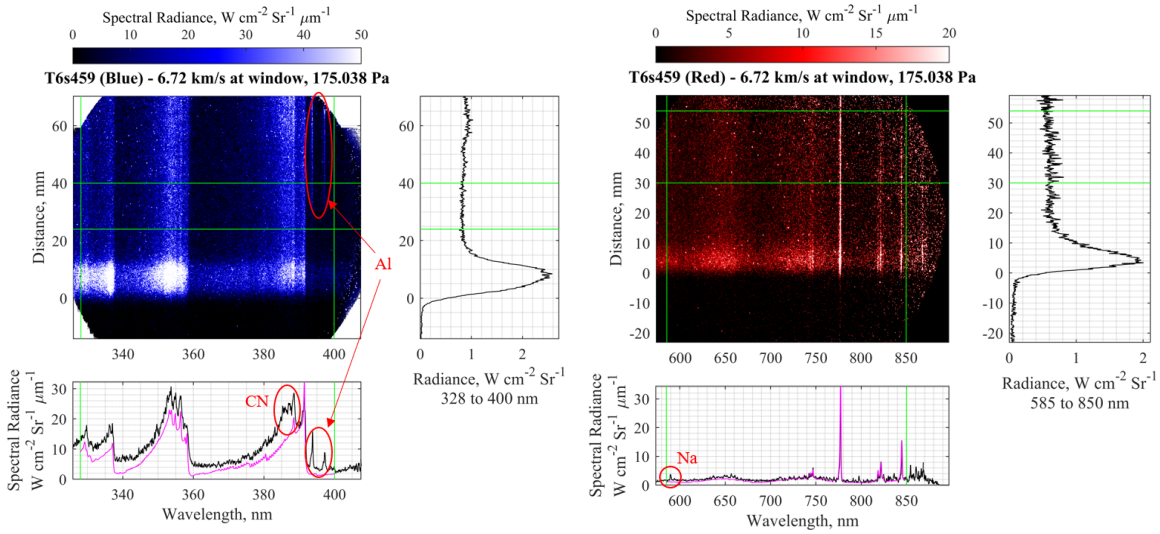


Fig. 4.3 Example shock speed profile typical of the nominal 7.1 km/s, 175 Pa, 1 bar post-shock condition targetted in the first stage of the campaign. Note that the shock trajectory is only shown for the AST section (after the conical expansion).

4.2.2 Calibrated Radiance Data

The telecentric OES arrangements provide spatially and spectrally resolved absolute radiance measurements of the post-shock test gas as it traverses the tube windows. Examples of the calibrated radiance data are shown in Fig. 4.4. Spatial axes are calibrated to a common datum, with the shock front located a 0 mm. The high resolution ultraviolet spectrum enables identification of both the CN violet band and atomic transitions from aluminium. Equilibrium spectral radiance plots are included below the 2D radiance maps, with CEA-NEQAIR predictions for comparison. The experimental equilibrium spectral profiles are attained by averaging the signal between the green horizontal lines, located after the non-equilibrium peak. Spatial radiance profiles are also shown to the right of the 2D radiance map. These are calculated by integrating the spectral radiance over the wavelength range indicated by the green vertical lines. This integration may be performed over any wavelength region, to capture the relaxation profile of different species, bands or atomic transitions. It's emphasised that all spectra plotted in this paper are acquired by averaging over the flat radiance plateau following the non-equilibrium peak immediately behind the shock, as illustrated in Fig. 4.4. This flat region implies a steady thermochemical state, which signifies the completion of thermal relaxation and chemical reactions, thus indicating that thermochemical equilibrium has been established. This was validated by comparing spectral traces averaged over the beginning and end of the plateau, to confirm their profiles agree. The exception of this behaviour is the case of some contaminant species which can show a spatial evolution through this region and are believed to emit from the growing boundary layer.

Table 4.1 summarises the spectral emission features that were detected during the low-speed T6 AST campaign, over both UV/Vis and Vis/NIR spectral channels. It shows the molecular bands and atomic transitions arising from the nitrogen and oxygen present in the test gas.



(a) T6s459 UV/Vis

(b) T6s459 Vis/NIR

Fig. 4.4 Calibrated spatio-spectral radiance data for T6s459 (6.72km/s, 175 Pa fill in synthetic air). Horizontal lines indicate spatial region averaged over to generate spectral radiance plot. Vertical lines indicate wavelength region integrated over to generate spatial radiance profile. CEA-NEQAIR spectral radiance prediction in synthetic air provided for comparison (in pink).

Table 4.1 Summary of test gas transitions observed in the new T6 AST low-speed synthetic air dataset, over the UV/Vis and Vis/NIR wavelength regions.

Name	**Transition**	**Region of emission**
NOγ	$A^2\Sigma^+ \rightarrow X^2\Pi$	200–400 nm
NOβ	$B^2\Pi \rightarrow X^2\Pi$	200–400 nm
NOδ	$C^2\Pi \rightarrow X^2\Pi$	200–280 nm
NOε	$D^2\Sigma^+ \rightarrow X^2\Pi$	200–280 nm
NOγ'	$E^2\Sigma^+ \rightarrow X^2\Pi$	200-400 nm
NOβ'	$B'^2\Delta \rightarrow X^2\Pi$	200-400 nm
N_2 first positive	$B^3\Pi_g \rightarrow A^3\Sigma_u^+$	500–1100 nm
N_2 second positive	$C^3\Pi_u \rightarrow B^3\Pi_g$	250–450 nm
N_2^+ first negative	$B^2\Sigma_u^+ \rightarrow X^2\Sigma_g^+$	300–450 nm
N_2^+ Meinel (A-X)	$A^2\Pi_u \rightarrow X^2\Sigma_g^+$	500–900 nm
N	$3p^4S \rightarrow 3s^4P$	744.2 nm
	$3p^4S \rightarrow 3s^4P$	746.8 nm
	$3p^4P \rightarrow 3s^4P$	821.6 nm
O	$3p^5P \rightarrow 3s^5S$	777.2 nm
	$3p^3P \rightarrow 3s^3S$	844.6 nm

4.3 Hydrodynamic Investigation

All numerical predictions of the equilibrium spectral radiance in this paper are generated via CEA-NEQAIR simulations, using the initial fill conditions and measured shock speed as it was imaged by the OES arrangements and assuming Boltzmann distributions. However, the presence of compression effects from the growing boundary layer and the influence of shock speed variations during a given test can introduce pressure and enthalpy variations through the test slug [126, 153, 152]. The effect of these in the context of the equilibrium offset has already been investigated in the prior works of Glenn et al [69] from the original low-speed air AST campaign, by performing comparisons against LASTA-NEQAIR simulations. LASTA is an in-house post-shot analysis code to account for the shock speed and compression effects [170]. Results can be fed into NEQAIR as a line of sight to predict the consequent radiance spatial variations, as shown in Fig. 4.5 for T6s198[2]. It's apparent from Fig. 4.5 that although these effects cause some increase in radiance towards the end of the test slug, it is negligible in comparison to the overall discrepancies. Since the T6s198 shock speed profile shows typical levels of shock speed variation for low-speed T6 AST tests, the CEA-NEQAIR comparisons used in the remainder of this paper are therefore deemed to be an appropriate reference to compare to the experimental equilibrium spectra.

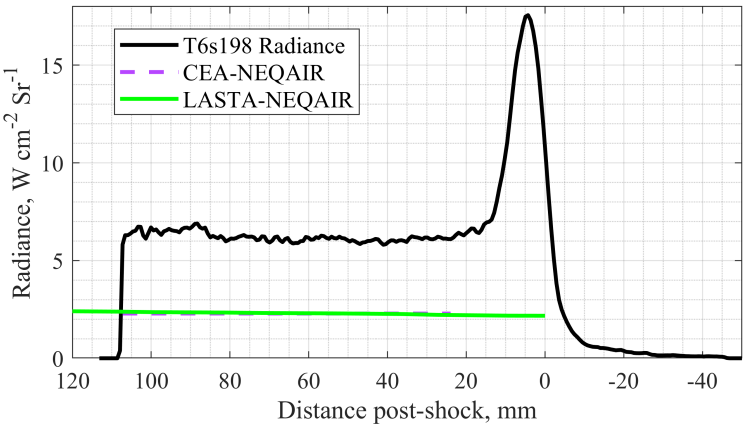


Fig. 4.5 Experimental ultraviolet radiance profile from T6s198 (6.55 km/s in 213.9 Pa synthetic air) compared to CEA-NEQAIR and LASTA-NEQAIR predictions. Adapted from Glenn et al. [69].

[2]Note that the simulation if Fig. 4.5 was run using version 1 of the LASTA code, which only performed equilibrium predictions, and thus does not produce a non-equilibrium peak.

4.4 Contamination Investigation

The next stage of this study investigates the contaminants observed in emission spectra acquired in the recent T6 AST low-speed campaign. Sources of contaminants in the test flow during standard operation can be summarised into three main categories: 1. leaks from the ambient air into the facility test volume; 2. outgassing from the tunnel walls while at low vacuum pressures; 3. particulate contaminants present on the tunnel walls. In the case of air experiments, the primary concern of the first two is the introduction of CO_2 and H_2O vapour into the test gas, enabling production of hydrocarbon species. In particular, the CN violet band emits intense UV radiation, which superimposes with the $N_2{}^+$ first negative band and is used as the parameter to gauge contaminant levels in this study.

Various particulate contaminants may be present on the tube walls. Matter builds up over time through standard use by a number of means, including: vapourisation of Mylar secondary diaphragms; trace amounts of capstan nut and o-ring greases permeating into the test volume; and piston buffer material blasting down the tube. Rigorous cleaning methods have been implemented to remove contaminants from the walls and achieve closer to "clean" test data. These are explained in the following subsections. Table 4.2 summarises the main contaminants that were observed and able to be identified during the recent AST campaign. A host of other contaminant species will likely also be present in the high-enthalpy test gas, though were not detectable using the OES systems.

Table 4.2 Summary of contaminant transitions observed in the new T6 AST low-speed dataset, over the UV/Vis and Vis/NIR wavelength regions.

Name	**Transition**	**Region of emission**
CN violet	$B^2\Sigma^+ \rightarrow X^2\Sigma^+$	350–430 nm
Aluminium	$3p^2P \rightarrow 4s^2S$	394, 396 nm
Hα (Balmer-alpha)	$3 \rightarrow 2$ (n=3 $\rightarrow$ n=2)	656.3 nm
Hβ (Balmer-beta)	$4 \rightarrow 2$ (n=4 $\rightarrow$ n=2)	486.1 nm
Sodium D Line	$3p\ ^2P \rightarrow 3s\ ^2S$	589.0–589.6 nm
NH	$A^3\Pi \rightarrow X^3\Sigma^-$	300–340 nm

4.4.1 Contaminant Gauging

The cyano-radical (CN) contaminant radiates intensely in the ultraviolet for the low-speed test conditions selected for study in this paper. It is therefore used as the parameter to gauge the amount contamination present across a range of tests. This spectral feature, along with atomic C and H transitions has been used in the work of Cruden et al. [39] to assess the performance of upgrades in the EAST facility in 2009. However, these authors performed tests at 10 km/s in 0.2 Torr air, which is relevant to peak heating lunar return conditions. The atomic C and H transitions are not observable at the lower speeds considered in this paper (except for the Hα line in some of the non-equilibrium spectra) and thus the CN provides the more appropriate reference. Analyses here and in later sections of this paper have performed spectral fitting of equilibrium ultraviolet spectra to extract the CN contaminant number densities and deduce their contribution to overall radiance levels. Tables 4.3 and 4.4 provide a summary of the conditions referred to later and their spectral fitting results. Information pertinent to the discussions in the following sections will be repeated or plotted when needed. Uncertainties in Table 4.4 are extracted from a Monte Carlo analysis. Contaminants NH and aluminium (Al) were also included in the spectral fits but were extracted with much less certainty due to their weaker radiance contributions.

Table 4.3 Summary of condition parameters for selected tests, split into high resolution ultraviolet spectra (top) and low resolution spectra (bottom).

Shot No.	**$U_{s,\,window}$, km/s**	**P_1, Pa**	**$P_{2,\,meas}$, kPa**	**Leak Rate, mPa/s**	**Res.**
T6s461	6.9	175	97.1	1.7	High
T6s462	6.9	175	94.6	20	High
T6s474	7	175	97.8	0.9	High
T6s501	7.25	20.0	20	0.9	High
T6s464	7.0	175	100.0	0.6	Low
T6s465	7.0	175	101.2	1.0	Low
T6s476	7.4	71.6	43	1.0	Low
T6s484	7.3	33.3	20.6	0.7	Low
T6s491	7.25	18	11.2	1.4	Low

Table 4.4 Summary of temperatures and number densities extracted by spectral fitting of the ultraviolet spectra for tests studied in this paper. CEA predictions are provided for comparison. Results are split into high resolution spectra (top) and low resolution spectra (bottom) as provided in Table 4.3. Uncertainties are extracted from a Monte Carlo analysis.

Shot		T_{CEA}, K	N_2, cm^{-3}	N_2^+, cm^{-3}	NO, cm^{-3}	CN, cm^{-3}	NH, cm^{-3}	Al, cm^{-3}
T6s461	Fit	6860	$4.7\pm0.2\times10^{17}$	$1.9\pm0.3\times10^{13}$	-	$2.9\pm0.09\times10^{12}$	$8.6\pm8.4\times10^{11}$	$5.3\pm2.1\times10^{10}$
	CEA		2.81×10^{17}	1.50×10^{13}	3.16×10^{15}	0	0	0
T6s462	Fit	6860	$4.8\pm0.4\times10^{17}$	$1.8\pm0.06\times10^{13}$	-	$6.5\pm0.2\times10^{12}$	$1.1\pm1.0\times10^{12}$	$8.5\pm8.1\times10^{10}$
	CEA		2.8×10^{17}	1.5×10^{13}	3.1×10^{15}	0	0	0
T6s474	Fit	6950	$5.5\pm0.5\times10^{17}$	$2.5\pm0.1\times10^{13}$	-	$2.6\pm0.4\times10^{12}$	$3.4\pm3.4\times10^{11}$	$6.1\pm4.0\times10^{10}$
	CEA		2.7×10^{17}	1.8×10^{13}	3.0×10^{15}	0	0	0
T6s501	Fit	6480	$3.5\pm2.1\times10^{16}$	$3.0\pm0.4\times10^{12}$	-	$6.0\pm0.2\times10^{12}$	$5.1\pm1.6\times10^{11}$	$2.4\pm1.8\times10^{10}$
	CEA		4.85×10^{16}	2.42×10^{12}	3.22×10^{14}	0	0	0
T6s464	Fit	6930	$3.4\pm1.3\times10^{17}$	$2.3\pm0.5\times10^{13}$	$6.6\pm0.1\times10^{15}$	$1.4\pm0.7\times10^{12}$	$3.6\pm3.5\times10^{11}$	$5.4\pm5.2\times10^{12}$
	CEA		2.7×10^{17}	1.7×10^{13}	3.0×10^{15}	0	0	0
T6s465	Fit	6950	$3.1\pm1.3\times10^{17}$	$2.2\pm0.4\times10^{13}$	$5.6\pm0.1\times10^{15}$	$2.9\pm1.5\times10^{12}$	$4.0\pm3.8\times10^{11}$	$4.6\pm4.5\times10^{10}$
	CEA		2.68×10^{17}	1.85×10^{13}	3.03×10^{15}	0	0	0
T6s476	Fit	6850	$1.2\pm0.6\times10^{17}$	$9.5\pm1.4\times10^{12}$	$1.6\pm0.04\times10^{15}$	$2.8\pm0.7\times10^{12}$	$3.1\pm3.0\times10^{11}$	$1.4\pm1.1\times10^{10}$
	CEA		9.51×10^{16}	8.58×10^{12}	8.21×10^{14}	0	0	0
T6s484	Fit	6540	$1.0\pm0.4\times10^{17}$	$4.0\pm0.4\times10^{12}$	$6.2\pm0.2\times10^{14}$	$2.7\pm1.7\times10^{12}$	$9.1\pm9.1\times10^{10}$	$5.2\pm4.1\times10^{9}$
	CEA		4.6×10^{16}	2.7×10^{12}	3.1×10^{14}	0	0	0
T6s491	Fit	6290	$2.7\pm0.6\times10^{16}$	$8.8\pm2.8\times10^{11}$	$1.5\pm0.2\times10^{14}$	$2.6\pm0.1\times10^{12}$	$9.4\pm3.0\times10^{10}$	$5.0\pm1.0\times10^{9}$
	CEA		2.6×10^{16}	1.0×10^{12}	1.4×10^{14}	0	0	0

4.4.2 Leak Rates and Manual Cleaning

Previous studies have investigated the effect of facility cleanliness on measurements performed in high-speed facilities. Particularly in the context of boundary-layer transition studies [94], where it has been demonstrated that particulate contamination is very effective in promoting free-stream disturbances and consequently transition [22, 154]. In the context of radiation measurements, transition isn't the concern but particulates from contaminants can still distort data. The methods documented from other high-speed facilities have thus been adopted to the T6 AST to help achieve clean results. The steps of the standard manual cleaning procedure are summarised below. Pipe cleaning "pigs" of different sizes and stiffnesses were trialled to optimise the process.

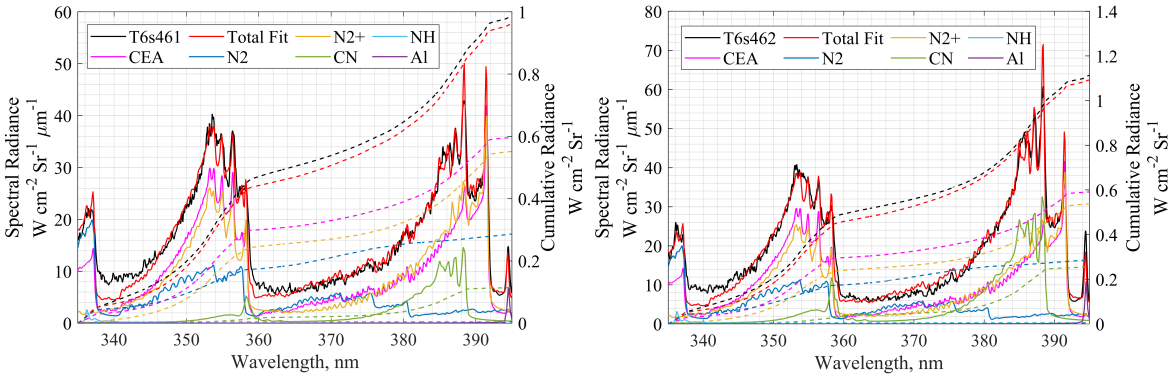
1. Pipe cleaning foam cylindrical pig is coated in acetone and pulled through shock tube (forwards and backwards being one pass)

2. Process is repeated until a new clean pig comes out clean after at least one pass (can be as many as 20 times)

3. Process is repeated again with pig coated in isopropyl alcohol to remove any acetone residue (typically 5 to 10 passes)

4. The ends of each tube are cleaned by hand with optical wipes, particularly around windows, with the same sequence of solvents.

Figure 4.6 plots the high resolution optical emission spectra acquired from two equivalent test cases, as summarised in Table 4.5. The spectral fit and associated components are plotted for comparison, along with the CEA-NEQAIR predictions. The leak rate into the test volume is routinely measured while at ultimate vacuum pump down pressure, before filling with the test gas. T6s462 was performed with a leak rate one order of magnitude higher than T6s461, which provides a reference for the contaminant levels with typical leak rates and the standard manual cleaning procedure. The spectral fit outputs indicate that multiplying the leak rate by 10 results in double the measured CN emission (and consequent number densities, due to an optically thin test gas). This confirms that leaks into the facility provide a mechanism to produce CN contaminants, confirming the importance of excellent sealing around the facility components and pipework. Additionally, since the considered test gas is very close to an optically thin mixture, one would expect that 10 times the leak rate would produce 10 times the CN contaminant, if leaks were the sole source of CN. The non-proportional increase therefore suggests another source of CN must be present. Plasma cleaning of the test volume walls was therefore trialled, as discussed in the following section.



(a) T6s461: 1.7 mPa/s leak rate

(b) T6s462: 20 mPa/s leak rate

Fig. 4.6 Spectral fit profiles and associated individual contributions over 335 to 395 nm for tests summarised in Table 4.5. CEA-NEQAIR predictions are also shown for comparison.

Table 4.5 Comparison of repeat shots T6s461 and T6s462 in 175 Pa synthetic air. CN radical radiance contributions and number densities are as extracted from spectral fits.

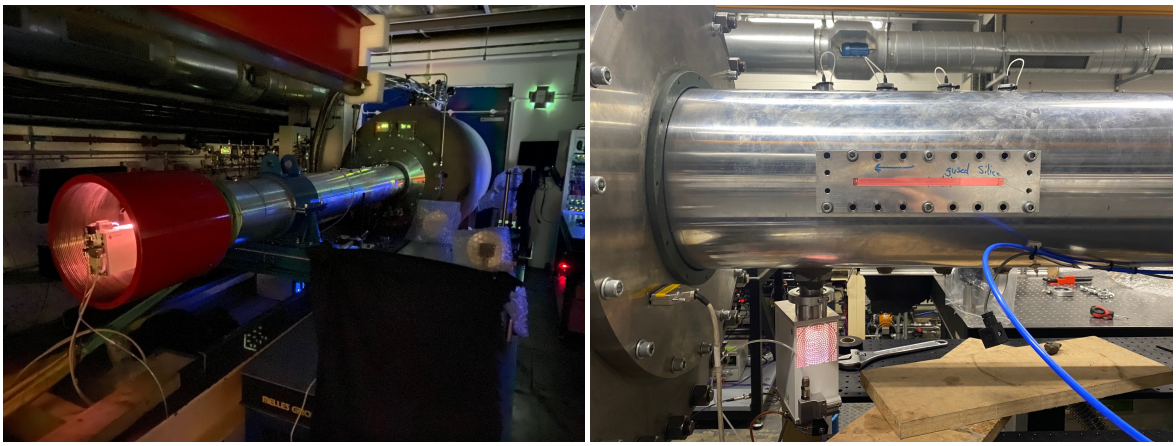
Shot No.	**U_s, km/s**	**Leak Rate, mPa/s**	**CN contribution, % (335-395nm)**	**CN no. density, cm^{-3}**
T6s461	6.9	1.7	11.6	2.9×10^{12}
T6s462	6.9	20	22.9	6.5×10^{12}

4.4.3 Plasma Cleaning

A GV10x 300W Downstream Asher from ibss Group Inc. was trialled during the campaign. This system produces oxygen (O) radicals which are transported into the shock tube via a pressure differential, to oxidise hydrocarbon species that they come into contact with (in a gaseous or solid state). Previous work from Cruden et al. [39] demonstrated that application of a similar system to the EAST test volume reduced the contaminant levels by removing hydrocarbons from the tunnel walls. This was therefore repeated in the T6 AST to assess if the same result may be achieved.

The products of oxidation reactions due to the plasma cleaning process (e.g. CO, CO_2, H_2O) are continually pumped out of the tunnel. Effective operation requires a high concentration of radicals, transported uniformly throughout the chamber. This was achieved by maintaining pressures of 2 to 20 Pa in the evacuated test volume. Only the final 2 m section of the AST was plasma cleaned during these tests, to assess if a noticeable difference can be seen over any spatial region in the captured radiance data. Figure 4.7 shows images of the plasma cleaner mounted to the upstream and downstream end of the final 2 m section of the AST. In both configurations, a pressure differential was generated that encouraged particles to travel along the tube. Visual identification of the reach of the plasma, from its glow inside the tunnel, was used to confirm that the combination of these two configurations enabled the O radicals to reach all portions of the final 2 m section of AST. The plasma cleaning process was only ever performed following the manual clean, to attempt to remove remaining contaminants on an atomic level. Long operation times of 12 hours attached to the upstream end (imaged in Fig. 4.7a) and 8 hours on the downstream end (imaged in Fig. 4.7b) were trialled.

Table 4.6 summarises the tests used to evaluate the effect of plasma cleaning, in both low and high resolution ultraviolet equilibrium spectra. The associated spectral fit plots are provided in Fig. 4.8 for the two tests which used the plasma cleaner. Although a reduction in CN contaminant levels is realised from the plasma-cleaned tests, it is not enough to warrant "clean" spectra. Additionally, the CN contaminant levels correlate to the measured leak rate



(a) Upstream (b) Downstream

Fig. 4.7 Implementation of GV10x 300W Downstream Asher from ibss Group, Inc. to the final 2 m section of AST on both (a) upstream and (b) downstream ends.

in the facility before firing and there are no improvements in the large discrepancy below 300 nm where NO dominates. This makes it hard to assess if the CN removal was in fact due to the plasma cleaning or just the effect of reduced leak rates. With this result, and considering the significant increase in turnaround time between shots when using the plasma cleaner, it was determined that relying on the manual cleaning process would provide the most efficient approach for the remainder of the campaign.

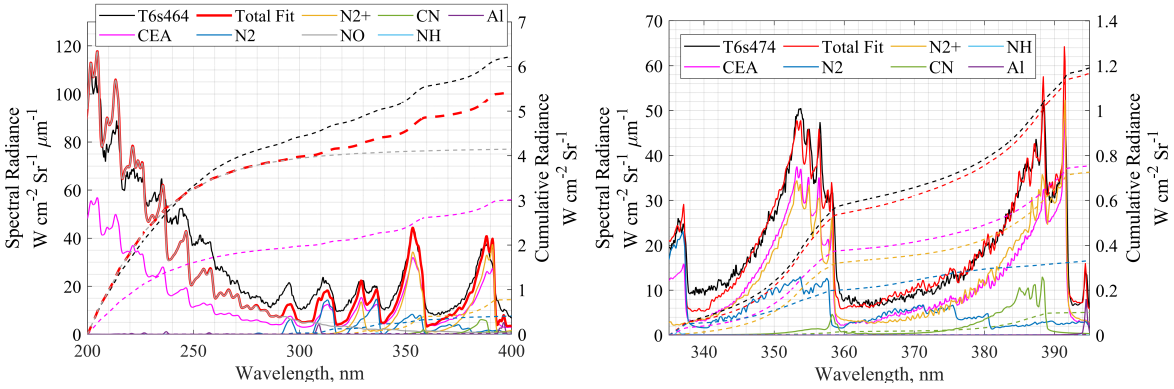
Table 4.6 Summary of shots to assess effect of plasma cleaning. Shock speeds quoted are at the window, all conducted in a 175 Pa test gas. Leak rate is measured once the facility is re-assembled and pumped down to ultimate pressure.

Shot No.	**U_s, km/s**	**Plasma?**	**Resolution**	**Leak Rate, mPa/s**	**CN radiance, % (335-395nm)**
T6s464	7.0	✓	Low	0.6	5.7
T6s474	7.0	✓	High	0.9	8.5
T6s465	7.0	×	Low	1.0	9.8
T6s461	6.9	×	High	1.7	11.6

This result is in some contrast to the findings of Cruden et al. [39] in the EAST facility at 10 km/s conditions, which showed significant reduction in CN by plasma cleaning. Possible reasons for this may be due to the different driver technologies. EAST uses a very powerful arc discharge driver, which deposits fluorocarbon contaminants down the tube from the discharge liner during each shot. Alternatively, the different tube diameters and pumping equipment may result in different rates of CO_2 and H_2O vapour outgassing from the tunnel walls. These molecules are adsorbed into the tube walls while at atmospheric pressure

between shots. Future experiments in T6 AST may try heating of the test volume walls to test if this improves the rate of outgassing, therefore reducing contaminants (as conducted at the EAST facility).

The key conclusion from this contamination study is that, while CN contamination is present in the flow and may be reduced by lowering the leak rate, it does not contribute to the discrepancies observed at the lower wavelengths, where NO bands dominate.



(a) T6s464: Low res.

(b) T6s474: High res.

Fig. 4.8 Low and high resolution ultraviolet spectra after plasma cleaning the final 2 m section of AST. Spectral fitting is used to provide estimates of CN contributions, as listed in Table 4.6.

4.4.4 Excess Free Electrons

One theory for the excess background continuum signal that has been discussed in the literature, is an excess of free electrons in the flow [46]. Yamada [196] quotes an order of magnitude higher electron number densities measured in shocked argon via Stark broadening, compared to equilibrium predictions. The presence of sodium atoms, which are easily ionised, is speculated as one possible cause for this excess of electrons. Figure 4.9 shows the effect of increasing the N^+ and E^- number densities by a factor of 30, for predictions of equilibrium spectral radiance in recent low-speed T6 AST air tests. This increases the atomic N bound-free radiation level predicted by the NEQAIR radiation model and improves agreement from 300 to 400 nm, however it's evident there's still a discrepancy below 300 nm, where NO radiates, and a worse agreement is demonstrated across the entire visible/near-infrared region. This scale factor is also comparable to the factor of 50 applied in the work of Tibère-Inglesse and Cruden [187]. Alternative combinations involving O^+ and E^- were also trialled and showed that varying levels of background emission can be produced, but they are all weighted towards the higher wavelengths, rather than the lower (where the dominant

discrepancies exist). Simulations were also trialled including Na and Na^+ species, however Na bound-free and free-free modelling is not implemented in the NEQAIR v15.1 code used in this work. Ultimately, this analysis shows that electron and ion number densities can affect the background radiance levels, but not significantly at the lower wavelengths where the main discrepancies are present. Additionally, it makes agreement with experimental data at the higher visible/near infrared wavelengths much worse. Measurements of electron number densities in future campaigns would be the best way to validate if this analysis is worth pursuing further.

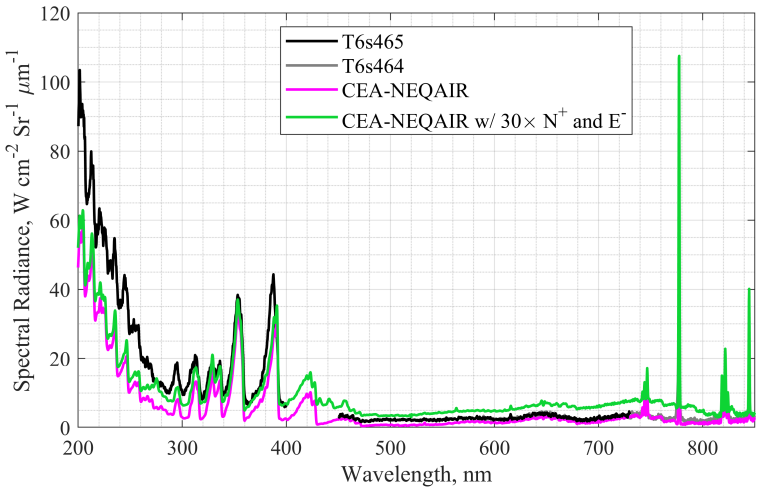


Fig. 4.9 Equilibrium spectra from T6s465 and T6s464 (both at 7 km/s, 175 Pa, 101.2 kPa post-shock) with CEA-NEQAIR predictions for different N bound-free background levels.

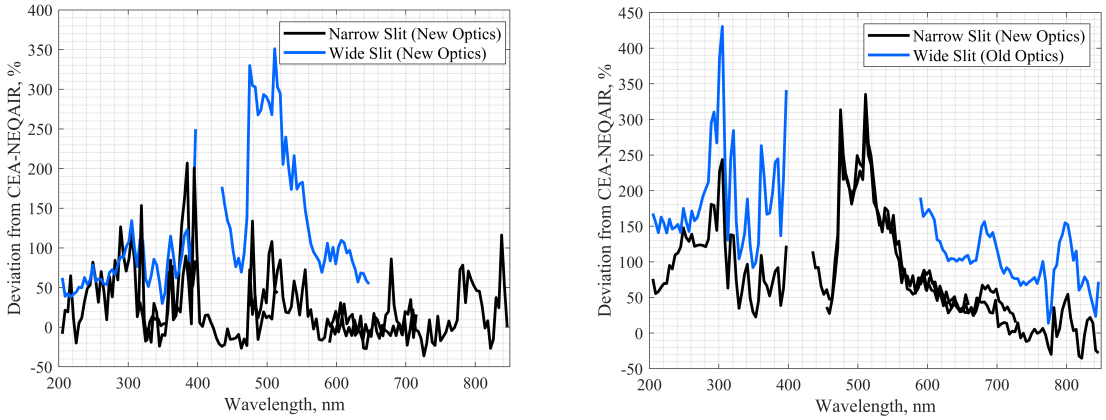
4.5 Optical Setup and Processing

4.5.1 Spectrometer Slit Width

The next step in this study considers the spectrometer slit widths. There is a constant compromise in any OES system between signal and resolution. Along the spectral axis, these are mostly determined by: the resolution of grooves in the diffraction grating installed in the spectrometer; and the width of the spectrometer slit, which radiation is focused into. When designing the optical path, it's important that the f-number of light rays entering the spectrometer slit is larger than the f-number of the focusing mirror collecting and collimating the light inside the spectrometer. Additionally, the optical path should enter the spectrometer perpendicular to the plane of the slit. These steps ensure all light entering the spectrometer lands on the initial focusing mirror and follows the intended optical path inside

the spectrometer. Multiple reflective surfaces and a diffraction grating inside the spectrometer casing provide opportunities for light rays to take an alternative path to the camera sensor array, in addition to the intended optical path. These internal reflections result in a "stray light" background signal in the spatio-spectrally resolved images acquired by the OES system. Steps during the calibration procedure are taken to characterise and remove stray light, as is shown in Section 4.5.3. However, opportunities for stray light can be minimised by ensuring all incident rays land on the initial focusing mirror inside the spectrometer.

During the trials with different spectrometer settings, to investigate stray light, it was determined that setting the slit widths of both the Blue and Red Isoplane 320 spectrographs to their minimum of 10 μm significantly reduced the experimental background signal, resulting in better agreement with CEA-NEQAIR predictions. Figure 4.10 presents equilibrium data across a series of tests at similar conditions with varying slit widths for the new telecentric OES systems (in Fig. 4.10a) and telecentric vs telescopic (in Fig. 4.10b). The data has been normalised with respect to the CEA-NEQAIR predictions to enable comparisons across shots. The telescopic OES systems used in previous T6 AST campaigns had wider slit widths of 170 μm and 100 μm in the Blue and Red channels respectively. These widths were applied for a single shot in the telecentric OES arrangements, to compare against the results from shots using the narrow 10 μm slits, to see if the increased offset from CEA-NEQAIR predictions could be replicated when all other aspects of the optical arrangement remain the same.



(a) Telecentric only

(b) Telecentric and telescopic

Fig. 4.10 Comparison of measured equilibrium spectral radiance normalised by CEA-NEQAIR predictions. (a) Data from 6.5–7.4 km/s with 40–50 kPa post-shock pressures, using telecentric OES. (b) Comparison of telecentric vs. telescopic OES at 7.1 km/s, 100 kPa. "Narrow" slits are 10μm, and "wide" slits are 170μm (Blue) and 100μm (Red).

The results shown in Fig. 4.10 suggest the wider slit widths produce a larger continuum background offset above the CEA-NEQAIR predictions, for both OES arrangements. This is believed to be a result of the narrower slit width restricting the incident rays from entering the spectrometer and thus reducing stray light signals. It's evident in both Fig.'s 4.10a and 4.10b that a more drastic improvement is made in the higher wavelengths, with offsets almost disappearing completely when using a 10 μm slit width. The remaining discrepancies in the ultraviolet wavelengths are studied in the following sections.

4.5.2 Telecentric vs Telescopic

For a given diffraction grating, a narrower slit width restricts the column of light entering the spectrometer and produces narrower spectral lines along the camera array, improving the resolution between the emission features. However, this is at the sacrifice of signal and thus puts harsher limits on the achievable signal levels in the intensified cameras for the low-speed conditions considered. The iris between the two focusing mirrors (prior to rays entering the spectrometer) can be used to adjust resolution along the spatial axis, analogously to the spectrometer slit for the spectral axis. After the improvement in equilibrium spectral agreement was realised by using narrower spectrometer slit widths, the 10 μm slits were maintained for all remaining tests. However, for the relatively low radiance emission of the low-speed conditions considered, this put the intensified cameras at the limit of their capability, in terms of workable signal levels. The iris between the two focusing mirrors was therefore kept fully open for most tests to achieve the best possible signal, at the sacrifice of optimum spatial resolution. The optical smear function (OSF) is a component of the SRF, which has been characterised for both the new telecentric and old telescopic OES arrangements. These were previously plotted in Fig. 3.14 to demonstrate that despite the full spatial resolution capabilities of the new telecentric optics not being utilised, the optical smearing component is still an improvement on the previous telescopic arrangements.

4.5.3 In-Test Stray Light Measurements

Measurements of stray light signal through different portions of the test slug were also conducted in this work, after implementing 10 μm slit widths. In theory, stray light should be measured at a location on the camera sensor array that corresponds to a spatial or spectral region with no radiation emission source, and sufficiently far from the SRF or ILS smearing effects. Cruden [41] provides a comprehensive review of the stray light removal methodology performed in EAST data, which has been adopted for all prior AST spectra generation. This involves gauging the stray light levels by looking ahead of the shock front. No radiation

emission signal should be present there due to negligible precursor effect at the considered low speeds and black surfaces on the window holders to negate reflections for opposing optical arrangements (as shown in Fig. 4.11). The stray light signal is fit with a third order polynomial spline function, to capture the signal profile and remove any spurious noise spikes. This spectral profile is assumed to be constant across the entire spatial FOV on the intensified camera array and is subtracted from the raw measured signal in all pixel rows.

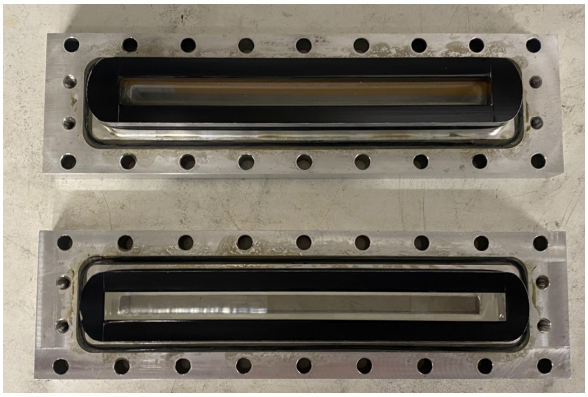
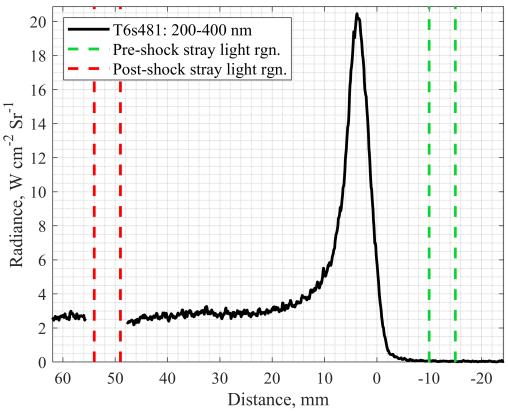
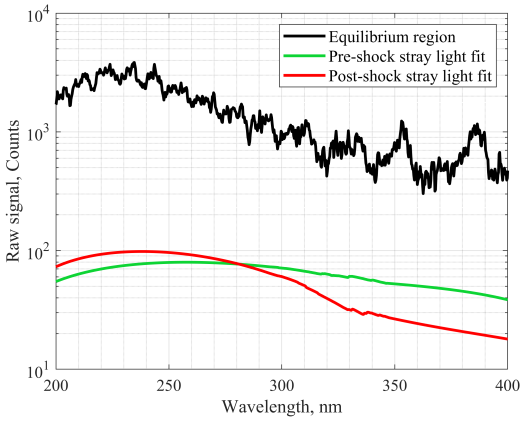


Fig. 4.11 Image of window holders installed into AST test section. Black surfaces are flush with tube inner wall to remove reflections in opposing spectral images.

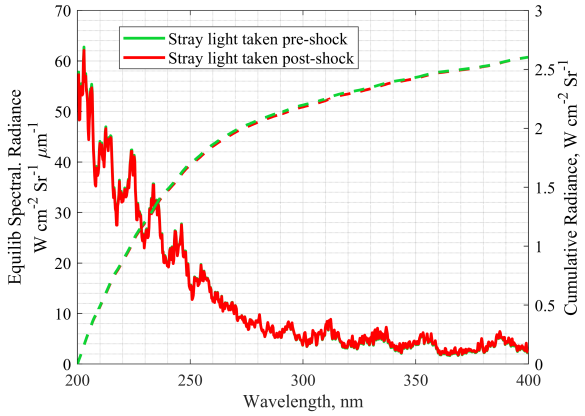
To validate if the assumption of the stray light signal spatial independence is correct, small spatial regions were blocked in the ultraviolet spectral channel so that the stray light signal post-shock could also be measured. A strip of plastic was used to block the radiation in the desired region at the window. Measurements of this are illustrated in Fig. 4.12. The gap in the radiance profile in Fig. 4.12a indicates the blocked signal region, which was purposely positioned away from the expected non-equilibrium peak location, to avoid losing any valuable post-shock relaxation information. The same third order polynomial spline fit was applied here to extract the corresponding stray light spectral profile. Figure 4.12b compares the pre- and post-shock stray light spectral profiles against the raw signal levels through the equilibrium portion of the radiance profile. Both stray light signal levels are significantly lower than signal in the equilibrium region, and show a gradual ramp up towards the lower wavelengths. This corresponds to pixel columns in the camera sensor array experiencing the most intense signal, from the NO bands. Despite slightly different profiles between the two stray light traces, negligible difference is realised after completing the calibration process, as shown by the resulting equilibrium spectral radiance profiles plotted in Fig. 4.12c.



(a) T6s481 radiance profile with pre- and post-shock stray light extraction regions.



(b) Spectral profile of raw signal in equilibrium region plotted with extracted stray light profiles.



(c) Calibrated equilibrium spectra afer taking pre- and post-shock stray light signals.

Fig. 4.12 Comparison of stray light levels taken pre- and post-shock and the resulting equilibrium spectra. Performed to the ultraviolet spectral channel of T6s481 (5.7 km/s, 261.1 Pa fill in synthetic air, 99.7 kPa post-shock).

4.6 Radiative Modelling

The previous sections of this paper indicate that despite improvements, a continuum offset remains at the lower wavelengths, between the experimental data and the equilibrium predictions. NO has various bands that radiate in this region, as listed in Table 4.1. Discrepancies between experiment and simulation could be due to an overpopulation of these excited states in the shock tube experiment. Alternatively, there may be other sources of radiation superimposing on these bands, that are not captured in the NEQAIR radiative modelling. The O_2 Schumann-Runge ($B^3\Sigma_u^- - X^3\Sigma_g^-$) bands also have transitions between bound levels that radiate in this wavelength region, though are dwarfed by the NO bands from typically $\sim$4000 K, as shown in previous plasma torch studies [102]. Recent works of Cruden and Tibère-Inglesse [42] incorporate cross-sections for O_2 photodissociation using the PyDiatomic code from the Australian National University [64], to improve NEQAIR agreement at test cases of $\sim$4 km/s and 10 Torr. This is to capture photodissociation and photorecombination of O_2, potentially occurring due to an increased population of higher rotational and vibrational levels at elevated temperatures [23, 99]. This new radiative modelling contribution has been trialled on the lowest speed and highest pressure synthetic air test case from the recent T6 AST campaign: T6s481 (5.7 km/s, 261.1 Pa fill and 99.7 kPa post-shock pressure). Figure 4.13 plots the spectral traces from NEQAIR predictions against that calibrated from the UV/Vis spectrometer. This demonstrates, for the shot where O_2 photorecombination would be most effective, that minimal improvement is achieved at these higher speeds and lower pressures. However, this does not completely invalidate that photodissociation and photorecombination may be contributing to the offset, since alternative cross-sections may improve agreement.

Also included in the plot is the effect of increasing the N bound-free emission, as was shown in Section 4.4.4. Here, the N^+ and E^- number densities were multiplied by 150, rather than 30 as used for previous 7 km/s case, to improve agreement above 300 nm. Additionally, simulation results using the SPECAIR [168, 102] radiative code are included in Fig. 4.13. Extensive analyses of spectra from inductively coupled plasma (ICP) torches have been performed to develop the SPECAIR radiative transport code for a range of high resolution ultraviolet and vacuum ultraviolet (VUV) datasets [121, 122]. However, the differences between experiments in ICP torches and shock tubes is yet to be explained. The largest difference between SPECAIR and NEQAIR predictions is in the NO region, demonstrating increased sensitivity to the radiative modelling at the lower wavelengths. Collectively, these comparisons demonstrate the radiative modelling used to generate equilibrium spectral predictions is an important consideration, though insufficient information is currently available to say if one is better than the other.

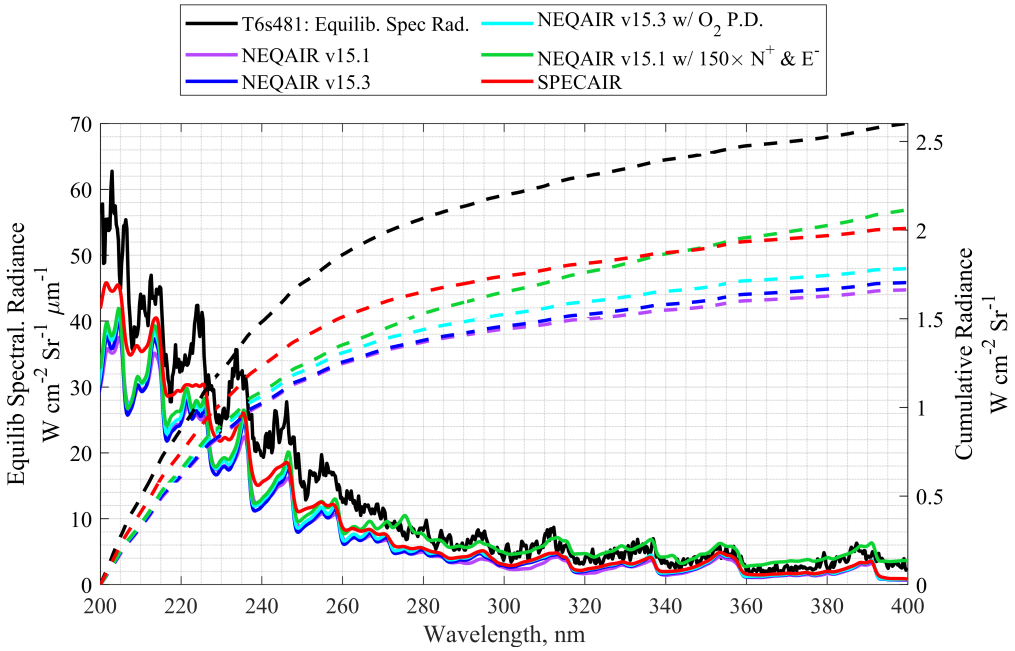


Fig. 4.13 Equilibrium ultraviolet spectral radiance of T6s481 (5.7 km/s, 261.1 Pa fill in synthetic air, 99.7 kPa post-shock). CEA simulation results were fed into NEQAIR and SPECAIR radiation codes. Attempts in NEQAIR using new O_2 photodissociation modelling [42] and increasing N bound-free emission are included. Dashed lines show cumulative radiance profiles on the right hand y-axis.

4.7 Condition Dependencies

4.7.1 Pressure

The preceding sections show that discrepancies still exist in the ultraviolet channel, particularly around the NO bands at lower wavelengths, between experimental and numerical equilibrium spectral radiance profiles. This section demonstrates the effect of post-shock pressure on these remaining offsets. Lower pressures also extend the non-equilibrium relaxation region, thus reducing the chances of reaching thermochemical equilibrium in the optics FOV. Figure 4.14 plots the ultraviolet spatial radiance profile for T6s491 - a 7.25 km/s shock with an 11.2 kPa post-shock pressure. This is the lowest pressure test from the recent campaign and thus has the longest relaxation profile. Figure 4.14 shows that despite the extended relaxation, a flat plateau is reached for the final $\sim$10 mm in the optics FOV. This suggests the lower pressure test cases to have useable equilibrium spectral radiance information, which is used in the following discussion. Spectral traces from the first and last third of this region were shown to coincide well, despite the relatively low S:N.

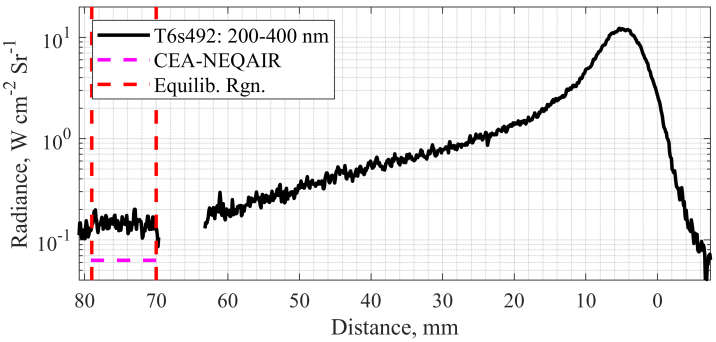
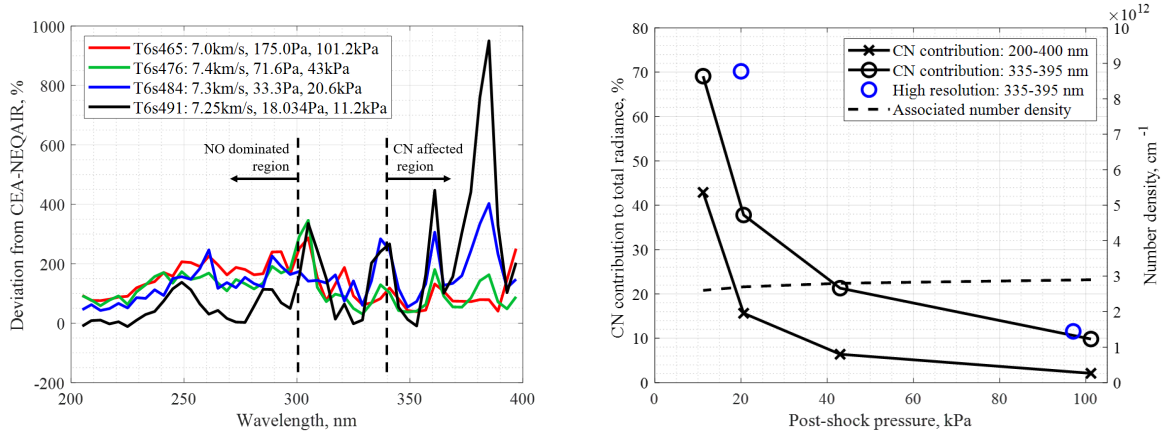


Fig. 4.14 Radiance profiles of lowest pressure synthetic air test: T6s491 (7.25 km/s, 18 Pa fill, 11.2 kPa post-shock). The relaxation profile displays a plateau at the end of the observable test slug, indicating valid thermochemical equilibrium data for the shot with longest relaxation time.

Figure 4.15a plots the normalised equilibrium spectral radiance traces for a series of synthetic air shots at a comparable shock speed but with post-shock pressures ranging from ∼10 to ∼100 kPa. The effect of pressure in these tests can be separated into two regions. From 340 to 400 nm, the CN contaminant violet band radiates intensely. It's evident in this region, that a higher pressure test results in closer agreement with CEA-NEQAIR. This effect is plotted as a function of post-shock pressure in Fig. 4.15b. The CN radiance contributions and associated number densities are calculated by spectral fitting of the ultraviolet emission spectra. It's apparent that the number density does not vary significantly across the range of tests, with only a small increase towards the higher pressure conditions. However, the CN contribution to the total radiance in the ultraviolet significantly increases for the lower pressure test cases due to CN number density making up a larger mole fraction of the test gas. This highlights the need for spectrally resolved radiance measurements to accurately characterise the emission levels in this region. Finally, equivalent shots with high-resolution spectra show close agreement to the quantities extracted in the low resolution ultraviolet spectra.

The normalised spectral profiles in Fig. 4.15a also suggest there to be a pressure dependence on the remaining continuum offset in the wavelengths below 300 nm, where NO dominates. This could be due to: incorrect use of the Boltzmann assumption in the NEQAIR radiative modelling; under prediction of NO number densities by CEA; calibration artefacts during the stitching of the Deuterium lamp calibration images; extra emission features unaccounted for in the NEQAIR radiative modelling; or increased bound-free contributions at higher pressures. The increased offset at lower wavelengths has been replicated in the EAST facility for comparable conditions [42], validating it across different facilities and OES



(a) Equilibrium spectral radiance deviations from CEA-NEQAIR predictions. All acquired using 10 μm slit widths.

(b) CN radiance contributions and associated number densities. Equivalent results from high resolution UV spectra also given to validate low resolution extraction of CN.

Fig. 4.15 Plots to assess the effect of post-shock pressure on remaining discrepancies in synthetic air ultraviolet equilibrium spectra, for shocks from 7 to 7.4 km/s.

arrangements. However, measurements in this region from an alternative optical diagnostic instrument would be a valuable addition to the dataset to confirm if this is truly a physical effect or the result of the calibration procedures used. Tunable diode laser absorption spectroscopy (TDLAS) is recommended as means to validate this in future experiments and is planned for upcoming T6 AST experiments. Regardless of the source, Fig. 4.15a for now demonstrates the apparent pressure dependence of ultraviolet equilibrium offsets and shows the advantage of low pressure test conditions in this region to achieve better agreement at lower wavelengths, at the compromise of signal levels and an increased fraction of CN radiation emission.

4.7.2 Shock Speed

A similar analysis has been performed to assess the ultraviolet offset at higher shock speeds. Figure 4.16 shows a comparison between tests of similar post-shock pressure, but with a 2 km/s delta between their measured shock speeds at the window. Both tests captured spectra using 10 μm spectrometer slit widths. It's evident the higher speed case has a significantly higher offset below 320 nm. Most the NO should have dissociated at 9.35 km/s, suggesting the background offset may be more likely from a bound-free background emission source. The peak at $\sim$248 nm is due to a strong atomic carbon line, which radiates intensely at the higher post-shock temperatures, and is not included in the CEA-NEQAIR simulations.

Conversely, the CN violet band makes up a smaller contribution at ∼380 nm. This shows the ultraviolet discrepancies discussed in the previous sections are not specific to low-speed air tests

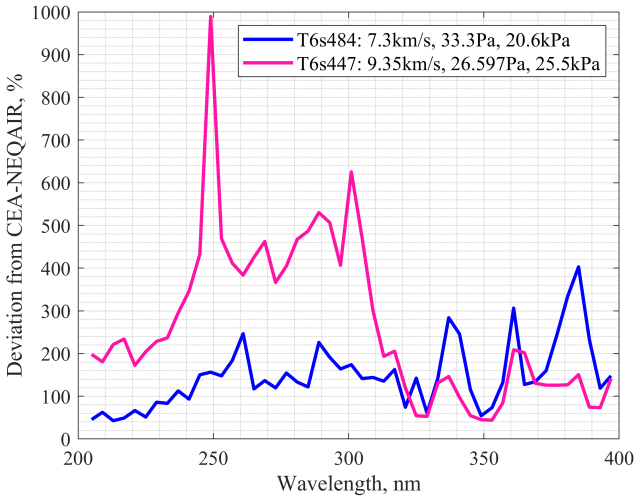
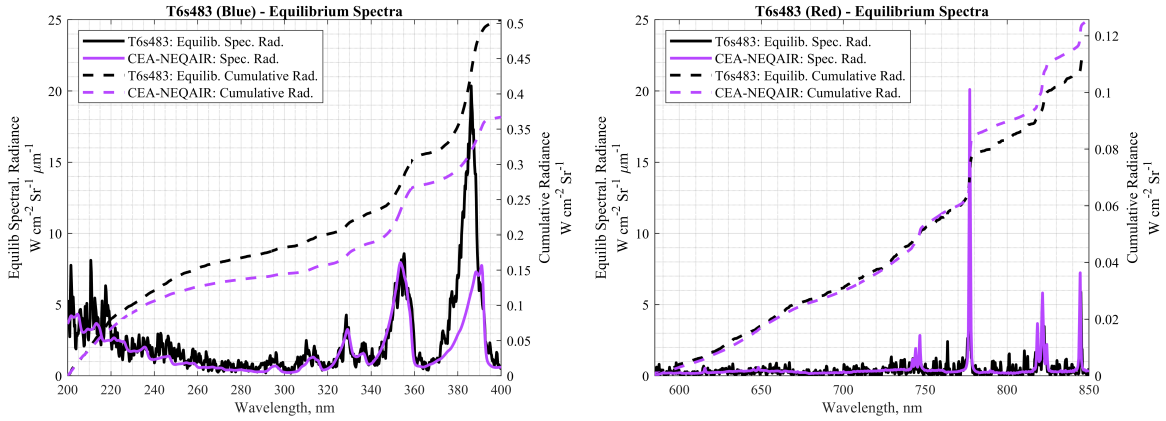


Fig. 4.16 Equilibrium spectral radiance deviations from CEA-NEQAIR predictions for synthetic air shots of similar post-shock pressure and different shock speeds.

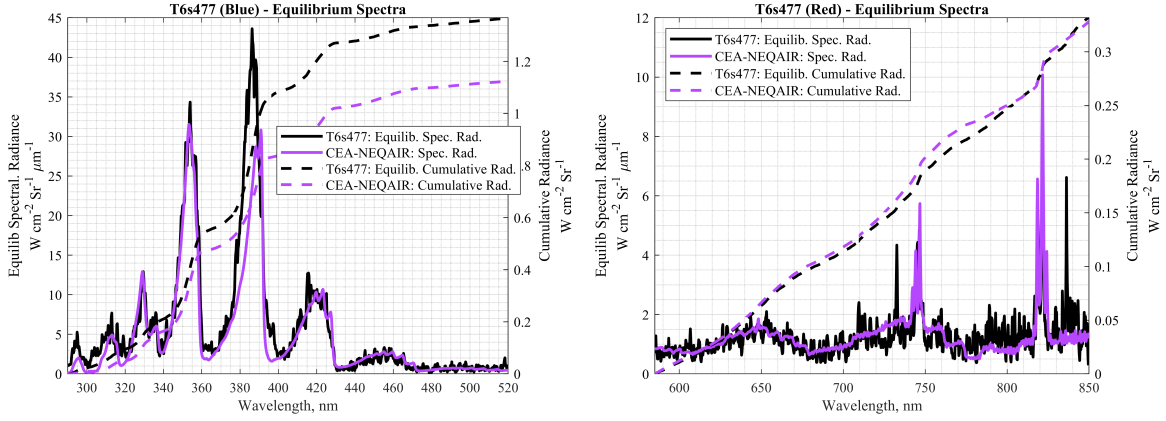
4.8 Summary of Improvements

The findings from the previous sections have shown the quality of air equilibrium spectra attained from shock tube experiments are dependent on a number of factors. New synthetic air and pure nitrogen low-speed datasets have been produced. Example equilibrium spectra for which are plotted in Fig.'s 4.17 and 4.18 respectively. Both NEQAIR simulations include only the intended species produced by the chosen test gas, i.e. no contaminants. Though discrepancies still exist at ∼380 nm, these are known to be the result of CN contaminants, which remain an inherent feature of shock tube experiments. These plots demonstrate a significant improvement from results of previous T6 AST and EAST low-speed studies and provide a reliable dataset for the future study of the non-equilibrium region.



(a) UV/Vis (b) Vis/NIR

Fig. 4.17 Example of experimental equilibrium spectra in close agreement with CEA-NEQAIR predictions for synthetic air test T6s483 (8.0 km/s, 33.0 Pa fill, 23.4 kPa post-shock pressure).



(a) UV/Vis (b) Vis/NIR

Fig. 4.18 Example of experimental equilibrium spectra in close agreement with CEA-NEQAIR predictions for pure nitrogen test T6s477 (7.4 km/s, 73 Pa fill, 41.7 kPa post-shock pressure).

4.9 Conclusion

A study into the equilibrium spectral radiance discrepancies between shock tube experiments and CEA-NEQAIR predictions has been conducted, primarily focusing on tests relevant to low Earth orbit return entry speeds. Contaminant spectral features in the flow are identified and the CN violet band is used to assess the removal of contaminants across a range of test conditions and levels of facility cleanliness. The origin of CN contaminants are shown to be from a range of sources, including leaks into the test volume. Trials of a GV10x 300W Downstream Asher from ibss Group Inc. to remove hydrocarbon matter from the last 2 m of the AST walls did not produce significant enough improvements to justify its repeated use. Nor did it improve any of the remaining discrepancies at the lower ultraviolet wavelengths. It's recommended that future works may trial heating of the T6 AST tube walls, as conducted at EAST, to assess if any increased outgassing may achieve a reduction in contamination levels. Free electrons are proposed as one contribution causing the remaining offsets in the ultraviolet spectra, though this approach can worsen the agreement at higher wavelengths. Direct measurements of electron density would be a useful addition to the dataset in future works. Additionally, TDLAS measurements in the NO bands would be useful to confirm the excess signals in this region, and validate that it is not an artefact of the OES calibration process. Modelling of the boundary layer is also neglected in this work and is highlighted as an area for future consideration.

Reducing the spectrometer slit widths was shown to significantly improve agreement of equilibrium spectra with CEA-NEQAIR predictions in the visible/near-infrared wavelengths. However, remaining discrepancies in the ultraviolet region are shown to have a dependence on post-shock pressure and shock speed. Lower pressure test cases demonstrate improved agreement with the NO bands, though CN contamination makes up a larger fraction of the measured radiance. It's also shown that the predicted radiance levels in the NO region are particularly sensitive to the radiation model used. Both NEQAIR and SPECAIR radiation models were trialled, along with alternative O_2 photodissociation cross-sections. Finally, examples of improved equilibrium spectral radiance traces are provided for synthetic air and pure nitrogen tests, showcasing much improved agreement to the CEA-NEQAIR predictions. The ultimate result of this study is the generation of a new low-speed synthetic air and pure nitrogen dataset, which can be used to investigate the associated chemical kinetics with more certainty, having resolved many of the equilibrium discrepancies.

Acknowledgments

The authors would like to thank Dr Tobias Hermann for the generous loan of the Deuterium calibration lamp, making acquisition of data from 200 to 300 nm feasible. Further thanks are given to Dr Christophe Laux and his team at Laboratoire EM2C, CentraleSupélec for kindly performing SPECAIR simulations used in this chapter. We would also like to thank Chris Hambidge for his relentless efforts to ensure these experiments were carried out successfully and safely. Finally, thanks are extended to Dr Brett Cruden and Dr Aaron Brandis at NASA Ames for their ongoing support and discussions.

Statement of Authorship

Title: Investigation into Equilibrium Radiance Offset in Air Shock Tube Tests
Status: Unpublished and unsubmitted work written in a manuscript style

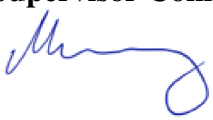
Author Contributions:

- **Alex Glenn**- Lead author, experimenter, data curation, formal analysis and writing.
- **Tristan Crumpton** - Championed preparation of plasma cleaner pipework and primary facility operator.
- **Peter Collen** - Supervision during paper review and results interpretation.
- **Matthew McGilvray** - Supervision as Principal Investigator, secondary facility operator and organised and managed funding.

Student Confirmation: **Date:** 14/10/2024



Supervisor Confirmation: **Date:** 15/10/2024



Chapter 5

Development and Validation of a Constrained Spectral Fitting Routine

If at first you don't succeed, call it version 1.0

Preamble

The second research aim of this thesis is to develop a means of converting the spatially and spectrally resolved radiance data into the temperature and species number density profiles through a given test slug. This chapter introduces a novel methodology for achieving this within the framework of a global two-temperature model, assuming Boltzmann distributions throughout. The key innovation lies in ensuring that the results adhere to the conservation laws of mass, momentum, energy, and charge. Validation of the new method is conducted using a series of artificial radiance datasets, incorporating experimental artefacts. The results show significant improvements in accuracy from previous methodologies and highlight additional measurements to be considered in future shock tube campaigns.

This chapter is a draft of work intended for future journal publication, which has been reformatted and adapted for inclusion in this thesis. A statement of authorship is provided at the end of the chapter, while references are contained within the main body of references at the end of the thesis. Section A of the thesis Appendix contains additional information relevant to this chapter, and is referenced in the main body of text when relevant.

5.1 Introduction

Thermochemical non-equilibrium can dominate large portions of a hypersonic vehicle shock layer. The bow shock ahead of the vehicle provides a mechanism to convert the kinetic energy of the vehicle to the internal energy of quiescent gas molecules. This causes a sudden increase in their internal energy and initiates dissociation, ionisation and radiation emission processes. Timescales of the thermal relaxation and chemical reactions relative to particle times of flight through the shock layer determine the reach of the non-equilibrium phenomena towards the vehicle. This can increase the heat flux incident on the vehicle surface, impact vehicle dynamics through aerothermodynamics effects, and lead to considerations for communications and observability. It's therefore desirable to characterise the thermochemical state of the gas through this region, to improve entry vehicle design for future missions.

Due to the expense of real flight experiments, ground test facilities have traditionally been used to recreate these high-enthalpy flow environments, so they may be studied. This allows clean radiation data, amongst other parameters, to be captured to inform computational models. The Electric Arc Shock Tube (EAST) at NASA Ames [41, 75] has captured radiation data since the 1960's to inform a range of proposed planet entry missions, including Earth [13, 16], Mars [14], Titan [17], Venus [49] and Gas Giants [43]. Their optical emission spectroscopy set-ups provide spatially and spectrally resolved absolute radiation measurements from $\sim$120 to $\sim$1700 nm [39], to inform of the radiative heating environments around planet entry vehicles. More recently, other facilities, such as the X2 facility at the University of Queensland [13, 159] and the new T6 Stalker at the University of Oxford [32, 35] have attained comparable datasets while operating in their respective shock tube modes. As well as quantifying the radiative heat flux, these spectrally resolved measurements can allow number densities of excited species and the distributions of their energy states to be inferred. When combined with the spatial resolution, the evolution of thermochemical states can also be characterised.

Historically, assessment of whether models predict correct thermochemical state evolution has been performed by feeding their results into a radiative transport solver and comparing against experimentally measured radiance profiles. The Post-SHock relAXation solver (POSHAX) [71, 147] from the University Of Queensland and Non-Equilibrium Shock Solver (NESS) [30] from the University of Oxford are two examples of one-dimensional relaxation solvers, to predict the thermochemical evolution through shock tube test slugs. They are able to utilise rates in the literature, to generate lines of sight that can be fed into a radiative transport code such as NEQAIR [192, 44] and thus predict the profile of radiation emission. Comparison of predictions against experimental data across a wider range of conditions allows rates to be updated. Numerical radiance profiles are convolved with the

Spatial Resolution Function (SRF) [41] of the associated optical arrangements, to account for experimental artefacts and allow a like-for-like comparison between the two.

Alternatively, a spectral fitting approach can provide a faster means of extracting temperatures and species number densities through the shock layer. This intrinsically assumes the radiation has been captured by a line of sight looking through a homogeneous flowfield, thus lending itself to the largely one-dimensional flow of shock tubes. Cruden and Brandis [46] have applied the NEQAIR spectral fitting program to pure nitrogen EAST data at 10.3 km/s to obtain number densities of electronic states responsible for radiation, along with temperatures, as a function of position behind the shock. They trialled both Boltzmann and non-Boltzmann distributions to achieve close fits in the UV and visible respectively, as well as inclusion of contaminant species such as C, H and CN to improve their fits. Tibère-Inglesse and Cruden [187] performed a similar analysis to slower speed 7 km/s pure nitrogen cases from the same EAST dataset, where molecular species contribute to a greater portion of the observed spectral radiance. They state that thermal and possibly chemical equilibrium may not be achieved as far back as 50 mm/80 μs from the shock front. A two-temperature (2T; T=T_{rot} and T_{vib}=T_{el}) analysis revealed differences between rotational temperatures of different species, as well as between rotational and vibrational temperatures of a single species, through the non-equilibrium region. Temperature profiles generated from different wavelength regions were shown to have some discrepancies. They also state that the distribution assumption (i.e. Boltzmann or non-Boltzmann) had no significant influence on the resulting temperatures. Other spectral fitting studies in pure nitrogen at relevant enthalpies have been performed by Tang et al. [180] from temporally-resolved relative-intensity shock tube ultraviolet spectra and in recombining plasma torch flows by Tibère-Inglesse et al. [188], both using SPECAIR spectral fitting software [102, 168] to show similar trends. Additionally, spectral fitting of NO and OH has successfully been performed in slower Mach $\sim$7 flows by Sharma et al. [155] and Yanes et al. [199], to assess the degree of thermal non-equilibrium immediately behind stationary shock fronts. Hence, it's been well demonstrated that spectrally resolved radiation measurements are a valuable means to characterise the thermochemical state through high-enthalpy flows. However, previous applications to shock tubes make no attempt to ensure conservation of mass, momentum and energy through the test slugs for the extracted temperatures and densities.

The study herein develops a new spectral fitting methodology that ensures these fundamental conservation laws are obeyed through the test slug. This helps to limit the myriad of possible spectral fit outputs to more physically correct solutions, and enables shock deceleration effects to be taken into account. The methodology is developed within the framework of a 2T model and Boltzmann distributions are assumed at all locations. This simplifies the

initial development and produces results that can be easily compared against well-established thermochemical models, such as the Park 2T [144, 145]. Section 5.2 begins by explaining the steps of the proposed constrained spectral fitting routine. A series of validation trials are carried out in Section 5.3 by testing the routine against artificial spatio-spectral radiance data with a succession of experimental artefacts. Finally, the constrained spectral fitting routine is applied to EAST-62-40 real shock tube radiance data in Section 5.4. Results are compared against that of Tibère-Inglesse and Cruden [187], from prior spectral fitting analyses, and the effect of accounting for strong shock deceleration effects is shown.

5.2 Methodology

5.2.1 Underlying Physics and Shock Tube Analogy

In a shock tube experiment, a normal shock wave processes a controlled test gas to emulate the shock layer stagnation line ahead of a hypersonic vehicle, up to the boundary layer edge. At high enthalpy conditions, this allows full recreation of the thermochemical evolution through the partially ionised plasma. An optical set up that provides spatial resolution of radiance, such as Optical Emission Spectroscopy (OES), therefore enables spectra to be extracted at various points through the test slug, each corresponding to a different state during the post-shock relaxation phase. Figure 3.21 in Chapter 3 provided examples of such OES images for a 6.65 km/s shock in 90 Pa of pure nitrogen - this is the condition used for development and validation of the constrained spectral fitting methodology herein. The vehicle - shock tube analogy was also illustrated in Fig. 3.6. The conservation laws that should be obeyed across the normal shock during a shock tube experiment are summarised below. Equation 5.4 states that the ratio between all oxygen and nitrogen atoms should be maintained across a shock through an air test gas, regardless of the new species they redistribute to form. The total number of atoms is accounted for by mass conservation.

$$\text{Conservation of Mass:} \quad \rho_1 u_1 = \rho_2 u_2 \tag{5.1}$$

$$\text{Conservation of Momentum:} \quad p_1 + \rho_1 u_1^2 = p_2 + \rho_2 u_2^2 \tag{5.2}$$

$$\text{Conservation of Energy:} \quad h_1 + \frac{u_1^2}{2} = h_2 + \frac{u_2^2}{2} \tag{5.3}$$

$$\text{Conservation of O:N atom ratio:} \quad \frac{X_{\Sigma O,1}}{X_{\Sigma N,1}} = \frac{X_{\Sigma O,2}}{X_{\Sigma N,2}} \tag{5.4}$$

5.2.2 Constrained Spectral Fitting Routine

Overview

A novel constrained spectral fitting routine has been developed, to ensure conservation of mass, momentum, energy, charge and atomic ratios through a test slug during thermochemical state characterisation. Fundamentally, it is a method to convert spectral radiance data through a shock tube test slug, into spatially or temporally resolved temperature and number density profiles. This information helps to describe the evolution of the thermochemical state through the test slug. An outline of the inputs and outputs of the routine are summarised in Table 5.1. The routine operates within the framework of a 2T model and assumes Boltzmann distributions at all locations.

Table 5.1 Summary of inputs and outputs of the constrained spectral fitting routine.

Inputs	**Outputs**
1. Initial P, T and composition of test gas (defining total atomic ratios to maintain)	**1.** Rotational and vibrational temperature profiles
2. CEA prediction for chosen species (and initial guess for CN radical)	**2.** Number density profiles for chosen species
3. Define enthalpy constraints from either:	**3.** Corresponding physical property evolution:
(a) Assuming constant shock speed	(a) Pressure
(b) Accounting for shock speed variations	(b) Enthalpy
4. Define pressure constraints from either:	(c) Density
(a) Constant P_0 and Mirels $U_{2,s}$	
(b) P trace from experiment or simulation	
5. Experimental spectra and associated ILS	
6. Tube Diameter	

The uncertainties associated with the extracted temperatures and number densities at each point are evaluated by performing a Monte Carlo analysis. A series of randomly distributed initial guesses are trialled at each point and the standard deviations are used to calculate the 95% confidence limits, indicated by error bars in the results shown in following sections. This represents only the uncertainties associated with the spectral fitting process, and not those associated with the calibration of the radiance data. The inner workings of the constrained spectral fitting methodology are provided in the following subsection. The terminologies used in the rest of this paper are emphasised here: "constrained" implies spectral fitting performed while enforcing the conservation laws defined by Equations 5.1 to 5.4; "unconstrained"

performs the spectral fit without consideration of conservation laws, and results thus rely solely on the fitting against the spectral profile (which is equivalent to previous spectral fitting studies).

Inner workings

The constrained fitting procedure is performed within Matlab 2023b's Optimization Toolbox, calling NASA's NEQAIR v15.1 radiative transport code and Oxford's in-house thermo-chemistry and transport property library, OCEAN [152, 30]. These are used to generate synthetic spectra and track enthalpies and pressures respectively. The fitting process is performed within the framework of a 2T model ($T=T_{rot}$ and $T_{vib}=T_{el}$). The NEQAIR spectra are generated from a tangent slab calculation across the shock tube diameter, while utilising experimentally measured Instrument Line Shape (ILS) [41] functions to account for the broadening of the optical instrumentation. This enables a like-for-like comparisons between experimental and artificial spectra. Experimental spectra are extracted at multiple points through the test slug and the spectral fitting routine is executed to retrieve temperatures and number densities. This methodology intrinsically assumes a uniform homogeneous core flow across the diameter of the shock tube and thus neglects differences in radiative transport properties between the core flow region and boundary layer. Additionally, all results rely on the underlying assumptions of the NEQAIR radiation model. Figure 5.1 summarises the key aspects of the new spectral fitting routine, while the remainder of this subsection discusses some of the finer details.

Before spectral fitting can begin, a distribution of energy states must be selected. In this study, a Boltzmann distribution has been assumed, and the rotational and vibrational temperatures are treated as identical across species. Additionally, the species to be included in the routine must be defined to apply across all locations through the test slug. Only pure nitrogen low-speed data is considered in this paper to simplify initial applications, which involves 5 species (N_2, N_2^+, N, N^+, E^-), plus the addition of contaminant species such as the cyano-radical (CN) where relevant.

The procedure begins by first fitting a spectrum furthest away from the shock front and therefore closest to equilibrium. This is generated by averaging over a given spatial region. A CEA shock problem is run to generate an initial first guess for the temperatures and number densities at this location, using information of the shock speed at the window, as well as test gas fill pressure and composition. An estimation of any contaminant species number densities that are observed in experimental spectra is also included for the initial guess. By calling NEQAIR v15.1, these values are converted into the corresponding artificial spectral trace, to compare against the experimental data. The Matlab optimisation routine then iterates through

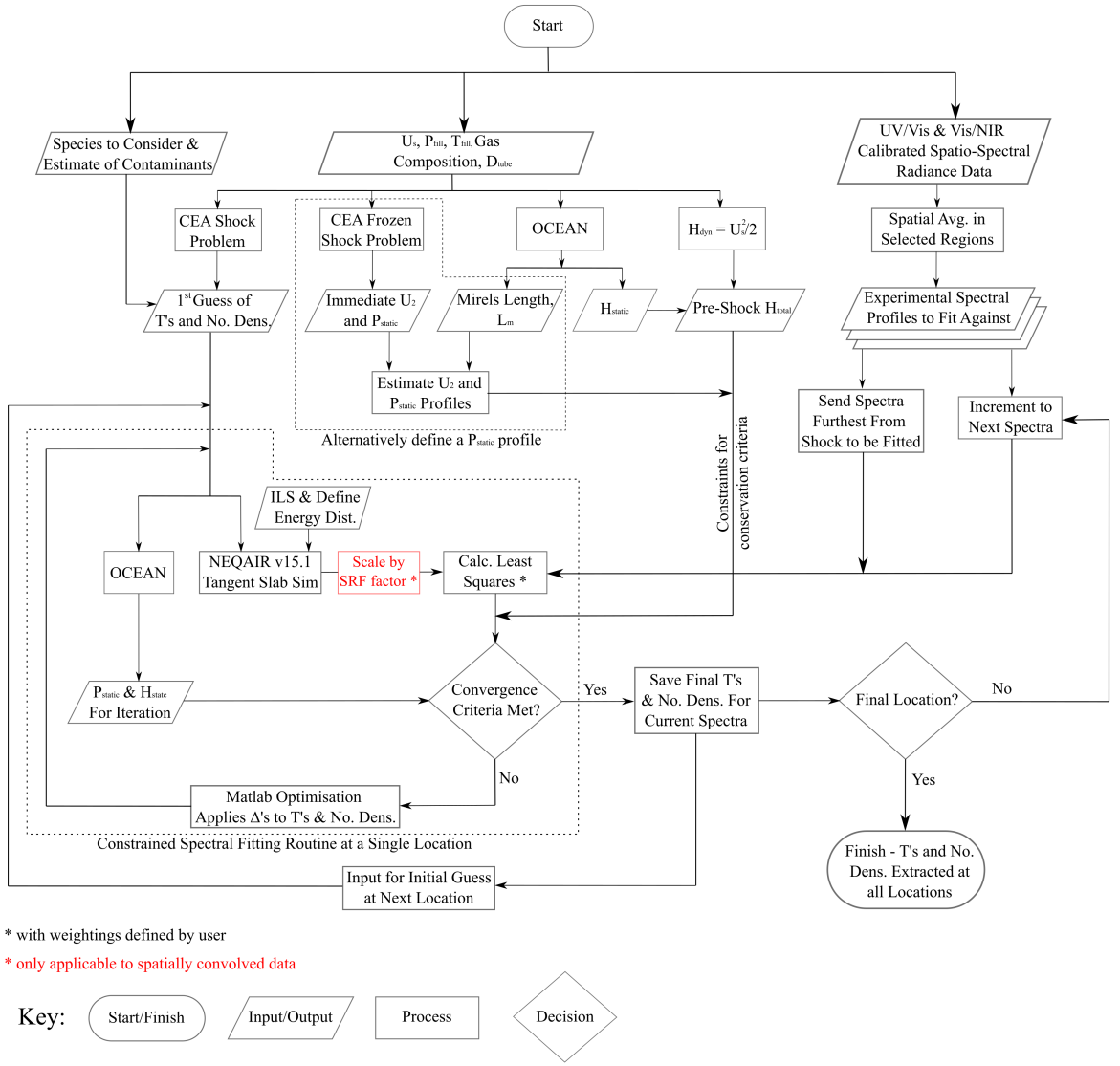


Fig. 5.1 Flow diagram of the constrained spectral fitting routine. The SRF scaling is explained in Section 5.3.4

consecutive attempts at varying the temperatures and number densities until an acceptable spectral fit is attained. The corresponding temperatures and number densities from which are used as the initial guess for fitting at the next spectral trace. It's noted that time to converge to a solution at each point can be reduced by limiting solutions to expected trends. For example, temperatures should both initially monotonically increase as you move closer to the shock front, to a point. The process is successively repeated, incrementing closer to the shock front with each step. Higher resolution of points is required closer to the shock front in order to capture the more rapidly transitioning state of the test gas. Acceptability of the fits at each

location is based on a Least Squares Analysis (LSA) between the artificial and experimental spectra, plus some penalties to ensure conservation laws are obeyed.

The novelty of this new methodology lies in the restriction of the myriad of possible temperature and species number density combinations that produce a good fit against experimental data, to those which obey conservation of mass, momentum and energy. This is implemented into the routine by calculating total enthalpy and static pressure during the optimisation process. The Matlab optimisation output is penalised if deviations above 1% occur, proportionally to the magnitude of the discrepancy. First, the total enthalpy of the pre-shocked test gas is calculated in the shock frame of reference by summing the static and dynamic components. This provides a benchmark value for the spectrally fitted points through the test slug. In the shock frame of reference, the dynamic enthalpy is simply ${U_\mathrm{S}}^2/2$, while the static enthalpy is calculated by OCEAN. The same calculations are performed at the spectral fitting locations through the test slug, though the static enthalpy has a much larger contribution after the test gas is processed by the normal shock wave. For cases with strong shock speed variations, a LASTA analysis [153, 152, 170] can be incorporated into the procedure, to adjust the total enthalpy and static pressure targets through the test slug accordingly. The post-shock velocity profile as a function of distance behind the shock is attained from Equation 5.5, derived from Eq. 33 from Mirels [126], where X_S and L_m are post-shock distance and Mirels length respectively. The dynamic enthalpy component through the test slug can therefore be calculated in the shock frame of reference as ${U_{2,\mathrm{s}}}^2/2$.

$$U_{2,s} = \frac{\rho_1 U_1}{\rho_2}\left(1 - \sqrt{\frac{X_S}{L_m}}\right) \tag{5.5}$$

A constraint is also placed on the static pressure output from each iteration though the test slug. This can either be derived from: the calculated post-shock velocity profile and density ($P_{2,\mathrm{static}} + \frac{1}{2}\cdot\rho_2\cdot{U_{2,\mathrm{S}}}^2$) to maintain total pressure through the test slug; or the static pressure profile can be extracted from a NESS [30] simulation of the condition; or alternatively the static pressure profile measurement from a shock timing station (STS) near the shock at the time of camera gating may be used when available. In all cases, this stops the total number of atoms (whether in atomic or molecular form) from diverging past densities that adhere to the expected static pressure. It is acknowledged that the assumption of constant total pressure may not hold true through regions of non-equilibrium. However, based on the works of Sopek et al. [163] - which report the total pressure predicted in front of a Pitot probe to differ by less than 1% when thermochemical non-equilibrium effects are accounted for - the assumption of constant total pressure is therefore considered reasonable. While their case studies involve lower enthalpies than considered in this paper, the small deviation is a good

indicator that the assumption of constant total pressure after the shock is suitable for the purposes of this work.

For gas mixtures with more than one type of atom (e.g. synthetic air - N_2 and O_2) the ratio between the atom number densities is also constrained, as defined by Equation 5.4. As with the total enthalpy, the pressure and ratio constraints are restricted to be within $\pm 1\%$ of the conserved values. Atoms introduced from contaminant species, i.e. carbon (C) and Hydrogen (H), have no number density restrictions in relation to other atoms since their variation through the test slug is dependent on a multitude of variables. They are thus only inherently constrained by the minimisation of the spectral fitting LSA and their total enthalpy and static pressure contributions. The value in implementing these physical constraints is demonstrated in later sections of this paper, by comparing results of a constrained spectral fit against an equivalent unconstrained routine. It's emphasised that during this constrained spectral fitting process, the optimisation routine is unaware of any reaction mechanisms or rates. Results are based purely on attaining an acceptable match between spectral trace plots whilst adhering to the aforementioned constraints.

The methodology proposed here features several key differences from the spectral fitting routines applied in earlier works. Previously, a spectral region in which the species of interest dominates is isolated and fitted independent of the remaining spectral information, although some works have used the entire spectrum of a given spectral channel [187]. However for the constrained methodology proposed herein, it's desirable to include as much spectral (or more generally, species) information as is available. The goal is to gather information on the widest range of atomic and molecular species and bands, thereby capturing the most significant contributions to total enthalpy and static pressure. This enables a closer match to the experimental case. However, species which radiate negligibly can not convey their number density information via emission spectroscopy measurements. Instead, the number densities of these remaining species is inferred from the aforementioned constraints. In the recent T6 AST campaign, spectral information was captured in the Ultraviolet/Visible (UV/Vis) and Visible/Near-Infrared (Vis/NIR) for low-speed pure nitrogen and synthetic air test cases. The initial analysis in this paper therefore confines itself to these two spectral channels, though it is emphasised that generally - the more information that can be supplied to the fitting routine, spectral or otherwise, the more accurate the final result should be. Section 5.3.5 provides an example of the routines wider applicability by feeding electron number density measurements in addition to emission spectra, for an artificial validation case. Both the UV/Vis and Vis/NIR spectral channels are fit simultaneously during the fitting process. Weightings can be assigned to given spectral regions so that small radiating features can still influence the fitting outcome accordingly. This informs the fitting routine to approach a more

accurate set of temperatures and number densities, while still attaining an acceptable global fit. Charge neutrality is ensured from the spectral fitting outputs at all locations, which is expected to hold true at scales above the Debye shielding length.

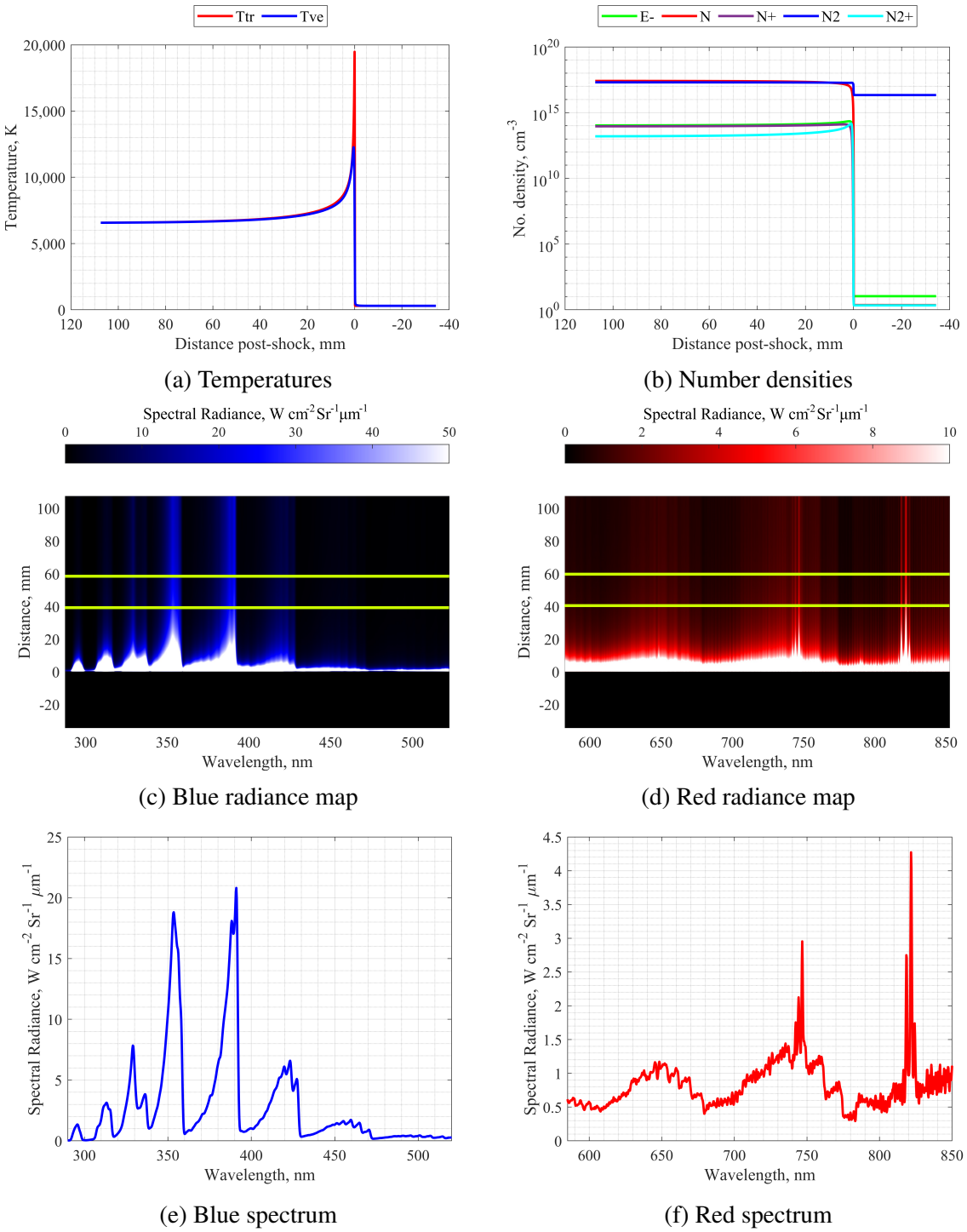
5.3 Validation

5.3.1 Validation Procedure Against NESS-NEQAIR

The constrained spectral fitting routine is validated in this section by applying it to artificial spatio-spectral data generated from NESS-NEQAIR simulations. NESS [30] is a one-dimensional solver to calculate the evolving properties behind a shock front, including the effects of mass loss to the boundary layer in a shock tube experiment. Figures 5.2a and 5.2b show the results of a 2T NESS simulation of T6s492 - a 6.65 km/s shot in 90 Pa pure nitrogen performed in the T6 Aluminium Shock Tube at the University of Oxford. This information can be used as a line of sight in the NEQAIR radiative transport code to create artificial spatio-spectral radiance data. The corresponding UV/Vis and Vis/NIR radiance maps are shown in Fig.'s 5.2c and 5.2d, with spectral resolutions equivalent to the real shot data. Spectra are extracted by averaging over different spatial portions of the test slug, as is the case with real data and exemplified in Fig.'s 5.2e and 5.2f. Park 93 [145] rates were used to perform the NESS simulations.

Since the temperatures and number densities through the simulated radiance data are known (from the NESS output) this provides a means to assess the capability of the proposed 2T constrained spectral fitting methodology, to revert the spectral radiance traces back to the NESS output. The agreement of the spectral fitting results to the original NESS output is used as a measure of the performance of the spectral fitting routine. During this assessment, radiation parameters used in the spectral fitting iterations are kept exactly the same as the original NESS-NEQAIR simulations (i.e. Boltzmann assumption, ILS function and tangent slab calculation). By ensuring commonality in all these variables, it's ensured that an exact spectral match is possible, and thus retrieving the original NESS temperatures and number densities is as well. How close the results are to the original NESS outputs is therefore solely a measure of the performance of the spectral fitting routine.

The ILS used in the NEQAIR v15.1 simulations is the square root of a Voigt function [41], fitted to the experimentally measured line shapes of the OES setups shown in Fig. 3.15. In the UV/Vis region, the Gaussian FWHM is 1 nm and the Lorentzian FWHM is 0.0001 nm. In the Vis/NIR wavelength region, the Gaussian FWHM is 0.6 nm and the Lorentzian FWHM is 0.00005 nm.



(a) Temperatures

(b) Number densities

(c) Blue radiance map

(d) Red radiance map

(e) Blue spectrum

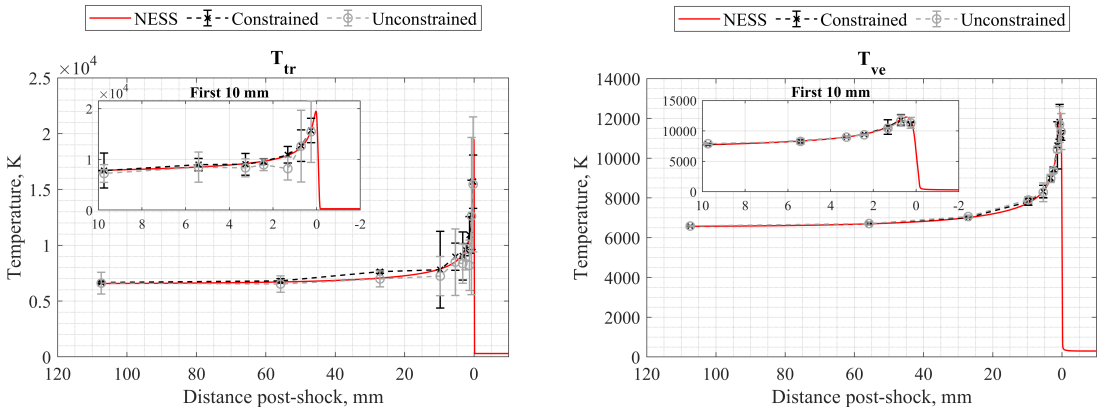
(f) Red spectrum

Fig. 5.2 Steps to generate artificial NESS-NEQAIR spectra of T6s492 (6.65 km/s in 90 Pa pure nitrogen): (a) and (b) are produced by NESS and fed into NEQAIR to make (c) and (d); averaging over chosen spatial region, as shown by green lines, produces spectra as shown in (e) and (f).

5.3.2 Constrained vs Unconstrained

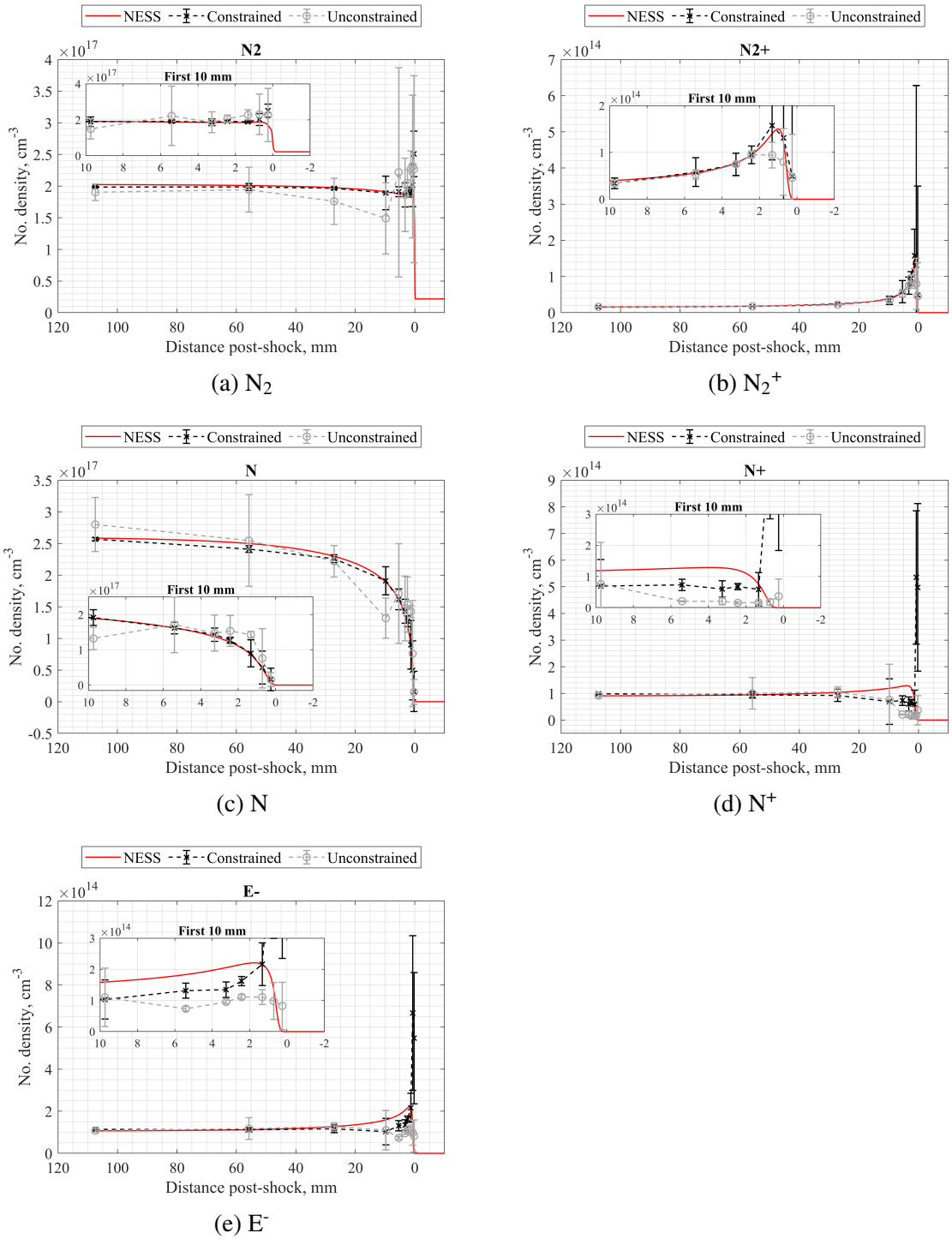
The first step in the validation process is to apply the spectral fitting routine to the artificial NESS-NEQAIR data illustrated in Fig. 5.2. Two versions of the fitting routine are performed: one in which conservation of mass, momentum and energy is ensured ("constrained"); and one in which they are not ("unconstrained"). This provides an initial example of results for both cases, for a simplified set of radiance data. Real shock tube data contains a number of experimental artefacts, such as contaminants and spatial smearing, which will be evaluated separately in the following sections. These initial results represent examples of the best achievable outcomes for both constrained and unconstrained approaches, for the current emission data inputs. This provides early evidence of the advantages gained by incorporating conservation laws, which is a key contribution of this study.

Ten locations through the NESS generated shock layer have been used to create artificial spectra. Fits arrived at from the constrained spectral fitting routine are provided in Section A.1 of the Appendix, showcasing close agreement to the original artificial traces for different stages of the post-shock relaxation process. Figure 5.3 shows the temperatures extracted from constrained and unconstrained attempts. Both closely follow the NESS outputs, though smaller 95% confidence limits for the T_{ve} suggest greater confidence and fit sensitivity to this parameter. Confidence limits of T_{tr} in the non-equilibrium region reach ∼6500 and ∼ 14,000 K for constrained and unconstrained results respectively. Other than this, there is little improvement gained by implementing the constraints for the extracted temperature profiles.



(a) T_{tr} (b) T_{ve}

Fig. 5.3 Comparison of T_{tr} and T_{ve} attained from constrained and unconstrained spectral fitting against the original NESS profiles.



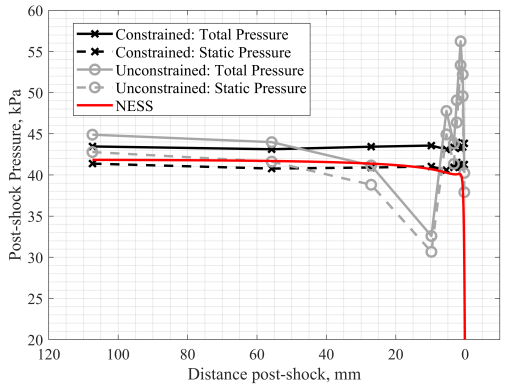
(a) N_2 (b) N_2^+

(c) N (d) N^+

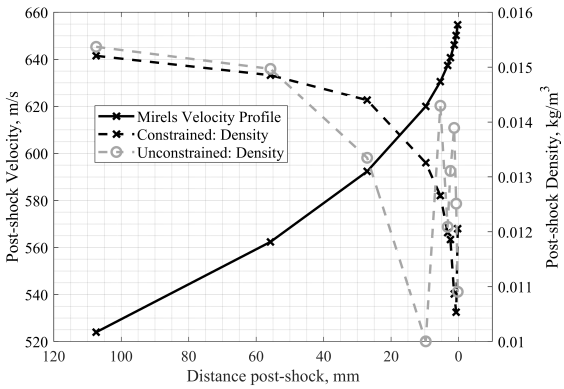
(e) E^-

Fig. 5.4 Comparison of species number densities attained by constrained and unconstrained spectral fitting against the original NESS profiles.

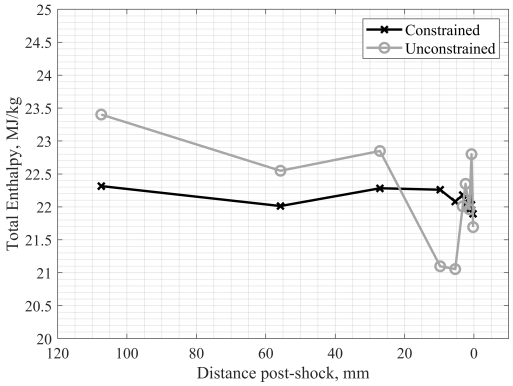
The number density outputs are shown in Fig. 5.4. It's apparent that the species which emit significant radiation from their excited states (i.e. N_2, N_2^+ and N) are in close agreement with the NESS traces. This is especially true for the constrained results, which capture the NESS profiles very accurately. The improvements in results by implementing conservation constraints are thus much more evident in the number density profiles than the temperatures. However, radiation from N^+ is negligible relative to the other species, meaning its number density is not conveyed through the spectra (for the chosen wavelengths at least) and is dictated by the need to satisfy the constraints. The electron number densities ensure charge conservation at every point in the test slug, and thus discrepancies in N^+ induces similar discrepancies in E^-. Values for these parameters therefore have a weaker effect over the resultant spectral fits and have minimal impact on total enthalpy and pressure due to low number densities with respect to other species in the flow. Consequently, their evolution through the test slug is not captured well by the chosen spectral fitting methodology.



(a) Pressures



(b) Velocity and density



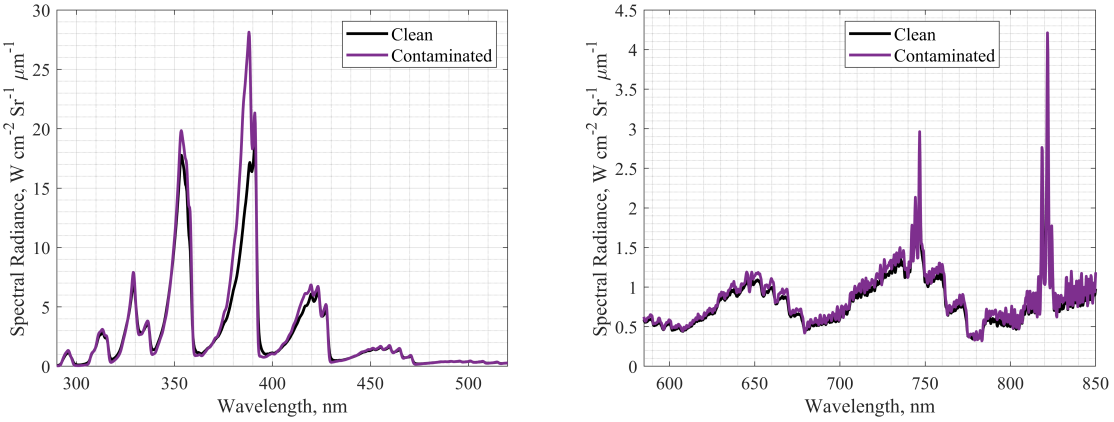
(c) Total Enthalpy

Fig. 5.5 Post-shock physical properties corresponding to the temperature and species number density profiles attained by constrained and unconstrained spectral fitting.

The resultant pressure, density and total enthalpy profiles can be generated from the spectral fit results by calling OCEAN. Figure 5.5 emphasises the improvements from the constrained outputs, with much less variations in all parameters and trends more representative of real data. This is exemplified by the static pressure trace of the constrained output lying very close to the NESS static pressure output. The Mirels post-shock velocity profile is applied for both cases, though the constrained density output is much more realistic. An exception being the last point, which deviates from the expected trend, corresponding to an over-prediction of N_2. Deviations here are likely because it's in the location of steepest transients, just 0.25 mm behind the shock front. However, it's not likely to become an issue for real shock tube data, since spectra will not be resolvable so close to the shock front.

The encouraging initial results allow progression to the next stage of evaluating the constrained spectral fitting routine: examining how experimental artefacts affect result accuracy. The following sections address the effects of contaminants and spatial smearing, which were determined to be the most detrimental artefacts. Additional artefacts, which were also examined and found to have minimal impact, are shown in Sections A.5 to A.8 of the Appendix. Only T_{ve}, N_2, N_2^+ and N results will be plotted in the remaining sections of the main body of this paper, since the constrained spectral fitting routine is shown to reproduce these parameters with high accuracy. However, results will be given in full for some cases in the Appendix. The purpose of these analyses are to check if the parameters of interest can still be reliably extracted in the presence of complications from real shock tube data.

5.3.3 Contaminants



(a) UV/Vis (b) Vis/NIR

Fig. 5.6 Simulations of equilibrium spectral radiance for T6s492 (6.65 km/s, 90 Pa fill in pure nitrogen) with and without contaminants.

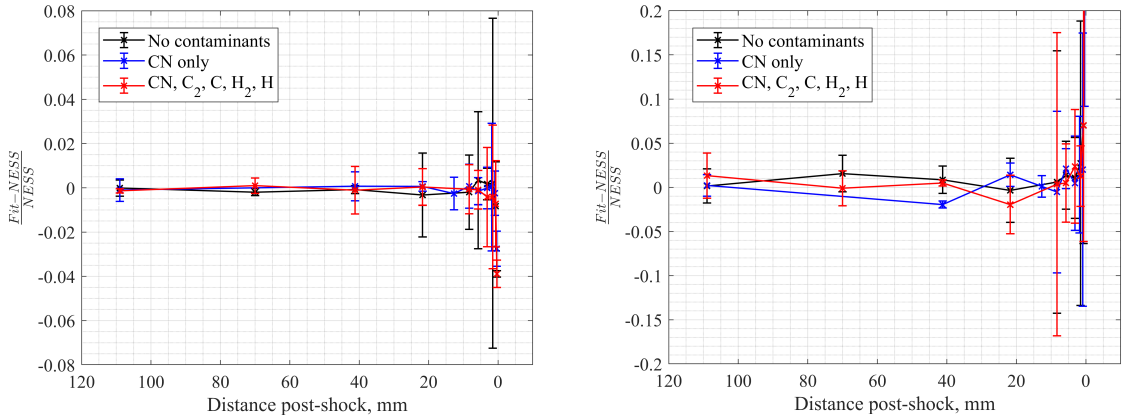
In the case of real shock tube data, a range of contaminant species may exist in the test slug. Studies by Cruden et al. [39] and Chapter 4 of this thesis have investigated the origin and removal of hydrocarbon species from shock tube radiation data, as measured in EAST and T6 AST respectively. Though every effort is made to keep contaminant species to a minimum, they remain an inherent feature of shock tube radiation experiments. The NESS-NEQAIR T6s492 simulation have been repeated, this time including the standard five species of nitrogen, plus 12 contaminant species (C, H, C^+, H^+, CO, C_2, CN, CH, OH, H_2, C_3 and C_2H) by doping the test gas with 0.05% C_2 and 0.01% H_2 mole fractions. This is typical of the contaminant levels expected in the flow from previous investigations [31]. The effect this has on the predicted equilibrium spectra can be seen in Fig. 5.6. In particular, the cyano-radical (CN) violet band radiates intensely at UV wavelengths, and superimposes on the N_2^+ first negative band, despite the relatively low number densities on the order of 10^{12} cm^{-3} (compared to N_2 at 10^{17} cm^{-3}). Inclusion of all 17 species into the constrained spectral fitting would take days while running the routine in series on a local machine. This section therefore evaluates the effect of including additional species in increments, to assess how many are necessary. Spectral fitting was performed for the contaminated NESS-NEQAIR spectra with the 5 pure nitrogen species and:

1. No contaminants
2. CN
3. CN, C_2, C, H_2, H

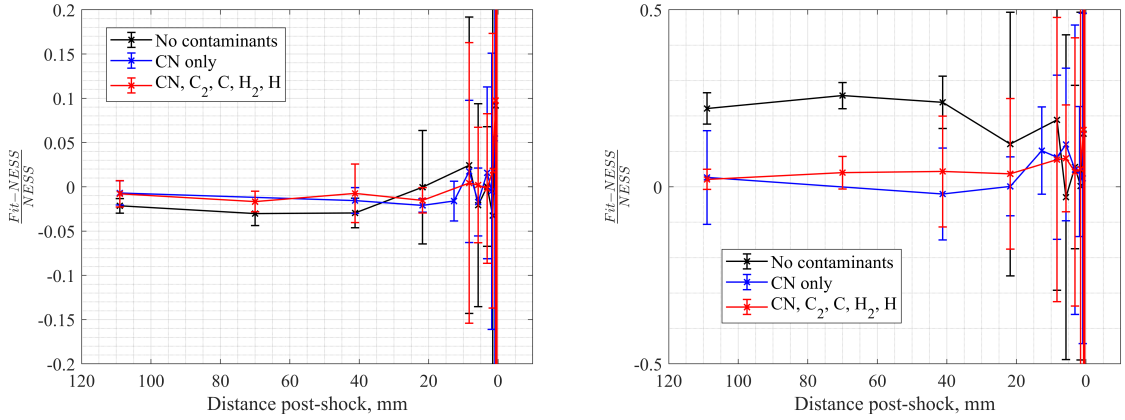
The first of these assesses how well the parameters of interest are extracted when no contaminants are included in the spectral fitting. Then, a single contaminant species which emits significant radiation (CN) is added to the species. This allows the routine to account for the additional spectral feature, without significantly increasing the computational effort. Finally, CN plus four more contaminants of negligible radiation (for the current condition and number densities) are considered to see if any benefit can be gained, at the cost of a moderate increase in computations.

Figure 5.7 shows the constrained spectral fitting results for each of the three cases for T_{ve}, N_2, N_2^+ and N. The results have been normalised against the NESS values, so they may all be co-plotted easier, thus values closer to zero represent a closer match. Figure 5.7d shows that an improvement in N_2^+ extraction is achieved by including CN. This makes sense, since the CN violet band superimposes over the N_2^+ first negative band. However, no further improvements are realised by increasing the number of species further. This is likely due to extremely small mole fractions (thus negligible impact on enthalpy and pressure

calculations) and undetectable radiation emission in the presence of the other species. It's therefore concluded that CN should be added to the species in the spectral fitting routine of real data for pure nitrogen or similar gas mixtures at shock speeds relevant to LEO return missions. Results from the contaminant studies of this section are provided in full in Section A.2 of the Appendix.



(a) T_{ve} (b) N_2



(c) N (d) N_2^+

Fig. 5.7 Results from spectrally fitting a contaminated NESS-NEQAIR simulation of T6s492. Contaminant species included in the spectral fitting routine (in addition to N_2, N_2^+, N, N^+ and E^-) are labelled.

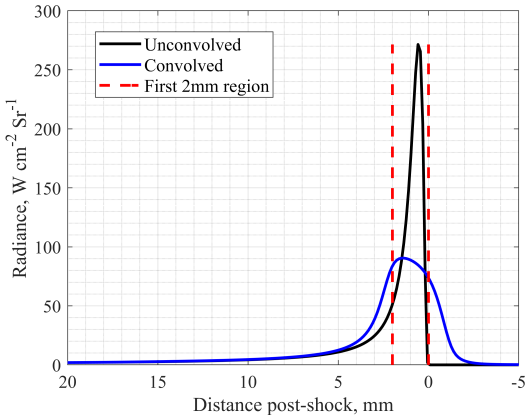
5.3.4 Spatial Convolutions

In order to acquire radiation data during a shock tube experiment, an intensified camera's sensor must be exposed for some amount of time, to capture light from the hot test gas as it traverses the measurement region. An example of a setup to achieve this is the telecentric Optical Emission Spectroscopy (OES) arrangement used for the recent T6 AST campaign, as described in Chapter 3 and based on similar setups used on the EAST facility [74, 39]. Fundamentally, these are a chain of optical components to focus the radiation onto a camera sensor, with horizontal and vertical axes providing spectral and spatial resolution respectively. One-dimensional flow is assumed, with the space axis aligned to the tube centreline.

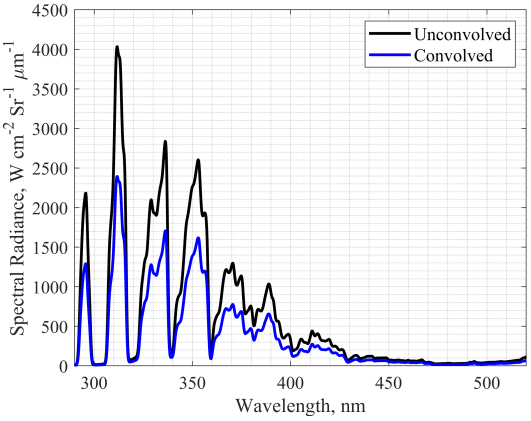
Although camera gating times of typically sub-microsecond are used during these experiments, the shock may still travel a significant distance in this time. For example, NESS-NEQAIR simulations in this paper are based on T6s492 - a pure nitrogen case with a shock travelling at 6.65 km/s past the window. For the camera gating time of 0.5 μs used, this equates to 3.325 mm of shock travel. This causes a spatial smearing effect on the radiance profile as described in the works of Cruden [41], which may often be approximated by the convolution of a square pulse with width equal to the distance of shock travel. This usually contributes the major smearing component of the SRF, formed from gating, optical and camera blurring effects. Figure 3.17 shows the resultant SRF functions characterised for both Blue and Red spectral channels of T6s492, including their associated components. This section evaluates the effect this has on the extracted profiles for the parameters of interest when performing spectral fitting, and shows one way in which consequent discrepancies may be reduced.

The smearing induced by the camera gating causes radiance data at any location on the camera pixel array to be averaged with signal from adjacent spatial locations (by a weighted distribution which is characterised by the SRF). In the equilibrium region, where radiance remains steady, this can have negligible effect on spectra acquired since the spectral profile is constant at all nearby locations. However, immediately behind the shock, the radiance jumps from zero to the peak value typically within 1 mm, followed by initial rapid relaxation. This is consequently an area of steep transients and the peak non-equilibrium signal is averaged with the much lower signals surrounding it. This results in an apparent reduction in signal in peak radiance on the camera array, from the true emission profile. Figure 5.8 illustrates this effect around the first 2 mm of radiance post-shock in the ultraviolet and visible/near-infrared wavelength regions. The unconvolved NESS-NEQAIR radiance profiles of T6s492 in Section 5.3.2 have been convolved by their respective SRFs, shown in Fig. 3.17. By comparing the unconvolved and convolved spectral profile generated from the first 2 mm behind the shock front, the reduction in peak signal can be seen. Spectra from real data extracted in

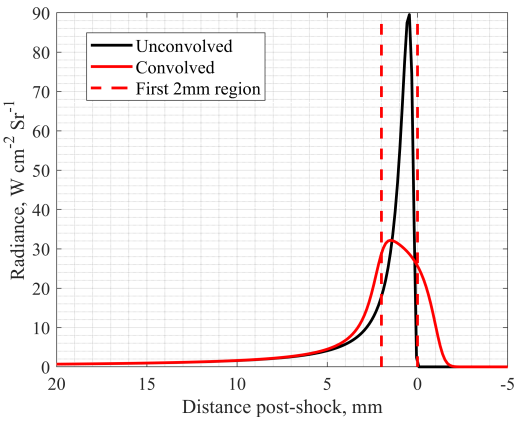
this region are therefore not representative of the true emission, nor thermochemical states present. Spectral fitting outputs will thus also be skewed by this artefact. The deconvolution of real shock tube data, to retrieve the unsmeared profiles is prevented by the S:N, resulting in uninterpretable noisy traces.



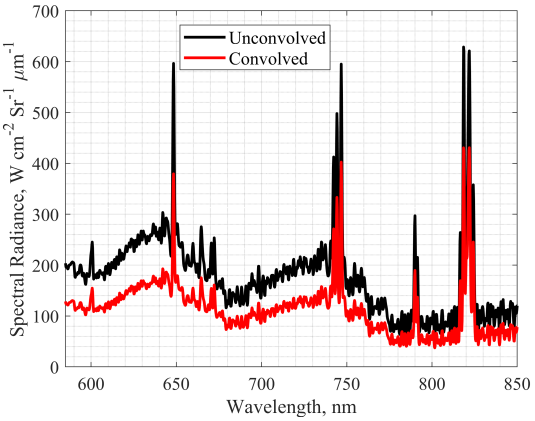
(a) Blue: radiance profiles



(b) Blue: first 2 mm spectra



(c) Red: radiance profiles

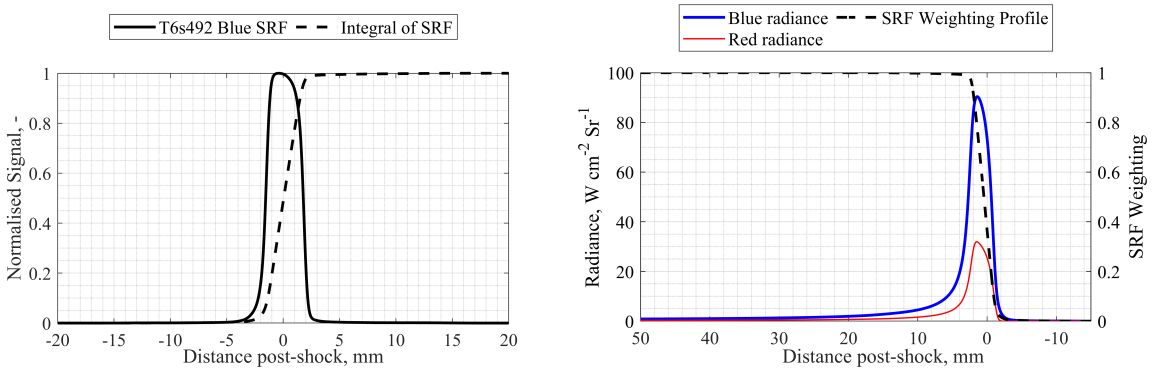


(d) Red: first 2 mm spectra

Fig. 5.8 Spatial and spectral profiles before and after applying spatial convolutions, immediately behind the shock. Blue and Red radiance profiles are based on NESS simulations of T6s492. Convolutions in each channel are performed with the corresponding SRF functions.

An approximation to correct for the smearing caused by camera gating is now proposed. This involves calculating the cumulative integral profile for the SRF of a given channel, as shown in Fig. 5.9a. Normalising this profile to a maximum of 1 produces an "SRF Weighting Profile" which can be mapped to the convolved radiance profiles, as shown in Fig. 5.9b. Spectral trace outputs from NEQAIR during the spectral fitting routine are multiplied by the value of this weighting profile for the considered location, to mimic the signal losses experienced by the convolved/real radiance data around the peak. In the fully relaxed region,

the value is equal to 1 and thus spectra are unaffected. The value drops from 1 to zero close to the non-equilibrium peak, where steep transients are present, following the profile extracted from the integrated SRF. This represents the fraction by which the measured signal has approximately been reduced from the true signal, by averaging with the zero signal region ahead of the shock. A rule of thumb for the positioning of the SRF weighted profile in space with respect to the radiance profile was used in this work. The centre of the weighted profile (i.e. the x value corresponding to 0.5 on the y-axis) was positioned 0.3 times the SRF FWHM downstream of the convolved peak. This was chosen after assessing the shifts in the peak-radiance typical from convolving raw radiance profiles with SRFs of various widths.



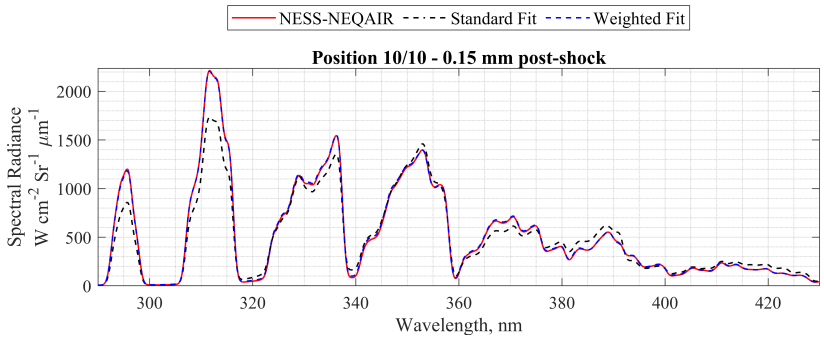
(a) Integrated SRF Profile

(b) SRF weighting mapped against radiance profiles

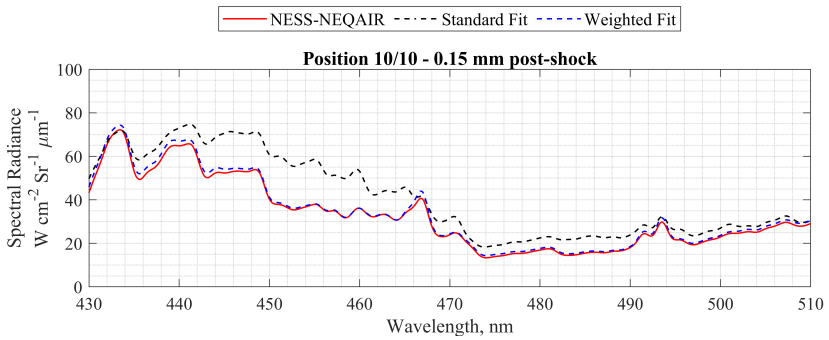
Fig. 5.9 Plots to illustrate the generation of the SRF weighting profile and positioning against artificially convolved NESS-NEQAIR radiance profiles.

This SRF scaling step is included in red in the summary flowchart of Fig. 5.1. An additional complication of the process when performing spectral fitting of two spectral channels arises since the SRF's of different spectral channels for a given shot are generally not the same. In the case of T6s492, very similar optical setups and exact same gating times were used for each channel, and thus the resulting Blue and Red SRF's are very similar to one another. In cases where these differ, a choice has to be made between selecting one SRF over the others, or generate an average, or produce a separate weighting profile for each channel.

Figure 5.10 demonstrates the improvements in spectral fit outputs from portions of the ultraviolet spectrum, for a spectral trace generated by averaging the first 0.3 mm behind the shock front of the convolved NESS-NEQAIR data. This represents the immediate peak non-equilibrium region, which will be most affected by the spatial convolution. It's evident that the fitting routine attained much closer spectral fits to the convolved NESS-NEQAIR radiance data when incorporating the described SRF weighting methodology. The corresponding T_{ve}



(a) 290 - 430 nm



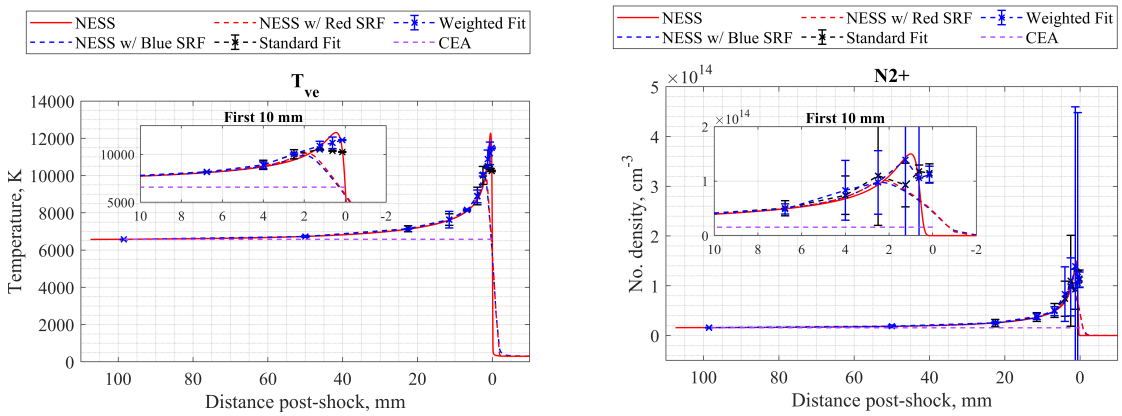
(b) 430 to 510 nm

Fig. 5.10 Standard and weighted spectral fit results against the convolved NESS-NEQAIR simulated data averaged over the first 0.3 mm behind the shock for portions of the UV spectrum.

and N_2^+ profiles extracted for the standard and weighted fitting attempts are shown in Fig. 5.11. It's highlighted that constraints were included for both. Results from each only differ in the first $\sim$2 mm behind the shock (which is the region affected by the spatial smearing for the relevant SRFs). However, the weighted results are closer to the original NESS outputs for both parameters. These parameters were selected since they have the steepest immediate transients of those reliably extracted from the constrained spectral fitting routine (as shown in Section 5.3.2) and therefore are most effected by the spatial smearing. Results for the remaining parameters are provided in Section A.3 of the Appendix. Additionally a continuation study to evaluate the effect of shorter gating times is provided in Section A.4 of the Appendix.

This concludes the study of experimental artefacts in the main body of this paper. The effects of other experimental artefacts were also examined during these investigations, though were deemed to be less consequential to the constrained spectral fitting routine results. However, results for these remaining artefacts are summarised in Sections A.5 to A.8.

Namely, these assess the effects of noise, spatial averaging, boundary layer mass losses and diffusion. Finally, Section A.9 of the Appendix amalgamates a combination of artefacts into one artificial dataset, to provide the closest possible evaluation of constrained spectral fitting performance against real shock tube data.

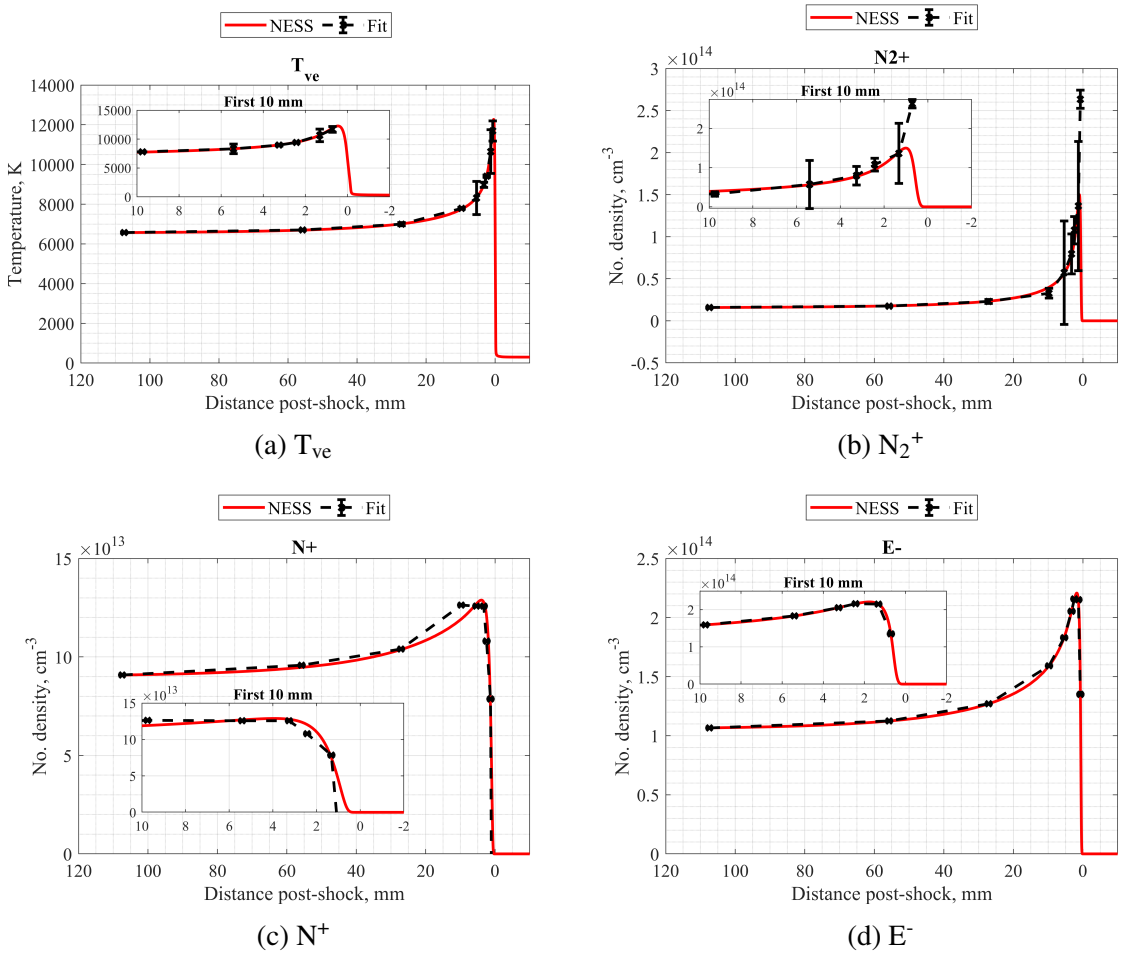


(a) T_{ve} (b) N_2^+

Fig. 5.11 T_{ve} and N_2^+ extracted by spectrally fitting convolved data with and without the SRF weighting correction.

5.3.5 Adding Electron Number Density Information

A sample of results from a side-study into the wider applicability of the constrained spectral fitting routine is shown here. The fitting of the initial NESS-NEQAIR comparisons, from Section 5.3.2, was repeated with electron number densities fed into the constrained routine, in addition to the OES data. The effects of this are shown in Fig. 5.12. Obviously, the electron number densities agree exactly, since they were fed into the routine. However, this has a knock-on effect to also significantly improve the N^+ profile, and therefore the overall thermochemical characterisation of the test slug. The remaining N_2 and N profiles were also still captured well. This demonstrates that by implementing the conservation constraints into the spectral fitting routine, it has capabilities beyond the current limits of the OES datasets currently available from shock tube studies. Furthermore, it can be used as a valuable tool to identify other parameters which should be measured in future shock tube studies, to improve overall thermochemical state characterisation. In this case, it's evident that measurements of electron number densities would be a valuable contribution for low-speed pure nitrogen datasets. Further measurements are explored in Section A.10 of the Appendix.



(a) T_{ve} (b) N_2^+

(c) N^+ (d) E^-

Fig. 5.12 Results from including electron number densities into the constrained spectral fitting routine.

5.4 Real shock tube data: EAST-62-40

The final test in this paper is to apply the constrained spectral fitting routine to real shock tube data. Pure nitrogen shot 40 from EAST Test Release 62 (EAST-62-40) is selected, as it is a similar condition to T6s492 on which simulations were based in this work. Additionally, in-depth spectral fitting studies have already been performed by Tibère-Inglesse and Cruden [187] for this test case, providing a means to compare against results of alternate spectral fitting methodologies. Figure 5.13 shows the shock speed trajectory through a 26.6 Pa test gas, which drops by 2 km/s along the tube before reaching a quoted velocity of 6.88 km/s at the window, where spectrally and spatially resolved images are taken. Two versions of the spectral fitting routine are therefore applied. The first assumes constant shock speed (taken at

the window) and the second incorporates shock deceleration effects by feeding the results of a LASTA simulation [170, 38]. This accounts for total enthalpy and static pressure variations through the test slug as a result of different portions of gas being processed by a shock of varying strength.

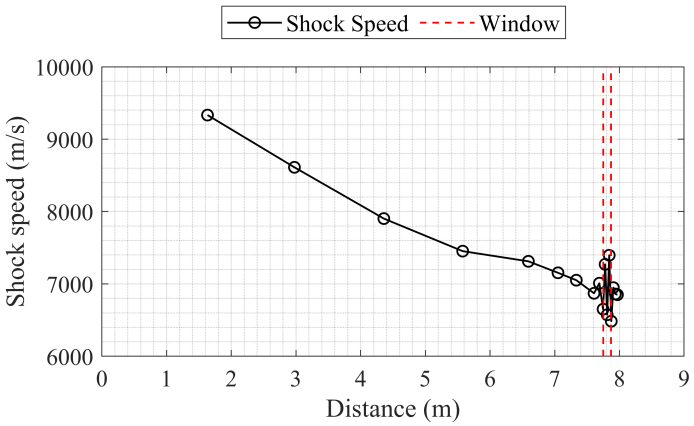


Fig. 5.13 Shock speed profile for EAST-62-40 in 26.6 Pa pure nitrogen.

This condition is particularly interesting since most thermochemical rate models are based on flows dominated by ionisation chemistry, such as the two-temperature Park model [144]. This is the case for higher speed entry velocities, where thermalisation of the vibrational temperature with the electronic temperature is ensured by the presence of free electrons from the highly ionized flow. At lower speeds, interactions involving molecular nitrogen take up the role of re-distributing enthalpy amongst the internal energy modes [24], ultimately leading to the production of NO [76] which is the dominant radiator at such low speeds in air (where oxygen is also present). Figure 5.14 shows a comparison of the vibrational temperatures extracted from the various fitting methodologies. It's evident that only a small change in vibrational temperature is realised by implementing the shock deceleration effects. The method of Tibère-Inglesse and Cruden extracted different profiles from the two camera channels and state there to be possible thermal non-equilibrium within the first 50 mm of test slug. It's also evident from the constrained results that the temperature does not reach the CEA equilibrium prediction within the observable test slug, suggesting thermal relaxation may still be underway as far as $\sim$90 mm post-shock.

The corresponding number density profiles are shown for N_2, N_2^+ and N in Fig 5.15 for both constrained outputs. A greater difference here is realised by incorporating the shock deceleration effects, which demonstrate increased dissociation of N_2 to form N towards the tail end of the observable test slug. This makes sense since these slices of test gas were processed by a faster shock and thus imparted more enthalpy, which in turn affects

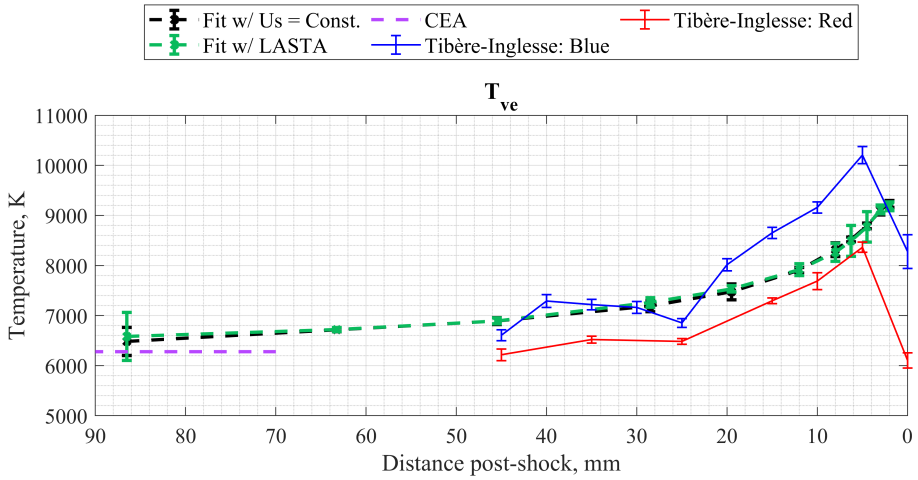
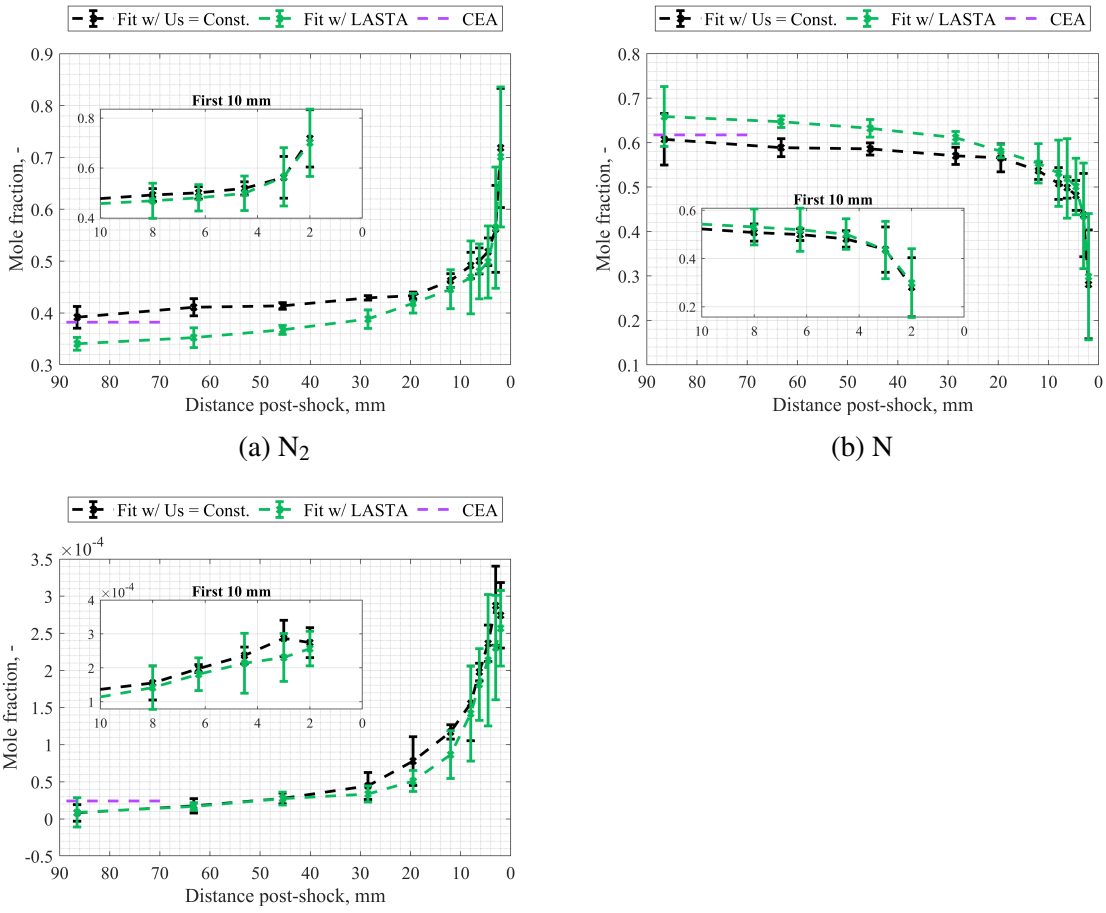


Fig. 5.14 Vibrational temperature profiles extracted for EAST-62-40 via alternate spectral fitting methodologies.

the equilibrium mole fractions each gas slice is to approach. The CEA reference lines were calculated from the shock speed at the window, where the spectral images were taken. Interestingly, the start and end points of the N_2^+ profiles are very similar, though the shock deceleration effects suggest a more rapid reduction in the N_2^+ mole fraction.

Finally, it's noted that due to the different spectral ranges covered by the EAST spectrometers, the constrained spectral fitting was performed over 330 to 480 and 480 to 880 nm in the Blue and Red channels respectively. Though these are different to the regions used during the validation process, they encapsulate the same species, and therefore thermochemistry, with similar spectral resolutions. Examples of the spectral fits achieved from both constrained attempts is shown in Fig. 5.16 for different regions of the relaxing test slug. Each show close agreement to the experimental data, though both interestingly under predict the N_2 first positive signal in the near-infrared in the immediate post-shock region. This may be a result of non-Boltzmann effects. Or alternatively, it could be a result of stray light within the spectrometer instruments owed to the broad slit widths used. This effect was discussed in Chapter 4 and is suggested since this effect was not seen when spectral fitting was performed on the T6 AST data, where narrow slit widths had been used in an effort to minimise the stray light effects. The results of applying the constrained spectral fitting routine to the T6 AST LEO return data are shown in chapters 6 and 7, for pure nitrogen and synthetic air respectively.

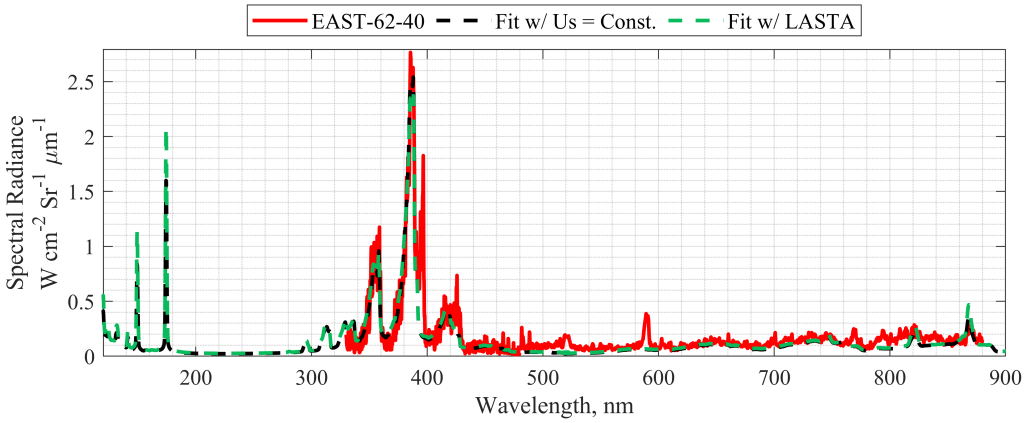


(a) N_2

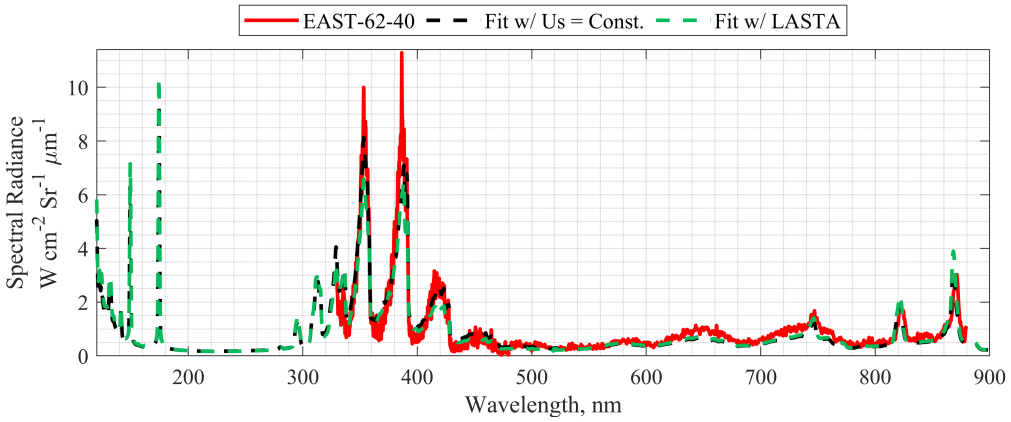
(b) N

(c) N_2^+

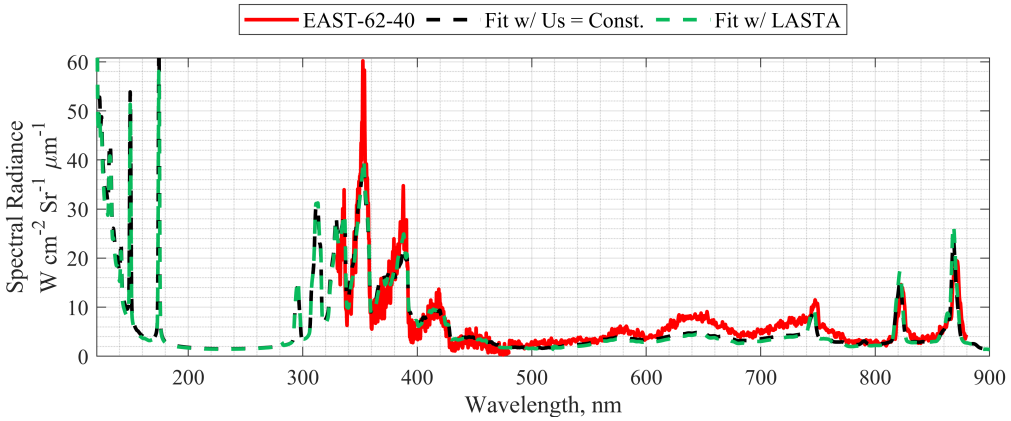
Fig. 5.15 Number density profiles attained from constrained spectral fitting of EAST-62-40 with and without shock deceleration effects.



(a) Near equilibrium



(b) Relaxation



(c) Immediate post-shock

Fig. 5.16 Constrained spectral fit results of EAST-62-40 by fitting with and without the effects of shock deceleration.

5.5 Conclusion

A constrained spectral fitting routine has been developed to conserve mass, momentum and energy in the temperature and number density outputs when spectrally fitting shock tube radiance data. It has been tested against artificial spatio-spectral radiance data and the effect of various experimental artefacts evaluated. This includes the assumptions of a two-temperature ($T=T_{rot}$ and $T_{vib}=T_{el}$) model and a Boltzmann distribution at all points through the test slug. The current application is limited to ultraviolet and visible/near-infrared wavelength regions, as is available from recent T6 Aluminium Shock Tube tests for Low Earth Orbit return studies. These are also wavelengths commonly available from other shock tube facilities in the context of shock layer radiation studies. Though it's highlighted the code is capable of handling data from other wavelength ranges. These inputs enable the routine to successfully capture molecular N_2 and N_2^+ bands, as well as atomic N for a 6.65 km/s artificial test case in pure nitrogen. Fitting results for the spectral regions and resolutions trialled also show strong dependence on vibrational temperature. Rotational temperature generally shows the correct trend, however has high uncertainty.

The constraints are demonstrated to improve robustness of the fitting routine, to reliably produce number densities for the aforementioned parameters in the presence of contaminants and spatial smearing effects. Additionally, an "SRF weighting" technique to approximate the smearing effect close to the shock front is shown to improve extraction of the desired unconvolved profiles. Furthermore, trial cases outside the limits of currently available datasets demonstrate the measurement of electron number densities to be a valuable addition to pure nitrogen shock tube studies.

Finally, the constrained spectral fitting routine has been applied to real EAST shock tube data. This has shown good comparisons against previous spectral fitting results and the incorporation of shock deceleration effects show the enthalpy profile defined can influence the extent of N_2 dissociation predictions in the latter portions of the test slug. The next step of this work is to apply the validated methodology to a new T6 Aluminium Shock Tube dataset of LEO return conditions in both pure nitrogen and synthetic air.

Statement of Authorship

Title: Development and Validation of a Constrained Spectral Fitting Routine
Status: Unpublished and unsubmitted work written in a manuscript style

Author Contributions:

- **Alex Glenn** - Lead author, primary code developer, formal analysis and writing.
- **Justin Clarke** - Secondary code developer and performed simulations using Oxford's Non-Equilibrium Shock Solver "NESS" to create validation cases.
- **Peter Collen** - Supervision as Postdoctoral Research Assistant.
- **Luca Di Mare** - Assisted in code conceptualisation.
- **Matthew McGilvray** - Supervision as Principal Investigator.

Student Confirmation: **Date:** 14/10/2024



Supervisor Confirmation: **Date:** 15/10/2024



Chapter 6

Thermochemical Characterisation of Shock-Heated Pure Nitrogen

The most important skill in writing a thesis? The ability to drink absurd amounts of coffee.

Preamble

After achieving better agreement between shock tube equilibrium radiance data and numerical predictions, and developing a new method for obtaining temperature and species number density profiles through the test slug (as detailed in the previous chapters), these techniques are now applied to process absolute radiation data from the non-equilibrium relaxation region of pure nitrogen tests.

When shocked, pure nitrogen generates a simplified test slug with five species interacting through four reaction mechanisms. This is much simpler than the typical nitrogen-oxygen mixtures, which involve 11 species and 21 reactions. As a result, pure nitrogen provides a more straightforward dataset for testing the new spectral fitting routine, while also offering valuable data on isolated nitrogen radiance and thermochemistry.

This chapter is a draft of work intended for future journal publication, reformatted and adapted for inclusion in this thesis. A statement of authorship is provided at the chapter's end, and references included in the main reference list. Appendix B contains additional relevant information, referenced where appropriate.

6.1 Introduction

Thermochemical non-equilibrium phenomena can dominate the shock layer ahead of a hypersonic vehicle, after a strong bow shock wave causes a sudden increase in the internal energy of the atmosphere's quiescent molecules. This results in dissociation, ionisation and radiation emission, as species in excited energy states relax to a new equilibrium. Timescales of the thermal relaxation and chemical reactions relative to particle times of flight through the shock layer, determine the reach of the non-equilibrium phenomena towards the vehicle surface. This can increase the heat flux incident on the vehicle surface, as well as causing communications, visibility and aerothermodynamic coupling issues. It is therefore desirable to characterise the thermochemical state of the gas through this region.

Although the high-temperature gas effects can be detrimental to the vehicle, the radiation emission provides a means to perform non-intrusive optical spectroscopy measurements. Due to the expense of real flight experiments, ground test facilities have traditionally been used to recreate these high-enthalpy flow environments. This allows radiation data to be captured, amongst other parameters, to inform computational models. Experiments are routinely run on a number of ground test facilities, including impulse facilities such as the Electric Arc Shock Tube (EAST) at NASA Ames [41, 39] and steady facilities such as the Inductively Coupled Plasma (ICP) Torch at CentraleSupélec [102] - both capturing spectrally resolved radiance measurements. The Oxford T6 Stalker Tunnel (T6) is a relatively new high-enthalpy multi-mode transient ground test facility for aerothermodynamics research. While operating in Aluminium Shock Tube (AST) mode, it is capable of re-producing benchmark EAST data [37] - the works of Collen et al. [32, 35] and McGilvray et al. [116] provide a comprehensive summary of T6 commissioning and capabilities. In addition to replicating the radiance of real atmospheres and trajectories, spectral radiance analyses can be simplified by using a less complicated gas mixture such as pure nitrogen [18].

Cruden and Brandis [46] applied the NEQAIR [192, 44] spectral fitting program to pure nitrogen EAST data at 10.3 km/s to obtain number densities of electronic states responsible for radiation, along with rotational and vibrational temperatures, as a function of position behind the shock. Both Boltzmann and non-Boltzmann distributions were trialled to achieve close fits in the ultraviolet and visible respectively, as well as inclusion of contaminant species such as C, H and CN to improve their fits. Tibère-Inglesse and Cruden [187] performed a similar analysis to slower speed 7 km/s pure nitrogen cases from the same EAST dataset, where molecular species contribute to a greater portion of the observed spectral radiance. They state that thermal and possibly chemical equilibrium may not be achieved as far back as 50 mm/80 μs from the shock front. A Two-Temperature (2T; $T=T_{rot}$ and $T_{vib}=T_{el}$) analysis revealed differences between rotational temperatures of different

species, as well as differences between rotational and vibrational temperatures through the non-equilibrium region. Temperature profiles generated from different wavelength regions were shown to have some discrepancies. They also state that the distribution assumption (i.e. Boltzmann or non-Boltzmann) had no significant influence on the resulting temperatures. Other spectral fitting studies in pure nitrogen at relevant enthalpies have been performed by Tang et al. [180] from temporally-resolved relative-intensity shock tube ultraviolet spectra and in recombining plasma torch flows by Tibère-Inglesse et al. [188], both using SPECAIR spectral fitting software [102, 168] to show similar trends. Hence, it's been well demonstrated that spectrally resolved radiation measurements are a valuable means to characterise the thermochemical state through high-enthalpy flows. However, previous works make no attempt to ensure conservation of mass, momentum and energy through the test slugs for the extracted temperatures and densities.

The work herein applies the recently developed constrained spectral fitting routine from the University of Oxford Hypersonics group to characterise the thermochemical state through pure nitrogen test slugs from the T6 AST. Test cases ranging from shock speeds of 6.2 to 7.4 km/s are selected from the wider data set to perform an initial study. Limiting the species to pure nitrogen provides simplified test cases to trial numerical methods, before increasing the complexity by matching closer to the true flight case. Reducing the number of reactants in turn reduces the number of possible collision partners and the complexity of energy exchange reactions. Brandis and Cruden [18] have shown that by removing oxygen from synthetic air studies, the 11 species and 21 chemical reactions to consider are simplified to only 5 species (N, N^+, N_2, N_2^+, E^-) and 4 reaction mechanisms, summarised as:

$$N_2 + M \longleftrightarrow N + N + M \tag{6.1}$$

$$N + E^- \longleftrightarrow N^+ + E^- + E^- \tag{6.2}$$

$$N + N \longleftrightarrow N_2^+ + E^- \tag{6.3}$$

$$N^+ + N_2 \longleftrightarrow N_2^+ + N \tag{6.4}$$

Section 6.2 summarises the T6 test cases selected for study in this work. Section 6.3 then provides a brief overview of the spectral fitting routine and outlines the detectable molecular and atomic transitions expected over the ultraviolet and near infrared wavelength regions. Section 6.4 plots the vibrational temperature and mole fractions of molecular N_2, N_2^+ and

atomic N extracted for the chosen test cases. Finally, results are discussed and compared against predictions of the well-established Park 2T model [144, 145] and comparable data from the EAST facility.

6.2 Experimental Campaign

6.2.1 The Oxford T6 Stalker Tunnel in Aluminium Shock Tube Mode

The T6 Stalker Tunnel at the University of Oxford is a high-enthalpy transient ground test facility. The Aluminium Shock Tube (AST) is shown in Fig. 6.1. It is used to generate entry vehicle stagnation line flows at ground level. Chapter 3 provided detailed descriptions of the facility, its operation, and the telecentric Optical Emission Spectroscopy (OES) diagnostics used to capture normal shocks passing the test region.



Fig. 6.1 The T6 Aluminium Shock Tube, connected to the secondary driver (left) and dump tank (right). Taken from Glenn et al. [69].

Figure 3.21 in Chapter 3 showed examples of spatio-spectrally resolved images for T6s492 - a 6.65 km/s shock travelling through a 90 Pa pure nitrogen test gas. The non-equilibrium peak can be seen in both spectral channels immediately behind the shock, followed by a relaxation region, as the thermochemical state approaches equilibrium. Radiation is more intense in the UV/Vis region where N_2 second positive and N_2^+ first negative molecular bands dominate. Atomic N transitions are captured in the Vis/NIR, sat on an underlying N_2 first positive background. Data at lower pressures is favoured in these studies to reduce frequency of particle collisions and thus stretch the non-equilibrium region, enabling better spatial resolution of the states during the post-shock relaxation. However, this also

reduces the number of radiating particles in the test flow and can thus bring S:N challenges. The spectral traces extracted in Fig. 3.21 show relatively week S:N compared to other shock speeds and atmospheres traditionally performed in shock tube experiments, particularly in the Vis/NIR. Signal improves towards the non-equilibrium peaks, where radiation is more intense. The radiance profiles can be seen to just reach a steady plateau within the optics FOV, making them ideal for the present study to characterise the full thermochemical state evolution from initial excitation to (supposedly) equilibrium.

6.2.2 Test Summary

Figure 6.2 maps the pure nitrogen conditions achieved in the recent T6 AST low-speed campaign. A series of post-shock pressures were targetted to stretch out the non-equilibrium region by varying degrees. Initial studies of this dataset are given alongside equivalent synthetic air tests in the works of Glenn et al. [68]. The three pure nitrogen tests selected for spectral fitting analysis in this paper have been highlighted and are summarised in Table 6.1. These were selected to study the effect of shock speed variations for tests with similar post-shock pressures. The spectral fitting was performed using data from both ultraviolet and visible/near-infrared spectral channels simultaneously, over wavelength regions 290 to 520 nm and 585 to 850 nm respectively. Associated Instrument Line Shapes (ILS) for each channel are summarised in Table 6.2. The slit function is the same for all three T6 shots, since the same low resolution grating, centre wavelength and slit widths were used.

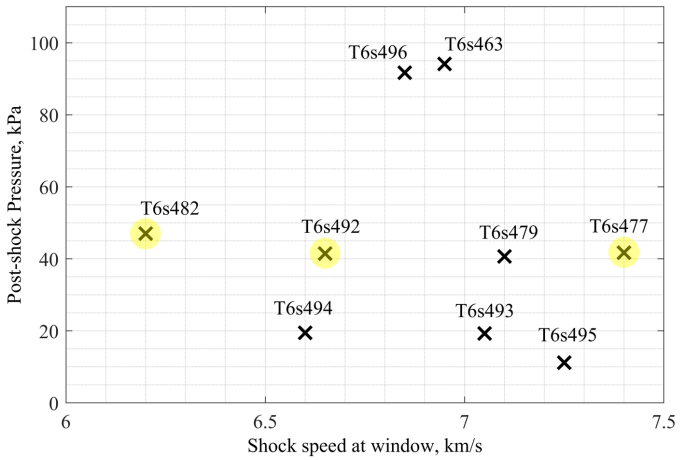


Fig. 6.2 Map of pure nitrogen conditions from recent T6 AST campaign. The tests for which spectral fitting have been performed in this paper have been highlighted. Adapted from Glenn et al. [68].

The T6 AST OES arrangements both maintained the narrowest slit width possible of 10μm, based on the findings of Chapter 4, to minimise the offset between equilibrium experimental data and CEA-NEQAIR. Equilibrium spectral radiance comparisons against CEA-NEQAIR are given in the Appendix B.1 for each test case. Additionally, the total SRF's characterised for each shot and spectral channel are also plotted in the Appendix B.2.

Table 6.1 Selected T6 test conditions to perform spectral fitting (top). Plus similar low and high pressure tests (bottom).

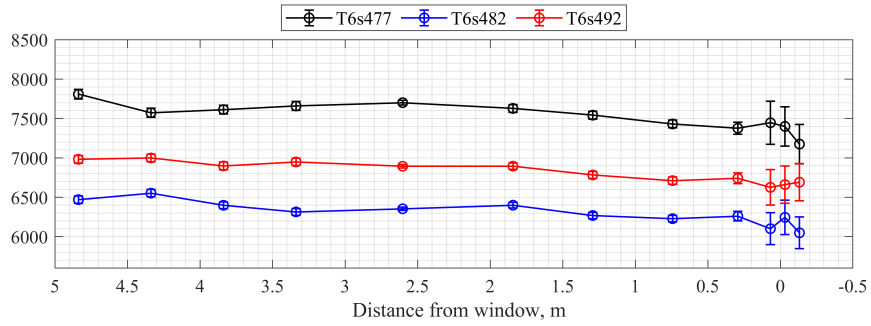
Shot No.	**$U_{s,\,window}$, km/s**	**P_{fill}, Pa**	**$P_{2,\,meas}$, kPa**	**Leak Rate, mPa/s**
T6s477	7.4	73	41.7	1.1
T6s482	6.2	107.5	47	0.7
T6s492	6.65	90	41.5	1.1
T6s494	6.6	40.5	19.5	1.2
T6s496	6.85	175	91.7	1.3

Table 6.2 ILS FWHM's used for spectral fitting of T6 data, fitted to the square root of a Voigt function. The same slit functions apply to all three T6 tests selected.

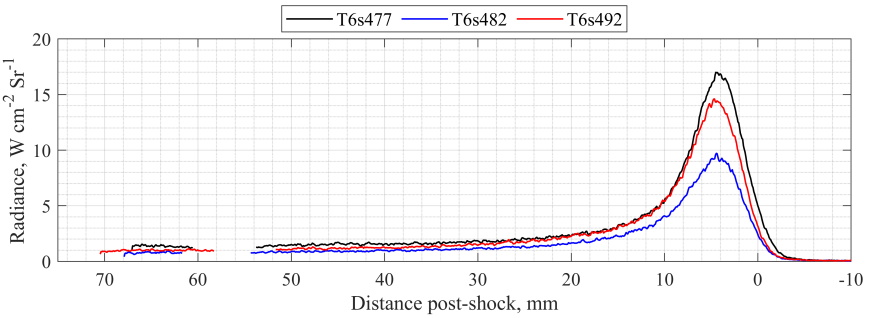
UV/Vis, Å		**Vis/NIR, Å**	
Gauss.	**Lorentz.**	**Gauss.**	**Lorentz.**
10	0.001	6	0.0005

6.2.3 Conditions Selected for Spectral Fitting

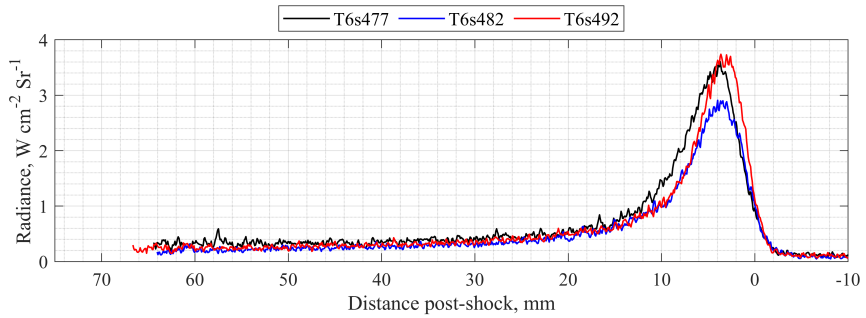
Figure 6.3 plots the shock speed and radiance profiles from each spectral channel, for the T6 pure nitrogen tests selected for study by spectral fitting in this paper. The shock profiles are only shown for the AST section of the facility, to avoid data before the conical expansion from the secondary driver, which will not be relevant to the final imaged test slug. The radiance profiles demonstrate the effect of increasing shock speed for tests with comparable post-shock pressures of ∼45 kPa.



(a) Shock speed profiles



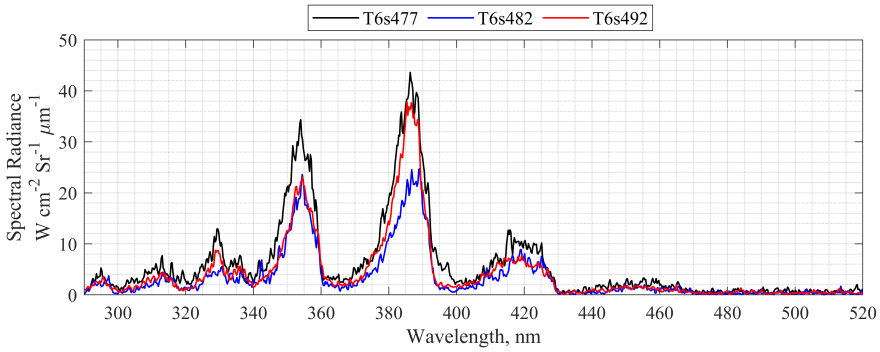
(b) UV/Vis radiance (290 - 520 nm)



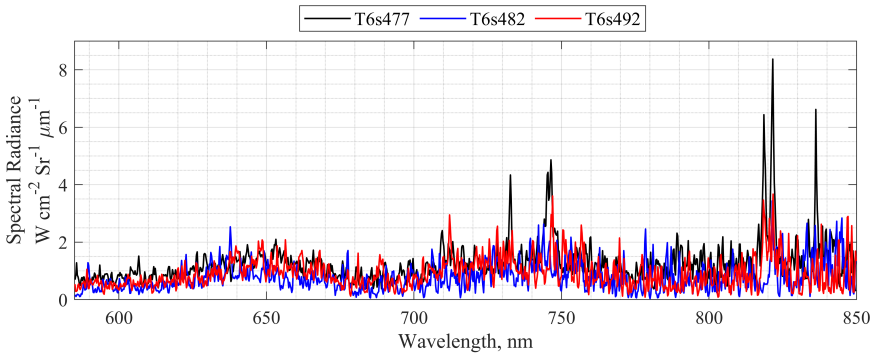
(c) Vis/NIR radiance (585 - 850 nm)

Fig. 6.3 Shock speed and radiance profiles of the T6 tests selected for spectral fitting in this paper. Shock profiles are only plotted for the AST section of T6

Spectrally resolved profiles are also plotted in Fig.'s 6.4 and 6.5 for the same three tests, extracted from the end of the observed test slugs and their non-equilibrium peaks respectively. Spectral resolution enables identification of species in excited energy states, which is valuable for thermochemical state characterisation.

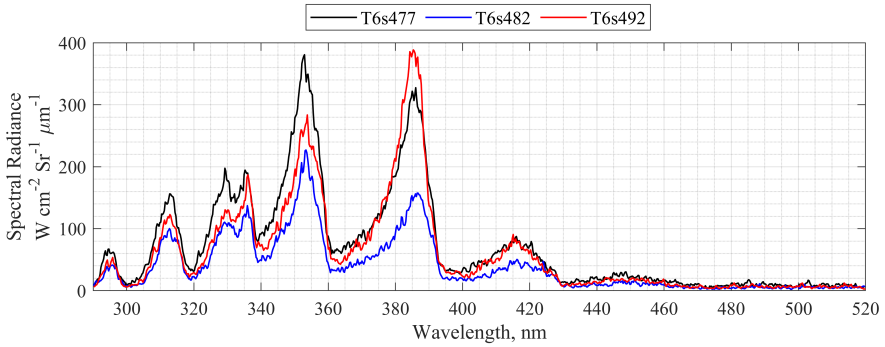


(a) 290 - 520 nm

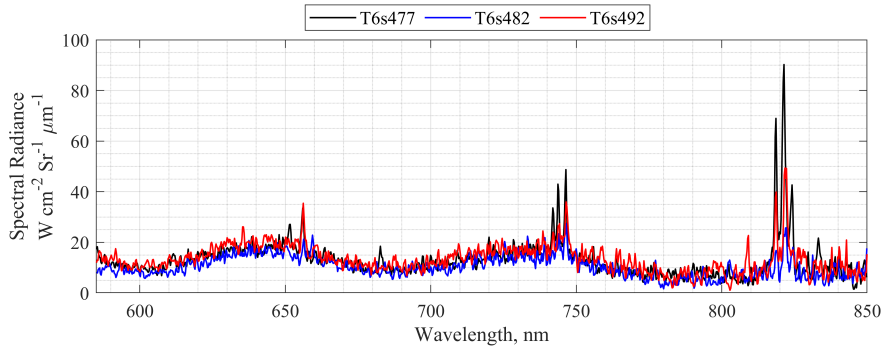


(b) 585 - 850 nm

Fig. 6.4 Spectra for T6 AST pure nitrogen tests selected for spectral fitting, from the end of each test slug.



(a) 290 - 520 nm

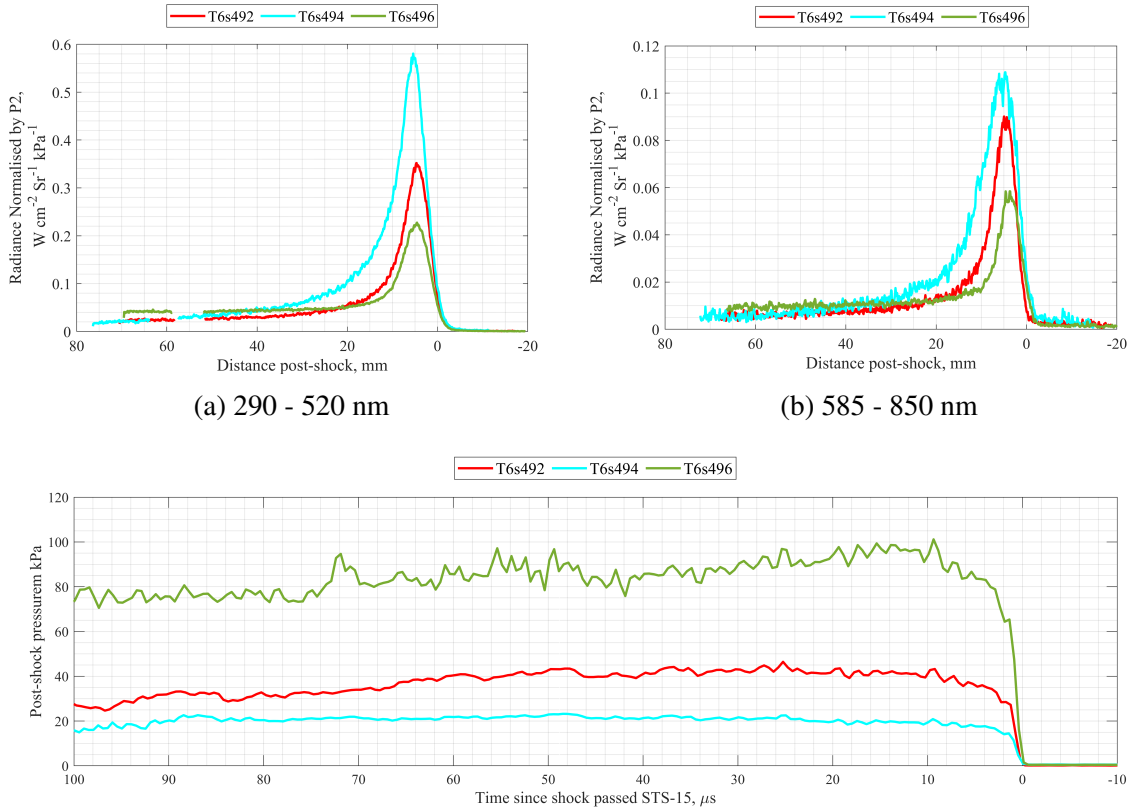


(b) 585 - 850 nm

Fig. 6.5 Spectra for T6 AST pure nitrogen tests selected for spectral fitting, taken over the peak 2 mm region.

6.2.4 The Effect of Pressure

Although they are not studied in this paper, the wider test matrix included tests of similar shock speed over a range of post-shock pressures. Lower pressure conditions reduce the frequency of collisions between particles in the test slug and hence prolong the relaxation phase. This helps to increase the spatial resolution of non-equilibrium phenomena, at the sacrifice of S:N. Figure 6.6 provides an example of such tests, shot details for which are included in Table 6.1. The radiances have been normalised by their respective post-shock pressures to help illustrate the continued relaxation for the lower pressure cases, as well as the proportionally higher non-equilibrium peak as pressure reduces. The corresponding pressure traces are provided in Fig. 6.6c. These are extracted from the penultimate STS-15, just before the shock is imaged.



(a) 290 - 520 nm

(b) 585 - 850 nm

(c) Static pressure profiles

Fig. 6.6 Radiance profiles of T6 AST tests with similar shock speeds (as listed in Table 6.1) normalised by respective post-shock pressures, to emphasise the extended relaxation in lower pressure tests. Static pressure traces from the penultimate STS before camera gating are also provided.

6.3 Constrained Spectral Fitting

6.3.1 Methodology

A novel constrained spectral fitting routine has been developed to convert spectral radiance data through a shock tube test slug, into spatially or temporally resolved temperature and number density profiles. This information helps to describe the evolution of the thermochemical state through the test slug. Chapter 5 provided a detailed account of the methodology and its validation, and demonstrates successful reproduction of vibrational temperature (T_{ve}), molecular N_2, N_2^+ and atomic N profiles through a series of NESS-NEQAIR [29, 44] 1D simulations with implementation of various experimental artefacts. An outline of the inputs and outputs of the routine were summarised in Table 5.1.

The routine operates within the framework of a 2T model and assumes Boltzmann distributions at all locations. The uncertainties associated with the extracted temperatures and number densities at each point are evaluated by performing a Monte Carlo analysis. A series of randomly distributed initial guesses are trialled at each point and the standard deviations of the results calculated. The 95% confidence limits are plotted for all results in Section 6.4, corresponding to $\pm$ two standard deviations. This represents only the uncertainties associated with the spectral fitting process, and not those associated with the calibration of the radiance data.

6.3.2 Spectral Information

Large amounts of radiation originate from molecular species at the considered low-speed conditions, as opposed to atomic species in the faster Earth return missions. Table 6.3 lists the main molecular transitions relevant to the pure nitrogen tests, which emit in the wavelength regions being used for spectral fitting in the present study. The cyano-radical (CN) is included, since carbon contamination is an inherent characteristic of shock tube facilities despite rigorous efforts to minimise it (as demonstrated in Chapter 4). The CN violet band superimposes on the N_2^+ first negative band, which can create difficulties in distinguishing between the two unless high resolution spectra are attained. Table 6.4 also provides the nitrogen atomic line transitions seen in the Vis/NIR, for which the upper and lower energy level values are quoted.

Table 6.3 Summary of molecular transitions observed in selected pure nitrogen test cases. The energy of the upper level of each species is given relative to their ground states. CN is included due to the presence of carbon contamination.

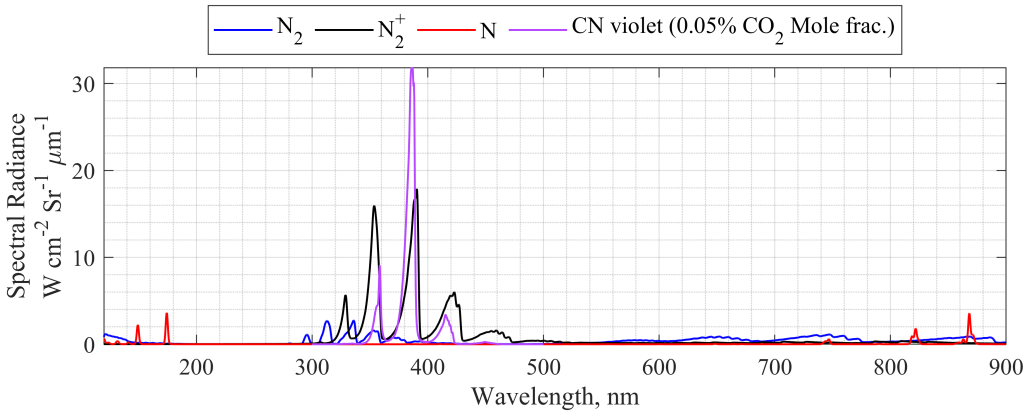
Name	**Transition**	**Energy of upper level (cm^{-1})**	**Region of emission**
N_2 first positive	N_2: $B^3\Pi_g \rightarrow A^3\Sigma_u^+$	59,619	500–1100 nm
N_2 second positive	N_2: $C^3\Pi_u \rightarrow B^3\Pi_g$	89,137	250–450 nm
N_2^+ first negative	N_2^+: $B^2\Sigma_u^+ \rightarrow X^2\Sigma_g^+$	25,461	300–450 nm
N_2^+ Meinel (A-X)	N_2^+: $A^2\Pi_u \rightarrow X^2\Sigma_g^+$	9167	500–900 nm
CN violet	CN: $B^2\Sigma^+ \rightarrow X^2\Sigma^+$	25,753	350–430 nm

Figure 6.7 plots the spectral radiance contributions of the listed molecular and atomic transitions, from a CEA-NEQAIR [115, 192] prediction of test case T6s492. Results have been convolved with the line shapes given in Table 6.2. A 0.05% mole fraction of CO_2 is included to give a realistic CN contamination level in the equilibrated post-shock gas. It is evident that even in its small concentrations, CN can dominate regions in the UV/Vis.

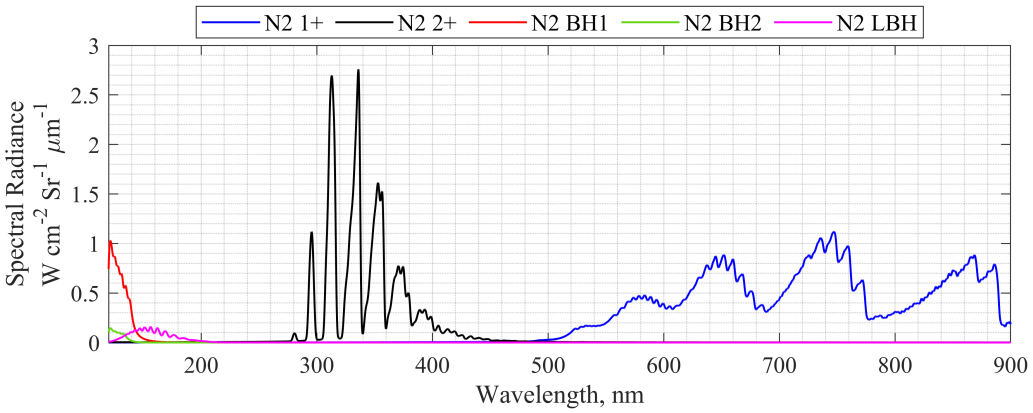
Table 6.4 List of atomic nitrogen lines observed in Vis/NIR of selected tests.

Wavelength (nm)	**Upper level**			**Lower Level**			**Einstein**
	Energy (cm^{-1})	**designation**	**g**	**Energy (cm^{-1})**	**designation**	**g**	**coefficient (s^{-1})**
742.364	96,750.8	$3p^4S$	4	83,280.32	$3s^4P$	2	5.64×10^6
744.23	96,750.8	$3p^4S$	4	83,314.09	$3s^4P$	4	1.19×10^7
746.831	96,750.8	$3p^4S$	4	83,360.89	$3s^4P$	6	1.96×10^7
821.634	95,532.1	$3p^4P$	6	83,361.23	$3s^4P$	6	2.26×10^7
824.239	95,493.7	$3p^4P$	4	83,361.3	$3s^4P$	4	1.31×10^7
868.028	97,805.8	$3p^4D$	4	86,217.29	$3s^4P$	4	2.67×10^7
868.028	94,881.8	$3p^4D$	2	83,361.43	$3s^4P$	4	2.53×10^7
868.342	94,830.9	$3p^4D$	6	83,314.67	$3s^4P$	6	1.88×10^7
871.17	94,793.5	$3p^4D$	4	83,314.68	$3s^4P$	4	1.29×10^7

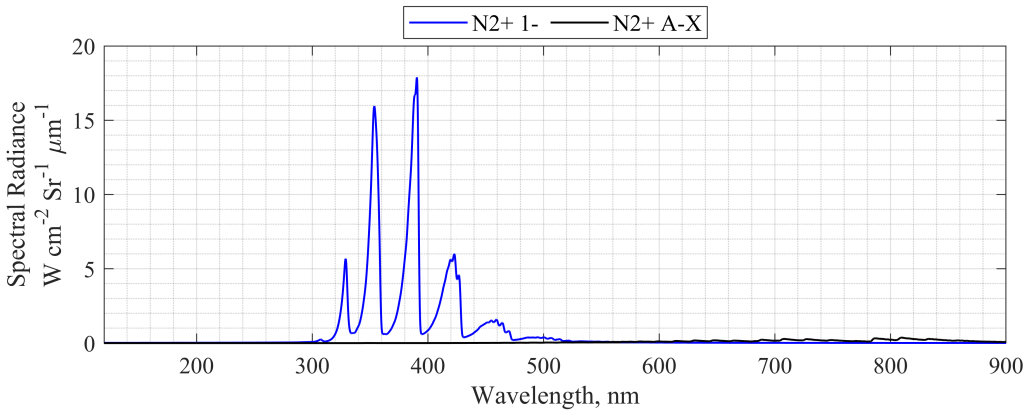
Despite this, the validation study in Chapter 5 showed the constrained spectral fitting routine to accurately capture the species of interest, in the presence of contaminants in their expected densities. Additionally, work by Clarke et al. [31] shows that within the framework of a 2T thermochemistry model, the addition of carbon contaminants (representative of the amounts measured in spectra) does not significantly affect the temperature profiles nor the molecular species present in the flow. This implies that, for optically thin cases, spectra attained from a shock tube experiment are a superposition of carbonaceous species with the species intended to exist in the radiating test gas. All spectral information is therefore still valid, providing the two can be resolved from one another. The ease of this is improved by keeping contaminant levels to a minimum, and by capturing higher resolution spectra. The spectral fit results from the real T6s492 radiance data are plotted in Fig. 6.8 through different portions of the thermochemically relaxing test slug.



(a) T6s492: Nitrogen species at equilibrium plus CN

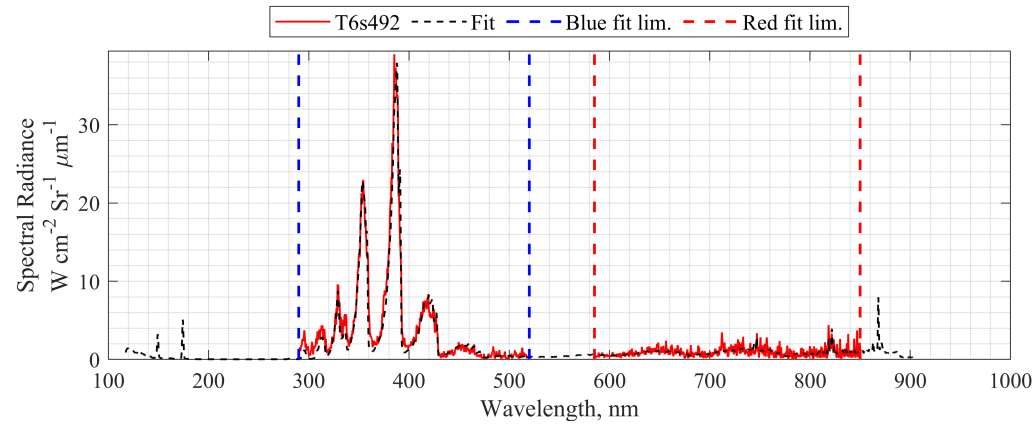


(b) T6s492: N_2 bands

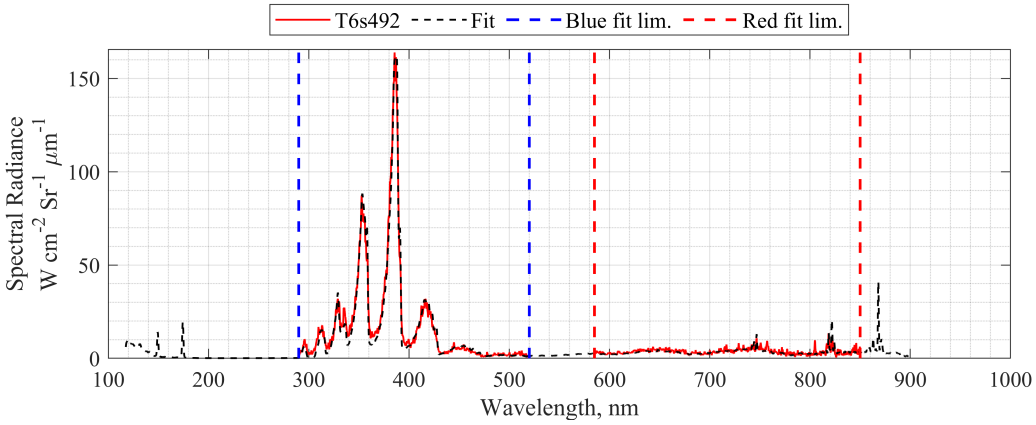


(c) T6s492: N_2^+ bands

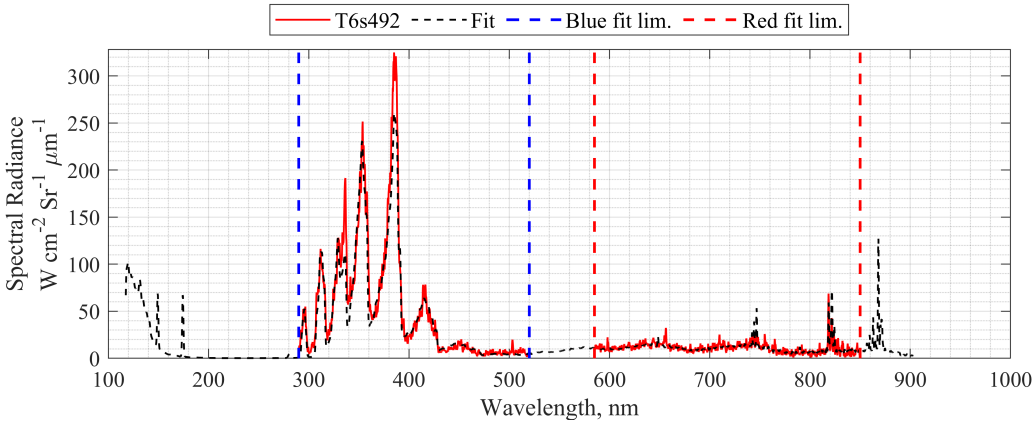
Fig. 6.7 CEA-NEQAIR v15.1 simulation results for T6s492 (6.65 km/s at window, 89.95 Pa fill pressure, ∼41.5kPa post-shock pressure) in pure nitrogen with 0.05% CO_2 mole fraction. Individual species and molecular bands are plotted separately within subplots. N+ and other N2 bands have been ignored since they are negligible in comparison. Spectra have been convolved with ILS of the experimental data.



(a) End of observed test slug (∼110 μs)



(b) Relaxing (20 μs)



(c) Peak non-equilibrium (5μs)

Fig. 6.8 Spectral fit results for nominal T6s492, through different stages of the excited test slug. Results are exemplary of typical spectral fit agreements.

6.4 Results

The extracted vibrational temperatures, molecular N_2, N_2^+ and atomic N number density profiles for the selected test cases are now plotted and discussed. These parameters were confirmed to be accurately characterised during the prior validation studies in Chapter 5. Although the OES systems enable spatial resolution of the spectral evolution through the test slug, the spectral fitting outputs have been plotted against the time passed since being processed by the normal shock. This conversion is made via Equation 6.5, where $U_{2,s}(x)$ is the post-shock velocity profile as a function of distance post-shock (in the shock's frame of reference) as defined by using the assumption of a Mirels boundary layer [126]. The integration shown enables conversion of the spatial axis from each shot into a common temporal axis. Plotting against time also provides a universal reference to compare results between shock tubes of different diameters, as is done between T6 AST and EAST at the end of this section, since the spatial domain is augmented by boundary layer mass consumption [29].

$$t = \int \frac{dx}{U_{2,s}(x)} \tag{6.5}$$

All T6 AST spectral fits have been performed by assuming constant shock speed (equal to the value quoted at the window) as listed in Table 6.1. This should be valid since there's relatively little shock deceleration during the shock trajectories. CEA predictions are also shown as a reference, using the same shock speed. The reader is also reminded that the uncertainties shown in the following plots refer to the fitting routine, and do not account for the uncertainties of the radiance measurements.

6.4.1 Vibrational Temperature (T_{ve})

The work of Chapter 5 showed the spectral radiance profiles to be strongly dependent on T_{ve} at the considered low speeds. Figure 6.9 plots the T_{ve} profiles acquired for the chosen test cases, ranging from 6.2 to 7.4 km/s at the window. All tests follow the same general trend, demonstrating peak temperatures after initial processing by the shock wave and monotonically and asymptotically decreasing until settling at approximately the CEA prediction, indicating the end of thermal relaxation. For the selected tests, all with similar post-shock pressures of $\sim$45 kPa, the time for thermal relaxation shows little dependence on shock speed. It takes approximately 60 to 100 μs for the fastest and slowest to reach the CEA value. Interestingly, the initial T_{ve} of T6s492 begins higher than the faster T6s477 test case and demonstrates a more rapid initial relaxation. The spectral fitting has been repeated

to validate this. Calibration results have been inspected and no obvious flaws identified. The result is therefore believed to be physical, though repeat tests are recommended.

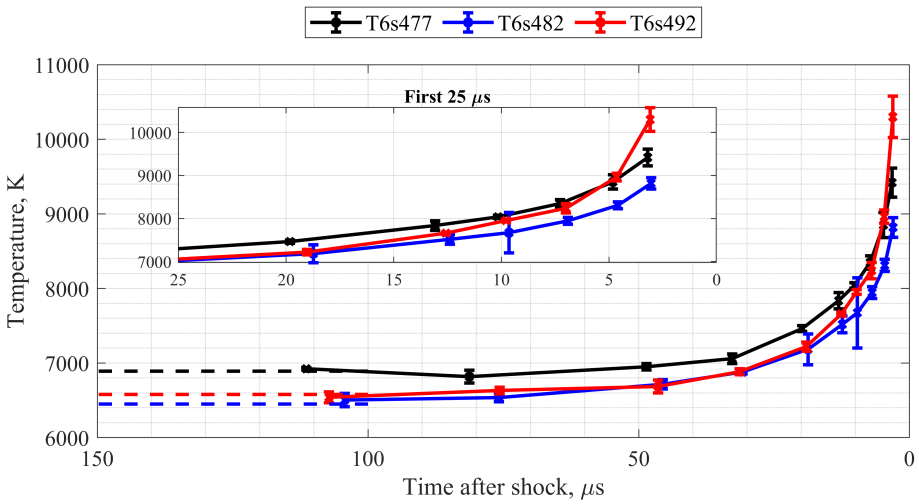


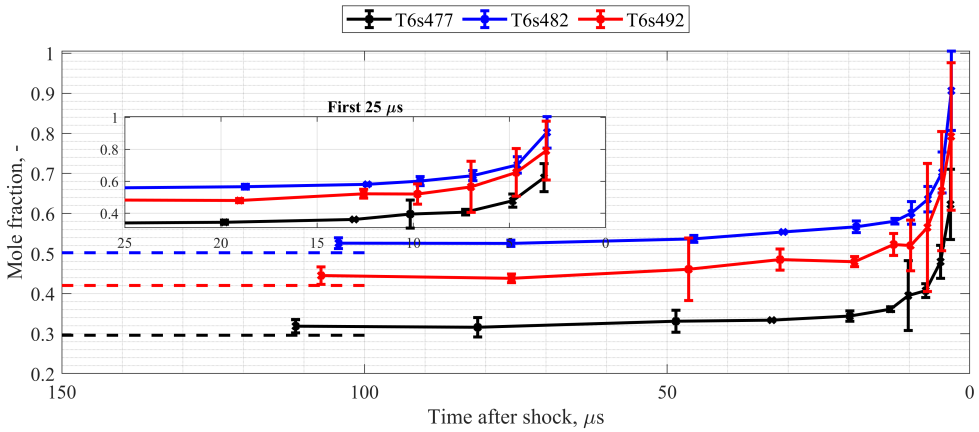
Fig. 6.9 Vibe-electronic temperature profiles extracted by constrained spectral fitting for the selected pure nitrogen shots. Dashed lines show CEA predictions.

6.4.2 Species number densities

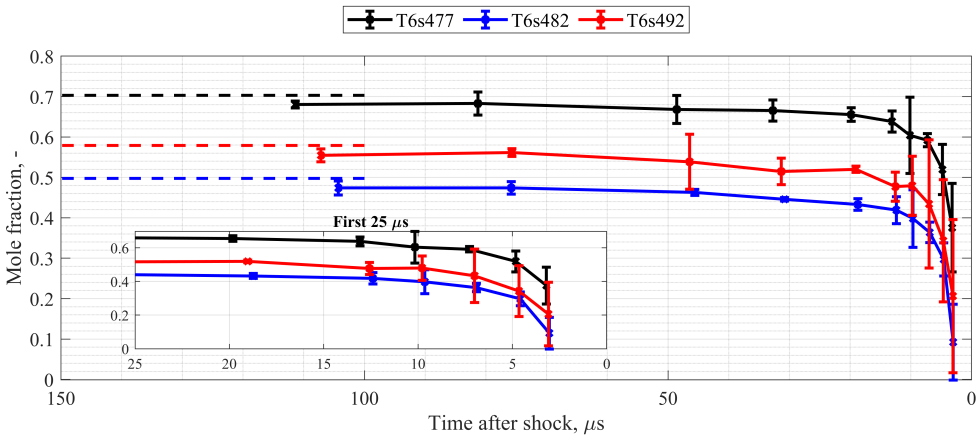
Figure 6.10 plots the mole fraction profiles for molecular N_2, N_2^+ and atomic N for each test. The results are discussed one at a time in the following subsections.

N_2

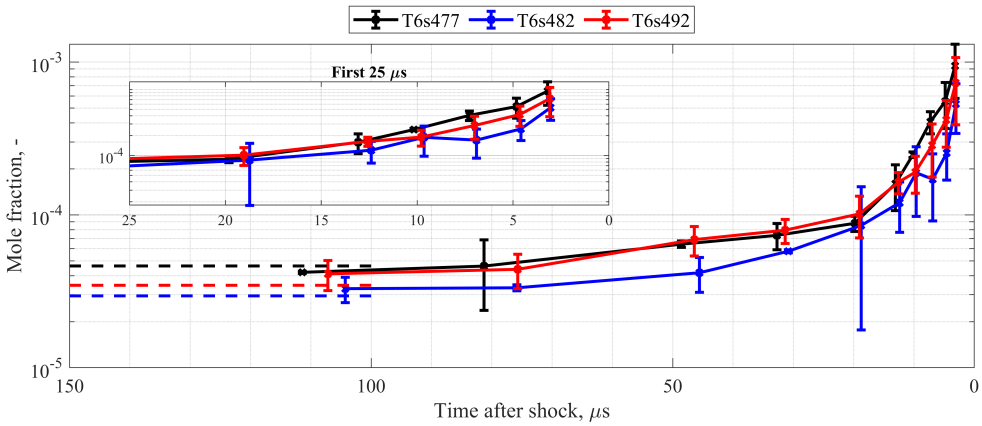
Excited N_2 molecules emit detectable radiation for both Blue and Red spectral channels. The N_2 second positive band emits in the UV from 300 to 400 nm, while the N_2 first positive band creates a background signal at the higher Vis/NIR wavelengths. This provides the fitting routine information to accurately capture the N_2 number densities through the test slug. Figure 6.10a plots the constrained spectral fit N_2 outputs of the selected test cases. All mole fractions continue to monotonically and asymptotically decrease towards the CEA mole fraction. Although most N_2 dissociation appears to take place within the first $\sim$25 μs post-shock, the CEA predictions are not reached for any of the tests within the observable test slugs. This suggests chemical non-equilibrium effects may be sustained through all observable test gas, which is also supported in the analysis by Clarke et al. [31]. A clear shock velocity dependence is demonstrated across the chosen test cases, with higher shock speeds causing more N_2 reduction through all portions of the test slug.



(a) N_2



(b) N



(c) N_2^+

Fig. 6.10 Mole fraction profiles extracted by constrained spectral fitting for the selected pure nitrogen shots. Dashed lines show CEA predictions.

N

Figure 6.10b plots the mole fractions of atomic N extracted from the constrained spectral fitting routine. In contrast to N_2, the atomic N follows a monotonic and asymptotic increase through the shock layer, approximately the inverse of N_2. This is therefore a strong indication of N_2 depletion producing atomic N in almost exactly a 1:2 ratio (since the number densities of ionised species are 3 to 4 orders of magnitude lower). This confirms the reaction mechanism to be dissociation. The most rapid N production corresponds with the most rapid N_2 depletion immediately behind the shock front, where vibrational temperature (and consequently the the dissociation rate) is highest. Furthermore, the decay in gradients between the N_2 and N profiles align closely. It's evident that N production continues through the observable test slug, not quite reaching the CEA equilibrium predictions for all T6 AST cases. This further supports the notion of chemical non-equilibrium being sustained within the observable 100 μs of test slug for all tests.

A strong shock velocity dependence is again demonstrated, showing a $\sim$300% increase in N mole fractions immediately behind the shock, by increasing from 6.2 to 7.4 km/s, and over 40% after 100 μs of relaxation. This demonstrates the thermochemical state of the non-equilibrium region has a high sensitivity to shock speed, even over a relatively small velocity range.

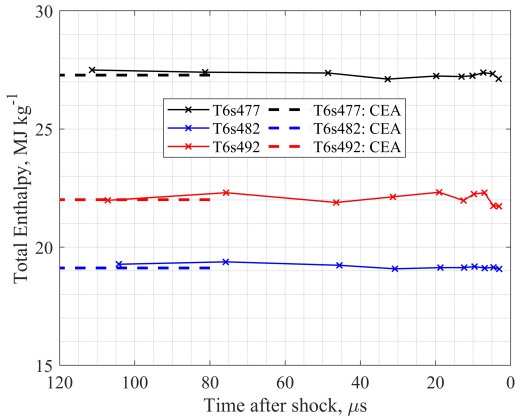
N_2^+

The N_2^+ first negative band emits intensely in the UV/Vis wavelengths, allowing N_2^+ to be detected despite having number densities 3 to 4 orders of magnitude less than the neutrally charged N and N_2 species. This in itself demonstrates that although ionisation does occur at these low speeds (to produce a so-called "partially ionised plasma") the vast majority of species remain neutral. Figure 6.10c plots the N_2^+ mole fraction profiles extracted by spectral fitting of the selected tests.

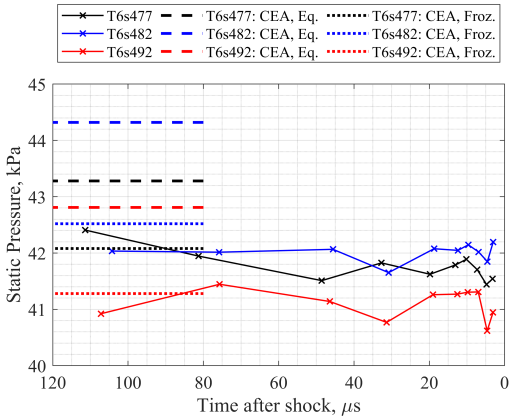
The N_2^+ number densities drop by two orders of magnitude from 3 μs to 100 μs after being processed by the shock (hence logarithmic y axes are used to resolve the later stages of relaxation). This suggests there to be an initial surge in N_2^+ production by ionisation of N_2 molecules and higher T_{ve} values. Dissociation reactions lower the flow temperature, increasing the likelihood of recombination during the relaxation process. For the observable test slugs, N_2^+ relaxes closer to the CEA predicted mole fractions than previously seen for the neutral species, mostly within 100 μs.

6.4.3 Physical properties

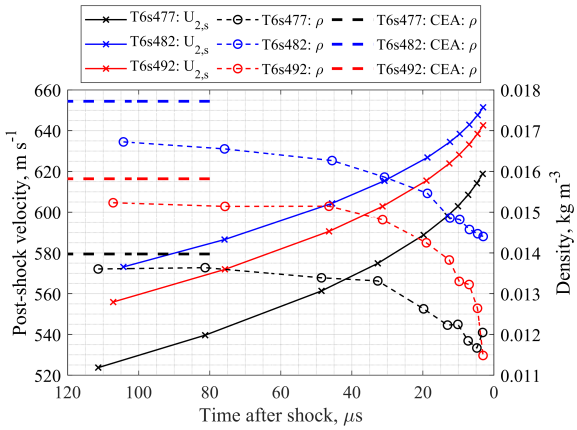
Figure 6.11 plots the corresponding physical properties extracted through the selected pure nitrogen test slugs. These are generated by feeding the final results into the in-house thermochemical property and transport library, OCEAN. Predictions from CEA are also shown for comparison. These are provided to supplement the current and any future analyses of the chosen test cases.



(a) Total enthalpies



(b) Static Pressures

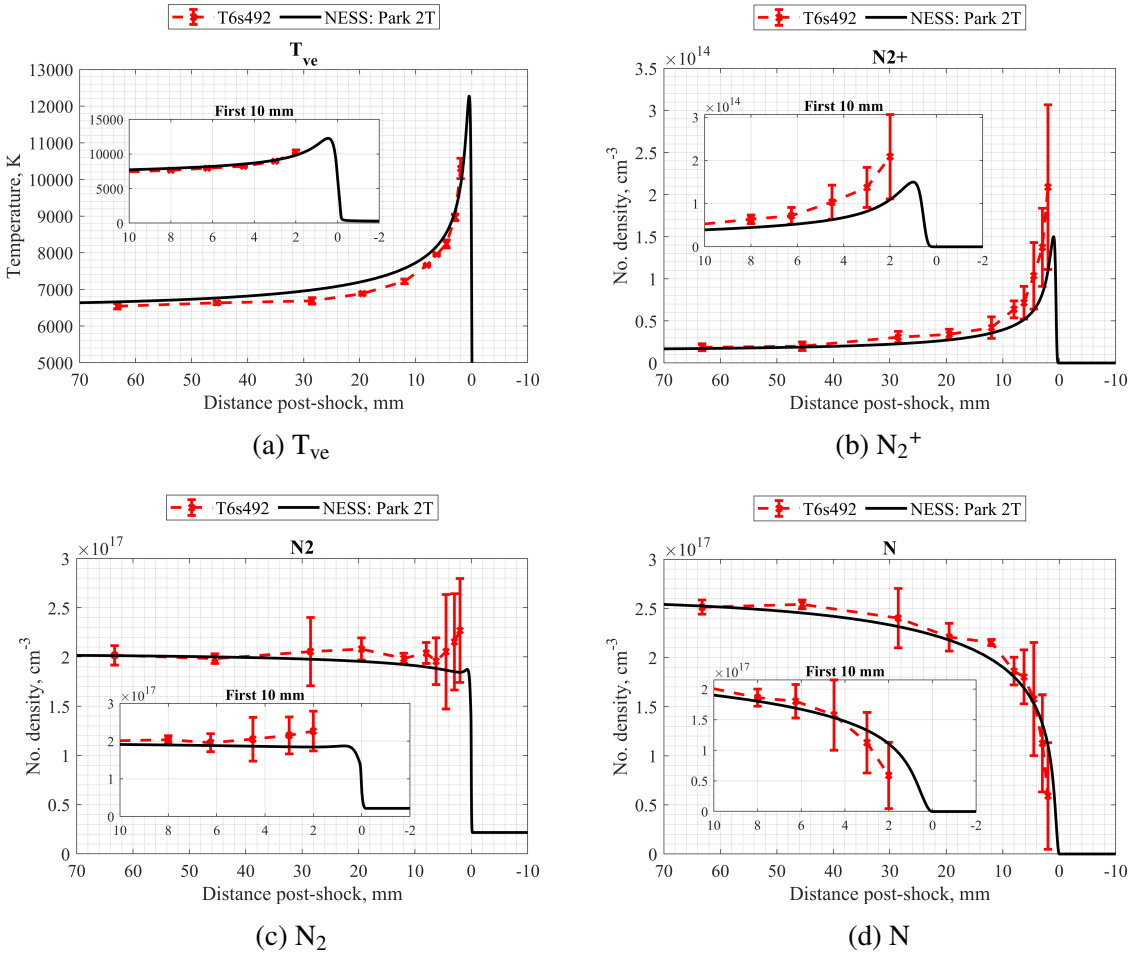


(c) Velocity and densities

Fig. 6.11 Post-shock physical properties corresponding to the spectral fitting results of the selected pure nitrogen tests.

6.4.4 Comparison Against Park 2T

The next step in this analysis is to compare results extracted from the constrained spectral fitting routine against that of the well-established Park 2T model predictions. Figure 6.12 compares the profiles attained from fitting of T6s492 emission spectra against the one-dimensional predictions of the Non-Equilibrium Shock Solver (NESS) [30] using the Park 2T model and rates [144, 145].



(a) T_{ve} (b) N_2^+

(c) N_2 (d) N

Fig. 6.12 Comparison of profiles extracted for T6s492 against the predictions of NESS 1D solver using Park 2T model and Park rates.

Results show the vibrational temperature compares reasonably well between the two, though there is a slightly more rapid decrease from the experimental data. The N_2^+ profile shows Park 2T to have a significant under prediction in the non-equilibrium region, compared to the experimental profile. Finally, both the molecular N_2 and atomic N number density profiles suggest the Park 2T model and rates predict an initial more rapid dissociation of N_2

than seen in the experimental data. Dissociation in 2T models is determined by a $\sqrt{T_{tr} \times T_{ve}}$ relation, suggesting a method to accurately extract T_{tr} would compliment this study. The T_{tr}'s extracted from the considered low resolution pure nitrogen data showed large uncertainties, and sometimes unrealistic profiles, and thus have been omitted from this study. Overall, these comparisons provides an early indication of how rates at low-speed conditions may be modified, though this analysis should be continued for a wider range of test cases in future work.

6.4.5 Comparison Against EAST

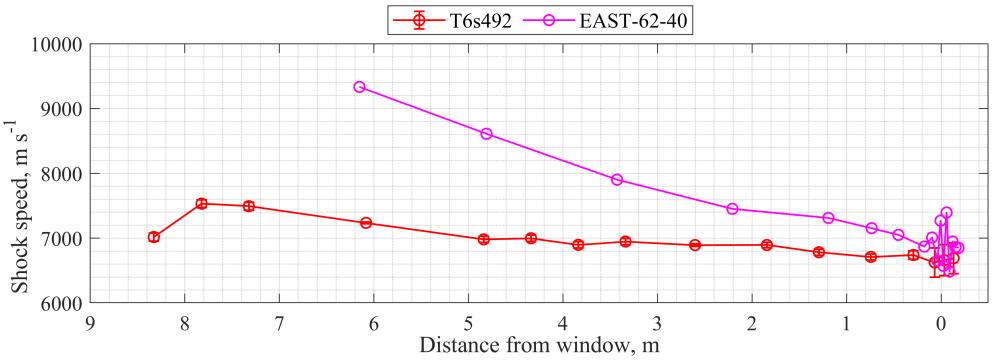


Fig. 6.13 Shock speed profiles of T6s492 and EAST-62-40 relative to optical access location.

Figure 6.13 compares the nominal T6 test T6s492 shock trajectory to that of EAST shot 40 from test series 62 [18] ("EAST-62-40"). This EAST case has been previously analysed in the constrained spectral fitting validation work in Chapter 5 and was used to demonstrate the significance of shock deceleration effects on the fitting outputs. Here, these results are plotted with the T6 AST test case of most comparable shock speed to provide a cross-facility comparison. Table 6.5 summarises the parameters of each test. Although the spectral limits differ between T6 AST and EAST spectral channels, they encapsulate the same emitting species and therefore thermochemistry. Different Instrument Line Shapes between the facilities are also summarised in Table 6.6.

Table 6.5 Selected T6 and EAST test conditions for analysis. Wavelength ranges used for spectral fitting are listed. Shock speeds quoted are as measured at windows.

Shot No.	**U_s, km/s**	**P_{fill}, Pa**	**$P_{2,\,meas}$, kPa**	**Leak Rate, mPa/s**	**UV/Vis (nm)**	**Vis/NIR (nm)**
T6s492	6.65	90	41.5	1.1	290-520	585-850
EAST-62-40	6.88	26.6	13.6 (CEA)	-	330-480	480-880

Table 6.6 ILS FWHM's used for spectral fitting of selected tests, fitted to the square root of a Voigt function.

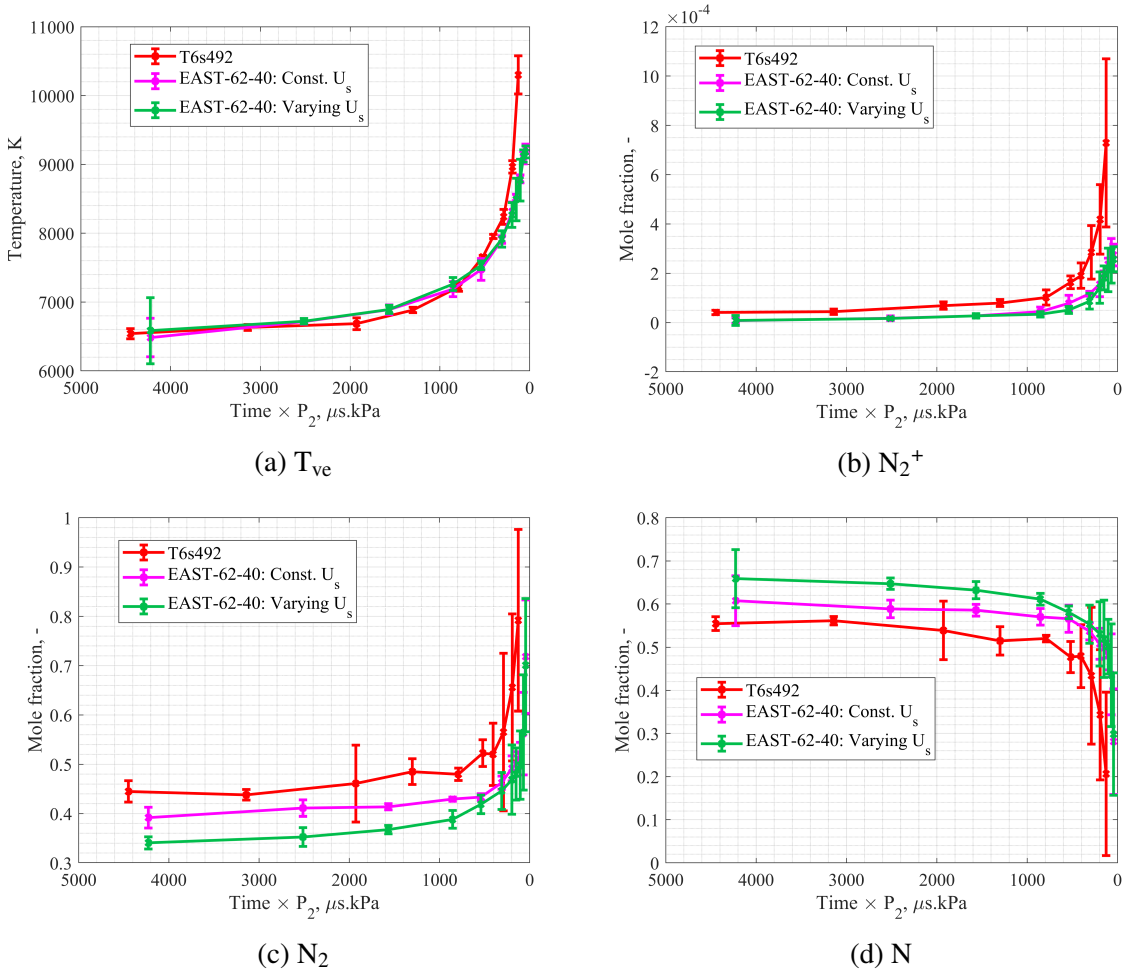
Shot No.	UV/Vis, Å		Vis/NIR, Å	
	Gauss.	Lorentz.	Gauss.	Lorentz.
T6s492	10	0.001	6	0.0005
EAST-62-40[18, 187]	8.442	0.446	24.1	0.6

Figure 6.14 plots T_{ve}, molecular N_2, N_2^+ and atomic N profiles extracted from both tests. The x-axis used to compare results between tests is the time post-shock multiplied by the respective nominal post-shock pressures, as stated in Table 6.5. As was previously explained, converting post-shock distance to post-shock time via Eq. 6.5 removes the augmentations caused by different boundary layer consumptions. This is an important step since EAST has a smaller tube diameter of 101.6 mm, compared to T6 AST's 225 mm. Additionally here, since the EAST test is of a lower pressure than the considered T6 AST tests, the non-equilibrium region is thus stretched out (as has been illustrated in Section 6.2.4). The profiles have therefore been normalised by the post-shock pressure to approximately account for the pressure difference between the two. In addition, two iterations of the EAST spectral fitting were carried out: one assuming constant shock speed at the window; and one using the in-house LASTA code [170] to account for enthalpy variations owed to the shock deceleration effects.

The T_{ve} profiles in Fig. 6.14a demonstrate close agreement between the two tests, with profiles almost overlapping. This is an extremely valuable result as it shows the temperature profiles can be extracted consistently across facilities with different driver technologies, shock trajectories and spectral arrangements. It is strong evidence to suggest the thermal relaxation has been characterised correctly and validates the normalisation used as a reasonable approximation.

The molecular N_2 and atomic N profiles have previously been shown to have increased sensitivity to shock speed trajectories. This is demonstrated again in Fig.'s 6.14c and 6.14d, where there is evidently more N_2 dissociation in the EAST-62-40 test, which is of slightly higher shock speed at the window and has much stronger shock deceleration.

Finally, the N_2^+ profile is interesting since the slower speed T6s492 demonstrates increased ionisation. This aligns with the slightly higher T_{ve} immediately behind T6s492 and the relatively high N_2^+ first negative peak at $\sim$380 nm in Fig. 6.5a. A possible explanation is excess CN contribution for this particular shot, though the measured leak rate was comparable to other T6 tests studied in this paper and the spectral fitting routine has previously been shown to account for CN contributions well by including CN in the fitting procedure.



(a) T_{ve} (b) N_2^+

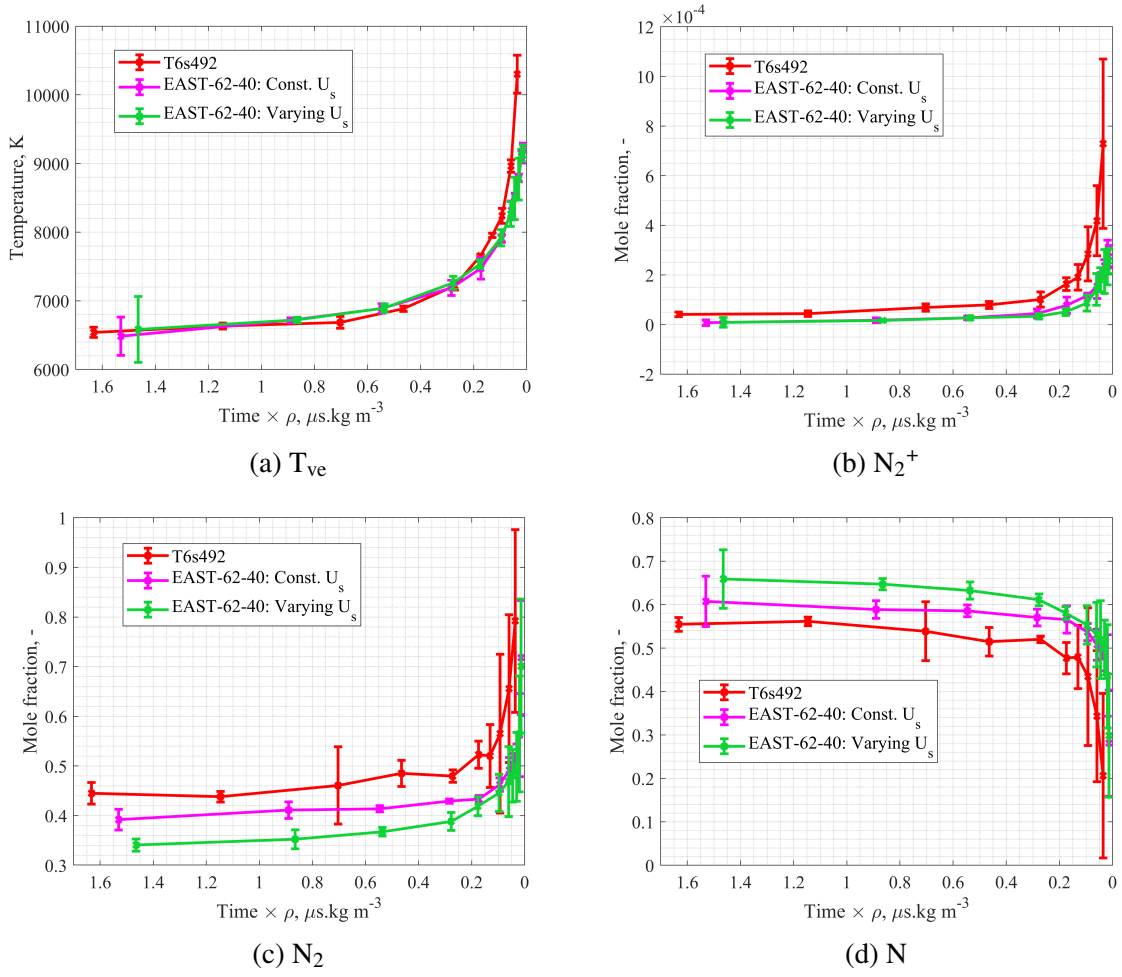
(c) N_2 (d) N

Fig. 6.14 Comparison of T6s492 and EAST-62-40 outputs from constrained spectral fitting. x-axes have been normalised by multiplying the time post-shock by the nominal post-shock pressures listed in Table 6.5.

Additionally, the T6s492 N_2^+ profile fits in between the faster and slower T6s477 and T6s482 results respectively, as shown in Fig. 6.10c, suggesting it's not a result particular to just T6s492. It's therefore recommended that further spectral fitting is performed over a wider range of T6 and EAST test cases of comparable conditions to test this result, and evaluate if this finding is within shot-to-shot variations. This also in itself suggests higher resolution spectra around the N_2^+ first negative band would be useful in future experiments, to help confidently resolve it from the CN violet contributions.

An alternative approach to normalising by the post-shock pressure is to use the density profiles extracted from the spectral fitting routine. Figure 6.15 thus repeats the data from Fig. 6.14, with the time post-shock multiplied by the local inferred density to normalise the x-axes. The resulting profiles exhibit trends that closely mirror those obtained from

post-shock pressure normalisation. Consequently, all the conclusions drawn earlier remain valid, and both parameters - post-shock pressure and local density - are demonstrated as a valid means to normalise the non-equilibrium relaxation across the range of conditions considered.



(a) T_{ve} (b) N_2^+

(c) N_2 (d) N

Fig. 6.15 Comparison of T6s492 and EAST-62-40 outputs from constrained spectral fitting. x-axes have been normalised by multiplying the time post-shock by the local densities inferred by the spectral fitting routine.

6.5 Conclusion

A new constrained spectral fitting routine has been applied to pure nitrogen absolute radiance measurements acquired from the University of Oxford's T6 Aluminium Shock Tube for shots between 6.2 and 7.4 km/s, to characterise the thermochemical state evolution one-dimensionally behind the shock fronts. Results demonstrate various degrees of thermal and chemical non-equilibrium through the test slugs. For the selected tests of ∼45 kPa post shock pressure, the CEA equilibrium temperature is reached within 60 to 100 μs after being processed by the shock. Significant sensitivity to shock speed is shown for both molecular N_2 and atomic N number densities. Furthermore, experimental profiles extracted suggest current Park 2T models and rates may be over predicting the rate of N_2 dissociation immediately behind the shock. Though failure to reach CEA mole fractions suggests chemical non-equilibrium exists within the observable test slugs. The $N_2{}^+$ mole fractions appear to be very sensitive to the T_{ve} temperature profile, as they drop by approximately two orders of magnitude over the observable test slugs. Comparisons to both Park 2T and EAST shows a high $N_2{}^+$ density of the nominal T6 AST 6.65 km/s test case. Spectral fitting of a wider range of conditions between facilities is recommended to further investigate this and high resolution spectra around the $N_2{}^+$ first negative band are recommended in future campaigns. Finally, good agreement is shown in the cross-facility comparison of T6 AST and EAST data with similar shock speeds, with a pressure or density scaling applied. This study has demonstrated successful results from both the new T6 AST dataset and the constrained spectral fitting technique, providing results to complement that of prior spectral fitting studies. Revisions and improvements may be necessary as new measurement techniques yield additional information for integration into the routine, alongside updates to the NEQAIR radiative modelling.

Acknowledgments

The authors would like to thank Dr Tobias Hermann for the generous loan of the Deuterium calibration lamp, making acquisition of data from 200 to 300 nm feasible. We would also like to thank Tristan Crumpton for his exhaustive efforts operating T6 during testing. Additional thanks go to Chris Hambidge for his relentless efforts to ensure these experiments were carried out successfully and safely. Finally, thanks are extended to Dr Brett Cruden and Dr Aaron Brandis at NASA Ames for their ongoing support and discussions.

Statement of Authorship

Title: Thermochemical Characterisation of Shock-Heated Pure Nitrogen
Status: Unpublished and unsubmitted work written in a manuscript style

Author Contributions:

- **Alex Glenn** - Lead author, primary code developer, data curation, formal analysis and writing.
- **Justin Clarke** - Secondary code developer.
- **Peter Collen** - Supervision as Postdoctoral Research Assistant.
- **Luca Di Mare** - Assisted in code conceptualisation.
- **Matthew McGilvray** - Supervision as Principal Investigator, and organised and managed funding.

Student Confirmation: **Date:** 14/10/2024



Supervisor Confirmation: **Date:** 15/10/2024



Chapter 7

Thermochemical Characterisation of Shock-Heated Synthetic Air

> Research is what I'm doing when I don't know what I'm doing.
>
> Wernher von Braun

Preamble

The ultimate goal of this thesis is to characterise the non-equilibrium relaxation through a synthetic air shock layer, providing data directly applicable to the stagnation line of a Low Earth Orbit return vehicle - from the bow shock to the boundary layer edge. This chapter completes that aim. It begins with a summary of radiance data and key spectral features observed in low-speed synthetic air conditions achieved in the T6 Aluminium Shock Tube. A 7.3 km/s test case is then selected for detailed spectral fitting analysis, yielding temperature and species number density profiles through the relaxing test slug. By normalising the data based on the time elapsed since being processed by the shock and the nominal post-shock pressure, thermochemical state information is obtained that is directly relevant to the vehicle's stagnation line, thereby fulfilling the primary objective of this thesis.

This chapter is a draft of work intended for future journal publication, which has been reformatted and adapted for inclusion in this thesis. A statement of authorship is provided at the end of the chapter, while references are contained within the main body of references at the end of the thesis. Relevant sections of the appendix, containing additional information, are referenced as needed throughout this chapter.

7.1 Introduction

During a Low Earth Orbit (LEO) return mission, the entry vehicle travels at hypersonic speeds (of up to Mach 25) and must endure the consequent harsh, high-temperature environment. A strong bow shock ahead of the vehicle provides a mechanism to raise the internal energy of the gas molecules and initiate dissociation, ionisation and radiation emission. These processes must occur for the shocked gas to attain a new state of thermochemical equilibrium. Timescales of the thermal relaxation and chemical reactions, relative to particle times of flight through the shock layer, determine the reach of the non-equilibrium phenomena towards the vehicle surface. This can increase the heat flux incident on the vehicle surface, as well as affecting communications, visibility and aerothermodynamic coupling interactions. It's therefore desirable to characterise the thermochemical state of the gas through this region.

Correlations from Brandis and Johnston [20] demonstrate that the radiative heating component during this low-speed descent is mostly negligible in comparison to its convective counterpart. However, new motivation to improve LEO return vehicle designs has been generated with the introduction of re-useable rocket technologies (from companies such as SpaceX [167, 149] and Blue Origin [9]) and the relevance to national security and defence sectors. Although radiation measurements directly quantify the radiative heating component and inform of the vehicle observability at points along its trajectory, spectral resolution of the radiation also enables identification of species in excited energy states. Simultaneous spatial or temporal resolution allows characterisation of their evolution behind the strong shock wave. This information is pertinent to accurately predicting convective heat flux, solving communications issues (from the presence of free electrons), and understanding aerothermal effects. Additionally, although the radiative heat flux may be negligible to a LEO return vehicle forebody, the temperatures and consequent thermochemistry present are relevant to flow around the afterbody of higher speed lunar return vehicles [96], where radiative heat flux plays a more dominant role.

Due to the expense of real flight experiments, ground test facilities have traditionally been used to recreate these high-enthalpy flow environments. This allows radiation data at targetted conditions to be captured, amongst other parameters, to inform computational models. The Oxford T6 Stalker Tunnel is a high-enthalpy multi-mode transient ground test facility at the University of Oxford [36, 33, 116]. When operating in Aluminium Shock Tube (AST) mode [32, 37], it is able to recreate the high-enthalpy stagnation line ahead of an entry vehicle. Discrepancies in time of flight between the two flow fields can be addressed through spatial transformations or by converting to the temporal domain [29]. Recent data from AST has been used to validate and compare against spectral radiance measurements

from the Electric Arc Shock Tube at NASA Ames [39, 41] for a range planet entry missions [69, 162, 51].

In 2017, studies by Cruden and Brandis [45] reported new parameters for the rate chemistry and non-Boltzmann modelling from air tests in the EAST facility at 7 to 9 km/s. Since then, a range of equilibrium spectral comparisons have been performed for air, ranging from 3 to 7 km/s in AST and EAST facilities collectively [42, 68, 69]. Additionally, comprehensive studies of equilibrium thermochemistry relevant to the enthalpies of LEO return missions have been conducted in inductively coupled plasma torch facilities [102, 122]. The T6 AST dataset presented in this paper provides a new series of results, covering a wider range of pressures and enthalpies, to build on the previous efforts and furthermore, takes the additional step to characterise aspects of the non-equilibrium thermochemistry behind the shock front.

This chapter applies the constrained spectral fitting routine to 7.3 km/s shocks in synthetic air (20.9% O_2/ 79.1% N_2). Section 7.2 provides a summary of the low-speed synthetic air test conditions achieved in the T6 Stalker Tunnel while operating in Aluminium Shock Tube mode. Section 7.3 summarises cumulative radiance trends for NO, N_2 first positive and atomic O excited states. Section 7.4 shows results extracted from real T6 AST data that directly relate to the thermochemical state evolution along the stagnation line of an LEO return vehicle. The effect of fitting over different spectral regions and resolutions is shown and comparisons are made against equivalent EAST data (in Section 7.5) and the predictions of the Park 2T model [144] with modified Cruden rates [45] (in Section 7.6).

7.2 Test Summary

Figure 7.1 maps the synthetic air conditions achieved in the recent T6 AST low-speed campaign. The quoted test gas composition is 20.9% O_2/ 79.1% N_2 by volume. A series of post-shock pressures were targetted to provide different levels of spatial resolution, since less particles in the flow results in less frequent collisions and therefore slower reactions, thus stretching out the non-equilibrium region. The trade-off between improved spatial resolution and worse signal at low pressure conditions has been demonstrated for pure nitrogen shots in Fig. 6.6 of Chapter 6. The T6s484 and T6s501 test conditions selected for spectral fitting in this chapter have been highlighted in Fig. 7.1. The combination of both these tests provides low and high resolution ultraviolet spectra for a nominal 7.3 km/s, 33.3 Pa fill and 20 kPa post-shock test condition. Availability of high resolution UV data was identified as a valuable addition to the low spectral resolution pure nitrogen dataset in Chapter 6, to help resolve the N_2^+ first negative from the CN violet bands.

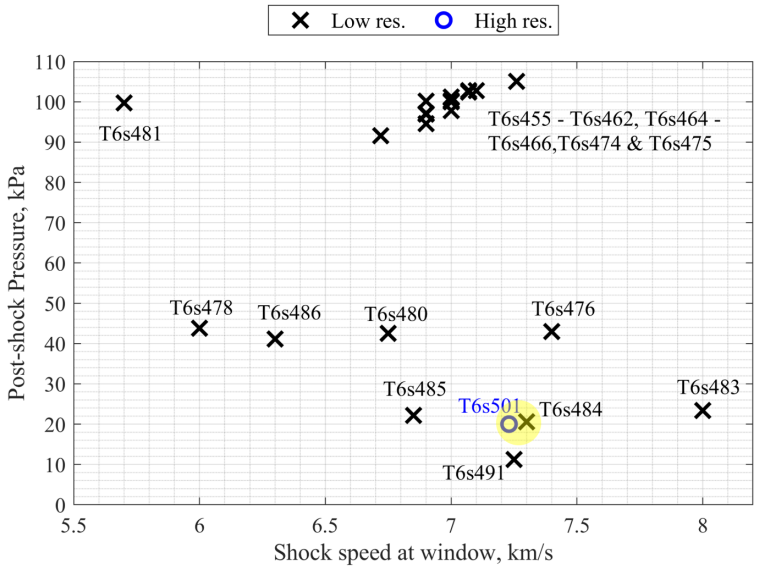
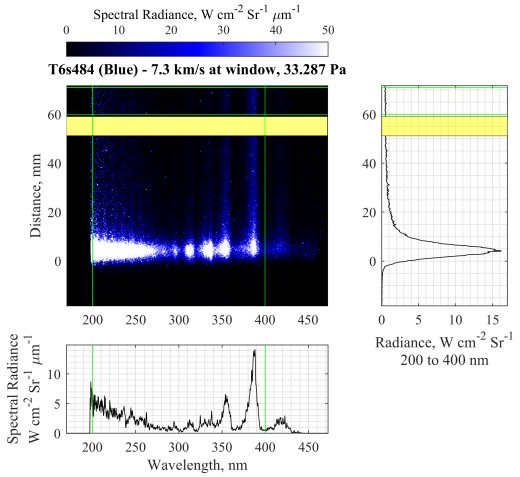


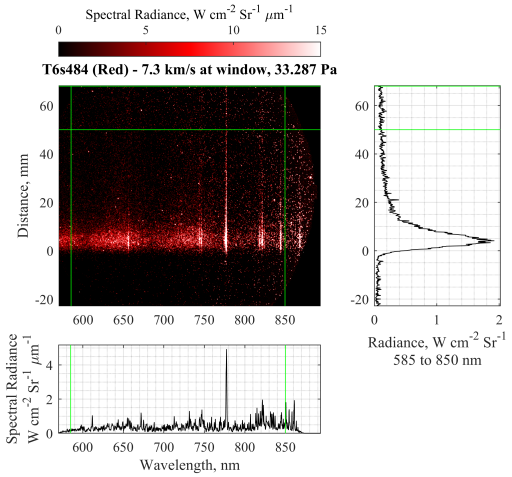
Fig. 7.1 Map of synthetic air conditions from recent T6 AST campaign. Selected tests for spectral fitting, T6s484 and T6s501 of ∼7.3 km/s, 33.3 Pa fill and ∼20 kPa post-shock, have been highlighted.

7.3 Radiance Data

Figure 7.2 shows calibrated spatio-spectral 2D radiance maps of T6s484 from both the UV/Vis and Vis/NIR spectral channels. The data is spatially calibrated for the shock front to be located at 0 mm, providing a common datum between the spectral channels. Equilibrium spectral radiance traces are plotted below the 2D radiance maps, by averaging over regions furthest from the shock front and therefore closest to thermochemical equilibrium, indicated by the green horizontal lines. Spatially resolved radiance traces are acquired by integrating across the wavelengths between the vertical green lines, and plotted to the right of the 2D radiance maps. The non-equilibrium peak can be seen in both spectral channels immediately behind the shock, followed by a relaxation region, as the thermochemical state approaches equilibrium. Radiation is evidently more intense in the UV/Vis region where molecular species (NO, N_2, N_2^+) dominate. Atomic transitions from O and N species are captured in the Vis/NIR, protruding above the N_2 first positive background. Figure 7.3 provides examples of spectra extracted from both equilibrium and non-equilibrium portions of the test slug. Table 7.1 gives a summary of the molecular and atomic transitions observed in both spectral channels.

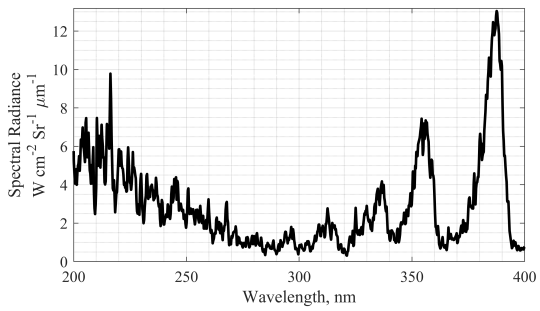


(a) T6s484 UV/Vis

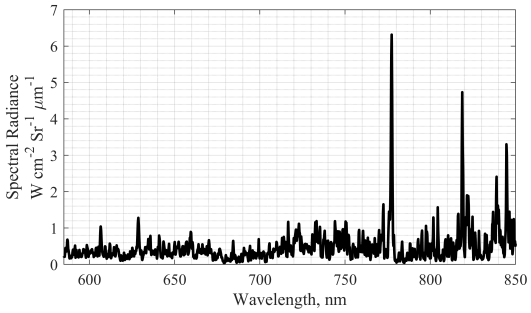


(b) T6s484 Vis/NIR

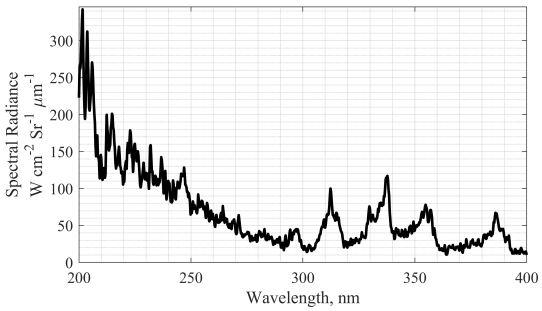
Fig. 7.2 Calibrated spatio-spectral radiance data for T6s484 (7.3km/s, 33.3 Pa fill in synthetic air). Horizontal green lines indicate spatial region averaged over to generate spectral radiance plot. Vertical green lines indicate wavelength region integrated over to generate spatial radiance profile. The yellow shaded region was purposely blocked in the Blue channel to gauge stray light on the camera sensor array.



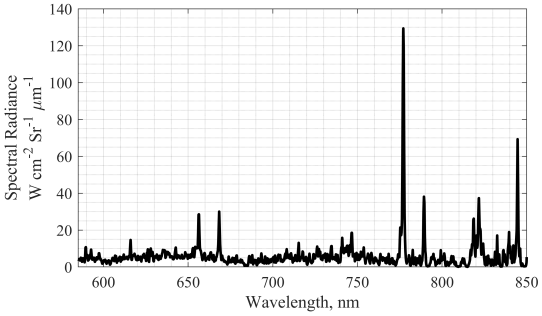
(a) End of test slug: UV



(b) End of test slug: Vis/NIR



(c) Initial peak 2 mm: UV



(d) Initial peak 2 mm: Vis/NIR

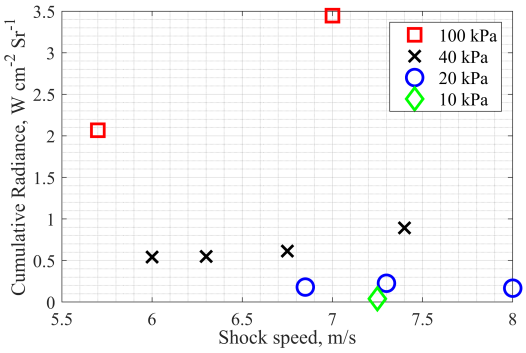
Fig. 7.3 Spectra acquired for T6s484 from both ultraviolet and visible/near-infrared spectral channels in different portions of the test slug.

Table 7.1 Summary of synthetic air and contaminant spectral features observed in the selected tests, over the UV/Vis and Vis/NIR wavelength regions.

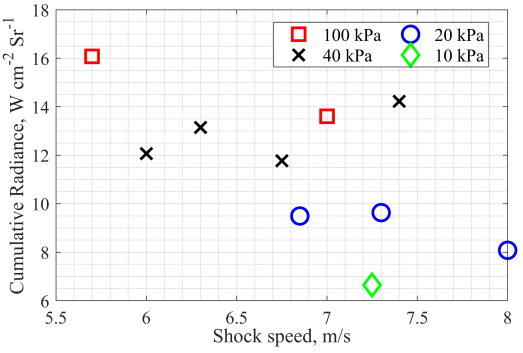
Name	**Transition**	**Region of emission**
NOγ	$A^2\Sigma^+ \rightarrow X^2\Pi$	200–400 nm
NOβ	$B^2\Pi \rightarrow X^2\Pi$	200–400 nm
NOδ	$C^2\Pi \rightarrow X^2\Pi$	200–280 nm
NOε	$D^2\Sigma^+ \rightarrow X^2\Pi$	200–280 nm
NOγ'	$E^2\Sigma^+ \rightarrow X^2\Pi$	200-400 nm
NOβ'	$B'^2\Delta \rightarrow X^2\Pi$	200-400 nm
N_2 first positive	$B^3\Pi_g \rightarrow A^3\Sigma_u^+$	500–1100 nm
N_2 second positive	$C^3\Pi_u \rightarrow B^3\Pi_g$	250–450 nm
N_2^+ first negative	$B^2\Sigma_u^+ \rightarrow X^2\Sigma_g^+$	300–450 nm
N_2^+ Meinel (A-X)	$A^2\Pi_u \rightarrow X^2\Sigma_g^+$	500–900 nm
N	$3p^4S \rightarrow 3s^4P$	744.2 nm
	$3p^4S \rightarrow 3s^4P$	746.8 nm
	$3p^4P \rightarrow 3s^4P$	821.6 nm
O	$3p^5P \rightarrow 3s^5S$	777.2 nm
	$3p^3P \rightarrow 3s^3S$	844.6 nm
CN violet	$B^2\Sigma^+ \rightarrow X^2\Sigma^+$	350–430 nm
Aluminium	$3p^2P \rightarrow 4s^2S$	394, 396 nm
Hα (Balmer-alpha)	$3 \rightarrow 2$ (n=3 $\rightarrow$ n=2)	656.3 nm
Hβ (Balmer-beta)	$4 \rightarrow 2$ (n=4 $\rightarrow$ n=2)	486.1 nm
Sodium D Line	$3p\ ^2P \rightarrow 3s\ ^2S$	589.0–589.6 nm
NH	$A^3\Pi \rightarrow X^3\Sigma^-$	300–340 nm

Figure 7.4 provides a brief summary of cumulative radiance trends over the shock speeds and post-shock pressures achieved in the new synthetic air dataset. The dominant species from each spectral channel were selected: NO for the ultraviolet; and the N_2 first positive band in the visible/near-infrared. Additionally, the atomic oxygen line at 777 nm has been frequently analysed in prior works [32, 30] and so is included here.

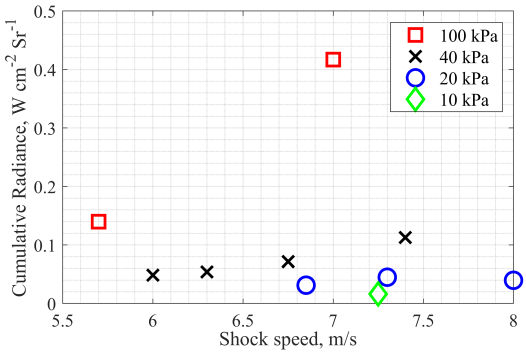
It's evident that NO produces a large portion of the total radiation over the considered low-speed tests. Equilibrium comparisons in Fig. 7.4a show the NO radiance to increase with shock speed until $\sim$8 km/s, where increased dissociation begins to reduce NO emission levels. Similar trends can be seen for the equilibrium N_2 first positive band in Fig. 7.4c, except radiance levels are notably less intense. The atomic O radiance levels in Fig. 7.4e however show a continued increase across all shock speeds. This is owed to the increased O_2 dissociation and energy at the higher post-shock temperatures, leading to higher populations of O atoms in excited states.



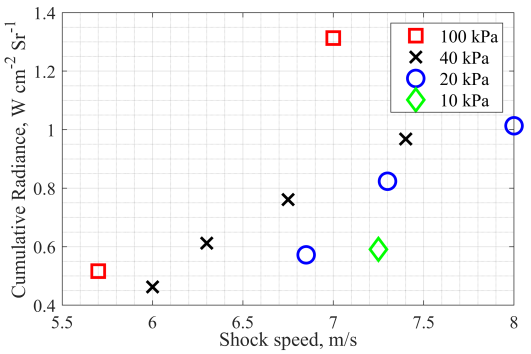
(a) Equilibrium NO: 200 to 280 nm



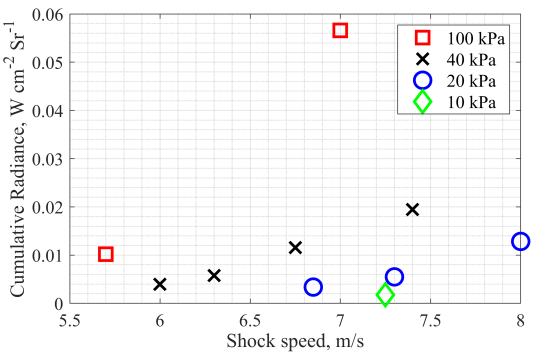
(b) Peak 2 mm NO: 200 to 280 nm



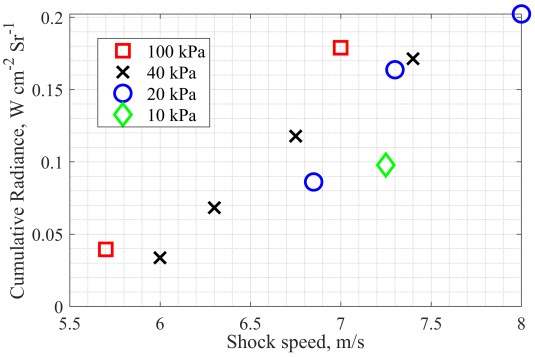
(c) Equilibrium N_2 (1^{st} +ve): 590 to 730 nm



(d) Peak 2 mm N_2 (1^{st} +ve): 590 to 730 nm



(e) Equilibrium O: 775 to 779 nm



(f) Peak 2 mm O: 775 to 779 nm

Fig. 7.4 Cumulative radiance trends across shots from new synthetic air dataset. Pressures quoted are nominal post-shock levels, though there are some deviations between tests.

In the non-equilibrium region, NO radiance levels still significantly exceed those from other species, although show more irregular trends across the shock speeds and pressures. These tests operate within the realms where rates of NO production and dissociation are sensitive to temperature, thus there are a number of competing factors that have resulted in the observed trends. The NO radiance from the low-speed ∼5.7 km/s, 100 kPa post-shock test, exceeds that of its ∼7 km/s counterpart, for example. Conversely, the N_2 first positive

band displays an almost linear trend in the non-equilibrium data plotted in Fig. 7.4d, as shock speed increases. Similar can be said for the atomic oxygen non-equilibrium radiance levels in Fig. 7.4f, which also show a reduced sensitivity to post-shock pressure.

It's highlighted from these comparisons that NO displays both the highest radiance levels, as well as the highest unpredictability in this speed regime. Accurate characterisation of its thermochemical state evolution is therefore particularly important for the observability considerations when designing future hypersonic vehicles and their associated trajectories.

7.4 Spectral Fitting of T6 AST Data

7.4.1 Methodology

A novel constrained spectral fitting routine was developed in Chapter 5. Fundamentally, it is a method to convert spectral radiance data through a shock tube test slug, into spatially or temporally resolved temperature and number density profiles. This is done within the framework of a 2T model and Boltzmann distributions are assumed at all locations. This information helps to describe the evolution of the thermochemical state through the test slug. Chapter 5 demonstrated successful reproduction of vibrational temperature (T_{ve}), molecular N_2, N_2^+ and atomic N profiles in pure nitrogen data through a series of NESS-NEQAIR 1D simulations, with implementation of various experimental artefacts. An outline of the inputs and outputs of the routine were summarised in Table 5.1. Appendix C.1 shows a continuation of that work to validate the methodology for air tests. The error bars in the following plots represent the 95% confidence limits from a Monte Carlo analysis during the fitting routine (corresponding to ± 2 standard deviations) but do not account for any uncertainties from the radiation measurements. Species included in the spectral fitting of real radiance data in the following sections are: N_2, O_2, NO, N, O, N_2^+, O_2^+, NO^+, N^+, O^+, CN, NH and E^-. However, only results for T_{ve}, NO, N_2, N_2^+, N and O are shown, since they are the parameters shown to be extracted accurately in Appendix C.1.

7.4.2 Selected Condition

Table 7.2 summarises T6s484 and T6s501 selected for study by the constrained spectral fitting routine in this chapter. Difficulties were encountered gaining close fits in the lower wavelengths (below 300 nm) where the NO bands dominate, especially as the fitting routine progressed to the non-equilibrium peak. The spectral fitting was therefore performed for two iterations of T6s484 ("A" and "B") covering different portions of this wavelength region. A comparison of results between the two is used to assess the resulting fit quality achieved and

the associated sensitivities of the extracted temperatures and species number densities. The Instrument Line Shapes (ILS) [41] used for each test and spectral channel during spectral fitting are stated in Table 7.3 - these are the convolution functions applied during the spectral fitting. T6s501 provides a comparable reference, with high resolution ultraviolet data over the N_2 second positive and N_2^+ first negative bands. Although this data carries no NO radiance information, it also avoids the uncertainties around it and should provide a reliable reference for N_2 and N_2^+ number densities.

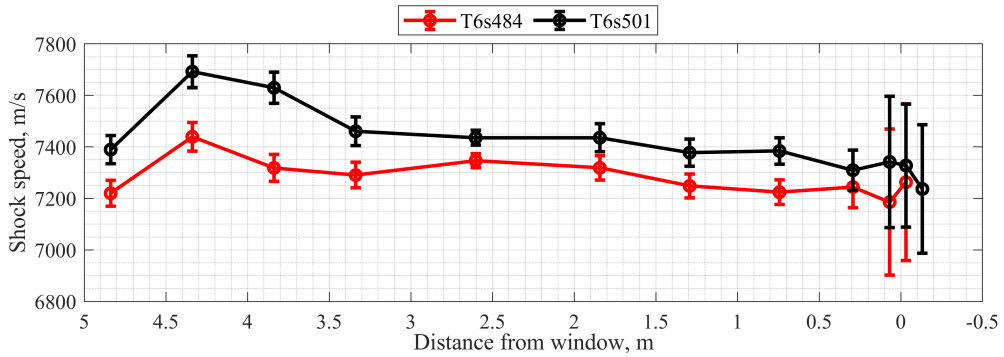
Table 7.2 Selected T6 tests for spectral fitting analysis. Wavelength ranges used for spectral fitting are listed. T6s484 trialled spectral fitting over two UV regions to assess the effect of uncertainties around radiative modelling of NO in the lower wavelengths.

Shot No.		**$U_{s,\,window}$, km/s**	**P_{fill}, Pa**	**$P_{2,\,meas}$, kPa**	**Leak Rate, mPa/s**	**UV/Vis, nm**	**Vis/NIR, nm**
T6s484	A	7.3	33.3	20.6	0.7	200-400	585-850
	B					250-400	
T6s501		7.25	33.4	20.0	0.9	340-396	585-850

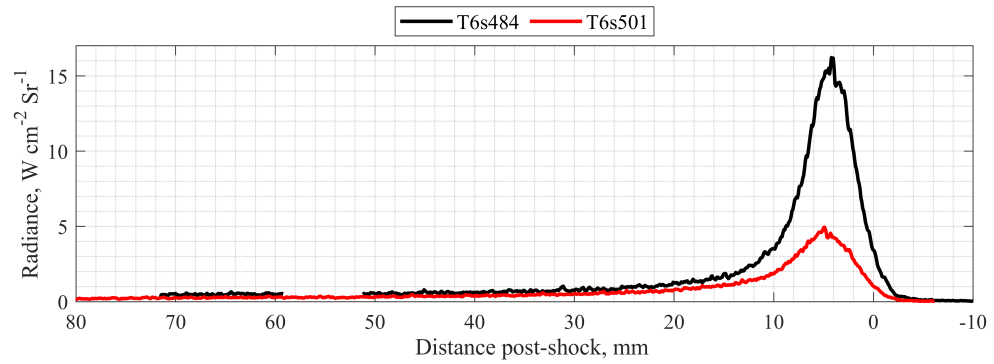
Table 7.3 ILS FWHM's used for spectral fitting, applied to the square root of a Voigt function.

Shot No.	**UV/Vis, Å**		**Vis/NIR, Å**	
	Gauss.	**Lorentz.**	**Gauss.**	**Lorentz.**
T6s484	10	0.001	6	0.0005
T6s501	2.4	0.088		

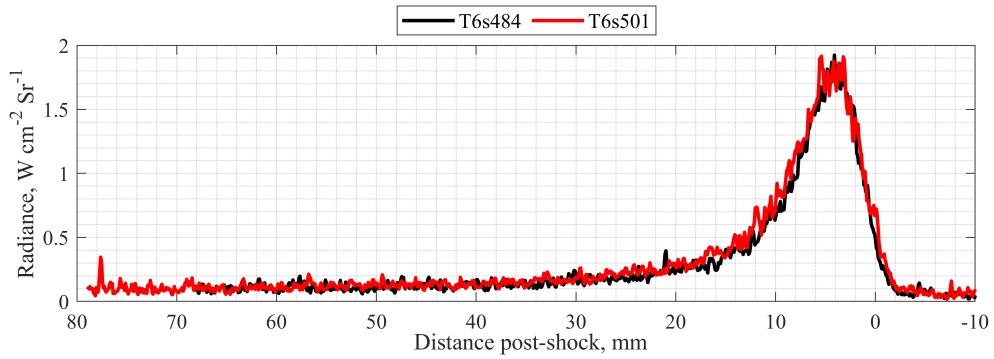
Shock speed and radiance profiles for the chosen test cases are plotted in Fig. 7.5. The shock profiles are only shown for the AST section of the facility, to avoid data before the conical expansion from the secondary driver, which will not be relevant to the final imaged test slug. Close comparisons are evident between the Vis/NIR radiance profiles, confirming the test slugs to have very similar thermochemistry. The ultraviolet radiance profiles differ due to the different wavelength regions covered.



(a) Shock trajectories



(b) Ultraviolet Radiance

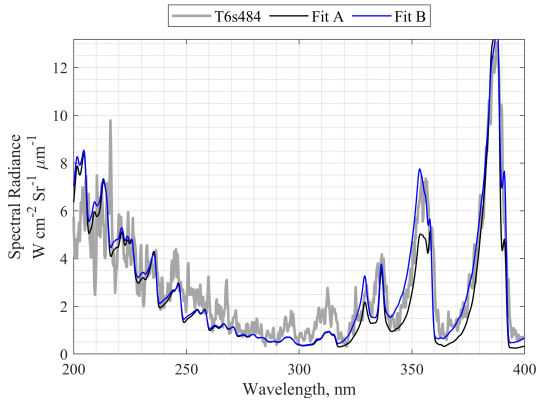


(c) Visible/Near-Infrared Radiance

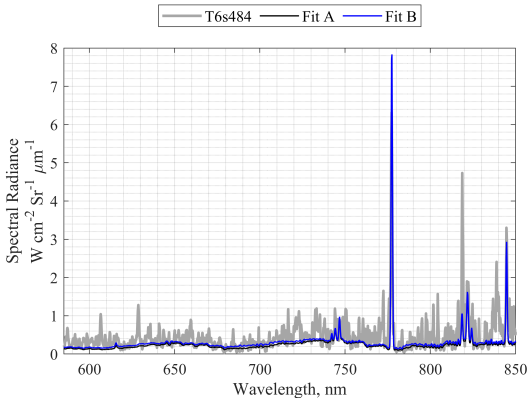
Fig. 7.5 Shock speed and radiance profiles for the selected test cases. Shock profiles are only plotted for the AST section of T6. Radiance profiles are generated by integrating over the spectral regions available for each test and channel.

7.4.3 Results

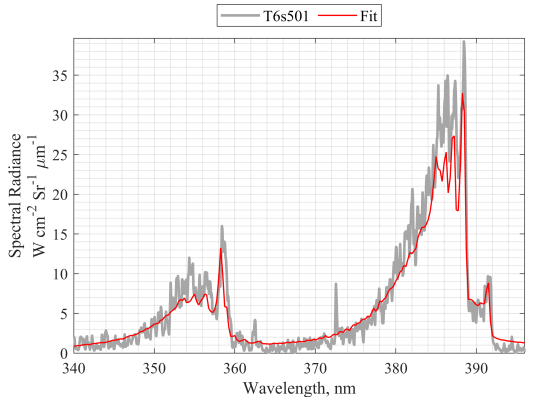
Figures 7.6 and 7.7 show examples of the spectral fits achieved for T6s484 and T6s501, towards the end of the observed test slugs and immediately post-shock, respectively. As was explained in Section 7.4.2, the spectral fitting was performed over two different ultraviolet wavelength regions for T6s484 (termed trials "A" and "B") to adjust the weighting of the NO bands on the extracted quantities and assess the response of the spectral fit outputs. These are summarised in Table 7.2. It's evident that the extent of NO emission included in the spectral fitting routine affects the overall fits in both equilibrium and non-equilibrium regions through the test slug.



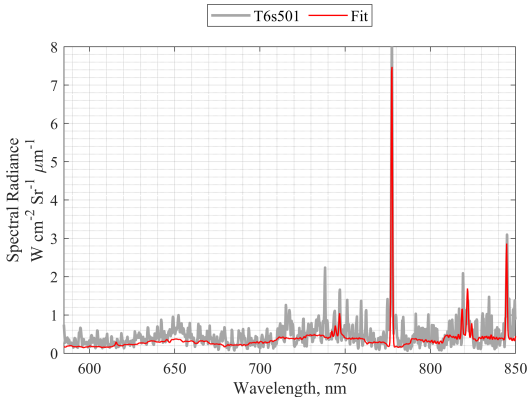
(a) T6s484: UV/Vis



(b) T6s484: Vis/NIR

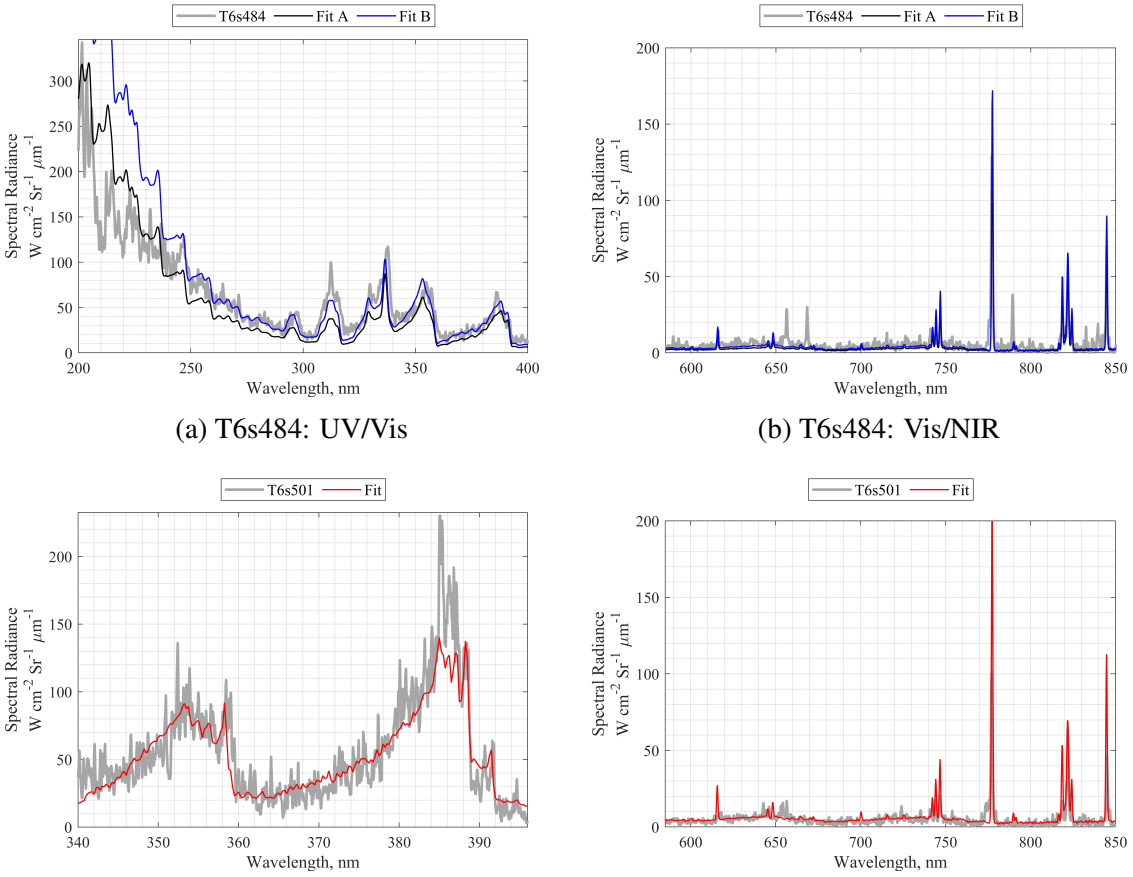


(c) T6s501: UV



(d) T6s501: Vis/NIR

Fig. 7.6 Spectral fits achieved towards the end of the test slugs for nominal test case of 7.3 km/s in 33.3 Pa synthetic air. Spectra limits and ILS functions used during fitting are as listed in Tables 7.2 and 7.3.



(a) T6s484: UV/Vis

(b) T6s484: Vis/NIR

(c) T6s501: UV

(d) T6s501: Vis/NIR

Fig. 7.7 Spectral fits achieved in the non-equilibrium peak for nominal test case of 7.3 km/s in 33.3 Pa synthetic air. Spectra limits and ILS functions used during fitting are as listed in Tables 7.2 and 7.3.

Discrepancies below 300 nm have been observed in air equilibrium spectra from both T6 AST and EAST facilities when compared to CEA-NEQAIR simulations [69, 68, 45]. Section C.2 of the Appendix includes a comparison of equilibrium spectra from the chosen test cases against CEA-NEQAIR predictions (including T6s484 in Fig. C.3). These show that, aside from CN violet contaminant emission in the ultraviolet around ∼380 and ∼350 nm, most notable offsets remain below 300 nm, where NO dominates. The work detailed in Chapter 4 significantly improved agreement of the overall spectral offset, as can be seen by comparisons against the EAST-59-51 equilibrium spectra with CEA-NEQAIR predictions (in Fig. C.5 in the Appendix). However, the source of remaining discrepancies are currently unknown. Recent works of Cruden [42] trialled an alternative O_2 photodissociation model [64] to improve agreement of equilibrium spectra for ∼4 km/s test cases, though this had negligible effect on T6 AST data at 5.7 km/s and above. The difficulties encountered in

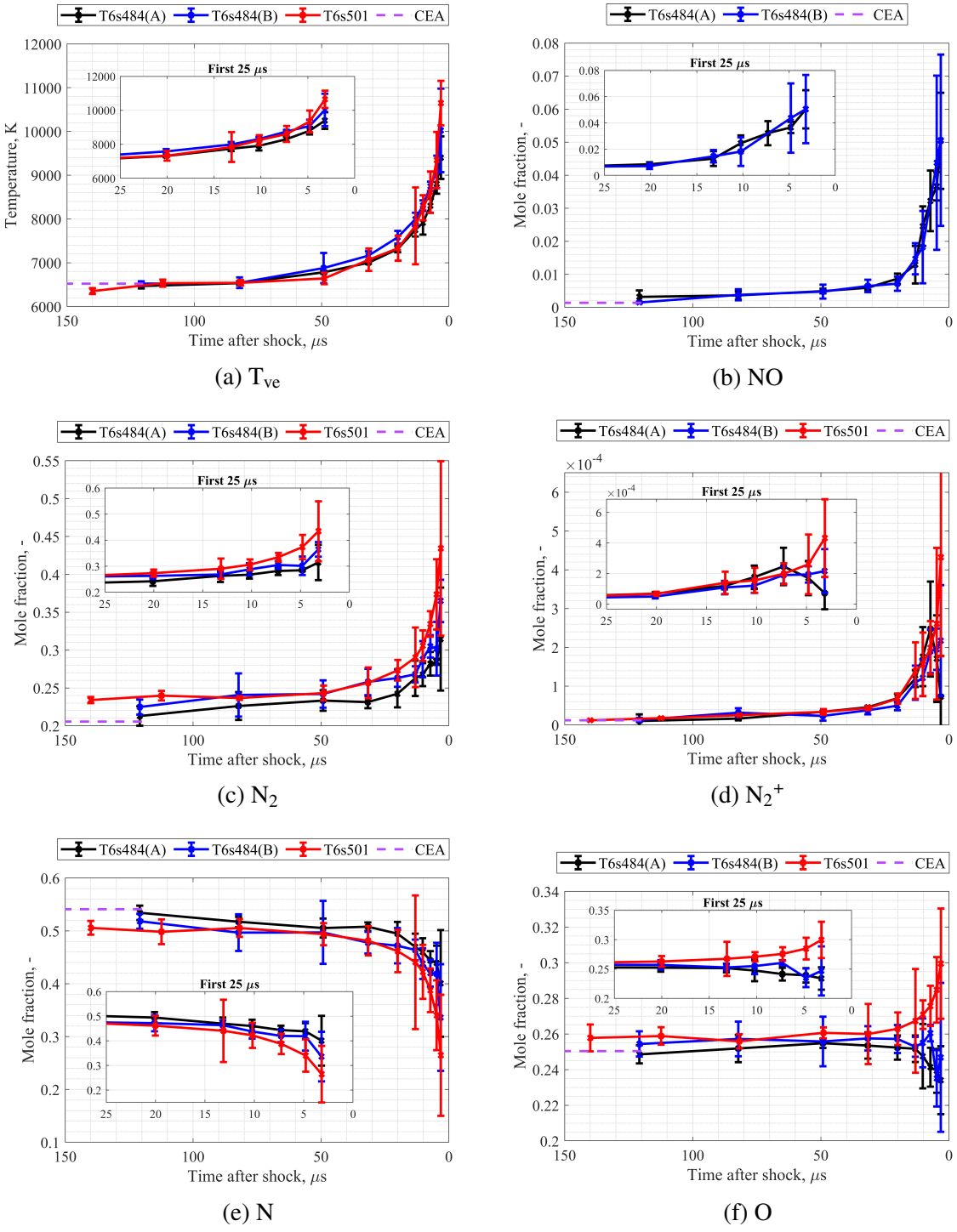
spectrally fitting the lower wavelengths here suggest these discrepancies between experiment and numerical predictions are also present through the non-equilibrium region.

Other sources for the discrepancy could include: the presence of non-Boltzmann distributions; artefacts from the Deuterium lamp calibration methodology for lower wavelengths; other spectral emission features not incorporated in the modelling of the NEQAIR radiative transport code; or the two-temperature model used in this work may be invalid. Section A.11 of the Appendix presents a comparison of Boltzmann and new non-Boltzmann quasi-state-specific (QSS) NEQAIR v15.3 predictions for different portions of a 7.3 km/s, 33.3 Pa synthetic air shock layer, as determined by the Non-Equilibrium Shock Solver (NESS) [30]. This demonstrates the strong dependence of predicted emission spectra on the chosen state distribution, particularly in the lower wavelengths where NO dominates. The importance of identifying the source of this discrepancy is emphasised in this study. One means of validating the emission spectroscopy measurements is to use an alternative optical diagnostic arrangement, such as tunable diode laser absorption spectroscopy (TDLAS). This can provide another measurement of NO state populations, in the region of largest discrepancies, to determine if it is consistent with the emission spectroscopy measurements.

Despite the discussed discrepancies at the lower wavelengths requiring further investigation in future works, this paper continues the analysis by assuming Boltzmann distributions through all portions of the test slugs. Although the OES systems enable spatial resolution of the spectral evolution through the test slug, the spectral fitting outputs have been plotted in Fig. 7.8 against the time passed since being processed by the normal shock. This conversion is made via Equation 7.1, where $U_{2,s}(x)$ is the post-shock velocity profile as a function of distance post-shock (in the shock's frame of reference) as defined by Mirels [126]. This removes the spatial domain augmentation caused by boundary layer mass consumption effects [29], so the data in no longer specific to the AST tube diameter along the x-axis.

$$t = \int \frac{dx}{U_{2,s}(x)} \tag{7.1}$$

All T6 AST spectral fits assume a constant shock speed, equal to the value at the window (see Table 7.2). This is valid due to minimal shock deceleration along the trajectories. CEA predictions are provided for reference, using the same shock speed. Including T6s501 allows for comparison with T6s484, helping validate T6s484 results by utilising higher resolution spectra in a region with negligible NO radiance. Although this excludes NO from the spectral fitting, it eliminates potential issues related to NO modelling, offering a reliable reference for N_2 and $N_2{}^+$, which also emit in the ultraviolet. The following subsections discuss results for each parameter.



(a) T_{ve} (b) NO

(c) N_2 (d) N_2^+

(e) N (f) O

Fig. 7.8 Comparison of spectral fit outputs for nominal test case of 7.3 km/s in 33.3 Pa synthetic air and ∼20 kPa post-shock. Different spectral limits used during fitting for each case are summarised in Table 7.2. NO was not captured in T6s501 and thus not plotted.

T_{ve}

Close agreement between all three profiles is achieved for the vibrational temperature, demonstrating minimal dependence on the extent of NO included in the spectral fitting routine. Additionally, agreement of T6s501 with the T6s484 outputs demonstrates good repeatability within the shot-to-shot variations, and suggests that a higher resolution ultraviolet spectrum without NO information does not affect the result. All cases show a monotonic and asymptotic decrease until settling at approximately the CEA prediction within 80 μs, indicating the end of thermal relaxation for this $\sim$20 kPa post-shock condition.

NO

Interestingly, the choice of wavelengths to perform the spectral fitting in the ultraviolet region does not have a significant impact on the resulting NO mole fractions for T6s484. Although, the highest variability is evident within the first $\sim$10 μs after being processed by the shock. The profiles suggest there's a large source of NO production within the first 3 μs immediately behind the shock front, which then rapidly depletes mostly within the first $\sim$25 μs. A gradual decrease continues, almost reaching the equilibrium prediction from CEA within the observable test slug. Results from T6s501 are not included since the NO bands do not emit in the narrower spectral region.

N_2

All three N_2 profiles show a monotonic and asymptotic decrease after being processed by the shock, as their mole fractions deplete. The majority of this is achieved within the first $\sim$25 μs, though continues throughout, with none of the cases reaching the CEA equilibrium prediction within the observable test slugs. This suggests a degree of chemical non-equilibrium exists within both test slugs and agrees with the conclusions from the pure nitrogen studies in Chapter 6. Additionally, T6s501 predicts a higher N_2 composition within the first $\sim$10 μs after being processed by the shock. This could partly be due to the slightly slower shock speed at the window, since N_2 dissociation has been shown to have strong sensitivity to the shock strength. Or alternatively, it could be due to improved capturing of the N_2 profile via the high resolution UV spectrum with no NO contribution. Finally, the T6s484 trial B, only fitting down to 250 nm, is closer to the T6s501 profile for the entire relaxation process. This suggests removing the lower portions of the NO bands from the fitting routine, where uncertainties are highest may produce more reliable profiles for N_2.

N

The results for atomic N are discussed next since they are essentially the inverse of N_2. All profiles show a monotonic and asymptotic increase in mole fractions as N is produced behind the shock. None reach the CEA prediction within the observable test slugs, further suggesting incomplete N_2 dissociation throughout. The largest discrepancy with T6s501 is again seen in the first $\sim$10 μs, though the results from T6s484 trial B agree well for the remainder of the test slug.

N_2^+

The N_2^+ first negative band emits intensely in the UV/Vis wavelengths, allowing N_2^+ to be detected despite having number densities 3 to 4 orders of magnitude less than the neutrally charged species. This in itself demonstrates that although ionisation does occur at these low speeds (to produce a so-called "partially ionised plasma") the vast majority of species remain neutral.

Variability between the fitting results is seen within the first 10 μs of the N_2^+ mole fractions, showing dependency of the spectral region and resolutions used. However agreement of all three closely align after this, to show a monotonic and asymptotic decrease, reaching the CEA prediction after $\sim$100 μs. This aligns closely with the time for thermal relaxation, thus showing strong sensitivity to temperature. The profiles suggest there to be an initial surge in N_2^+ production by ionisation of N_2 molecules from high temperatures immediately behind the shock. These are then rapidly removed by the consequent relaxation phase, as electrons recombine with the positively charged ions.

O

Production of atomic O species relies on dissociation of O_2 molecules, which occurs more rapidly than that of N_2. This is reflected in the T6s484 mole fractions in Fig. 7.8f, which show the O mole fraction to have reached the CEA prediction within the first $\sim$20 μs after being processed by the shock, though having reached $\sim$90% of the way there within the first 3 μs. The results are unaffected by selection of wavelength region between trials A and B. Conversely, the T6s501 result predicts a gradual reduction in atomic O mole fraction from immediately behind the shock. This is believed to be a result of over-compensating for the lack of NO information in the UV spectral region used, in an attempt to conserve the ratio of N:O atoms, which is built into the fitting routine. Some of the atomic O lines from the spectral fits in the non-equilibrium region of Fig. 7.7d exceed above the measured atomic transitions, which ties in with this conclusion.

Key findings going forward

These results present an initial study of the thermochemical state through a test slug relevant to LEO return missions. The largest sensitivity to spectral region and resolution in the UV is demonstrated in the first $\sim$10 μs of the N_2, N_2^+, N and O mole fractions. Results from fitting T6s484 B (fitting over 250 - 400 nm) are deemed to be the most reliable of the three, capturing information for all species and providing closest agreement to the T6s501 N_2 and N_2^+, which should be accurately captured by the high resolution spectra.

7.5 Comparison to EAST

In addition to the aforementioned T6 AST tests, shot 51 from test series 59 in the EAST facility was selected as an equivalent condition for comparison [45]. The shock speed profile of which is shown in Fig. 7.9. Quoted shock speed at the window is 7.39 km/s and a $\sim$57.5 kPa post-shock pressure. Here, the previous T6s484 (B) results are re-plotted with the outputs from EAST-59-51. The same spectral regions were used for both spectral fits and thus encapsulate the same thermochemistry to allow a fair cross-facility comparison. Figure 7.9 shows that, although the two tests arrive at a similar shock speed at the window, the EAST test exhibits much stronger shock deceleration effects. Two iterations of the EAST spectral fitting have therefore been performed: one in which the shock speed is assumed constant at the window; and one in which the shock deceleration is accounted for. The shock deceleration causes enthalpy gradients through the resulting test slug, which can be accounted for by using the in-house LAgrangian Shock Tube Analysis (LASTA) code [152, 170] and fed into the spectral fitting routine. Additionally, the x-axis used to compare results between tests is the time post-shock multiplied by the respective nominal post-shock pressures. As was previously explained, converting post-shock distance to post-shock time via Eq. 7.1 removes the augmentations caused by different boundary layer consumptions. Additionally here, the EAST test is of a higher pressure than T6s484, which compresses the non-equilibrium region due to a higher frequency of collisions. The profiles have therefore also been normalised by the post-shock pressure on the x-axis, to approximately account for the pressure difference between the two, as previously done for pure nitrogen data in Chapter 6.

Figure 7.10 plots the profiles extracted by spectral fitting. It's evident that the combination of higher pressure and longer spatial FOV from the EAST data enables a much larger extent of the thermochemistry to be captured. However, most of the non-equilibrium interactions are completed within the spatial extent of the T6s484 data.

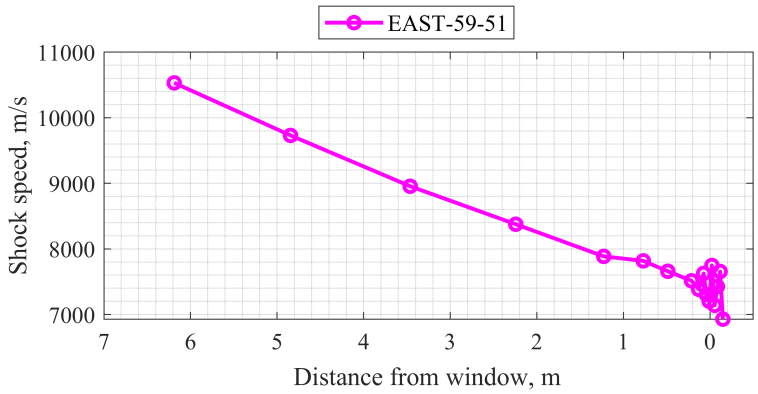


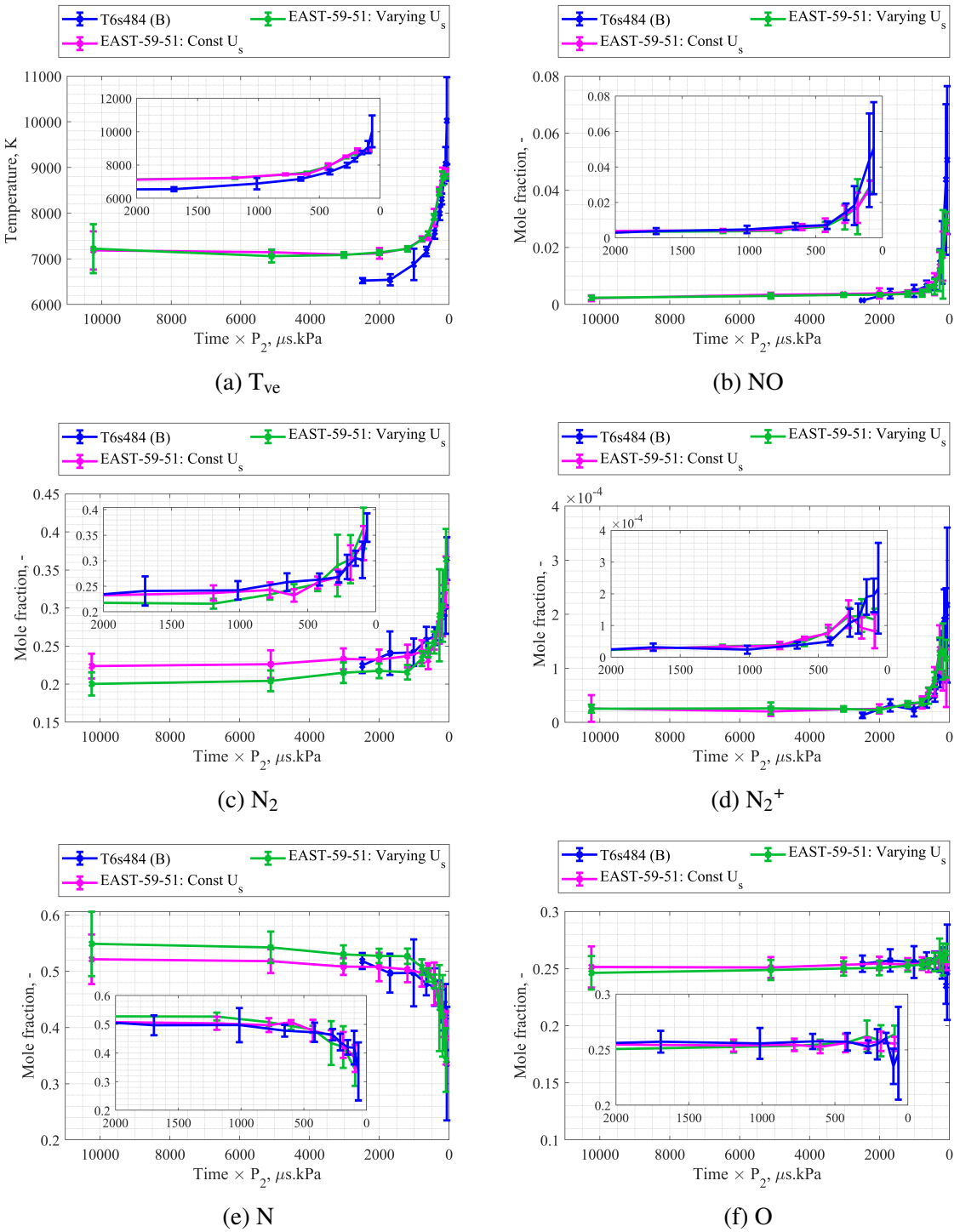
Fig. 7.9 Shock speed profile for EAST-59-51.

The T_{ve} profiles show close agreement in the initial post-shock region, however both EAST-59-51 profiles increase towards the latter portions of the test slug. Although this is likely due to the shock deceleration effect (and consequent increase in radiance towards the end of the test slug) there is no significant change by introducing the different enthalpy profiles. This shows the measured spectra have strong dependence on the vibrational temperature, as was seen for pure nitrogen tests at comparable conditions.

Close agreement in the initial non-equilibrium is shown between all cases for both N_2 and N profiles. However, the enthalpy differences towards the end of the EAST test slug has a stronger influence on the extent of N_2 dissociation predicted. This again ties in with previous findings in pure nitrogen data, showing the extent of N_2 dissociation to be sensitive to shock speed and trajectory.

The profiles extracted for NO show good agreement through the entire test slugs and appear to reach a steady value more rapidly than N_2 and N. Additionally, accounting for shock deceleration appears to have no significant influence on the extracted EAST profiles. This suggests the mechanisms leading to NO production and consequent depletion occur very quickly in comparison, and the chemical equilibrium composition of NO is largely dependent on the shock speed at a given instant, rather than its history. These results are exaggerated even more for the atomic O profiles, which are nearly all at a constant value throughout the observed test slugs. Confirming the rapid O_2 dissociation across both facilities.

Finally, some variability is shown in the N_2^+ mole fractions extracted immediately behind the shock. Though these quickly settle to show close agreement between the facilities and achievement of steady N_2^+ for the majority of the thermochemistry captured in EAST-59-51. This study gives good indication of the relative rates of production and depletion for multiple species, which correlates directly to that experienced along the shock layer stagnation line of a hypersonic vehicle.



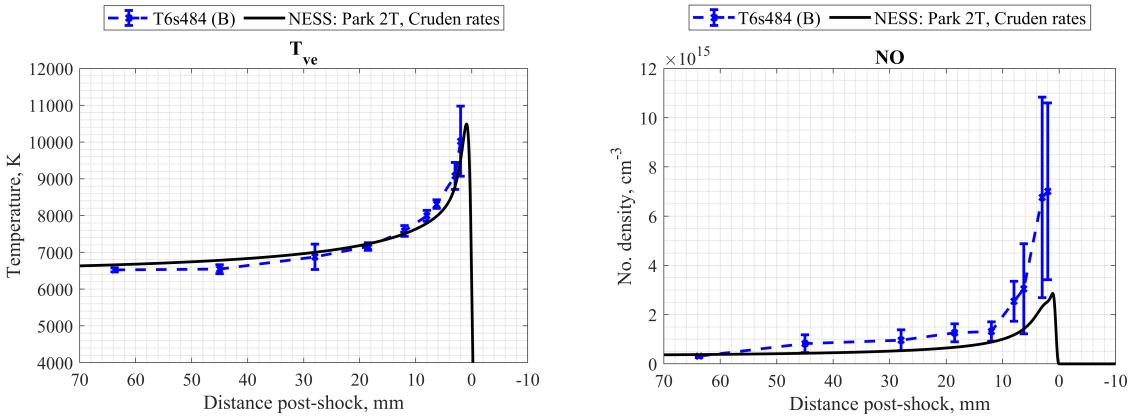
(a) T_{ve} (b) NO

(c) N_2 (d) N_2^+

(e) N (f) O

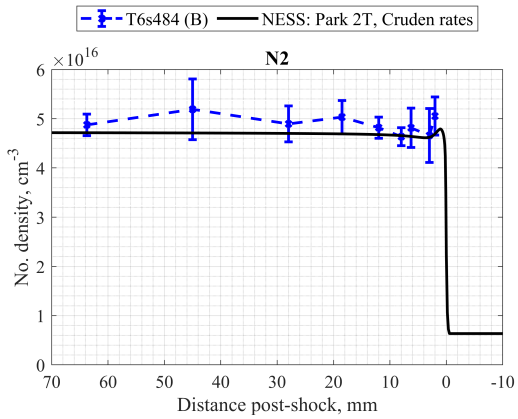
Fig. 7.10 Comparison of T6s484 and EAST-59-51 outputs from constrained spectral fitting. x-axes have been normalised by multiplying the time post-shock by the nominal post-shock pressures.

7.6 Comparison to 2T Model

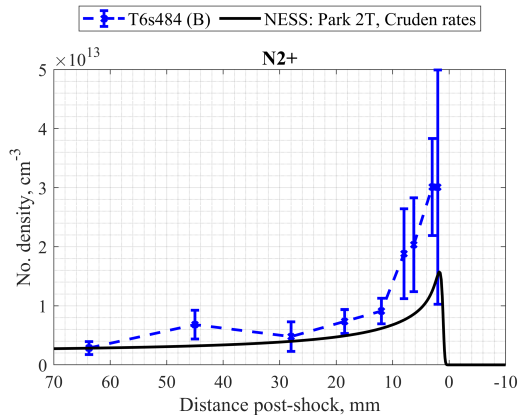


(a) T_{ve}

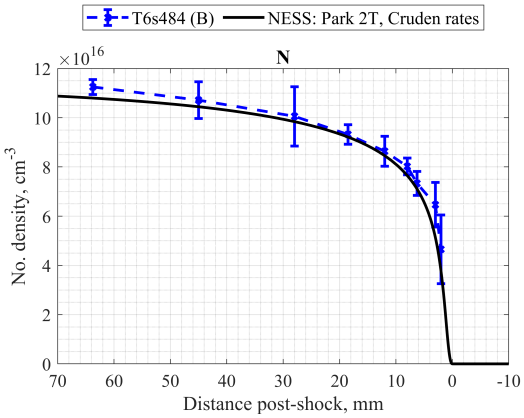
(b) NO



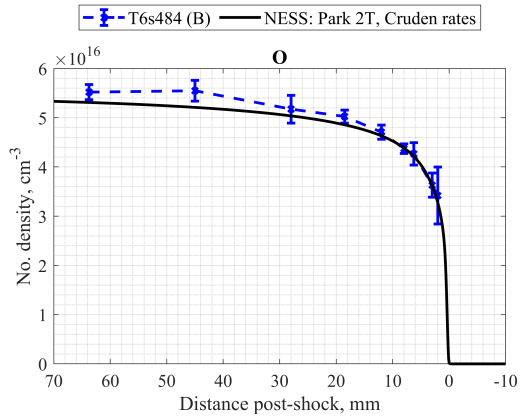
(c) N_2



(d) N_2^+



(e) N



(f) O

Fig. 7.11 Comparison of profiles extracted for T6s484(B) against the predictions of NESS 1D solver using Park 2T model and modified Cruden rates.

The final step of this paper is to compare the results of the T6s484 (B) spectral fit outputs against the predictions of a well-established two-temperature model and rates. Figure 7.11 plots the extracted profiles against the 1D NESS-NEQAIR simulation predictions. Results are plotted against post-shock distance on the x-axis and number densities are given for the species, rather than mole fractions. These were calculated using the Park 2T model [144] and modified rates from Cruden [45] based on studies at 7 to 9 km/s in the EAST facility.

It's evident that T_{ve} agrees well between the two, though a slightly more rapid decrease is displayed by the experimental data. Additionally, the atomic N and O profiles agree very well with the numerical model. The N_2 number densities extracted from the experiment lie slightly above the numerical predictions, and show a gradual rise extending further into the test slug. This is likely a result of the Mirels post-shock velocity profile assumed through the test slug and consequent gradual static pressure rise. The main discrepancies are seen in both NO and N_2^+ profiles, with both displaying significantly higher number densities immediately behind the shock, before showing closer agreement later in the test slug. This may correlate to an increased sensitivity to post-shock temperatures than is captured in the current models.

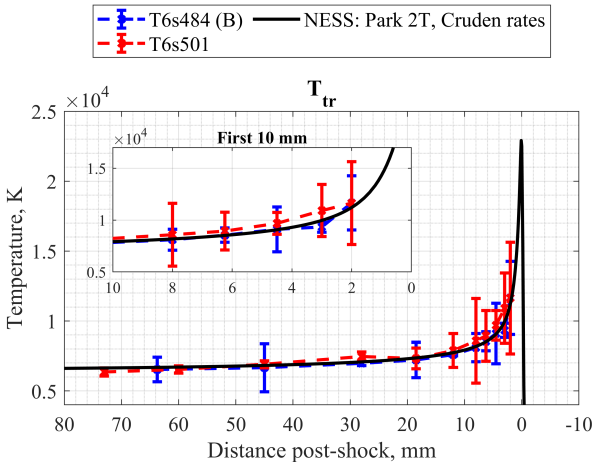


Fig. 7.12 Comparison of trans-rotational temperatures extracted for T6s484 (B) and T6s501 spectral fitting attempts against predictions of NESS 1D solver using Park 2T model and modified Cruden rates.

A brief comparison of trans-rotational temperatures (T_{tr}) extracted from T6s484 (B) and T6s501 spectral fits is provided in Fig. 7.12. Trans-rotational outputs have been left out of all results thus far, due to frequent poor matching of outputs encountered between spectral fits and NESS predictions. However, it was noticed the profiles extracted from T6s484 (B) and T6s501 fair well against the NESS profile using Park 2T model and modified Cruden rates. Though the large standard deviations show relatively weak dependence, with

possible temperature ranges covering up to ∼8000 K in the initial relaxation phase. Thus, the necessity for alternative measurements to validate these results is emphasised.

7.7 Conclusion

A new dataset of low-speed synthetic air tests has been produced from the T6 Aluminium Shock Tube, covering shock speeds from 5.7 to 8 km/s and post-shock pressures from 10 kPa to 100 kPa. Trends in molecular NO, N_2 first positive and atomic O are shown through the equilibrium and non-equilibrium regions. NO is identified to radiate significantly above other excited species and displays increased sensitivity to shock speed and pressure. A constrained spectral fitting routine has been applied to tests with 7.3 km/s shocks. Thermal relaxation is shown to be achieved within 80 μs for the ∼20 kPa post-shock AST tests, while N_2 dissociation appears to continue within the observable test slugs. Results compare well against EAST data and the inclusion of shock deceleration is shown to affect the extent of N_2 dissociation predicted in the latter portions of the test slug. Additionally, predictions of Park 2T and modified Cruden rates show close agreement, except for significant under prediction of the NO and N_2^+ densities immediately post-shock.

Uncertainties around the spectral fitting of the lower wavelengths where NO bands dominate are identified and emphasise the need of alternative optical diagnostic measurements to prove/disprove the radiance quoted in emission spectra. TDLAS is recommended as an alternative in this region, to determine if the discrepancies are a product of the spectral calibration procedure used at lower wavelengths, or if it is due to incorrect modelling of the NEQAIR radiative transport code (or incorrect use of the Boltzmann assumption). Despite these uncertainties, the study has produced valuable new data with direct applicability to the stagnation line ahead of a hypersonic vehicle during a Low Earth Orbit return mission. Future work will involve characterising a wider range of shock speeds and incorporating measurements from alternative diagnostics as they become available.

Acknowledgments

The authors would like to thank Dr Tobias Hermann for the generous loan of the Deuterium calibration lamp, making acquisition of data from 200 to 300 nm feasible. We would also like to thank Tristan Crumpton for his exhaustive efforts operating T6 during testing. Additional thanks go to Chris Hambidge for his relentless efforts to ensure these experiments were carried out successfully and safely. Finally, thanks are extended to Dr Brett Cruden and Dr Aaron Brandis at NASA Ames for their ongoing support and discussions.

Statement of Authorship

Title: Thermochemical Characterisation of Shock-Heated Synthetic Air
Status: Unpublished and unsubmitted work written in a manuscript style

Author Contributions:

- **Alex Glenn** - Lead author, primary code developer, data curation, formal analysis and writing.
- **Justin Clarke** - Secondary code developer.
- **Peter Collen** - Supervision as Postdoctoral Research Assistant.
- **Luca Di Mare** - Assisted in code conceptualisation.
- **Matthew McGilvray** - Supervision as Principal Investigator, and organised and managed funding.

Student Confirmation: **Date:** 14/10/2024



Supervisor Confirmation: **Date:** 15/10/2024



Chapter 8

Conclusions and Recommendations

"The light at the end of the tunnel"

8.1 Conclusions and Contributions

8.1.1 Conclusions

The primary aim of this thesis was to obtain accurate temperature and species number density data relevant to the stagnation line of a low Earth orbit return vehicle. Chapter 1 partitioned this into a series of four objectives, each building on the latter. Here, these are repeated in retrospect of the preceding work and conclusions are developed. In each case, key results which have contributed to the overall goal are highlighted.

1. **Reduce the discrepancies of shock tube equilibrium radiance measurements against numerical predictions.**

   Of all the thermochemical states to be characterised behind a shock front, the one of equilibrium is the most certain. Thus, good agreement between experimental data and numerical predictions here is essential before conducting non-equilibrium studies, which introduce added complexities from chemical kinetics and uncertainties in the evolving thermochemical state.

   Chapter 4 investigates the offsets of low-speed air equilibrium spectra present in previous T6 and EAST campaigns, from CEA-NEQAIR predictions. A reduction in spectrometer slit widths was shown to significantly improve agreement from $\sim$600

nm upwards, achieving close agreement with the N_2 first positive background signal, believed to be owed to a reduction in stray light inside the spectrometer casing. Discrepancies remaining at lower wavelengths were shown to be dependent on both shock speed and post-shock pressure. In particular, the NO bands from 200 to $\sim$280 nm improve at lower pressure conditions, at the expense of increased contaminant mole fractions, as gauged by the CN violet band contributions. Additionally, the predicted radiation levels are shown to have increased sensitivity to the selected radiative modelling at these lower wavelengths.

The effect of a leak rate reduction and trial of downstream plasma cleaning showed the CN contaminant levels may be influenced but ultimately had no effect on the remaining offsets at lower wavelengths. Excess electrons, above a whole order of magnitude from equilibrium predictions, were introduced into simulations to raise the atomic nitrogen bound-free background signal. This improved the agreement between simulations and measurements in the 300 to 400 nm range but had a lesser impact on the NO region and made agreement at higher wavelengths significantly worse. Hydrodynamic compression and shock deceleration effects towards the latter end of the T6 test slugs were also validated to be negligible, by comparison of CEA- vs LASTA-NEQAIR radiance level predictions.

Overall, this chapter reduced the discrepancies between shock tube equilibrium radiance measurements and predictions, as set out by the original aim, and characterises the trends remaining at the lower wavelengths. Section 8.2 discusses remaining possible causes and recommends areas for further work. This outcome ensures a more reliable dataset for thermochemical characterisation, increasing confidence that the extracted temperatures and number densities in later steps reflect the actual thermochemical state, rather than being skewed by fundamental inconsistencies from the outset.

2. **Develop a means to convert radiance through the shock layer into temperature and species number density profiles that obey conservation of mass, momentum and energy.**

   Chapter 5 developed a constrained spectral fitting routine to convert spatio-spectral radiance data from both ultraviolet and visible/near-infrared spectral channels into the temperatures and species number densities present through the test slug. The routine ensures results obey conservation of mass, momentum, energy, atomic ratios and charge, distinguishing it from prior shock tube spectral fitting studies, though limits itself to a two-temperature model and assumes Boltzmann distributions throughout. The conservation criteria are met by calling Oxford's in-house thermochemical property

and transport library, OCEAN, while NASA's NEQAIR radiation transport code is used to generate the spectral profiles. Validation using artificial NESS-NEQAIR radiance data, incorporating a range of experimental artefacts, demonstrates the routine's ability to significantly improve the accuracy of species number density extraction. However, the spectral traces show a strong sensitivity to the vibrational temperature, which is extracted accurately with and without the conservation criteria enabled.

Limitations of the methodology are identified. The primary one being that a species must emit detectable radiation in the observed wavelength regions for it to convey information to the fitting routine. The addition of electron number densities into the artificial pure nitrogen spectra during the validation studies improved the overall characterisation of the test slug, enabling the N^+ evolution to be inferred via the constraints. Thus, further demonstrating the value of implementing conservation criteria and identifying electron number density measurements as a priority in future shock tube campaigns. Finally, the constrained routine is applied to real pure nitrogen data from the EAST facility at NASA Ames. The vibrational temperature extracted compares well against previous spectral fitting attempts, and consideration of shock deceleration effects is shown to significantly influence the extent of N_2 dissociation predicted in the latter portions of the test slug.

To summarise, in the context of the greater aims of this thesis, chapter 5 develops a thermodynamically robust methodology for conversion of spatio-spectral radiance measurements into thermochemical state information, to accurately extract species which emit detectable radiation levels. This is an important step to enable thermochemical characterisation of high-enthalpy test slugs from the new low-speed datasets acquired for this thesis.

3. **Analysis of pure nitrogen non-equilibrium data.**

   Following from the previous chapters, T6 pure nitrogen data captured in the work of this thesis, is studied in chapter 6. A reduction in pressure for a given shock speed is shown to stretch out the non-equilibrium region, to improve spatial resolution of the evolving thermochemical state, at the compromise of reduced signal:noise ratio. The simplified test gas reduces the complexity of energy exchange interactions and provides a fundamental dataset for initial application of the constrained spectral fitting routine.

   T6 tests ranging from 6.2 to 7.4 km/s are analysed by spectral fitting, all with a common post-shock pressure of $\sim$45 kPa. Thermal relaxation for all cases is achieved within 60 to 100 μs after being processed by the shock. However, degrees of chemical

non-equilibrium are sustained, with N_2 dissociation failing to reach CEA predicted mole fractions within the observable test slug, corresponding to $\sim$110 μs of relaxation time. Close agreement is shown with results from an EAST test of comparable shock speed, after normalising the data by the time since being processed by the shock and the nominal post-shock pressures. However, differences in shock speed profiles have a strong influence on N_2 and N predictions in the latter portions of the test slug. Finally, a comparison against the well-established Park two-temperature and rate predictions suggests the model over predicts the initial rate of N_2 dissociation, while under predicting the N_2^+ number densities apparent immediately behind the shock front. However, the vibrational temperature predictions are very close to that extracted from the experimental data.

Overall, this chapter demonstrates the successful application of the constrained spectral fitting routine, to characterise the evolution of simplified test slugs. The results offer early insights into areas where thermochemical rates may require updating and support the extension of this approach to more complex, flight-relevant mixtures.

4. **Analysis of synthetic air non-equilibrium data.**

   Finally, chapter 7 presents radiation data acquired in T6 using a synthetic air test gas. This progresses from the previous chapter by introducing oxygen species, with correct mole fractions to emulate the true flight stagnation line ahead of a hypersonic vehicle, from the shock front to the boundary layer edge.

   Of the available test cases, a 7.3 km/s and $\sim$20 kPa post-shock pressure condition is selected for spectral fitting analysis. Thermal relaxation is complete within 80 μs after being processed by the shock front, while continued N_2 dissociation extends the chemical non-equilibrium effects through the observable test slug, similarly to that seen in pure nitrogen. Results from a comparable EAST test show close agreement, except in the latter portions, where shock deceleration influences the N_2 and N number densities. Additionally, normalisation by time since being processed by the shock and the nominal post-shock pressure provides thermochemical evolution data directly relevant to the stagnation line ahead of a hypersonic vehicle, from the shock front to the boundary layer edge. This completes the ultimate aim of this thesis, for the chosen shock speed. Future works should continue to apply this methodology to other test cases from the new T6 AST dataset, ranging from 5.7 to 8 km/s shock speeds and 10 to 100 kPa post-shock pressures, to extend this characterisation to a wider range of points along a LEO return trajectory. Furthermore, comparisons between the extracted data and predictions using a Park two-temperature model with modified Cruden rates

suggest the current models under predict the NO and N_2^+ production immediately behind the shock front.

Uncertainties around the spectral fitting of the lower wavelengths where NO bands dominate are identified and emphasise the need of alternative optical diagnostic measurements to prove/disprove the radiance quoted in emission spectra. This resonates with the results of chapter 4, where discrepancies remained in the equilibrium spectral comparisons where NO radiates. Despite this, comparisons between different ultraviolet spectral ranges and resolutions, incorporating different amounts of the NO spectrum, show reasonable agreement across all extracted parameters, except for atomic O. High-resolution ultraviolet spectra improves resolution of N_2 and N_2^+ but does not contain any information of the NO radiance. The lack of NO information causes the routine to over predict atomic O number densities immediately behind the shock to maintain atom conservation through the test slug. This demonstrates the pros and cons of high resolution data and highlights that combinations of both low and high resolution data across repeat shots may be required to perform the most reliable thermochemical state extraction.

Despite the remaining uncertainties around the lower wavelengths, chapter 7 has fulfilled the ultimate goal of this thesis, by thermochemically characterising the major radiators in a synthetic air test slug and normalising results to be directly relatable to a trajectory point during a LEO return mission. This is a significant contribution to the current literature.

8.2 Recommendations For Future Work

The research conducted in this thesis has highlighted several areas for future work, which are compiled and organised into the following subsections.

1. **Further Analysis of Current Datasets**

   The pure nitrogen and synthetic air datasets acquired during this thesis still provide ample opportunity for analysis and thermochemical characterisation studies. These can be summarised into:

   (a) **Continued application**: The constrained spectral fitting routine should be applied to more of the available pure nitrogen and synthetic air T6 test cases to extract thermochemical state information across a wider range of points during a LEO return trajectory.

(b) **Study closer to vehicle surface**: Extend the application of the routine further to T6 test data with varying levels of CO_2 and H_2 gases doped into the synthetic air test mixture, to investigate the effect these species have on the thermochemistry closer to the vehicle surface. Radiance data for this was acquired during the same T6 experimental campaign discussed in this thesis.

(c) **Calibration methodology**: Perform cross-comparisons of the calibration and stray light removal methodologies between T6, EAST and ICP torch spectral data to ensure consistency between facility datasets.

2. **Constrained Spectral Fitting Routine Improvements**

The current constrained spectral fitting routine can take over three days to complete for synthetic air data. To improve its speed, several strategies could be employed:

(a) **Parallelisation**: By distributing computations across multiple CPU cores or using GPUs, it is possible to significantly reduce run times. MATLAB's Parallel Computing Toolbox, for instance, enables parallel execution of independent tasks, such as fitting operations on different spectral bands or data segments.

(b) **Rewriting the code**: The existing MATLAB code could be re-implemented in more performant languages like C++, Python or Fortran. These languages offer greater control over memory management and optimisation, which can lead to substantial speed improvements. Libraries such as NumPy, SciPy (Python), or Eigen (C++) provide optimised routines for numerical computing that could accelerate the fitting process.

(c) **Migrating to a Linux-Based System**: Running the code directly on a Linux machine would eliminate the bandwidth limitations introduced by the current setup, where the Windows host and Linux virtual machine communicate. Linux is often more efficient for high-performance computing tasks, especially when combined with parallelised or optimised code.

3. **Future Shock Tube Campaigns**

These recommendations largely focus on resolving the remaining discrepancies between experiment and numerical predictions at lower wavelengths, where NO bands dominate, as well as further reducing the baseline contaminant levels.

(a) **Electrons**: Measuring electron number densities will complement the existing spectral dataset and improve overall thermochemical characterisation, as shown

for pure nitrogen in Chapter 5. This can be achieved optically via Stark broadening measurements of the Hα and Hβ lines, which has already been measured at 7 and 9.8 km/s during the experiments for this thesis. Analysing these tests will indicate if the signal:noise ratio is sufficient for lower-speed measurements. However, other broadening mechanisms, such as pressure broadening, must be carefully considered to ensure they do not obscure the Stark broadening effects arising from free electrons. Alternative measurement techniques include microwave interferometry and reflectometry, as well as Langmuir probes. The latter has already been developed and trialled for T6 testing, however presents complex data interpretation problems due to the additional bow shock formed over the probe in the hypersonic flow, thus changing the measurement from the desired freestream.

(b) **VUV data**: Extend emission spectroscopy data into the vacuum ultraviolet (VUV) wavelengths. This allows access to ground state transitions of atomic species which will be useful for validating the applicability of the Boltzmann distributions assumed in this work. Additionally, the VUV region is known to produce the most intense spectral radiance for the considered conditions and is also the area of highest uncertainty, due to its limited availability. Acquisition of data in this region will thus complement the work in this thesis and provide an important contribution to the wider literature.

(c) **Absorption measurements**: Implement tunable diode laser absorption spectroscopy (TDLAS) diagnostics to perform measurements of NO state populations. This is planned for T6 shock tube experiments in the near future and will help to identify if the discrepancies between experiment and predictions at the lower wavelengths are physical or due to artefacts of the emission spectroscopy calibration process.

(d) **Tube heating**: Implement a shock tube wall heating system on the T6 facility, similar to that used on the EAST facility at NASA Ames, to assess its effectiveness in reducing residual contaminant levels. This will help determine whether incomplete outgassing is contributing to the remaining contamination.

4. **Numerical Modelling**

To further address the remaining discrepancies between experimental results and numerical predictions, there are a number of numerical considerations which may contribute towards improved agreement.

(a) **Radiative modelling**: The spectral region with the remaining unexplained discrepancy, where NO radiates, also showed the greatest sensitivity to the selected radiative modelling, as demonstrated in Chapter 4. Investigating the differences between the chosen models and the necessary adjustments for achieving closer agreement would provide a valuable addition to the current work. The discrepancies may arise from non-Boltzmann NO distributions or unaccounted species contributions at these lower wavelengths, such as alternative O_2 photodissociation cross-sections. Investigations here will complement the calibration methodology comparisons and TDLAS measurements, to determine the source of the remaining offset at lower wavelengths.

(b) **Boundary layer**: In all analyses conducted in this thesis, a homogeneous core flow across the diameter of the shock tube has been assumed, neglecting any effects from the boundary layer along the tube wall. Accurately modeling these effects will help validate whether this assumption is correct or identify it as an additional factor that may influence the numerical spectral predictions.

References

[1] Anderson, J. D. (2006). *Hypersonic and high temperature gas dynamics, second edition*. Aiaa.

[2] Andrianatos, A., Gildfind, D., and Morgan, R. (2019). Testing a full-scale hayabusa model in a large expansion tube. In *Asia Pacific International Symposium on Aerospace Technology (2019: Gold Coast, Qld.)*, pages 43–59. Engineers Australia Gold Coast, Australia.

[3] Bakos, R. and Erdos, J. (1995). Options for enhancement of the performance of shock-expansion tubes and tunnels. In *33rd Aerospace Sciences Meeting and Exhibit*, page 799.

[4] Banerji, N., Leyland, P., Fahy, E., and Morgan, R. (2018). Venus entry flow over a decomposing aeroshell in x2 expansion tube. *Journal of Thermophysics and Heat Transfer*, 32(2):292–302.

[5] Barnhardt, M., Brandis, A., Wright, M., and Hughes, M. (2021). Recent advancements in modeling and simulation of entry systems at nasa. In *IEEE Aerospace Conference*.

[6] Beck, P. (2024). About us. Accessed on July 29, 2024. URL: https://www.rocketlabusa.com/about/about-us/.

[7] Beck, W. and Mackie, J. (1978). Application of the shock tube unsteady expansion wave technique to the study of chemical reactions. *Journal of Physics D: Applied Physics*, 11(9):1249.

[8] Bergin, C. (2024). Spacex begins 2024 with several record-breaking feats. Accessed on July 29, 2024. URL: https://www.nasaspaceflight.com/2024/04/spacex-quarter-1/.

[9] Blue Origin (2023). Blue origin. Accessed on April 6, 2024. Available at: https://www.blueorigin.com/about-blue.

[10] Bogdanoff, D. W. and Cruden, B. A. (2016). Optimizing facility configurations and operating conditions for improved performance in the nasa ames 24 inch shock tube. Technical report.

[11] Bowman, C. T. and Hanson, R. K. (1979). Shock tube measurements of rate coefficients of elementary gas reactions. *Journal of Physical Chemistry*, 83(6):757–763.

[12] Boyd, I. D. and Jenniskens, P. (2010). Modeling of stardust entry at high altitude, part 2: Radiation analysis. *Journal of Spacecraft and Rockets*, 47(6):901–909.

[13] Brandis, A., Cruden, B., Prabhu, D., Bose, D., McGilvray, M., Morgan, R., and Morgan, R. (2010a). Analysis of air radiation measurements obtained in the east and x2 shocktube facilities. In *10th AIAA/ASME Joint Thermophysics and Heat Transfer Conference*, page 4510.

[14] Brandis, A., Johnston, C., Panesi, M., Cruden, B., Prabhu, D., and Bose, D. (2013). Investigation of nonequilibrium radiation for mars entry. In *51st AIAA Aerospace Sciences Meeting including the New Horizons Forum and Aerospace Exposition*, page 1055.

[15] Brandis, A., Morgan, R., Laux, C., Magin, T., McIntyre, T., and Jacobs, P. (2007). Nonequilibrium radiation measurements and modelling relevant to titan entry. In *Proceedings of the 16th Australasian Fluid Mechanics Conference, 16AFMC*, volume 1, pages 594–601. School of Engineering, The University of Queensland.

[16] Brandis, A. M. and Cruden, B. A. (2017a). Benchmark shock tube experiments of radiative heating relevant to earth re-entry. In *55th AIAA Aerospace Sciences Meeting*, page 1145.

[17] Brandis, A. M. and Cruden, B. A. (2017b). Titan atmospheric entry radiative heating. In *47th AIAA Thermophysics Conference*, page 4534.

[18] Brandis, A. M. and Cruden, B. A. (2018). Shock tube radiation measurements in nitrogen. In *2018 Joint Thermophysics and Heat Transfer Conference*, page 3437.

[19] Brandis, A. M. and Cruden, B. A. (2019). Neqair v15. 0 release notes: Nonequilibrium and equilibrium radiative transport and spectra program. Technical report.

[20] Brandis, A. M. and Johnston, C. O. (2014). Characterization of stagnation-point heat flux for earth entry. In *45th AIAA Plasmadynamics and Lasers Conference*, page 2374.

[21] Brandis, A. M., Morgan, R. G., McIntyre, T. J., and Jacobs, P. A. (2010b). Nonequilibrium radiation intensity measurements in simulated titan atmospheres. *Journal of Thermophysics and Heat Transfer*, 24(2):291–300.

[22] Bushnell, D. (1990). Notes on initial disturbance fields for the transition problem. In *Instability and Transition: Materials of the workshop held May 15-June 9, 1989 in Hampton, Virgina Volume 1*, pages 217–232. Springer.

[23] Bykova, N. and Kuznetsova, L. (2008). Study of the absorption characteristics of molecular oxygen in the schumann-runge system at high temperatures: I. calculations of absorption spectra. *Optics and Spectroscopy*, 105:668–673.

[24] Cacciatore, M., Kurnosov, A., and Napartovich, A. (2005). Vibrational energy transfer in n2–n2 collisions: a new semiclassical study. *The Journal of chemical physics*, 123(17).

[25] Capra, B. R. (2007). Aerothermodynamic simulation of subscale models of the fire ii and titan explorer vehicles in expansion tubes.

[26] Capra, B. R. and Morgan, R. G. (2012). Radiative and total heat transfer measurements to a titan explorer model. *Journal of Spacecraft and Rockets*, 49(1):12–23.

[27] Casses, C. J., Bertrand, P. J., Jacobs, C., Macdonald, M. E., and Laux, C. O. (2013). Experimental characterization of ultraviolet radiation of air in a high enthalpy plasma torch facility. In *Progress in Flight Physics*, volume 7, pages 353–368.

[28] Chang, E., Schaefer, J., Valeinis, O., Buquet, M., and Hermann, T. (2023). Commissioning of the opg1 plasma wind tunnel.

[29] Clarke, J., Di Mare, L., and McGilvray, M. (2023a). Spatial transformations for reacting gas shock tube experiments. *AIAA journal*, 61(8):3365–3374.

[30] Clarke, J., Glenn, A., McGilvray, M., and di Mare, L. (2023b). Numerical simulation of a shock tube in thermochemical non-equilibrium. In *AIAA SCITECH 2023 Forum*, page 1797.

[31] Clarke, J., Glenn, A. B., Di Mare, L., and McGilvray, M. (2024). Numerical simulations of carbon contaminants in t6 shock tube tests.

[32] Collen, P. (2021). *Development of a High-Enthalpy Ground Test Facility for Shock-Layer Radiation*. PhD thesis, Univ. of Oxford, Oxford, UK.

[33] Collen, P., Doherty, L., Subiah, S., Hyslop, A., and McGilvray, M. (2019a). Performance capability experiments in t6: A hypervelocity, transient and multi-mode ground test facility for high-enthalpy aerothermodynamics research. ESA Conference Bureau.

[34] Collen, P., Doherty, L. J., and McGilvray, M. (2019b). Measurements of radiating hypervelocity air shock layers in the t6 free-piston driven shock tube. ESA Conference Bureau.

[35] Collen, P., Doherty, L. J., Subiah, S. D., Sopek, T., Jahn, I., Gildfind, D., Penty Geraets, R., Gollan, R., Hambidge, C., Morgan, R., et al. (2021). Development and commissioning of the t6 stalker tunnel. *Experiments in Fluids*, 62(11):1–24.

[36] Collen, P. L., Doherty, L., McGilvray, M., Naved, I., Penty Geraets, R. T., Hermann, T. A., Morgan, R. G., and Gildfind, D. (2019c). Commissioning of the t6 stalker tunnel. In *AIAA Scitech 2019 Forum*, page 1941.

[37] Collen, P. L., Glenn, A. B., Doherty, L. J., and McGilvray, M. (2023). Absolute measurements of air shock-layer radiation in the t6 aluminium shock tube. *Journal of Thermophysics and Heat Transfer*, pages 1–14.

[38] Collen, P. L., Satchell, M., di Mare, L., and McGilvray, M. (2022). Analysis of shock deceleration effects on radiation experiments in the nasa electric arc shock tube. In *AIAA SCITECH 2022 Forum*, page 0267.

[39] Cruden, B., Martinez, R., Grinstead, J., and Olejniczak, J. (2009). Simultaneous vacuum-ultraviolet through near-ir absolute radiation measurement with spatiotemporal resolution in an electric arc shock tube. In *41st AIAA Thermophysics Conference*, page 4240.

[40] Cruden, B. A. (2012). Electron density measurement in reentry shocks for lunar return. *Journal of Thermophysics and Heat Transfer*, 26(2):222–230.

[41] Cruden, B. A. (2014). Absolute radiation measurements in earth and mars entry conditions.

[42] Cruden, B. A. (2024). Radiative emission in incident air shocks from 3–7 km/s. In *AIAA AVIATION FORUM AND ASCEND 2024*, page 3653.

[43] Cruden, B. A. and Bogdanoff, D. W. (2017). Shock radiation tests for saturn and uranus entry probes. *Journal of Spacecraft and Rockets*, 54(6):1246–1257.

[44] Cruden, B. A. and Brandis, A. M. (2014). Updates to the neqair radiation solver. In *6th International Workshop on Radiation of High Temperature Gases in Atmospheric Entry*, number ARC-E-DAA-TN19271.

[45] Cruden, B. A. and Brandis, A. M. (2017). Measurement and prediction of radiative non-equilibrium for air shocks between 7-9 km/s.

[46] Cruden, B. A. and Brandis, A. M. (2019a). Analysis of shockwave radiation data in nitrogen. In *AIAA Aviation 2019 Forum*, page 3359.

[47] Cruden, B. A. and Brandis, A. M. (2019b). Revised shock layer radiation modeling for air. In *8th International Workshop on Radiation of High Temperature Gases for Space Missions*.

[48] Cruden, B. A., Brandis, A. M., White, T. R., and Bose, D. (2015). Radiative heating for msl entry: Verification of simulations from ground test to flight data. In *53rd AIAA Aerospace Sciences Meeting*, page 1894.

[49] Cruden, B. A., Prabhu, D., and Martinez, R. (2012). Absolute radiation measurement in venus and mars entry conditions. *Journal of Spacecraft and Rockets*, 49(6):1069–1079.

[50] Cruden, B. A., Tang, C. Y., Olejniczak, J., Amar, A. J., and Tanno, H. (2021). Characterization of radiative heating anomaly in high enthalpy shock tunnels. *Experiments in Fluids*, 62(7):142.

[51] Crumpton, T. J. (2024). Analysis of mars entry shock wave radiance in the t6 stalker hypersonic wind tunnel. In *AIAA SCITECH 2024 Forum*, page 0861.

[52] Danehy, P. M., Bathel, B. F., Johansen, C. T., Winter, M., O'Byrne, S., and Cutler, A. D. (2013). Molecular-based optical diagnostics for hypersonic nonequilibrium flows. Technical report, AIAA Progress Series.

[53] De Crombrugghe, G., Gildfind, D., Zander, F., McIntyre, T., and Morgan, R. (2014). Design of test flows to investigate binary scaling in high enthalpy co2-n2 mixtures. In *Proceedings of the 19th Australasian Fluid Mechanics Conference, AFMC 2014*, pages 325–1. RMIT University.

[54] Dunn, M. and Lordi, J. (1969). Measurement of electron temperature and number density in shock-tunnel flows. *AIAA J*, 7.

[55] Dunn, M. G. (1972). Use of positively biased electrostatic probes to obtain electron density in collisionless flows. *AIAA Journal*, 10(8):996–999.

[56] Erdman, P. W., Zipf, E. C., Espy, P., Howlett, C., Levin, D. A., Loda, R., Collins, R. J., and Candler, G. V. (1993). Flight measurements of low-velocity bow shock ultraviolet radiation. *Journal of Thermophysics and Heat Transfer*, 7(1):37–41.

[57] ESA (2023a). Ice giant exploration: Advancements in atmospheric entry technology. Accessed on July 30, 2024. URL: https://www.esa.int/Enabling_Support/Space_Engineering_Technology/Shaping_the_Future/Ice_Giant_Exploration_Advancements_in_Atmospheric_Entry_Technology.

[58] ESA (2023b). Juice, jupiter icy moons explorer. Accessed on July 30, 2024. URL: https://www.esa.int/Science-Exploration/Space-Science/Juice.

[59] Fahy, E. J. (2017). Superorbital re-entry shock layers: flight and laboratory comparisons.

[60] Ferreira, R. G. and da Silva, M. L. (2023). European shock-tube for high-enthalpy research combustion driver qualification. *arXiv preprint arXiv:2306.17310*.

[61] Fujita, K., Sato, S., Abe, T., and Ebinuma, Y. (2002). Experimental investigation of air radiation from behind a strong shock wave. *Journal of Thermophysics and Heat Transfer*, 16(1):77–82.

[62] Fujita, K., Suzuki, T., Takayanagi, H., Ozawa, T., Nomura, S., Takizawa, N., Matsuyama, S., Lemal, A., and Mizuno, M. (2019). Research on shock-induced aerothermodynamics for future planetary explorations. In *31st International Symposium on Shock Waves 1: Fundamentals 31*, pages 57–64. Springer.

[63] Geraets, R. T. P., McGilvray, M., Doherty, L. J., Morgan, R. G., James, C. M., and Buttsworth, D. R. (2020). Development of a fast-response diamond calorimeter heat transfer gauge. *Journal of Thermophysics and Heat Transfer*, 34(1):193–202.

[64] Gibson, S. (2016). Pydiatomic: Pydiatomic initial release (v0.1-alpha).

[65] Gildfind, D. E., James, C. M., Toniato, P., and Morgan, R. G. (2015). Performance considerations for expansion tube operation with a shock-heated secondary driver. *Journal of Fluid Mechanics*, 777:364–407.

[66] Gildfind, D. E., Morgan, R. G., and Jacobs, P. A. (2016). Expansion tubes in australia. *Experimental methods of shock wave research*, pages 399–431.

[67] Glenn, A., Collen, P., Jacobs, C., Laux, C., and McGilvray, M. (2022). Comparison of equilibrium radiation between shock tube and plasma torch spectroscopy for atmospheric pressure air.

[68] Glenn, A. B., Collen, P., and McGilvray, M. (2024). Radiation measurements of shockwaves in synthetic air and pure nitrogen. In *AIAA SCITECH 2024 Forum*, page 0226.

[69] Glenn, A. B., Collen, P. L., and McGilvray, M. (2021). Experimental non-equilibrium radiation measurements for low-earth orbit return.

[70] Gnoffo, P. A. (1999). Planetary-entry gas dynamics. *Annual Review of Fluid Mechanics*, 31(1):459–494.

[71] Gollan, R. (2008). Computational modelling of high-temperature gas effects with application to hypersonic flows.

[72] Gollan, R., Jacobs, C., Jacobs, P. A., Morgan, R. G., McIntyre, T. J., Macrossan, M. N., Buttsworth, D. R., Eichmann, T. N., and Potter, D. (2009). A simulation technique for radiating shock tube flows. In *Shock Waves: 26th International Symposium on Shock Waves, Volume 1*, pages 465–470. Springer.

[73] Goulard, R. (1961). The coupling of radiation and convection in detached shock layers. *Journal of Quantitative Spectroscopy and Radiative Transfer*, 1(3-4):249–257.

[74] Greenberg, R. B., Cruden, B. A., Grinstead, J. H., and Yeung, D. (2009). Collection optics for imaging spectroscopy of an electric arc shock tube. In *Novel Optical Systems Design and Optimization XII*, volume 7429, pages 155–165. SPIE.

[75] Grinstead, J. H., Wilder, M. C., Reda, D. C., Cornelison, C. J., Cruden, B. A., and Bogdanoff, D. W. (2010). Shock tube and ballistic range facilities at nasa ames research center. Technical report.

[76] Guerra, V. and Loureiro, J. (1995). Non-equilibrium coupled kinetics in stationary n2-o2 discharges. *Journal of Physics D: Applied Physics*, 28(9):1903.

[77] Hayne, M. J. (2004). Hypervelocity flow over rearward-facing steps.

[78] Hermann, T., Chang, E. W. K., Schäfer, J., Joglekar, C., and Boehrk, H. (2023). Development of small scale arc-jet facility opg1. In *AIAA SciTech 2023 Forum*, page 2331.

[79] Hermann, T., Loehle, S., Zander, F., Fulge, H., and Fasoulas, S. (2016). Characterization of a reentry plasma wind-tunnel flow with vacuum-ultraviolet to near-infrared spectroscopy. *Journal of Thermophysics and Heat Transfer*, 30(3):673–688.

[80] Hermann, T., Löhle, S., Bauder, U., Morgan, R., Wei, H., and Fasoulas, S. (2017a). Quantitative emission spectroscopy for superorbital reentry in expansion tube x2. *Journal of Thermophysics and Heat Transfer*, 31(2):257–268.

[81] Hermann, T., Löhle, S., Zander, F., and Fasoulas, S. (2017b). Measurement of the aerothermodynamic state in a high enthalpy plasma wind-tunnel flow. *Journal of Quantitative Spectroscopy and Radiative Transfer*, 201:216–225.

[82] Herzberg, G. and Spinks, J. W. T. (1944). *Atomic spectra and atomic structure*. Courier Corporation.

[83] Hollis, B. R. (2012). Blunt-body entry vehicle aerotherodynamics: transition and turbulent heating. *Journal of Spacecraft and Rockets*, 49(3):435–449.

[84] Hollis, B. R. and Prabhu, D. K. (2013). Assessment of laminar, convective aeroheating prediction uncertainties for mars-entry vehicles. *Journal of Spacecraft and Rockets*, 50(1):56–68.

[85] Hornung, H. (1990). Role and techniques of ground testing for simulation of flows up to orbital speed. In *16th Aerodynamic Ground Testing Conference*, page 1377.

[86] Hornung, H., Sturtevant, B., Belanger, J., Sanderson, S., Brouillette, M., and Jenkins, M. (1992). Performance data of the new free-piston shock tunnel t5 at galcit. In *Shock Waves: Proceedings of the 18th International Symposium on Shock Waves, Held at Sendai, Japan 21–26 July 1991*, pages 603–610. Springer.

[87] Hornung Han, G. (2010). Ground testing for hypervelocity flow, capabilities and limitations. Technical report, NASA: ADA581905.

[88] Huo, W. M., Liu, Y., Panesi, M., Wray, A., and Carbon, D. F. (2015). Electron-impact excitation cross sections for modeling non-equilibrium gas. In *53rd AIAA Aerospace Sciences Meeting*, page 1896.

[89] Jacobs, P. (2012). A microcontroller-based delay generator for predicting shock arrival in the x2 expansion tube.

[90] Jacobs, P. A., Gollan, R. J., and Potter, D. F. (2012). The compressible-flow cfd project.

[91] James, C., Gildfind, D., Lewis, S., Morgan, R., and Zander, F. (2018a). Implementation of a state-to-state analytical framework for the calculation of expansion tube flow properties. *Shock Waves*, 28(2):349–377.

[92] James, C. M., Cullen, T. G., Wei, H., Lewis, S. W., Gu, S., Morgan, R. G., and McIntyre, T. J. (2018b). Improved test time evaluation in an expansion tube. *Experiments in Fluids*, 59:1–21.

[93] Jewell, J. (2008). *Boundary layer transition in hypersonic flows*. PhD thesis, University of Oxford.

[94] Jewell, J. S., Parziale, N. J., Leyva, I. A., and Shepherd, J. E. (2017). Effects of shock-tube cleanliness on hypersonic boundary layer transition at high enthalpy. *AIAA journal*, 55(1):332–338.

[95] Jiang, H., Liu, J., Luo, S., Huang, W., Wang, J., and Liu, M. (2022). Thermochemical non-equilibrium effects on hypersonic shock wave/turbulent boundary-layer interaction. *Acta Astronautica*, 192:1–14.

[96] Johnston, C. O. (2021). Evaluating shock-tube informed biases for shock-layer radiative heating simulations. *Journal of Thermophysics and Heat Transfer*, 35(2):349–361.

[97] Johnston, C. O., Gnoffo, P. A., and Sutton, K. (2009). Influence of ablation on radiative heating for earth entry. *Journal of Spacecraft and Rockets*, 46(3):481–491.

[98] Kliche, D., Mundt, C., and Hirschel, E. (2011). The hypersonic mach number independence principle in the case of viscous flow. *Shock Waves*, 21:307–314.

[99] Krish, A., Streicher, J. W., and Hanson, R. K. (2020). Ultraviolet absorption cross-section measurements of shock-heated o2 from 2,000–8,400 k using a tunable laser. *Journal of Quantitative Spectroscopy and Radiative Transfer*, 247:106959.

[100] Laux, C., Gessman, R., and Kruger, C. (2002). Measurements and modeling of the absolute spectral emission of air plasmas between 185 and 800 nm. *JQSRT (to be submitted 2001)*.

[101] Laux, C. O. (1993). *Optical diagnostics and radiative emission of air plasmas*. PhD thesis, Stanford university.

[102] Laux, C. O., Spence, T., Kruger, C., and Zare, R. (2003). Optical diagnostics of atmospheric pressure air plasmas. *Plasma Sources Science and Technology*, 12(2):125.

[103] Lemal, A., Jacobs, C., Perrin, M., Laux, C., Tran, P., and Raynaud, E. (2015). Effect of heavy-particle impact excitation processes on post shock nonequilibrium air radiation. In *Proceedings of the 8th European Symposium on Aerothermodynamics for Space Vehicles*, pages 1–10. European Space Agency.

[104] Leyland, P., McIntyre, T., Morgan, R., Jacobs, P., Zander, F., Sheikh, U., Eichmann, T., Fahy, E., Joshi, O., Duffa, G., et al. (2013). Radiation-ablation coupling for capsule reentry heating via simulation and expansion tube investigations. In *Proceedings of the 5th European Conference for Aeronautics and Space Sciences (EUCASS)*.

[105] Lino da Silva, M., Chikhaoui, A., Smith, A., and Dudeck, M. (2012). Performance design and development of the new european shock-tube facility esther. *ESA Special Publication*, 714:20.

[106] Loehle, S., Fasoulas, S., Herdrich, G. H., Hermann, T. A., Massuti-Ballester, B., Meindl, A., Pagan, A. S., and Zander, F. (2016). The plasma wind tunnels at the institute of space systems: current status and challenges. In *32nd AIAA Aerodynamic Measurement Technology and Ground Testing Conference*, page 3201.

[107] Löhle, S. and Reimer, T. (2013). Experimental investigation of photogrammetric surface analysis of heat shield materials during plasma wind tunnel testing. In *7th European Workshop on Thermal Protection Systems and Hot Structures*.

[108] Löhle, S., Vacher, D., Menecier, S., Dudeck, M., Liebhart, H., Marynowski, T., Herdrich, G., Fasoulas, S., and André, P. (2010). Measurement campaigns on mars entry plasmas using icp torches. characterization by emission spectroscopy and probes techniques. In *Proceedings of the 4th International Workshop on Radiation and High Temperature Gases in Atmospheric Entry*.

[109] Lopez, B. and Lino Da Silva, M. (2016). Spark: a software package for aerodynamics, radiation and kinetics. In *46th AIAA thermophysics conference*, page 4025.

[110] Luque, J. (1999). Lifbase, database and spectral simulation for diatomic molecules. *SRI International Report*, 99.

[111] MacDonald, M. E., Brandis, A. M., and Cruden, B. A. (2018). Temperature and co number density measurements in shocked co and co2 via tunable diode laser absorption spectroscopy. In *2018 Joint Thermophysics and Heat Transfer Conference*, page 4067.

[112] MacDonald, M. E., Jacobs, C. M., Laux, C. O., Zander, F., and Morgan, R. G. (2015). Measurements of air plasma/ablator interactions in an inductively coupled plasma torch. *Journal of Thermophysics and Heat Transfer*, 29(1):12–23.

[113] MacLean, M., Dufrene, A., and Holden, M. (2013). Spherical capsule heating in high enthalpy carbon dioxide in lens-xx expansion tunnel. In *51st AIAA Aerospace Sciences Meeting including the New Horizons Forum and Aerospace Exposition*, page 906.

[114] Malik, M., Zang, T., and Bushnell, D. (1990). Boundary layer transition in hypersonic flows. In *2nd International Aerospace Planes Conference*, page 5232.

[115] McBride, B. J. (1996). *Computer program for calculation of complex chemical equilibrium compositions and applications*, volume 2. NASA Lewis Research Center.

[116] McGilvray, M., Collen, P., Doherty, L., Steer, J., Leader, J., Glenn, A., and Hambidge, C. (2022). The oxford t6 stalker tunnel: performance, upgrades and new modes of operation.

[117] McGilvray, M., Doherty, L. J., Morgan, R. G., Gildfind, D., Jacobs, P., and Ireland, P. (2015). T6: The oxford university stalker tunnel. In *20th AIAA International Space Planes and Hypersonic Systems and Technologies Conference*, page 3545.

[118] McGilvray, M., Jacobs, P. A., Morgan, R. G., Gollan, R. J., and Jacobs, C. M. (2009). Helmholtz resonance of pitot pressure measurements in impulsive hypersonic test facilities. *AIAA Journal*, 47(10):2430–2439.

[119] McGilvray, M., McIntyre, T. J., Glenn, A., and Morgan, R. G. (2024). Shock-tube measurements of radiation for titan atmospheric entry. *Journal of Thermophysics and Heat Transfer*, pages 1–8.

[120] McGilvray, M., Morgan, R., Potter, D., Buttsworth, D., and McIntyre, T. (2010). Shock tube measurements in the x2 facility of radiation from cev re-entry conditions: Final report. Technical report, Technical report, NASA Report EG-CAP-10-65.

[121] McGuire, S., Tibère-Inglesse, A., Cruden, B., and Laux, C. (2019). Uv and vuv emission measurements in an icp torch facility.

[122] McGuire, S. D., Jacobs, C., Mariotto, P. B., Grimaldi, C. H., Tibère-Inglesse, A., and Laux, C. O. (2023). Measurements and modeling of air plasma radiation in the vuv. *Journal of Thermophysics and Heat Transfer*, 37(4):821–832.

[123] McGuire, S. D., Tibere-Inglesse, A. C., Mariotto, P. B., Cruden, B. A., and Laux, C. O. (2020). Measurements and modeling of co 4th positive (a–x) radiation. *Journal of Quantitative Spectroscopy and Radiative Transfer*, 245:106855.

[124] McIntyre, T. J., Eichmann, T. N., Jacobs, C., Potter, D., McGilvray, M., Jacobs, P., and Morgan, R. (2011). Shock tube and expansion tunnel measurements of high temperature radiating flows. *Radiation of High Temperature Gases in Atmospheric Entry*, 689:37.

[125] Merhaben, C., McGuire, S., and Laux, C. (2024). Study of a reacting n2/ch4 plasma. In *AIAA SCITECH 2024 Forum*, page 0448.

[126] Mirels, H. (1963). Test time in low-pressure shock tubes. *The physics of Fluids*, 6(9):1201–1214.

[127] Morgan, R. (2014). Hooray for ray. Plenary presentation, 11th AIAA/ASME Joint Thermophysics and Heat Transfer Conference.

[128] Morgan, R., McIntyre, T., Buttsworth, D., Jacobs, P., Potter, D., Brandis, A., Gollan, R., Jacobs, C., Capra, B., McGilvary, M., et al. (2008). Impulse facilities for the simulation of hypersonic radiating flows. In *38th Fluid Dynamics Conference and Exhibit*, page 4270.

[129] Morgan, R., McIntyre, T., Jacobs, P., Buttsworth, D., Macrossan, M., Gollan, R., Capra, B., Brandis, A., Potter, D., Eichmann, T., et al. (2006). Impulse facility simulation of hypervelocity radiating flows. *European Space Agency (Special Publication)*, 629:1–6.

[130] NASA (2019). July 20, 1969: One giant leap for mankind. Accessed on July 29, 2024. URL: https://www.nasa.gov/history/july-20-1969-one-giant-leap-for-mankind/.

[131] NASA (2023a). Data parallel line relaxation code (dplr), version 4. Accessed on June 5, 2024. URL: https://software.nasa.gov/software/ARC-16021-1A.

[132] NASA (2023b). Mars. Accessed on July 30, 2024. URL: https://www.nasa.gov/humans-in-space/humans-to-mars/.

[133] NASA (2024a). About hubble. Accessed on July 29, 2024. URL: https://science.nasa.gov/mission/hubble/overview/about-hubble/.

[134] NASA (2024b). Artemis ii. Accessed on July 30, 2024. URL: https://www.nasa.gov/mission/artemis-ii/.

[135] NASA (2024c). Commercial crew program. Accessed on July 29, 2024. URL: https://www.nasa.gov/humans-in-space/commercial-space/commercial-crew-program/.

[136] NASA (2024d). International space station. Accessed on July 29, 2024. URL: https://www.nasa.gov/international-space-station/.

[137] NASA (2024e). Mars exploration rovers: Spirit and opportunity. Accessed on July 29, 2024. URL: https://science.nasa.gov/mission/mars-exploration-rovers-spirit-and-opportunity/.

[138] NASA (2024f). Mars science laboratory: Curiosity rover. Accessed on July 29, 2024. URL: https://science.nasa.gov/mission/msl-curiosity/.

[139] Neely, A. and Stalker, R. (1992). Hypervelocity flows of argon produced in a free piston driven expansion tube. In *In: Shock waves; Proceedings of the 18th International Symposium, Sendai, Japan, July 21-26, 1991. Vol. 2 (A93-45451 19-34)*. Springer-Verlag.

[140] Noeding, P. and Martinez Schramm, J. (2014). Numerical rebuilding of shock tube experiments in co2 flow under conditions relevant for mars entry probes. In *11th AIAA/ASME Joint Thermophysics and Heat Transfer Conference*, page 2549.

[141] Palmer, G., Prabhu, D., Brandis, A., Eichmann, T., Potter, D., and McIntyre, T. (2011a). Numerical simulation of radiation measurements taken in the x2 facility for mars and titan gas mixtures. In *42nd AIAA Thermophysics Conference*, page 3768.

[142] Palmer, G., Prabhu, D., Tang, C., and Brown, J. (2011b). Coupled fluids-radiation analysis of a high-mass mars entry vehicle. In *42nd AIAA Thermophysics Conference*, page 3495.

[143] Park, C. (1985). Nonequilibrium air radiation (neqair) program. *User's Manual*.

[144] Park, C. (1989). Nonequilibrium hypersonic aerothermodynamics.

[145] Park, C. (1993). Review of chemical-kinetic problems of future nasa missions. i-earth entries. *Journal of Thermophysics and Heat transfer*, 7(3):385–398.

[146] Petersen, E. L. and Hanson, R. K. (2001). Nonideal effects behind reflected shock waves in a high-pressure shock tube. *Shock Waves*, 10(6):405–420.

[147] Potter, D. (2011). *Modelling of radiating shock layers for atmospheric entry in Mars and Earth*. PhD thesis, Ph. D. Thesis, Univ. of Queensland, Brisbane, Australia.

[148] Ravichandran, R., Loehle, S., Hufgard, F., Leiser, D., Zander, F., Ferrière, L., Vaubaillon, J., Matlovič, P., and Tóth, J. (2024). Emission spectroscopy at high frame rates during ablation tests of meteorite samples in plasma wind tunnel. *Icarus*, 407:115818.

[149] Reddy, V. S. (2018). The spacex effect. *New Space*, 6(2):125–134.

[150] Reed, T. B. (1961). Induction-coupled plasma torch. *Journal of Applied Physics*, 32(5):821–824.

[151] Richardson, N. R. (1966). Project fire instrumentation for radiative heating and related measurements. Technical report.

[152] Satchell, M., Glenn, A., Collen, P., Penty-Garaets, R., McGilvray, M., and di Mare, L. (2021a). An analytical method of evaluating nonuniformities in shock tube flows. part 2: Application.

[153] Satchell, M., McGilvray, M., and Di Mare, L. (2021b). Analytical method of evaluating nonuniformities in shock tube flows: Theory and development. *AIAA Journal*, pages 1–15.

[154] Schneider, S. P. (2004). Hypersonic laminar–turbulent transition on circular cones and scramjet forebodies. *Progress in Aerospace Sciences*, 40(1-2):1–50.

[155] Sharma, M., Austin, J., Glumac, N., and Massa, L. (2010). No and oh spectroscopic vibrational temperature measurements in a post-shock relaxation region. *AIAA journal*, 48(7):1434–1443.

[156] Sharma, S. P. and Gillespie, W. (1991). Nonequilibrium and equilibrium shock front radiation measurements. *Journal of Thermophysics and Heat transfer*, 5(3):257–265.

[157] Sharma, S. P. and Park, C. (1990a). Operating characteristics of a 60-and 10-cm electric arc-driven shock tube. i-the driver. ii-the driven section. *Journal of Thermophysics and Heat Transfer*, 4(3):259–265.

[158] Sharma, S. P. and Park, C. (1990b). Operating characteristics of a 60-and 10-cm electric arc-driven shock tube-part 11: the driven section. *Journal of thermophysics and heat transfer*, 4(3):266–272.

[159] Sheikh, U. A., Morgan, R. G., and McIntyre, T. J. (2015). Vacuum ultraviolet spectral measurements for superorbital earth entry in x2 expansion tube. *Aiaa Journal*, 53(12):3589–3602.

[160] Smith, A. (2003). Esa plasma radiation database (parade). development history, status, current developments and future prospects. In *Radiation of High Temperature Gases in Atmospheric Entry*, volume 533, pages 75–83.

[161] Smith, R., Wagner, D., and Cunningham, J. (1998). A survey of current and future plasma arc-heated test facilities for aerospace and commercial applications. In *36th AIAA Aerospace Sciences Meeting and Exhibit*, page 146.

[162] Sopek, T., Glenn, A., Clarke, J., di Mare, L., Collen, P., and McGilvray, M. (2024a). Radiative heat transfer measurements of titan atmospheric entry in a shock tube. *Journal of Thermophysics and Heat Transfer*, pages 1–23.

[163] Sopek, T., Jacobs, P., Subiah, S.-D., Collen, P., and McGilvray, M. (2024b). Effect of non-equilibrium thermochemistry on pitot pressure measurements in shock tunnels (or: Is 0.92 really the magic number?). *Acta Astronautica*, 223:249–261.

[164] SpaceWorks (2024). Recap of all global launches for 2023. Accessed on July 29, 2024. URL: https://www.spaceworks.aero/recap-of-all-global-launches-for-2023/.

[165] SpaceX (2024a). Dragon sending humans and cargo into space. Accessed on July 29, 2024. URL: https://www.spacex.com/vehicles/dragon/.

[166] SpaceX (2024b). Falcon 9 first orbital class rocket capable of reflight. Accessed on July 29, 2024. URL: https://www.spacex.com/vehicles/falcon-9/.

[167] SpaceX (2024). Spacex mission information. Accessed on April 6, 2024. Available at: https://www.spacex.com/mission/.

[168] Specair (2012). Specair. Accessed on June 6, 2024. URL: https://spectralfit.com/.

[169] Stalker, R. (2006). Modern developments in hypersonic wind tunnels. *The Aeronautical Journal*, 110(1103):21–39.

[170] Steer, J., Clarke, J., McGilvray, M., and Luca, D. M. (2024a). Lasta 2.0: Validation of a reverse time integration method. In *AIAA SCITECH 2024 Forum*, page 0447.

[171] Steer, J., Collen, P., Glenn, A., Hambidge, C., Doherty, L. J., McGilvray, M., Sopek, T., Loehle, S., and Walpot, L. (2024b). Commissioning of upgrades to t6 to study giant planet entry. *Journal of Spacecraft and Rockets*, pages 1–18.

[172] Steer, J., Collen, P. L., Glenn, A. B., Hambidge, C., Doherty, L. J., McGilvray, M., Loehle, S., and Walpot, L. (2023a). Shock radiation tests for ice giant entry probes including ch4 in the t6 free-piston driven wind tunnel. In *AIAA SCITECH 2023 Forum*, page 1729.

[173] Steer, J., Collen, P. L., Glenn, A. B., Sopek, T., Hambidge, C., Doherty, L. J., McGilvray, M., Loehle, S., and Walpot, L. (2023b). Experimental study of a galileo sub-scale model at ice giant entry conditions in the t6 free-piston driven wind tunnel. In *AIAA SciTech 2023 Forum*, page 1339.

[174] Streicher, J. W., Barnes, S. C., Krish, A., and Hanson, R. K. (2024). Vibrational-state-resolved oxygen and nitric oxide time-history measurements in shock-heated, high-temperature air. In *AIAA SCITECH 2024 Forum*, page 0227.

[175] Streicher, J. W., Krish, A., Hanson, R. K., Hanquist, K. M., Chaudhry, R. S., and Boyd, I. D. (2020). Shock-tube measurements of coupled vibration–dissociation time-histories and rate parameters in oxygen and argon mixtures from 5000 k to 10 000 k. *Physics of Fluids*, 32(7).

[176] Subiah, S., Collen, P., Doherty, L., Penty Geraets, R., Hyslop, A., and McGilvray, M. (2019). Condition development and commissioning of the oxford t6 stalker tunnel in reflected shock tunnel mode.

[177] Sutton, K. and Graves Jr, R. A. (1971). A general stagnation-point convective heating equation for arbitrary gas mixtures. Technical report.

[178] Takayanagi, H. and Fujita, K. (2012). Absolute radiation measurements behind strong shock wave in carbon dioxide flow for mars aerocapture missions. In *43rd AIAA Thermophysics Conference*, page 2744.

[179] Takayanagi, H., Fujita, K., Ishida, H., Yamada, K., and Abe, T. (2014). Radiation intensity measurement in vuv wavelength region behind strong shock wave for future sample return missions. In *11th AIAA/ASME Joint Thermophysics and Heat Transfer Conference*, page 2965.

[180] Tang, W., Ding, T., Li, D., and Zhang, C. (2024). Experimental investigation of non-equilibrium spectra for nitrogen behind strong shock waves. *Acta Astronautica*, 215:44–50.

[181] Tanno, H., Itoh, K., Komuro, T., and Sato, K. (2000). Experimental study on the tuned operation of a free piston driver. *Shock Waves*, 10:1–7.

[182] Tauber, M. E. and Sutton, K. (1991). Stagnation-point radiative heating relations for earth and mars entries. *Journal of Spacecraft and Rockets*, 28(1):40–42.

[183] Team, L. (2023). What's up in leo? insights and analysis from 2022. Accessed on July 29, 2024. URL: https://leolabs.space/article/leo-annual-review-2022/.

[184] Thirani, S., Karpuzcu, I. T., and Levin, D. A. (2024). Experimental validation of modeling efforts to estimate nitric oxide emission in high mach number flows. In *AIAA SCITECH 2024 Forum*, page 0228.

[185] Thompson, K. B., Hollis, B. R., Johnston, C. O., Kleb, B., Lessard, V. R., and Mazaheri, A. (2020). Laura users manual: 5.6. Technical report.

[186] Thorne, A., Litzén, U., and Johansson, S. (1999). *Spectrophysics: principles and applications*. Springer Science & Business Media.

[187] Tibère-Inglesse, A. and Cruden, B. A. (2022). Analysis of nonequilibrium atomic and molecular nitrogen radiation in pure n2 shockwaves. *Journal of Quantitative Spectroscopy and Radiative Transfer*, 290:108302.

[188] Tibère-Inglesse, A. C., McGuire, S. D., Mariotto, P., and Laux, C. O. (2018). Validation cases for recombining nitrogen and air plasmas. *Plasma Sources Science and Technology*, 27(11):115010.

[189] Trimpi, R. L. (1962). *A preliminary theoretical study of the expansion tube: a new device for producing high-enthalpy short-duration hypersonic gas flows*. National Aeronautics and Space Administration.

[190] Vacher, D., Dudeck, M., André, P., Da Silva, M. L., Faure, G., Dubois, M., Hamwi, A., Menecier, S., and Rochette, D. (2009). Radiation from an icp plasma torch in the near-uv to near-ir spectral region for a titan-type n2-ch4 mixture. *Journal of technical physics*, 50(3):213–231.

[191] Ward, C., Wheaton, B., Chou, A., Gilbert, P., Steen, L., and Schneider, S. (2010). Boundary-layer transition measurements in a mach-6 quiet tunnel. In *40th Fluid Dynamics Conference and Exhibit*, page 4721.

[192] Whiting, E. E., Park, C., Liu, Y., Arnold, J. O., and Paterson, J. A. (1996). Neqair96, nonequilibrium and equilibrium radiative transport and spectra program: User's manual.

[193] Wright, M., Olejniczak, J., Brown, J., Hornung, H., and Edquist, K. (2005). Computational modeling of t5 laminar and turbulent heating data on blunt cones, part 2: Mars applications. In *43rd AIAA Aerospace Sciences Meeting and Exhibit*, page 177.

[194] Wright, M. J., White, T., and Mangini, N. (2009). Data parallel line relaxation (dplr) code user manual: Acadia-version 4.01. 1. Technical report.

[195] Yalin, A., Zare, R., Laux, C., and Kruger, C. (2002). Temporally resolved cavity ring-down spectroscopy in a pulsed nitrogen plasma. *Applied physics letters*, 81(8):1408–1410.

[196] Yamada, G. (2022). Electron density measurements of shocked argon using stark profile of the h β line. *AIAA Journal*, 60(10):5645–5651.

[197] Yamada, G., Suzuki, T., Takayanagi, H., and Fujita, K. (2011). Development of shock tube for ground testing reentry aerothermodynamics. *Transactions of the Japan Society for Aeronautical and Space Sciences*, 54(183):51–61.

[198] Yamada, G., Takayanagi, H., Suzuki, T., and Fujita, K. (2012). Shock layer radiation analysis using a hypervelocity shock tube (hvst). *Transactions of the Japan Society for Aeronautical and Space Sciences*, 55(1):37–43.

[199] Yanes, N. J. and Austin, J. M. (2019). Nitric oxide spectroscopic measurements in a hypervelocity stagnation flow. In *AIAA Scitech 2019 Forum*, page 0794.

[200] Zander, F., Buttsworth, D. R., Birch, B., Noller, L., Wright, D., James, C. M., Thompson, M., Apirana, S., Leis, J., Lobsey, C., et al. (2021). Australian rapid-response airborne observation of the hayabusa2 reentry. *Journal of Spacecraft and Rockets*, 58(6):1915–1919.

[201] Zander, F., Gollan, R., Jacobs, P., and Morgan, R. (2014). Hypervelocity shock standoff on spheres in air. *Shock Waves*, 24(2):171–178.

[202] Zong, Y., Brown, S. W., Meister, G., Barnes, R. A., and Lykke, K. R. (2007). Characterization and correction of stray light in optical instruments. In *Sensors, Systems, and Next-Generation Satellites XI*, volume 6744, pages 422–432. SPIE.

Appendix A

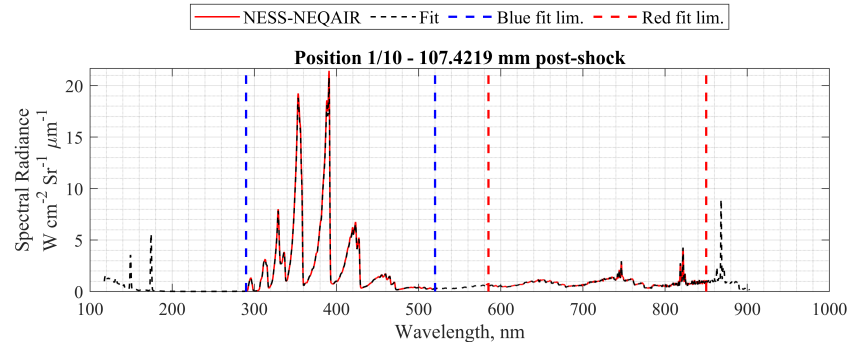
Supplementary Work During Development of Constrained Spectral Fitting Routine

This section of the Appendix presents the complete series of plots that were only partially shown in Chapter 5. It also includes results that assess the impact of less consequential experimental artefacts, which were omitted from the main body of work to maintain its flow.

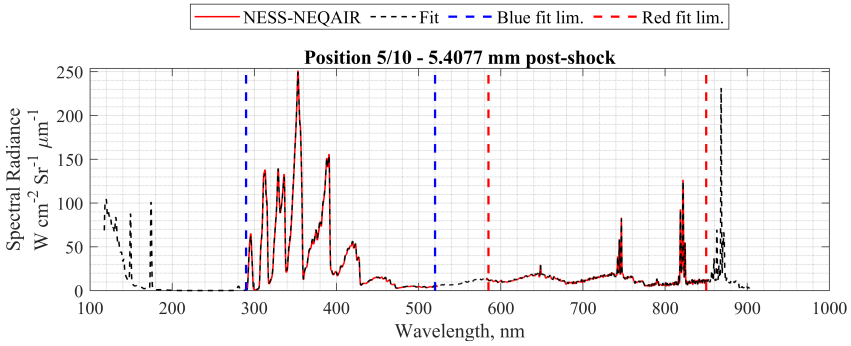
Additionally, this section studies the effect of reduced gating times to improve resolution of the non-equilibrium region immediately behind the shock front, suggesting improvements may be made in future shock tube campaigns. It then explores how measurements of different wavelength regions and physical parameters influence the overall test slug characterisation.

Finally, comparisons between Boltzmann predictions and new non-Boltzmann quasi-state-specific predictions are provided. These highlight the significance of selecting the appropriate energy distribution and demonstrates an alternative distribution beyond the Boltzmann utilised in the main body of work during spectral fitting analyses.

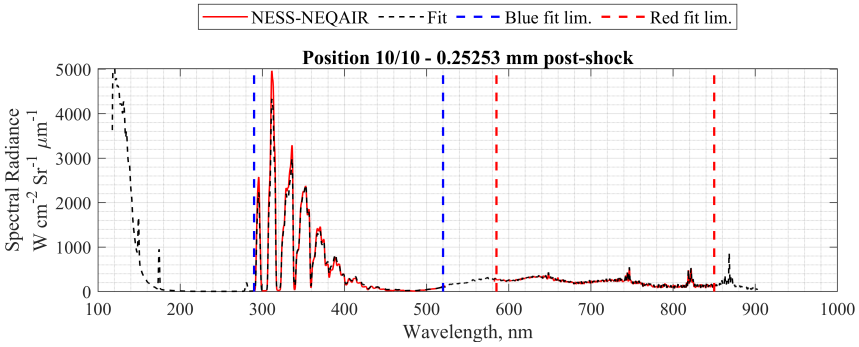
A.1 Spectral Fits of Constrained Spectral Routine for Initial NESS-NEQAIR Data



(a) Equilibrium



(b) Relaxation



(c) Immediate post-shock

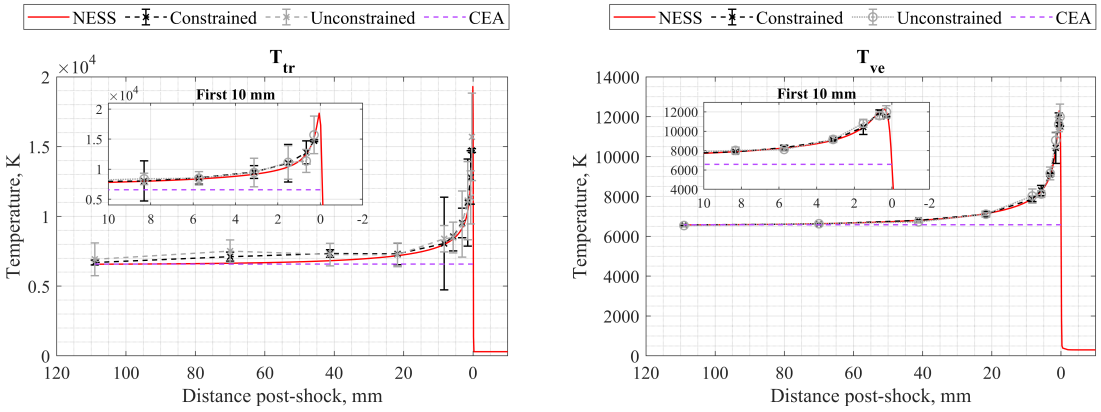
Fig. A.1 Spectral fit results in different portions of the test slug for first run of the constrained spectral fitting routine in Section 5.3.2. The blue and red limit lines indicate the wavelength regions where spectral fitting was performed. Final results are plotted from the VUV through to the NIR to serve as predictions in these areas, from the temperatures and number densities arrived at.

A.2 Contaminant Species Studies

This section provides the full set of results for the contaminant studies in Section 4.4. They are separated into the three groups of species as discussed in the main body of the paper.

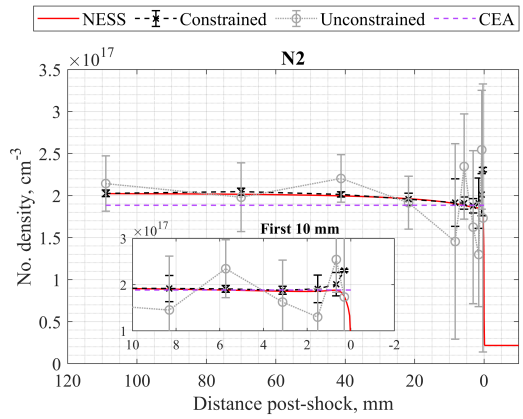
A.2.1 No contaminants

The spectral fitting with no inclusion of contaminant species was run with constraints toggled on and off, to give another example of the increased robustness in the spectral fitting methodology by obeying conservation laws. Temperatures, number densities and corresponding physical properties are plotted in Fig.'s A.2, A.3 and A.4 respectively.

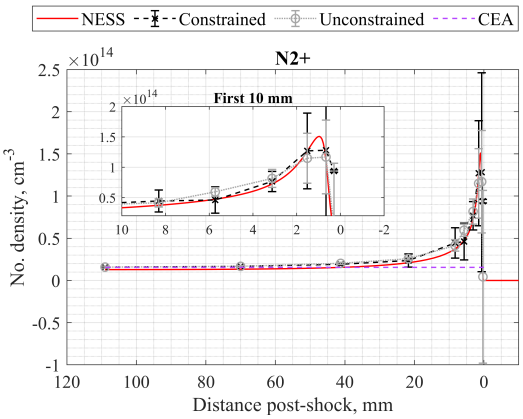


(a) T_{tr} (b) T_{ve}

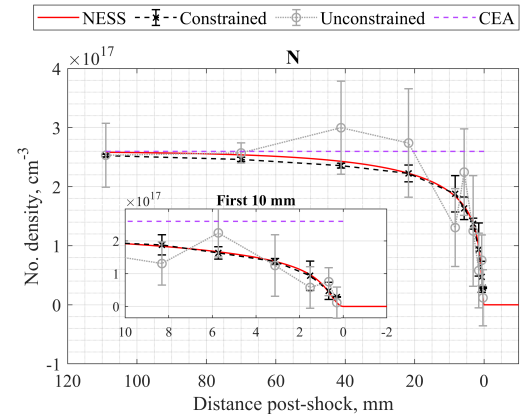
Fig. A.2 T_{tr} and T_{ve} extracted by spectrally fitting contaminated NESS-NEQAIR radiance, without including any contaminants in the fitting of both constrained and unconstrained attempts.



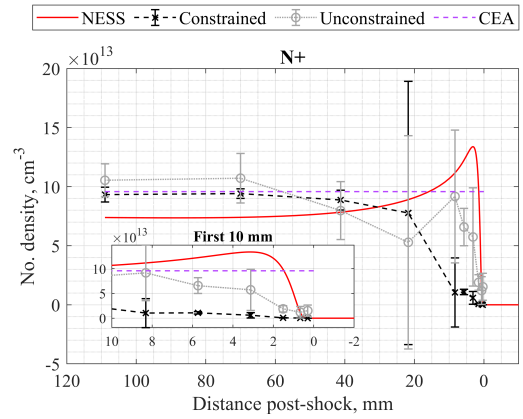
(a) N_2



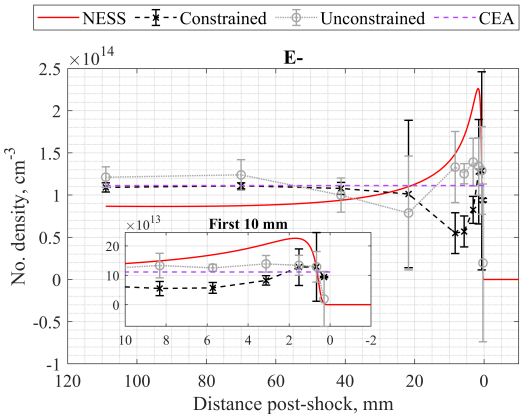
(b) N_2^+



(c) N

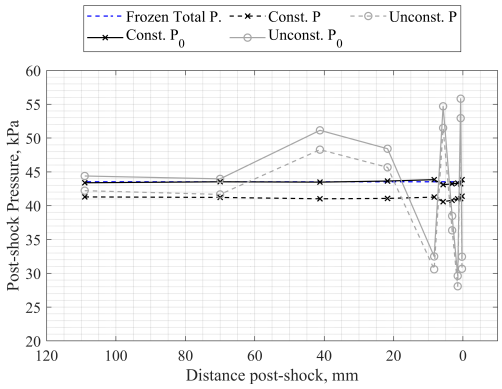


(d) N^+

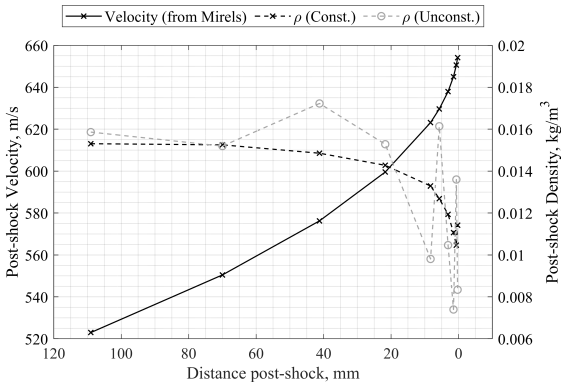


(e) E^-

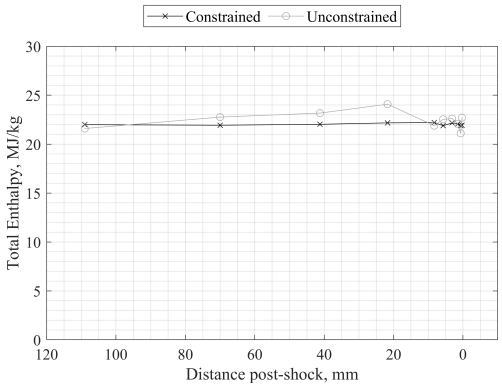
Fig. A.3 Number densities of the 5 species of interest, extracted by spectrally fitting contaminated NESS-NEQAIR radiance, without including any contaminants in the fitting of both constrained and unconstrained attempts.



(a) Pressures



(b) Velocity and density

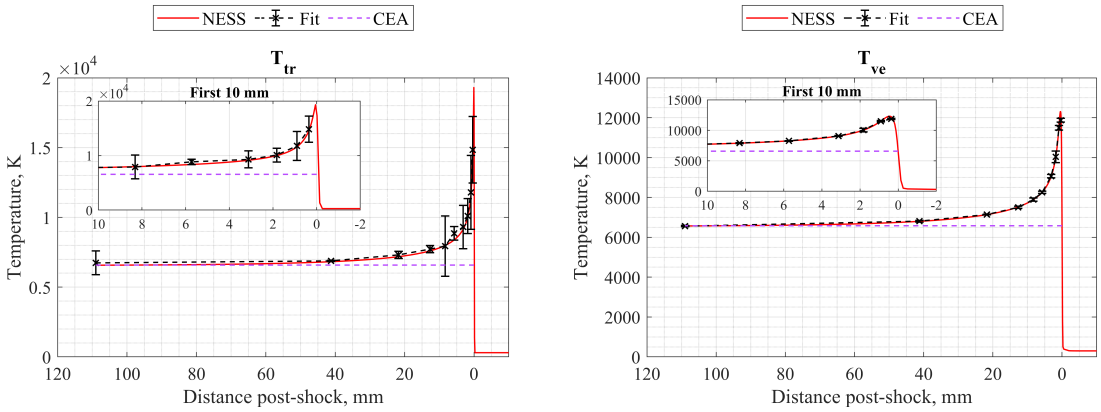


(c) Total Enthalpy

Fig. A.4 Post-shock physical properties corresponding to the temperature and species number density profiles attained by constrained and unconstrained attempts, without including any contaminants in the spectral fitting.

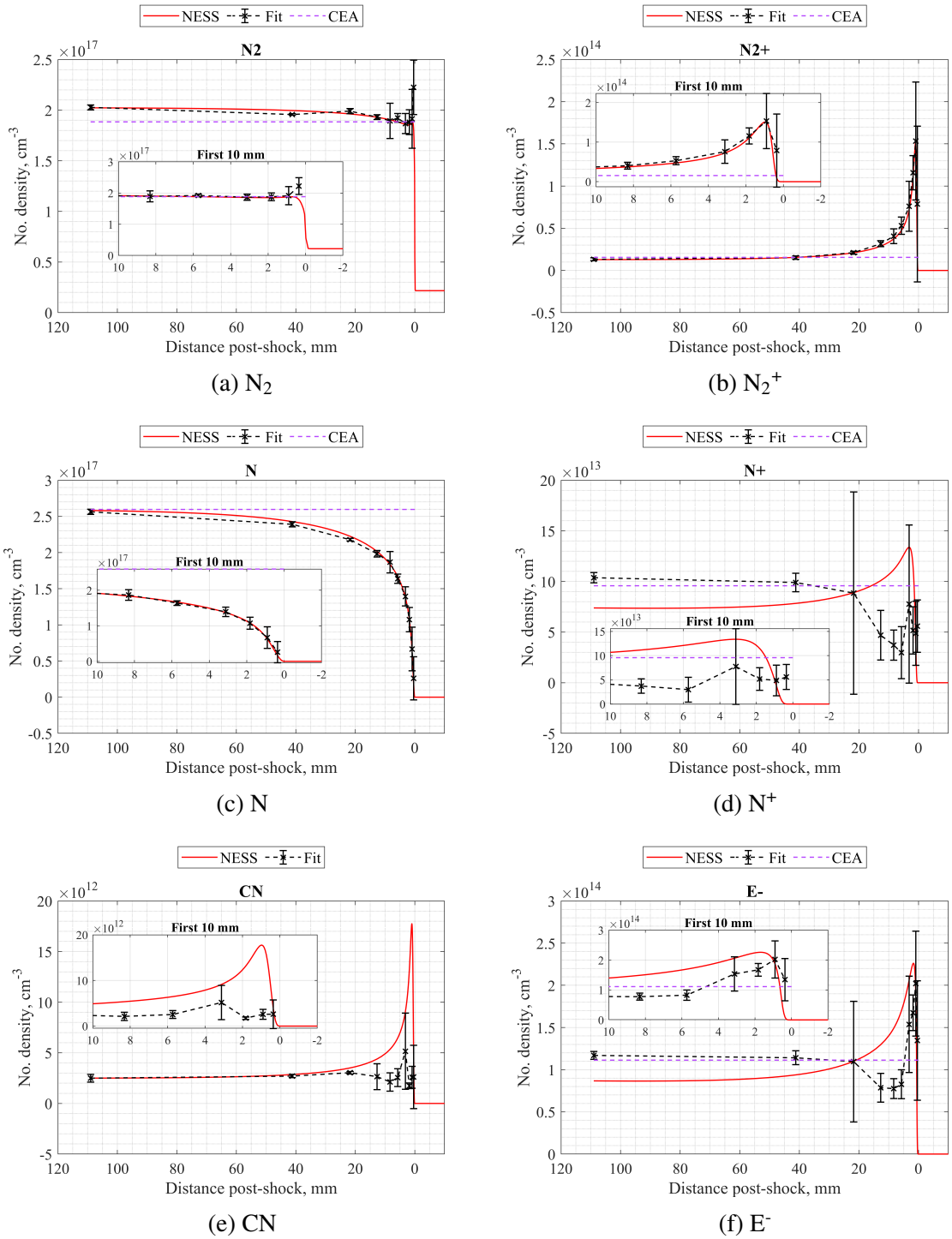
A.2.2 CN only

The results of including CN contaminant species into the constrained spectral fitting routine can be seen for temperature and number densities in Fig.'s A.5 and A.6 respectively. Additionally, the corresponding spectral fits for different portions of the test slug are included in Fig. A.7. Inclusion of CN improved the routine's ability to capture the NESS N_2^+ profile accurately.



(a) T_{tr} (b) T_{ve}

Fig. A.5 T_{tr} and T_{ve} extracted by spectrally fitting contaminated NESS-NEQAIR radiance and including CN in the routine.

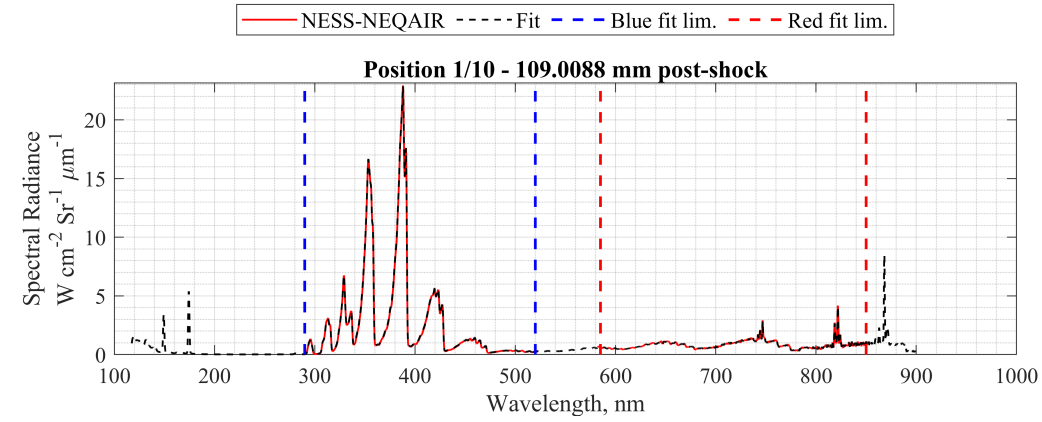


(a) N_2 (b) N_2^+

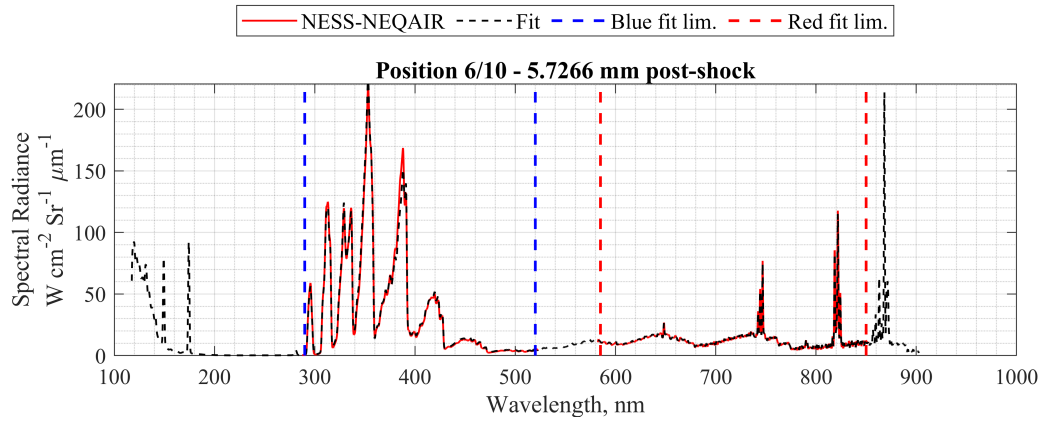
(c) N (d) N^+

(e) CN (f) E^-

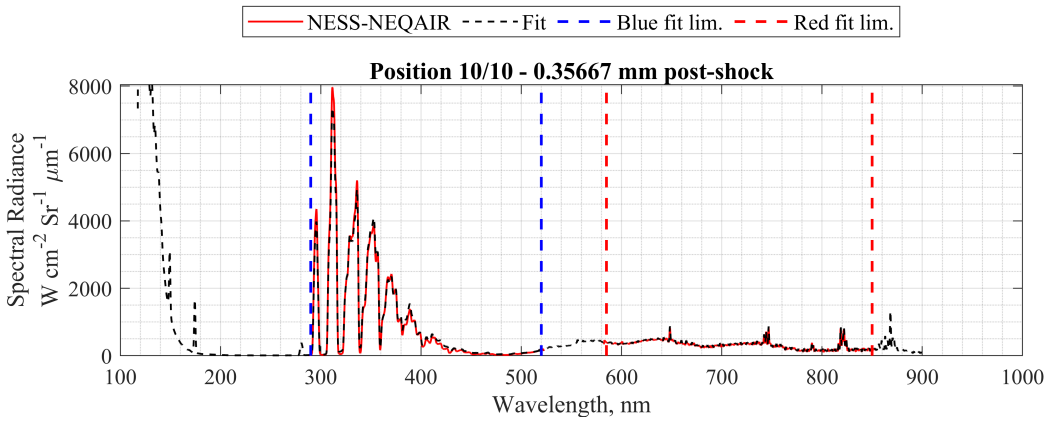
Fig. A.6 Number densities extracted by spectrally fitting contaminated NESS-NEQAIR radiance and including CN in the routine.



(a) Equilibrium



(b) Relaxation

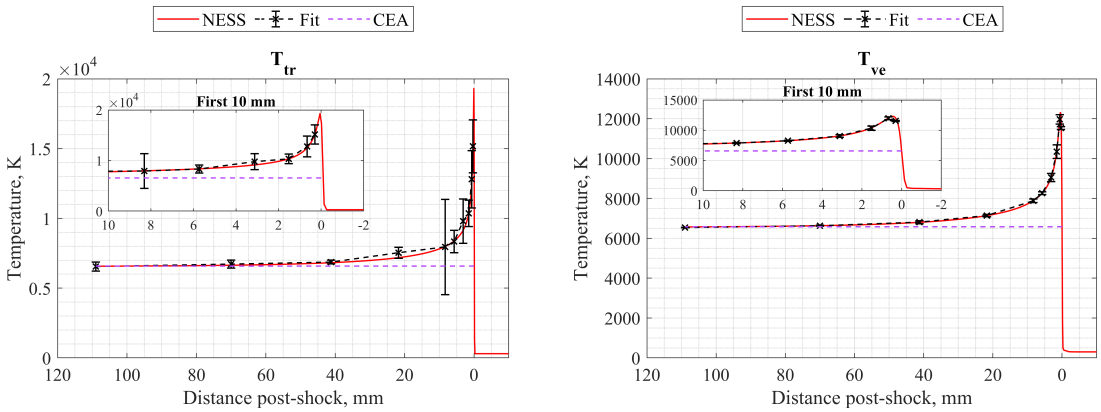


(c) Immediate post-shock

Fig. A.7 Spectral fit results from equilibrium, relaxation and peak non-equilibrium portions of the contaminated test slug, implementing N_2, N, N_2^+, N^+, CN and E^- species in the fitting routine. Blue and red limit lines indicate the wavelength regions where the spectral fit was performed.

A.2.3 CN, C_2, C, H_2, H

Next, the results from including five contaminant species into the constrained spectral fitting routine are given. Figure A.8 shows the temperatures extracted remain in close agreement with the NESS outputs, with no notable increase in the confidence limits. Figures A.9 and A.10 plot the number densities of the species of interest and the contaminant species respectively, comparing the spectral fit results against the true NESS values. The N_2, N_2^+ and N profiles are once again in close agreement with the NESS outputs, while contaminant species also show some improvement. The CN profile is captured better than the previous CN only results, along with the other contaminants loosely following the expected trends, except for C_2 and H_2 from 20 mm post-shock which have a steep rise that is not reproduced by the spectral fit results. In conclusion, there may be some improvement in characterisation of the actual contaminant species when more of the suspected contaminants are included in the spectral fitting routine. However, this bares no improvement over the capturing of species of interest from the test gas and increases run time of the routine.



(a) T_{tr} (b) T_{ve}

Fig. A.8 T_{tr} and T_{ve} extracted by spectrally fitting contaminated NESS-NEQAIR radiance, from adding CN, C_2, C, H_2 and H to the routines.

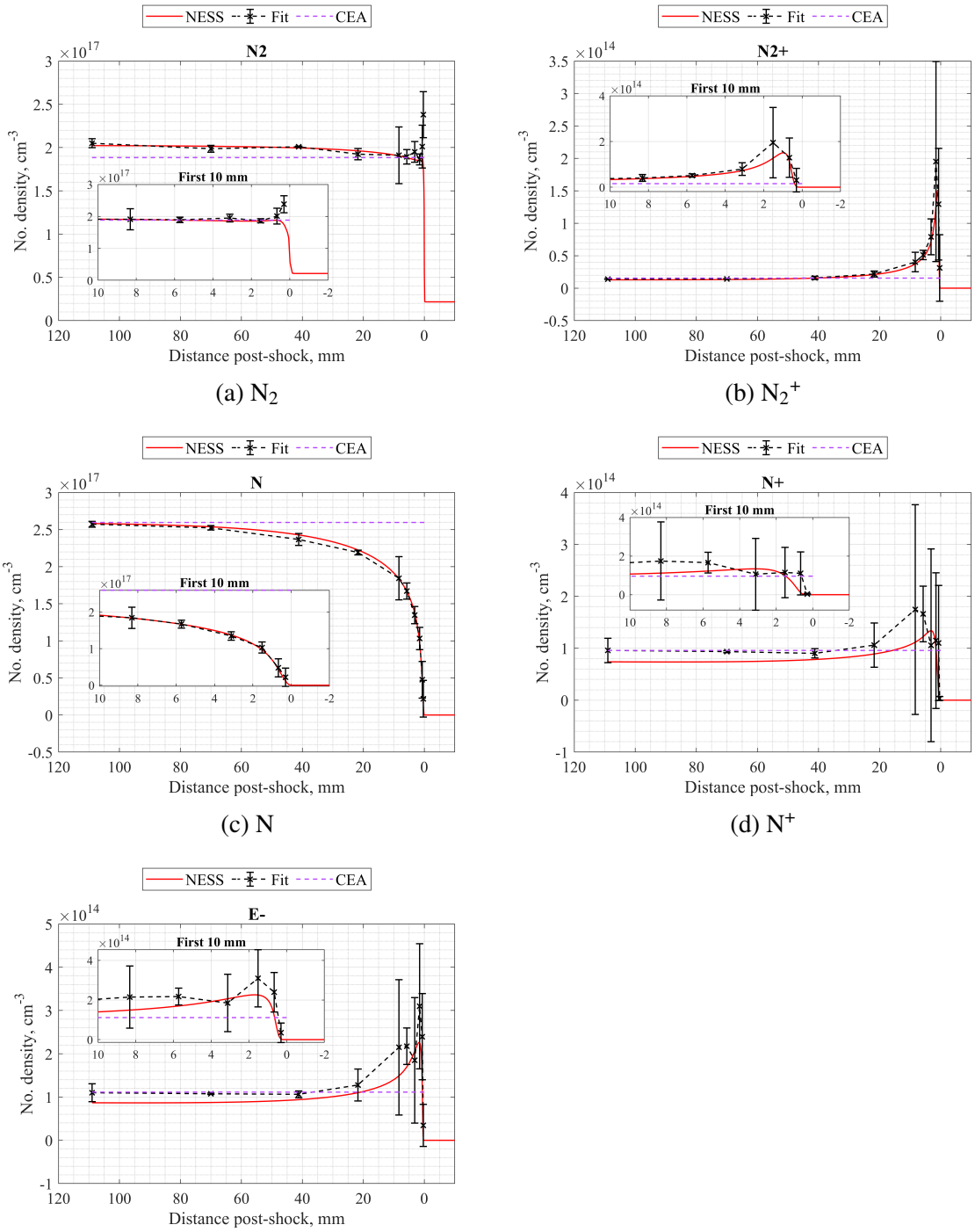


Fig. A.9 Number density profiles for species of interest extracted by spectrally fitting contaminated NESS-NEQAIR radiance, from adding CN, C_2, C, H_2 and H to the routine.

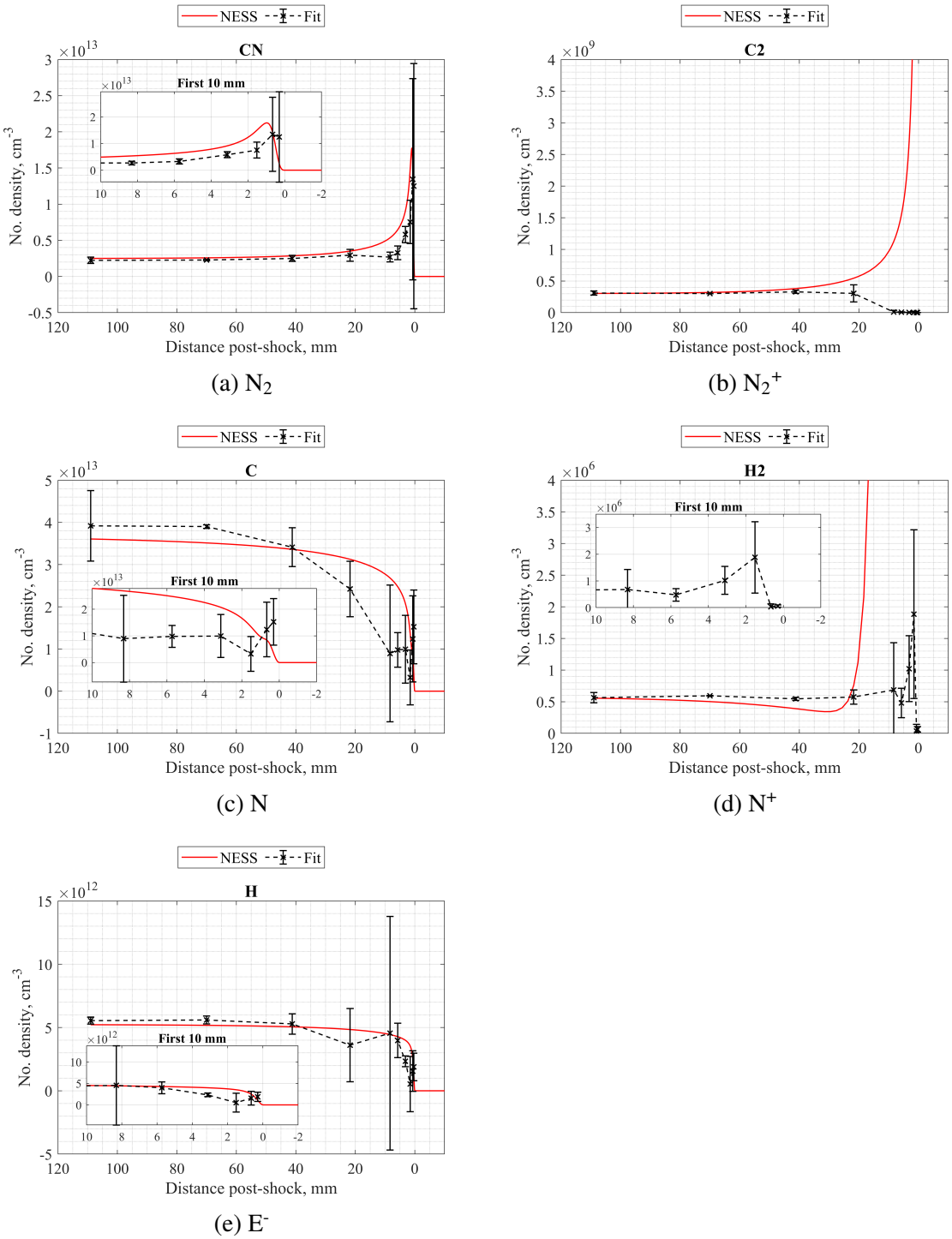
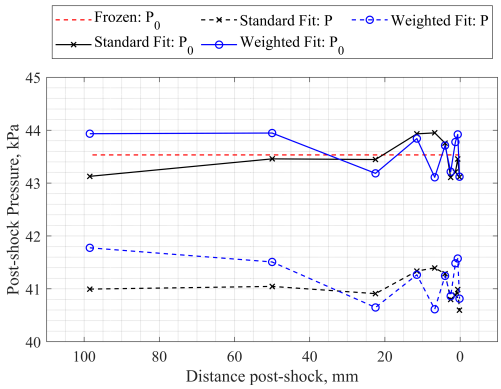


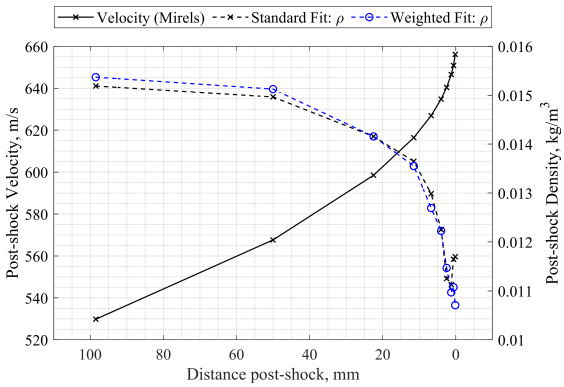
Fig. A.10 Number density profiles for contaminant species extracted by spectrally fitting contaminated NESS-NEQAIR radiance, from adding CN, C_2, C, H_2 and H to the routine.

A.3 Spatial Smearing Study Full Results

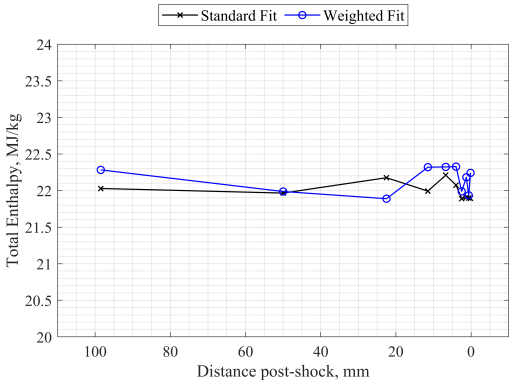
Figure A.11 plots the pressure, density and total enthalpy profiles from the "standard" and "weighted" fitting approaches shown in Section 5.3.4. While Fig. A.12 plots the rotational temperatures and complete set of species number densities, including those not shown in the main body. It's evident that implementing the SRF weighting has no adverse affect on the constrained spectral fitting routine's ability to attain results that are physically plausible. This is both an encouraging result for the SRF weighting and the implementation of constraints while performing spectral fits.



(a) Pressures

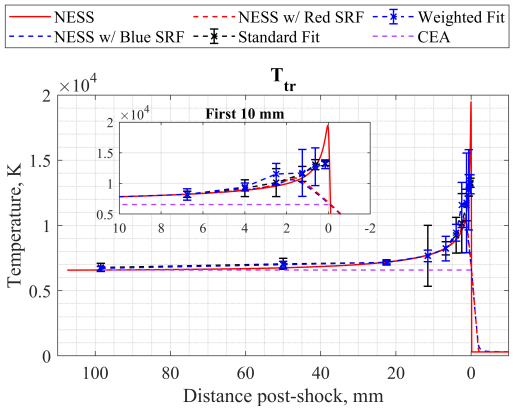


(b) Velocity and density

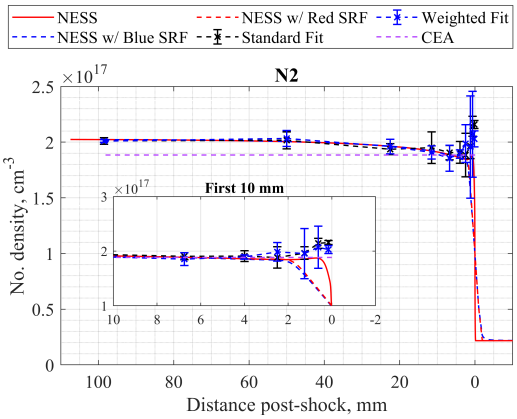


(c) Total Enthalpy

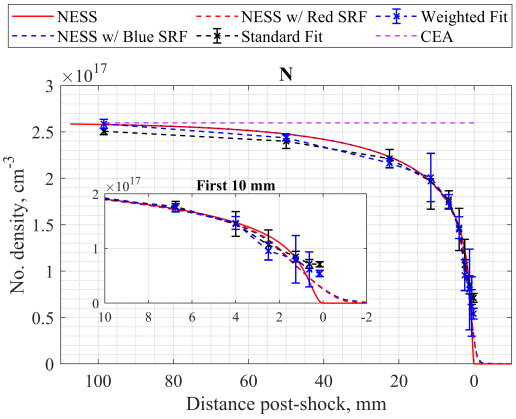
Fig. A.11 Post-shock physical properties corresponding to spectral fitting results of convolved data with and without the SRF weighting correction, as considered in Section 5.3.4.



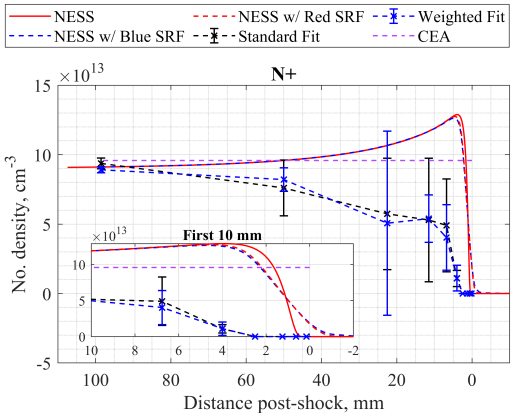
(a) T_{tr}



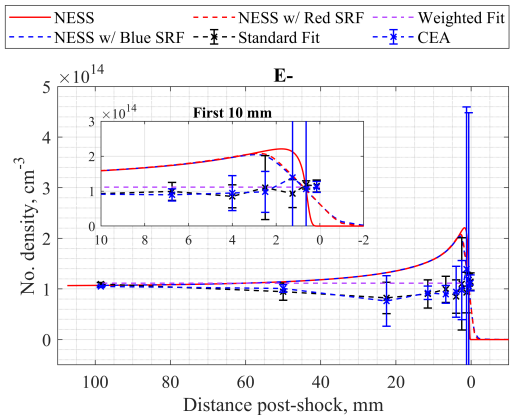
(b) N_2



(c) N



(d) N^+

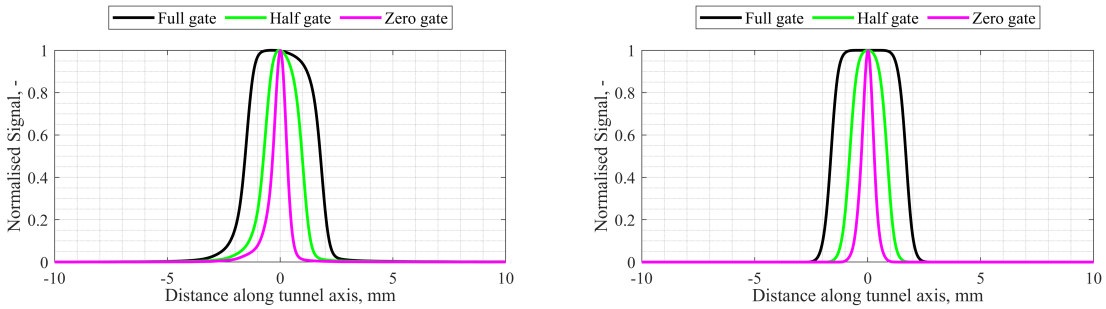


(e) E^-

Fig. A.12 Results of spectrally fitting convolved data with and without the SRF weighting correction for parameters not shown in Section 5.3.4.

A.4 Reduced Gate Width

It's been demonstrated in Section 5.3.4 that the most difficult portion of the spatially convolved radiance data to characterise by spectral fitting, is the peak non-equilibrium region immediately behind the shock. This is the location of the steepest gradients through the test slug, and thus most affected by the spatial smearing. The largest component of the SRF is the shock motion within the camera gating time. This section therefore provides an extension of the study from Section 5.3.4, to assess the improvements in resolution of the non-equilibrium peak that are theoretically possible by reducing the camera gating time. Two test cases are used - one in which the NESS-NEQAIR spatio-spectral radiance data is convolved by an SRF made from half the true gating time used for T6s492, and one in which the gating time is zero. The latter represents an asymptotic limit of what the telecentric optical setups used on T6 AST are capable of, or is equivalent to a stationary shock and therefore leaves only the optical and camera contributions to form the resultant SRF. Practically, this could only be achieved in radiation studies over stationary models in expansion or reflected shock tunnel tests, however it serves as a reference here to define the limit of shock tube studies at LEO return speeds. Figure A.13 plots the resultant SRF's against one another for both Blue (UV/Vis) and Red (Vis/NIR) spectral channels, to illustrate the enhanced spatial resolution achieved by reducing the gate width.



(a) Blue channel

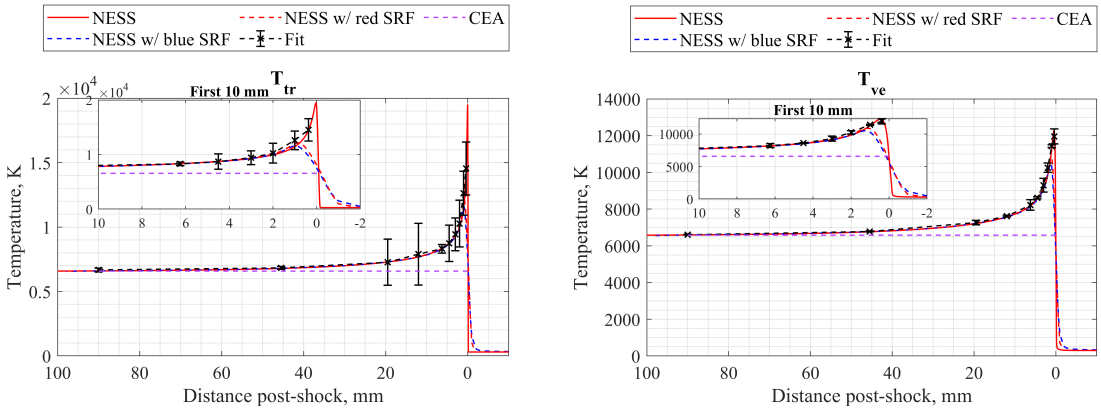
(b) Red channel

Fig. A.13 Comparison of SRF profiles for different camera gate widths for Blue and Red channels.

Both test cases were spectrally fit using the SRF weighting method described in Section 5.3.4, though in theory this becomes less necessary as the size of the SRF is reduced. Inclusion for all cases however maintains consistency for a fair comparison between test case results and ensures the methodology works for a range of SRF's. Figures A.14 and A.15 plot the temperature profiles extracted from the half gate width and zero gate width datasets respectively. It's evident that some improvement is gained by halving the gate width, by

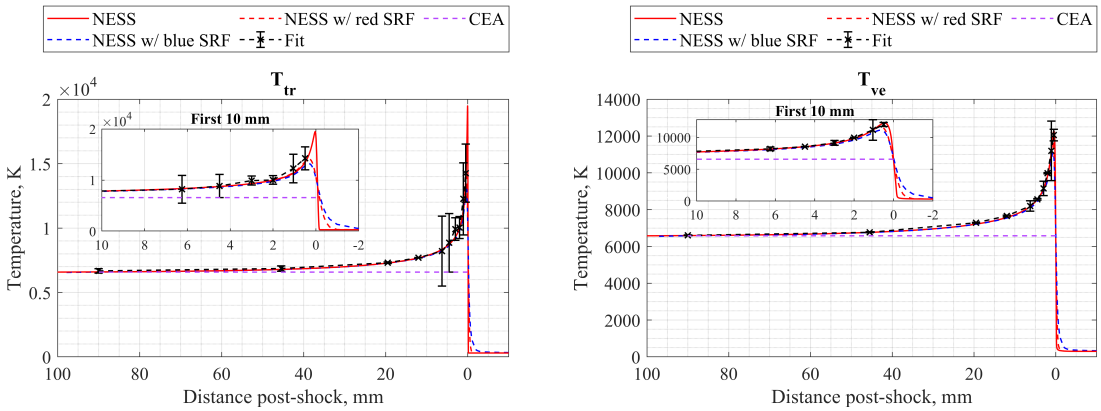
comparing results against those convolved by the true gating function in Fig. 5.11 of Chapter 5. However, there's comparatively little achieved by dropping to zero gate width.

Similar can be said for the spectrally fit number density profiles in Fig.'s A.16 and A.17, which again show close agreement to the unconvolved NESS profiles across the range of SRF's tested. Small improvements immediately behind the shock front are again evident from reducing the gating time, though reducing further to zero gating has negligible effect. This demonstrates the spatial smearing, and thus camera gating time, can be reduced to improve characterisation of the immediate post-shock region and validates the proposed weighted SRF correction across a range of spatial smearing severities.



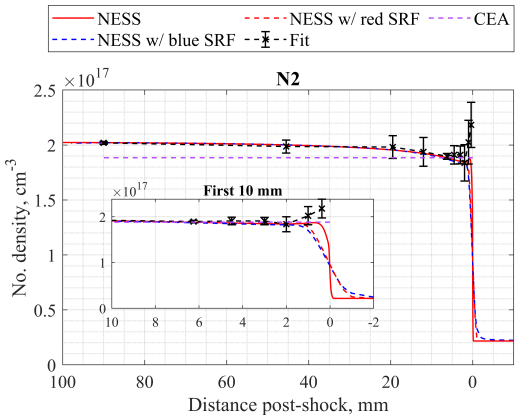
(a) T_{tr} (b) T_{ve}

Fig. A.14 Half gate width: T_{tr} and T_{ve} extracted from spectrally fitting artificial data convolved with half the true gating time.

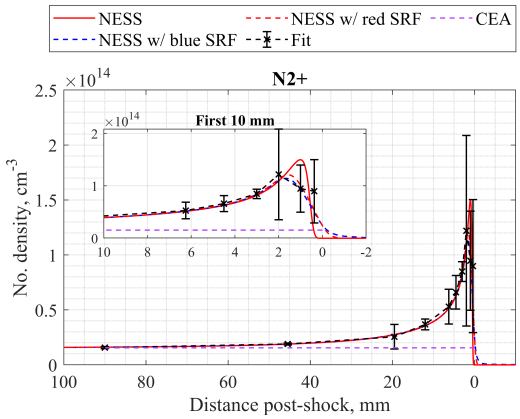


(a) T_{tr} (b) T_{ve}

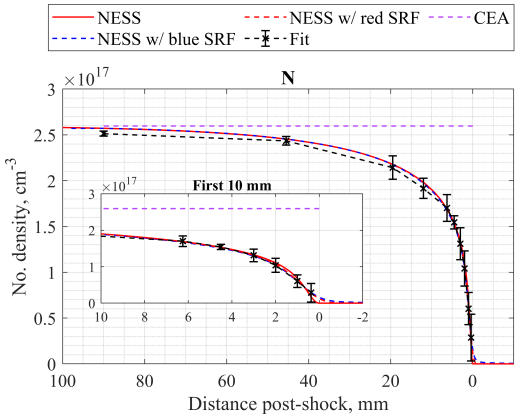
Fig. A.15 Zero gate width: T_{tr} and T_{ve} extracted from spectrally fitting artificial data convolved with SRF containing no gating contribution.



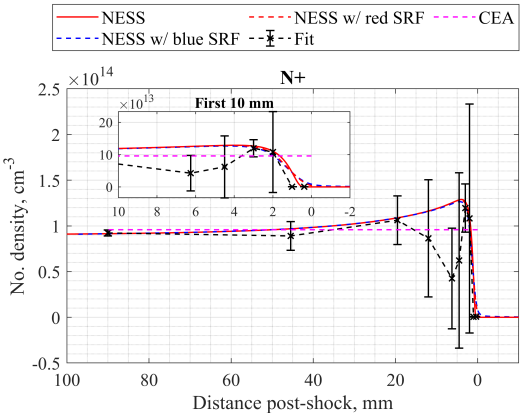
(a) N_2



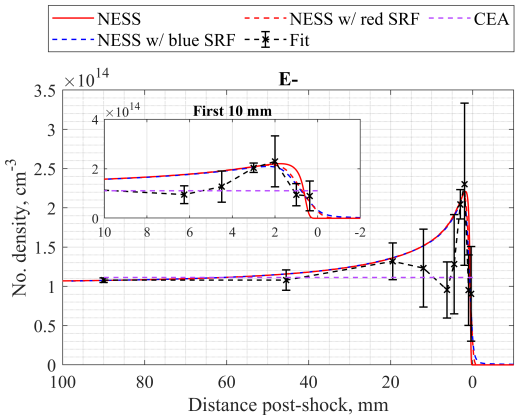
(b) N_2^+



(c) N

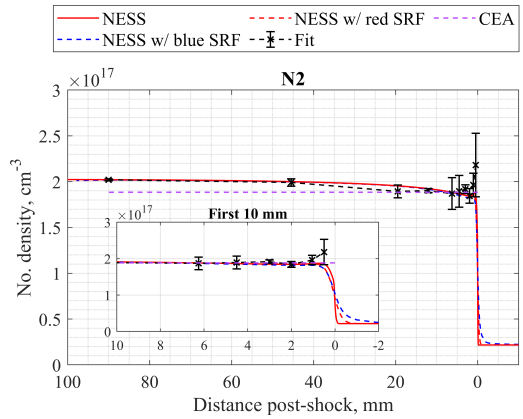


(d) N^+

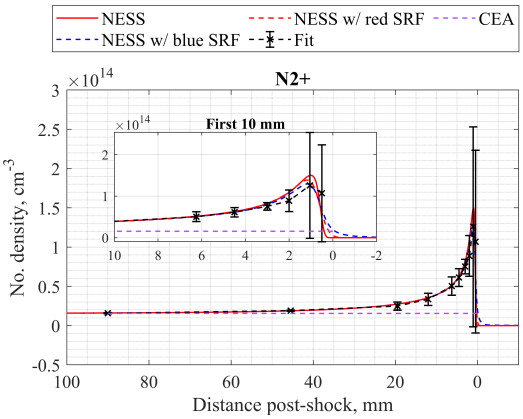


(e) E^-

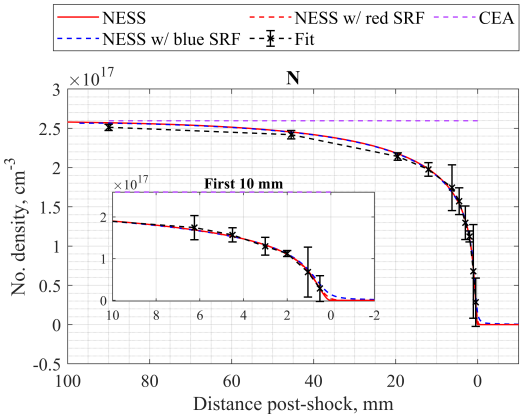
Fig. A.16 Half gate width: Number densities extracted from spectrally fitting artificial data convolved with half the true gating time.



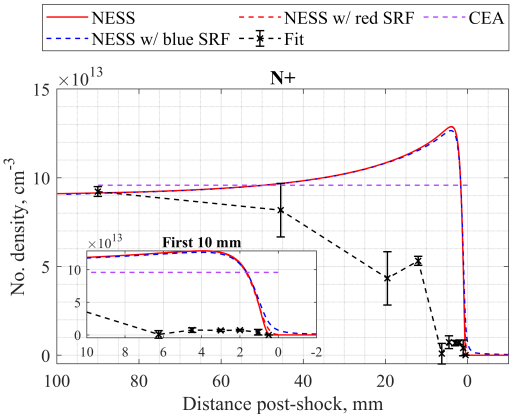
(a) N_2



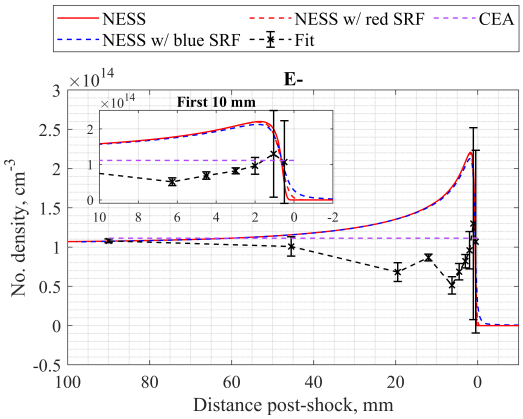
(b) N_2^+



(c) N



(d) N^+

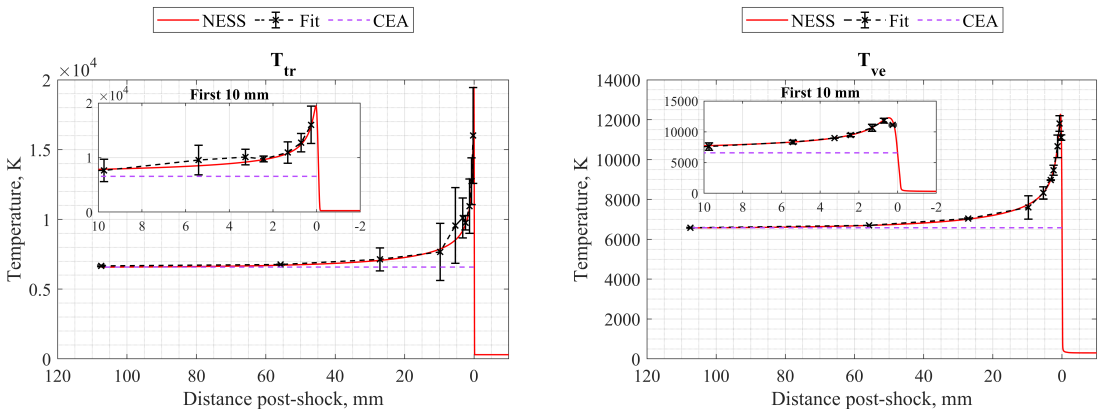


(e) E^-

Fig. A.17 Zero gate width: Number densities extracted from spectrally fitting artificial data convolved with SRF containing no gating contribution.

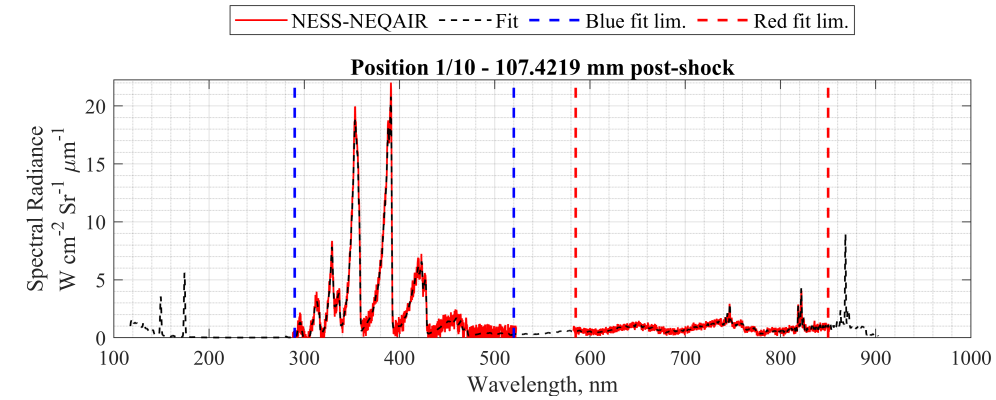
A.5 Artificial Noise

Unlike the synthetic data generated by NESS-NEQAIR simulations, real data suffers from noise. Particularly for the LEO return speeds of interest in this work, the radiance levels are comparatively low against other entry missions and planet atmospheres that have been studied in similar shock tube radiation emission experiments. In addition, to capture the non-equilibrium region (as is the intention of this work) the experimental data should be acquired with minimal exposure time, as has just been shown in Section A.4. This requires compromise of the achievable signal-to-noise (S:N) in the data acquired. Figure A.19 plots three of the NESS-NEQAIR simulated spectra of T6s492 at distinct points post-shock, each with random noise superimposed to a level representative of that seen in typical shot data. The corresponding spectral fits are plotted for comparison. It's evident that good matching to the NESS-NEQAIR simulated spectra is achieved despite the addition of noise, in the equilibrium, relaxation and peak non-equilibrium portions of the test slug. Figures A.18 and A.20 plot the corresponding temperature and number density profiles for the acquired spectral fits. The noise levels have negligible effect on the fitting routine's ability to attain accurate results.

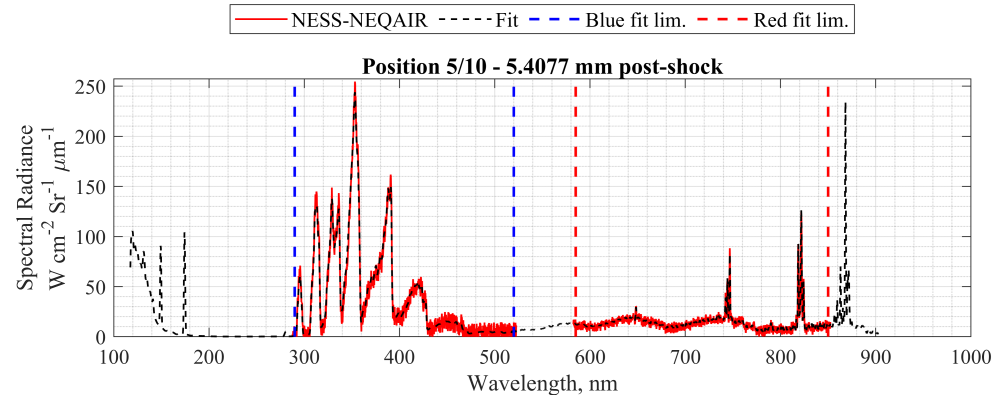


(a) T_{tr} (b) T_{ve}

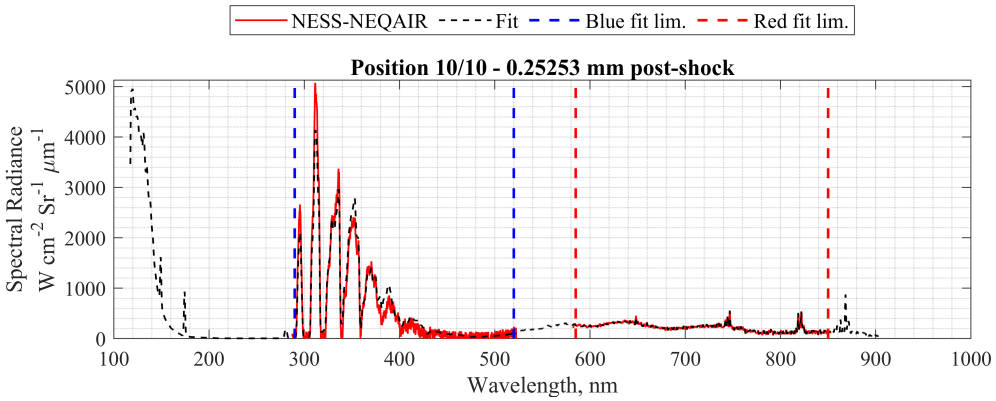
Fig. A.18 T_{tr} and T_{ve} extracted by spectrally fitting against noisy NESS-NEQAIR artificial spectra, plotted with the original NESS outputs and CEA equilibrium prediction for comparison.



(a) Equilibrium

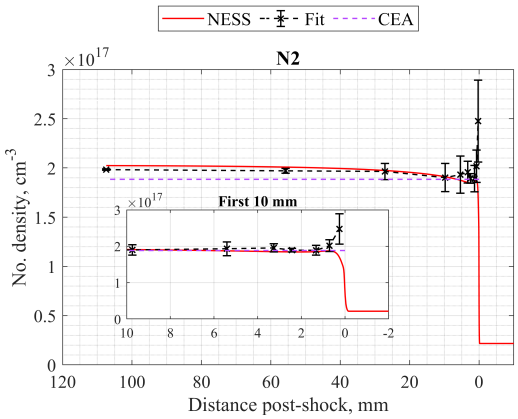


(b) Relaxation

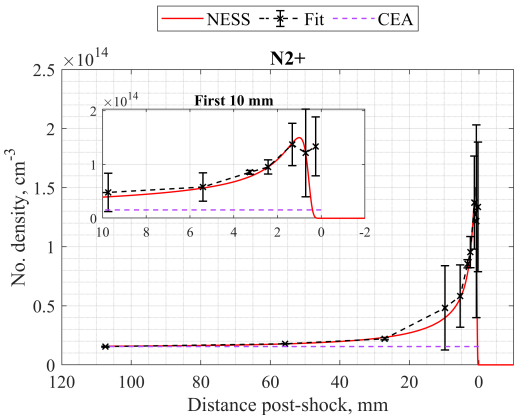


(c) Immediate post-shock

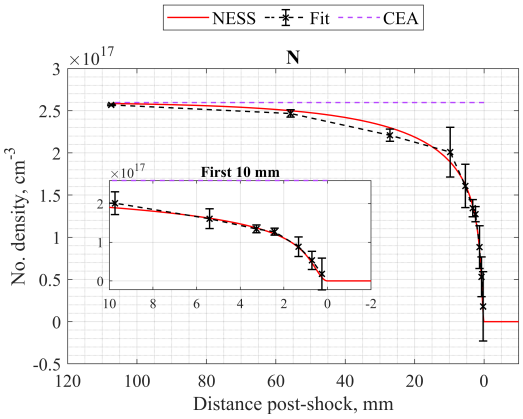
Fig. A.19 Spectral fit profiles in (a) equilibrium (b) relaxation and (c) immediate post-shock portions of the test slug, plotted against original NESS-NEQAIR spectral radiance traces with random noise superimposed. The noise level is representative of that in typical shot data.



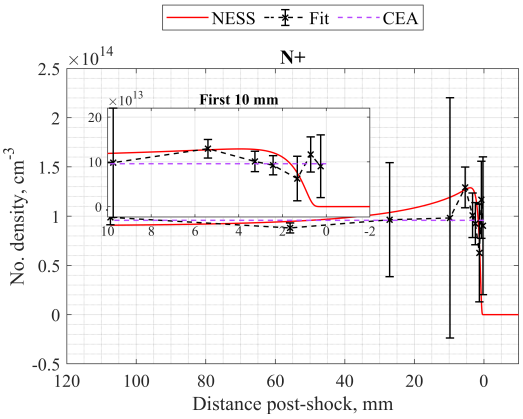
(a) N_2



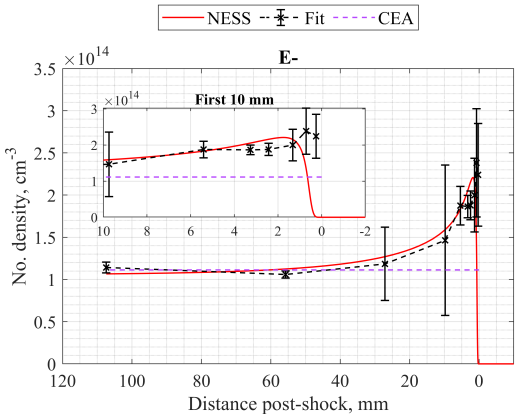
(b) N_2^+



(c) N



(d) N^+



(e) E^-

Fig. A.20 Species number density profiles extracted by spectrally fitting against noisy NESS-NEQAIR artificial spectra, plotted with the original NESS outputs and CEA equilibrium prediction for comparison.

A.6 Spatial Averaging

For all prior validation cases in this thesis, spectral fitting was performed at distinct locations defined by the NESS simulation to resolve the shock structure. In the case of real data, spectra are generated by averaging over a given spatial region, this is illustrated in Fig. A.21. If a steady state is maintained, as is the case when in thermochemical equilibrium, a large spatial region can be averaged over to improve the S:N of the generated spectra. However, in the rapidly transitioning non-equilibrium region closer to the shock, smaller regions are desirable in order to not lose spatial resolution of the rapidly transitioning thermochemical state. The enhanced radiation emission from the non-equilibrium region at LEO return speeds is beneficial to maintain reasonable S:N over these smaller regions. In theory, by averaging over a given spatial domain, one assumes a linear relationship across that region, since equal weighting is given to all portions. Radiation emission is a highly non-linear process, commonly known to be related with temperature to the power of four. The objective of this test therefore, is to check if the spectral fit results are affected by averaging over spatial regions as is commonly done for real experimental data.

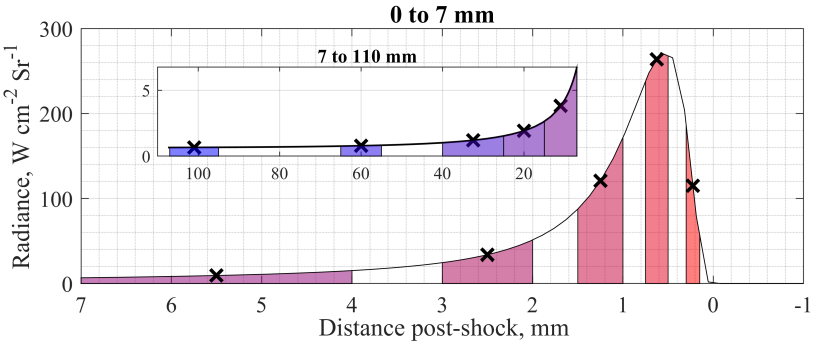
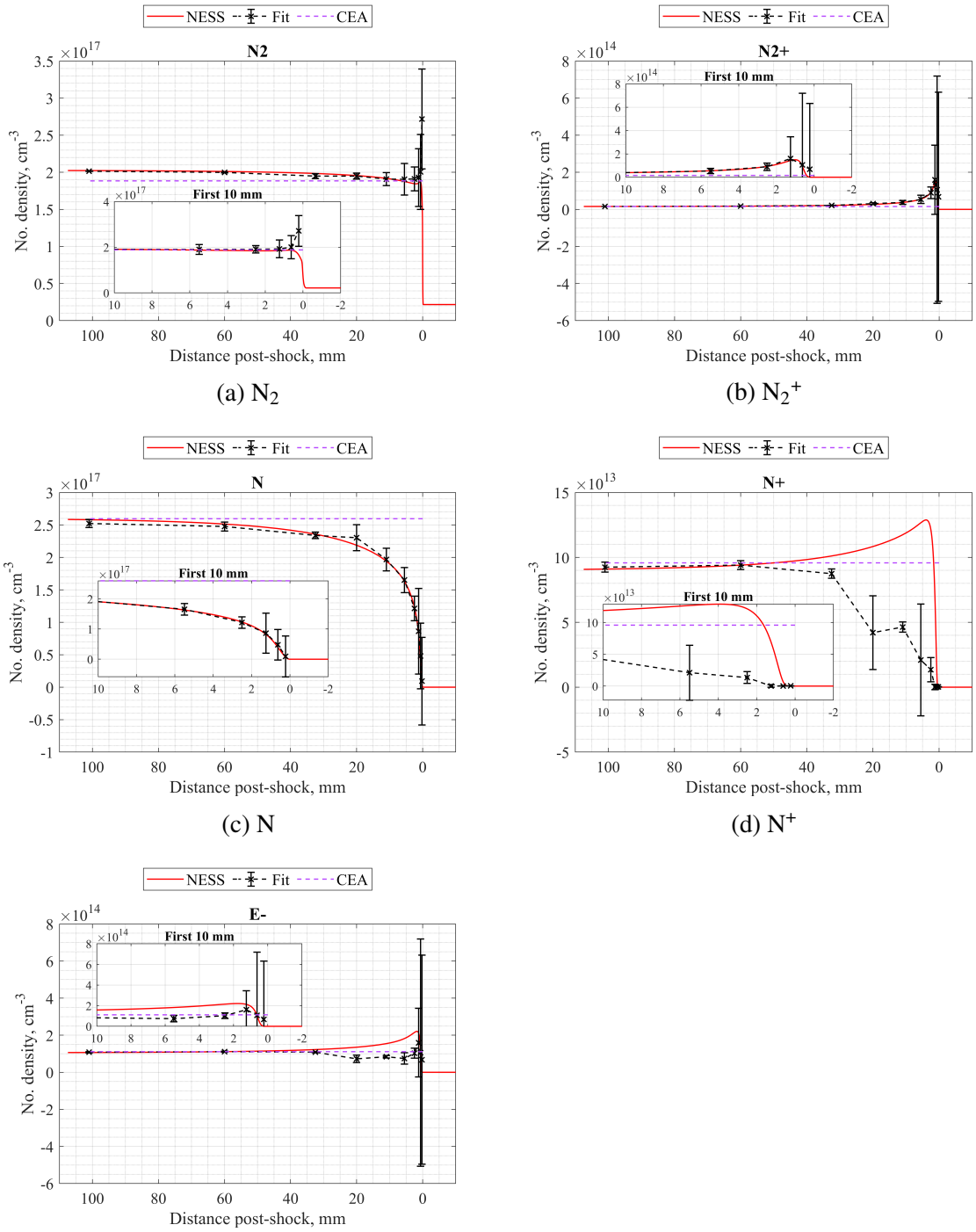


Fig. A.21 Radiance profile integrated over 290-520 nm, from the NESS-NEQAIR simulation of T6s492 (6.65 km/s, 90 Pa in pure nitrogen). Shaded regions illustrate the portions of the test slug averaged spatially to generate spectra, which are defined at the mid-point of each region as indicated by black crosses. An inset plot shows the later portions of the test slug, where radiance is much lower in magnitude than immediately behind the shock.

Figures A.22 and A.23 show the number densities and temperatures extracted are still very close to the NESS outputs. This demonstrates that spatial averaging of the spatio-spectral radiance data does not affect the fitting routine's ability to attain accurate results, which are representative of the true temperature and number density profiles through the test slug. Species N^+ and E^- are not captured well, as was previously the case.

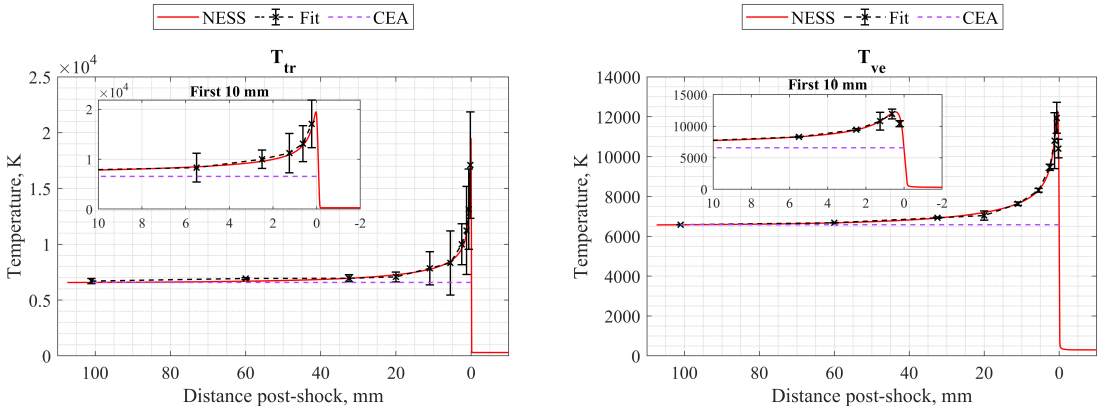


(a) N_2 (b) N_2^+

(c) N (d) N^+

(e) E^-

Fig. A.22 Species number density profiles extracted by fitting against average spectra, produced from different portions of the first 110 mm from the NESS-NEQAIR simulation. Original NESS outputs and CEA equilibrium predictions are plotted for comparison.

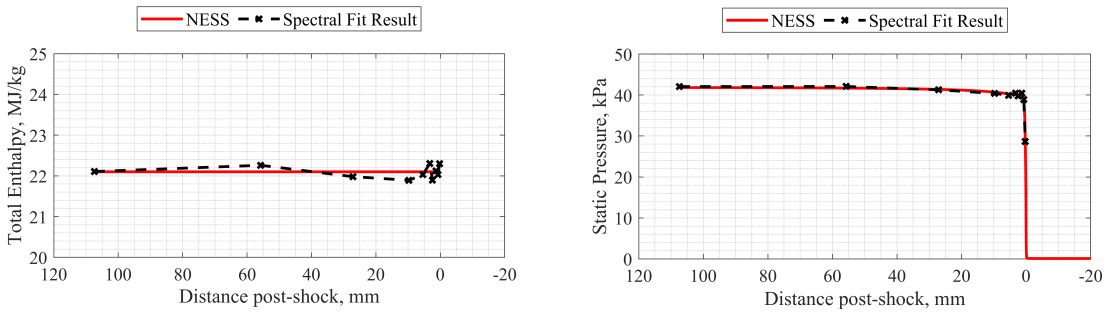


(a) T_{tr} (b) T_{ve}

Fig. A.23 T_{tr} and T_{ve} extracted by fitting against average spectra, produced from different portions of the first 110 mm from the NESS-NEQAIR simulation. Original NESS outputs and CEA equilibrium predictions are plotted for comparison.

A.7 Boundary Layer Mass Loss

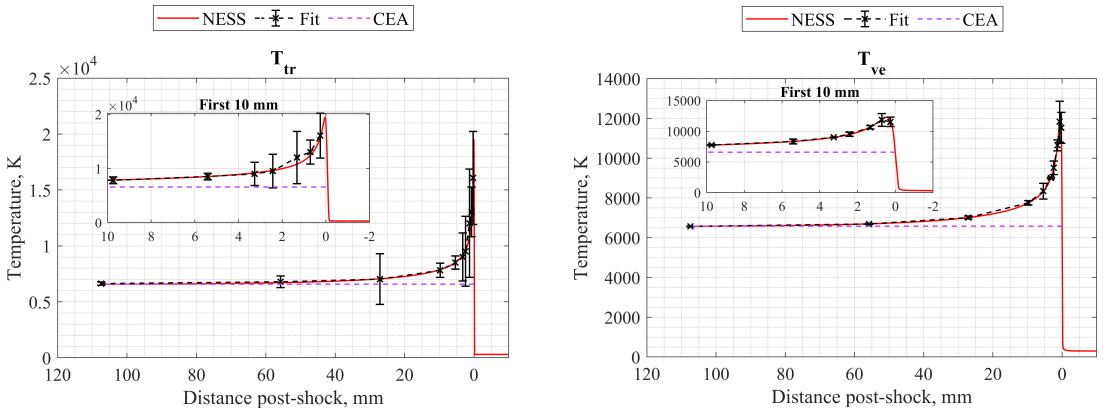
The flowchart shown in Fig. 5.1 of Chapter 5 illustrates there are multiple options for how the static pressure profile may be constrained. The previous examples utilised the post-shock velocity profile (from Mirels [126]) and density (from spectral fitting) to maintain total pressure through the test slug ($P_{2,\text{static}} + \frac{1}{2} \cdot \rho_2 \cdot {U_{2,S}}^2$). Alternatively, a static pressure profile may be assigned, either from a simulation or measured experimentally. The Non-Equilibrium Shock Solver (NESS) used for the validation simulations in these works inherently accounts for mass loss to the boundary layer in a shock tube experiment. This influences the static pressure profile through the test slug, which is captured in the simulation. Thus, by feeding the NESS static pressure profile into the constrained spectral fitting routine, it's possible to force the results to follow the expected static pressure profile. This ensures they account for boundary layer mass loss and the consequential reductions in species number densities in the core flow.



(a) Total Enthalpy (b) Static Pressure

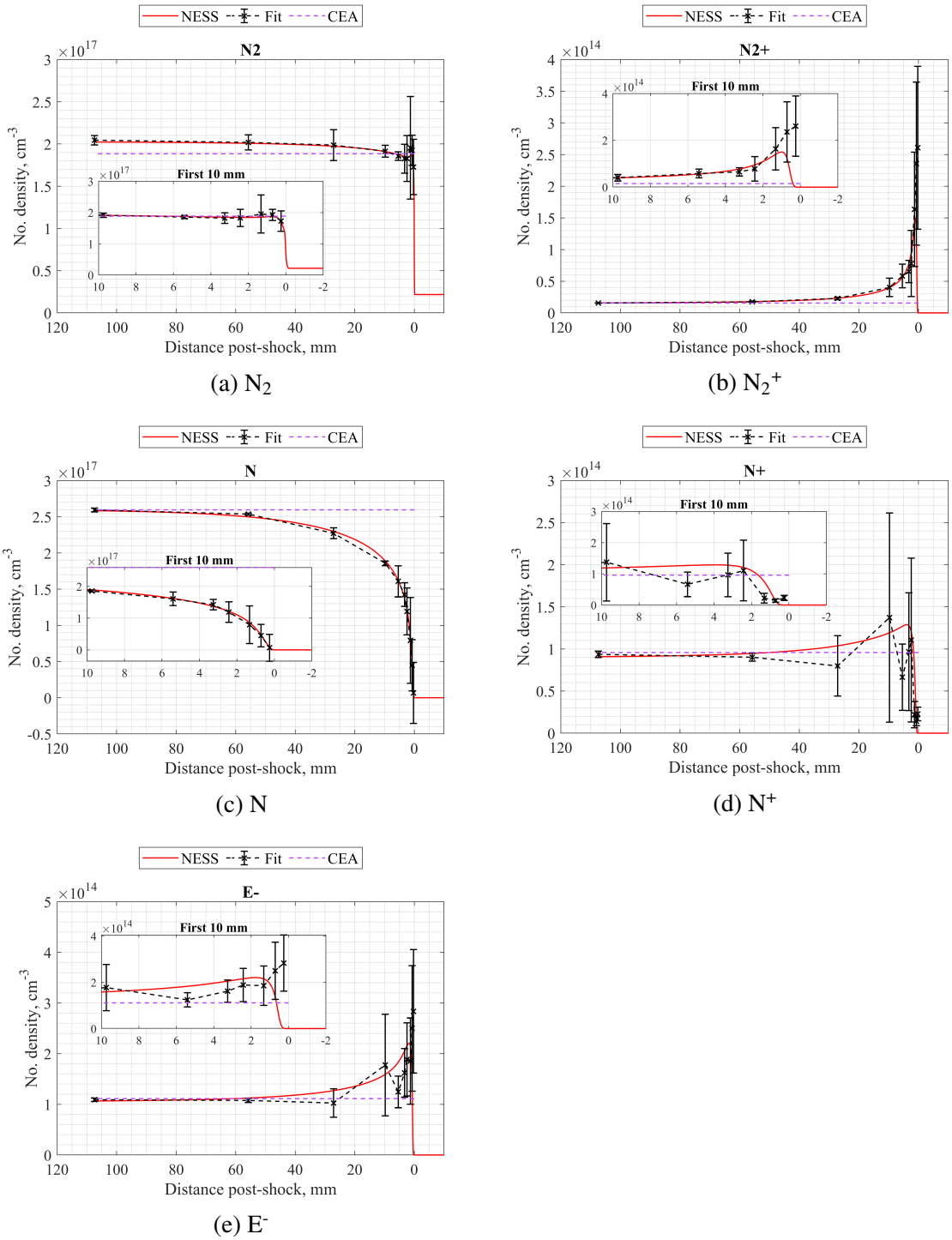
Fig. A.24 Plots of constraints defined from NESS and results of the constrained spectral fitting routine.

Figure A.24 shows the static pressure and total enthalpy profiles from NESS used to constrain the spectral fits for this test. Total enthalpy is constant since a single shock speed is assumed to have processed all portions of the test slug. The extracted temperature profiles are plotted in Fig. A.25, showing that close agreement with the NESS outputs has been maintained while incorporating the NESS static pressure profile, and similarly for the species number densities in Fig. A.26. The notable variations from previous results are N_2 agrees closer to the NESS profile at the very last point behind the shock, whereas N_2^+ over predicts and continues to increase rather than decrease. However, results after 1 mm still show close agreement, indicating that either method of constraining static pressure can be justified.



(a) T_{tr} (b) T_{ve}

Fig. A.25 T_{tr} and T_{ve} attained against the original NESS profiles after spectrally fitting by constraining with the NESS static pressure trace.



(a) N_2 (b) N_2^+

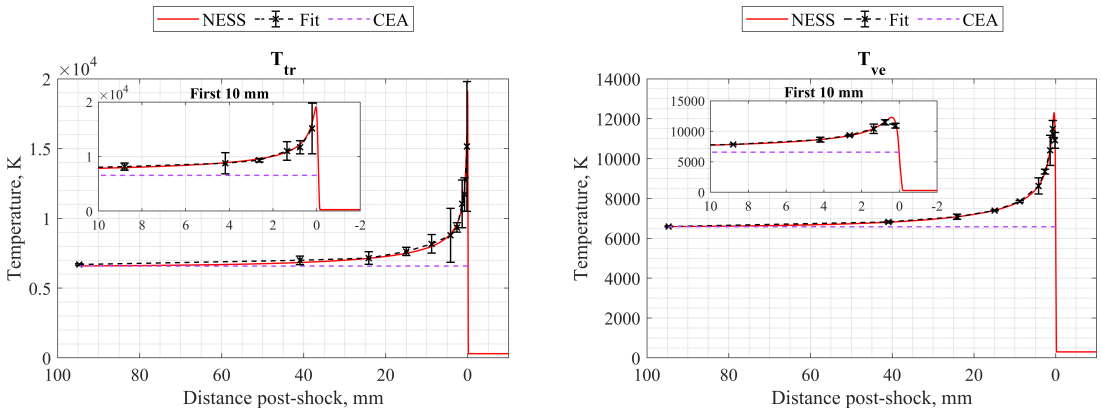
(c) N (d) N^+

(e) E^-

Fig. A.26 Species number densities attained against the original NESS profiles after spectrally fitting by constraining with the NESS static pressure trace.

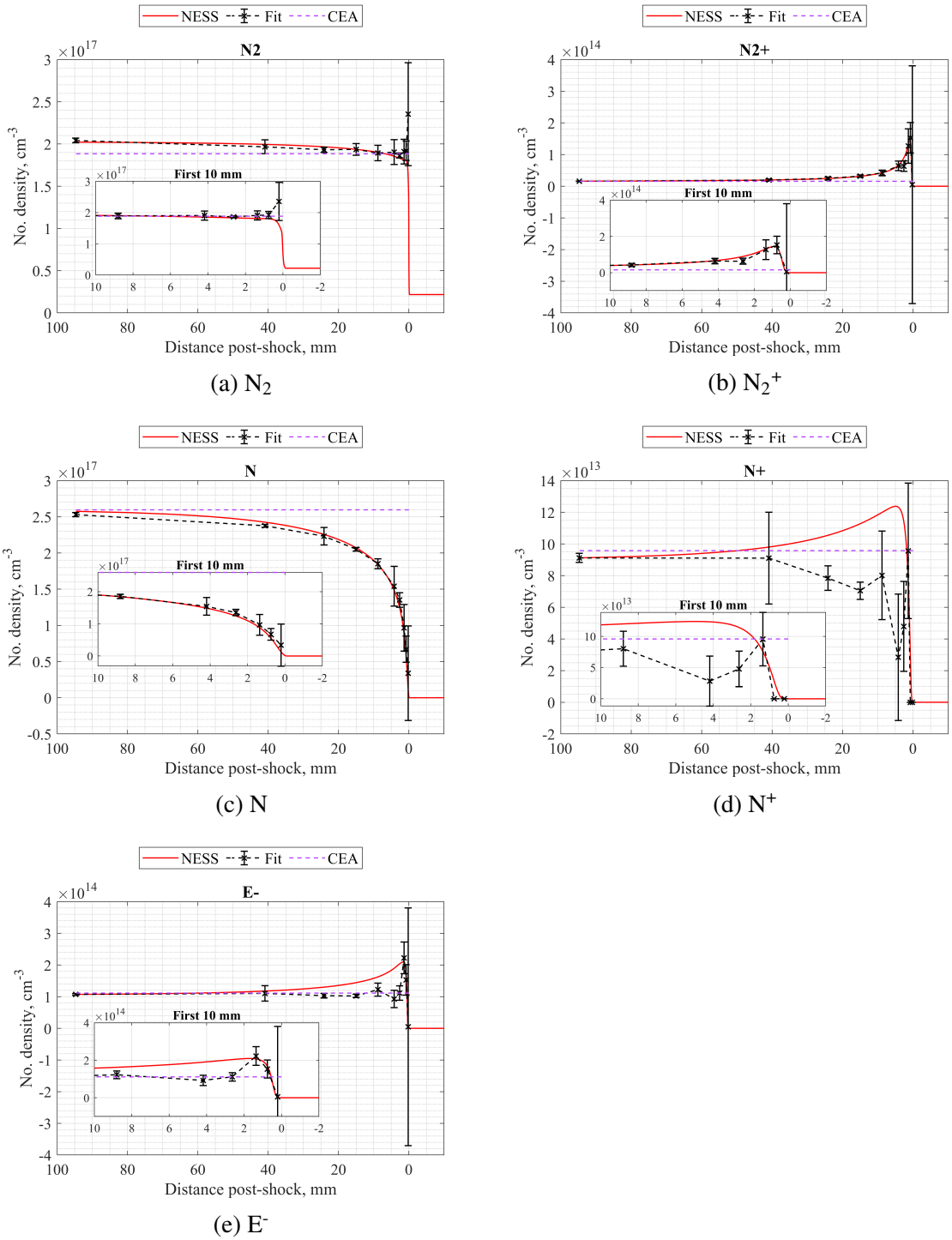
A.8 Diffusion

Diffusion effects were not considered in the nominal NESS-NEQAIR simulations of Chapter 5. Here, the synthetic spectra are regenerated with inclusion of diffusion effects and the constrained spectral fitting routine is re-applied. As is shown in Fig.'s A.27 and A.28, this results in very little change in the NESS temperature and species number density outputs, which are still captured well by the spectral fitting routine (aside from N^+ and E^- which are inferred by the constraints and charge neutrality assumption).



(a) T_{tr} (b) T_{ve}

Fig. A.27 T_{tr} and T_{ve} from spectrally fitting NESS-NEQAIR radiance data with diffusion effects included.



(a) N_2 (b) N_2^+

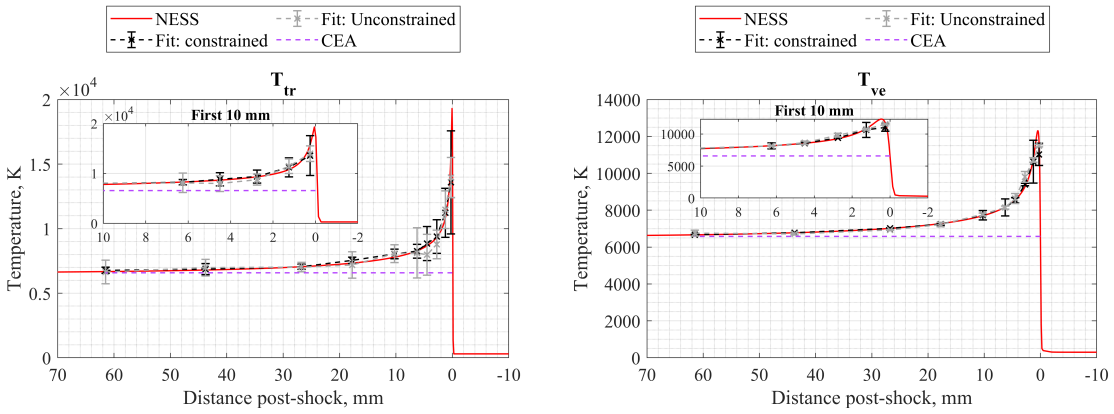
(c) N (d) N^+

(e) E^-

Fig. A.28 Species number density profiles from spectrally fitting NESS-NEQAIR radiance data with diffusion effects included.

A.9 Experimental Artefacts Combined

The final step in the validation of the constrained spectral fitting routine, is to combine all experimental artefacts that have been considered in this paper into one set of artificial radiance data. That is, contaminants, spatial smearing, noise, diffusion and spatial averaging are all included in one artificial NESS-NEQAIR radiance simulation of T6s492, to attempt to emulate the real shock tube data for both Blue and Red spectral channels. This offers the closest approximation of how the routine will perform against real data, for a case in which the correct temperature and number density profiles are still known. A constrained and unconstrained version of the spectral fitting routine has been run for this test case, to further emphasise the importance of including the novel constraints detailed in this work. The static pressure was constrained by maintaining total pressure through the test slug (via $P_{\text{static}} + \frac{1}{2} \cdot \rho_{2,\text{S}} \cdot {U_{2,\text{S}}}^2$), as it was shown results compared well against constraining by the NESS static pressure profile in Section A.7. Additionally the SRF weighting technique explained in Section 5.3.4 was applied for both versions. Based on the findings of Section 5.3.3, species N_2, N_2^+, N, N^+, CN and E^- were included in each spectral fitting attempt.



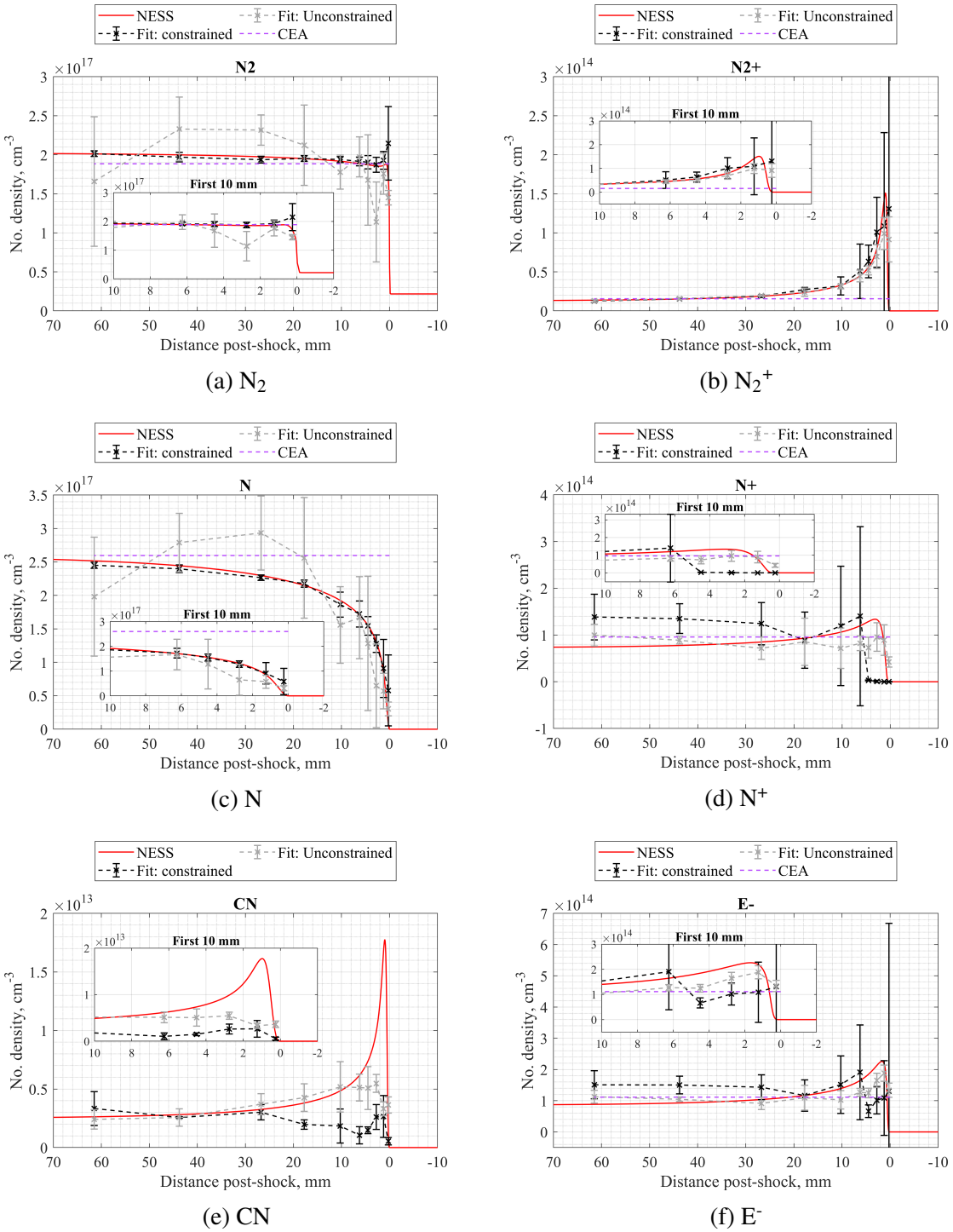
(a) T_{tr} (b) T_{ve}

Fig. A.29 T_{tr} and T_{ve} attained from constrained and unconstrained fitting of artificial data with multiple experimental artefacts included.

Figure A.29 plots the T_{tr} and T_{ve} temperature profiles extracted by each spectral fit. As was seen in Section 5.3.2, both constrained and unconstrained results capture the unconvolved temperature profiles well. However, the unconstrained results deteriorate when looking at the number density profiles plotted in Fig. A.30. It is the N_2 and N profiles, with the highest number densities (and therefore enthalpy and pressure contributions) which are not captured well despite achieving good spectral fits. The consequences of not constraining the spectral fit results to conserve mass, momentum and energy are reinforced by Fig. A.31. The

unconstrained results show unrealistic pressure, density and total enthalpy profiles, deviating strongly from the original NESS outputs to be matched. In contrast, the results from the constrained attempt are a much closer representation of the expected trends through a test slug.

The ultimate conclusion of this validation process is therefore that, the proposed novel constrained spectral fitting routine is capable of extracting realistic temperature and species number densities through a shock tube test slug. There are however strong limitations in feeding the routine only emission spectroscopy information, since only species with detectable radiation levels can be characterised. The method may be extended and improved in future works therefore, by incorporating results from other wavelength regions and alternative measurement techniques. Examples of this are shown in Section 5.3.5, for inclusion of electron number densities, and Section A.10 of the Appendix for a range of other parameters.

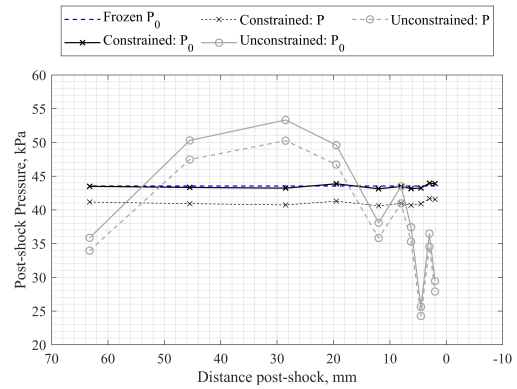


(a) N_2 (b) N_2^+

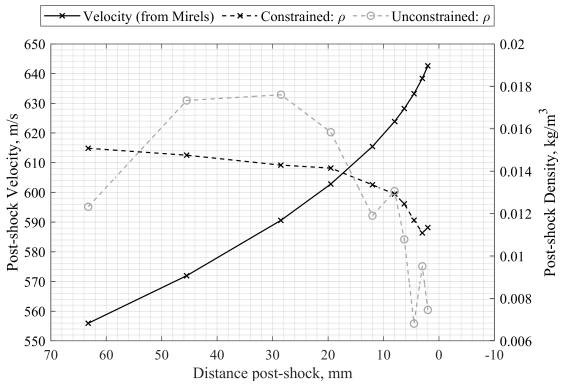
(c) N (d) N^+

(e) CN (f) E^-

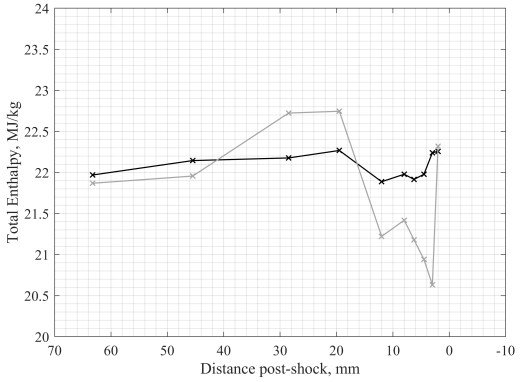
Fig. A.30 Number density profiles attained from constrained and unconstrained fitting of artificial data with multiple experimental artefacts included.



(a) Pressures



(b) Velocity and density



(c) Total Enthalpy

Fig. A.31 Post-shock physical properties corresponding to the constrained unconstrained spectral fits of artificial data with multiple experimental artefacts included.

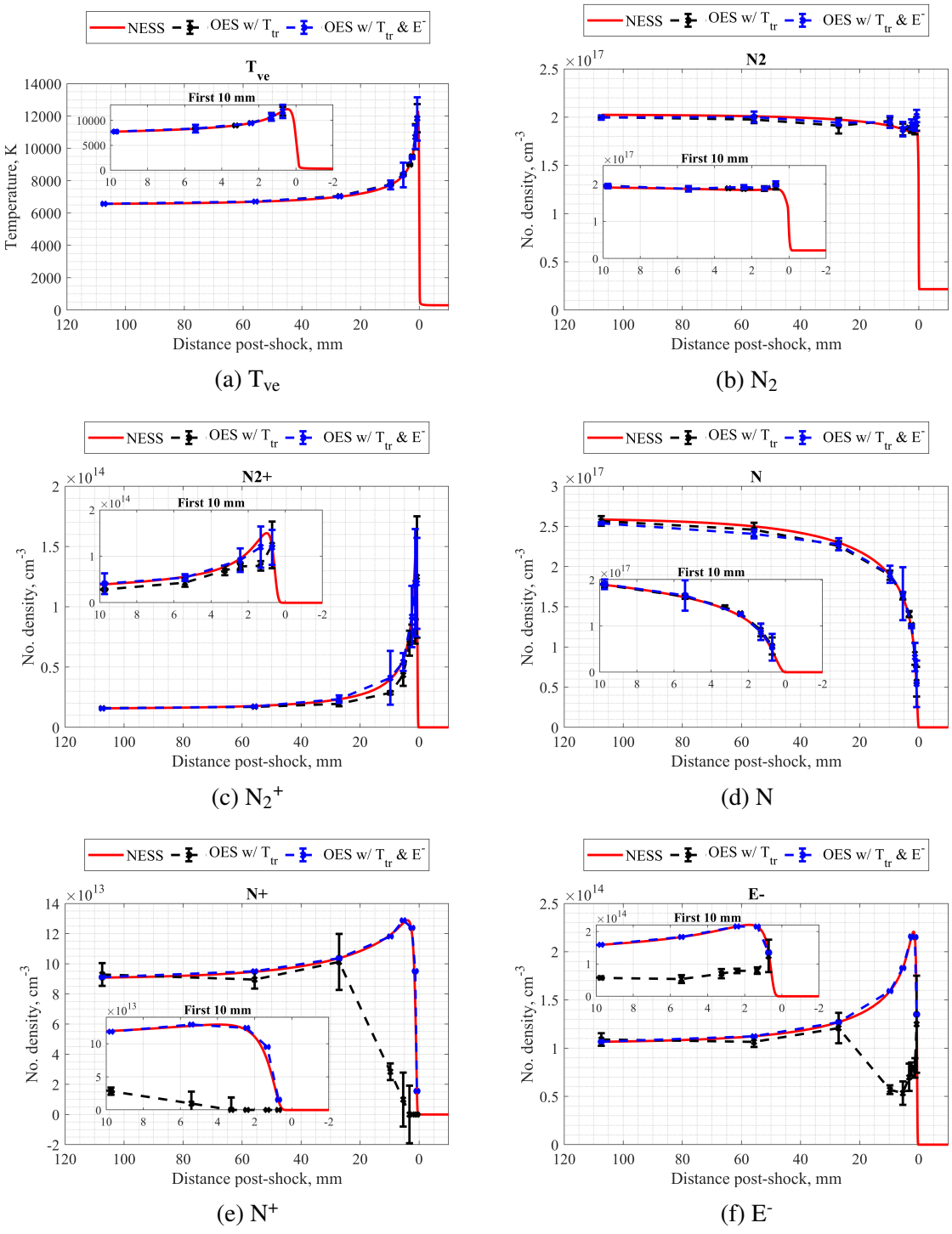
A.10 Further Application of Constrained Methodology

It was shown in Section 5.3.5 that adding the electron number density profile to the OES data inputs of the constrained spectral fitting routine helps to improve the overall characterisation of the test slug and validates electron number densities as a valuable measurement in future shock tube experiments. The addition of more data into the constrained routine is investigated further in this Section. It's separated into two subsections. In the first, the effect of including additional measurements is continued. This is in the form of adding T_{tr} values into the spectral fitting routine, as well as both T_{tr} and E^-. These parameters are chosen since they showed largest uncertainties in the previous analyses, which used only the spectral emission data as inputs. The second subsection explores the effect of measuring higher resolution spectra and a wider coverage of wavelength regions. High resolution data is generated in the ultraviolet wavelengths for the nominal T6s492 test case considered in the initial studies of

Section 5.3.2. The instrument line shape of real T6 AST high resolution data was used to convolve the artificial NESS-NEQAIR radiance data. Additionally, a "higher" resolution case was also generated with double the spectral resolution of the real high resolution T6 AST data, to further assess any effects it may have. For the wider wavelength region case, artificial spectra were generated over 120 to 500 nm in the Blue spectrum and 500 to 1700 nm in the Red. This gives the full measurable wavelength range capable from all spectral channels of the EAST facility. Thus, this represents the maximum coverage which is realistically achievable from real shock tube experiments. Results from these studies are plotted in the following subsections.

A.10.1 Including T_{tr} and E^-

Results in Fig. A.32 show that inclusion of electron number density measurements has a more profound effect than that of T_{tr}. Inclusion of T_{tr} alone has little effect on the remaining parameters of interest. However, adding E^- number density information improves the N^+ characterisation, and thus the overall thermochemical characterisation of the entire test slug. This result reflects what was shown in Section 5.3.5 in the main body of the paper.



(a) T_{ve} (b) N_2

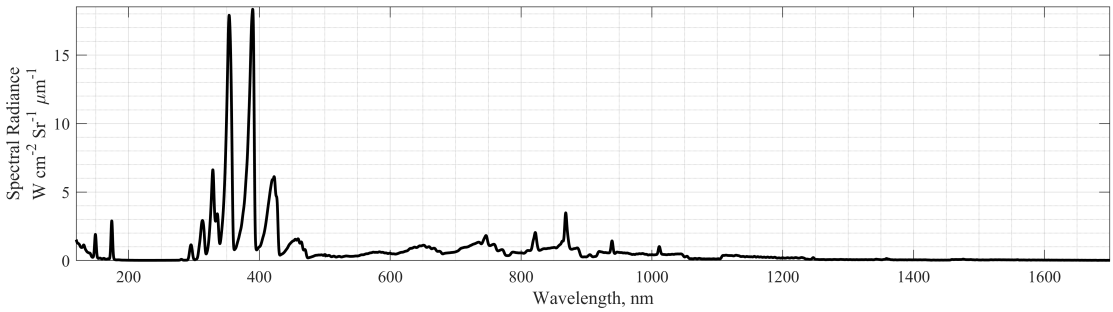
(c) N_2^+ (d) N

(e) N^+ (f) E^-

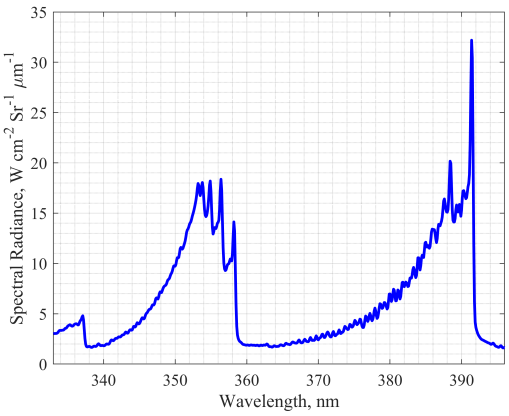
Fig. A.32 Results from performing constrained spectral fitting routine on initial NESS-NEQAIR data based on T6s492 (from Section 5.3.2) with the inclusion of T_{tr} data for one run, and T_{tr} and E^- for another.

A.10.2 Effect of higher and lower resolution spectral data

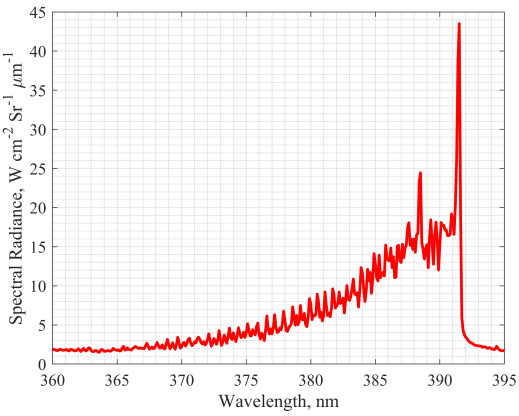
Due to finite camera pixel arrays, there is a constant compromise between spectral range and resolution. This is reflected in the artificial spectra generated for these studies. The high resolution spectra were thus generated over narrower wavelength regions. The centre wavelengths for each were chosen to include features from the N_2^+ first negative band, so to not lose any species information since N_2^+ does not emit significantly in the visible/near-infrared wavelength range. The equilibrium spectra for each of the three cases are shown in Fig. A.33, to illustrate the wavelength regions over which the constrained spectral fitting was performed. It's highlighted that visible/near-infrared data was also included for the high resolution simulation, though it was the same as that seen in Section 5.3.2 (with no change in resolution).



(a) Increased wavelength range



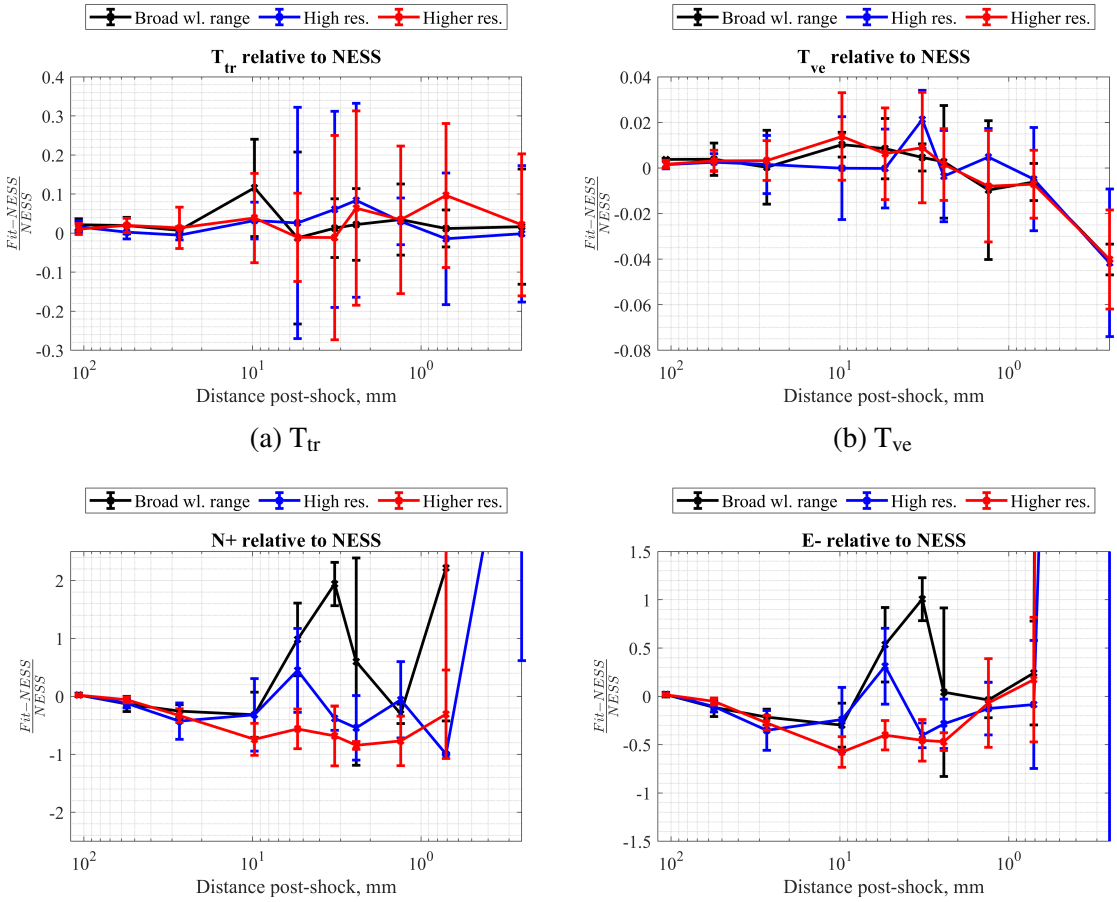
(b) High resolution



(c) Higher resolution

Fig. A.33 Examples of the artificial T6s492 NESS-NEQAIR spectral radiance traces from Section 5.3.2 with: (a) increased wavelength range; (b) high resolution ultraviolet data (equivalent to resolution of real high res. data); and (c) even higher resolution ultraviolet data (double that of real high resolution data).

An extract of results from applying the constrained spectral fitting routine to the artificial NESS-NEQAIR data is provided in Fig. A.34. Results have been normalised against the NESS outputs and a logarithmic x axis used to make plots clearer. Interestingly, it appears the confidence in the T_{tr} output closer to the shock front improves by including data from a wider range of wavelengths. This is the opposite to the expected output, since higher resolution data should help resolve the gradient of spectral bands and thus the rotational temperature. However, the increased resolution attempts showed no improvement from the nominal spectral fit results of Section 5.3.2. The N^+ and E^- profiles have also been plotted. It's evident that large errors still exist for all cases. This can easily be gauged by comparing the y-axis scales against that of T_{tr} and T_{ve}. Attempts at increasing the spectral resolution further were not attempted since it's extremely unlikely any distinguishable signal above the noise would be attained for real data, as photons are shared across more pixels. Finally, although it's not been plotted here, the profiles extracted for N_2, $N_2{}^+$ and N maintained their close fits to the NESS outputs, as has been seen throughout this study.



(a) T_{tr} (b) T_{ve}

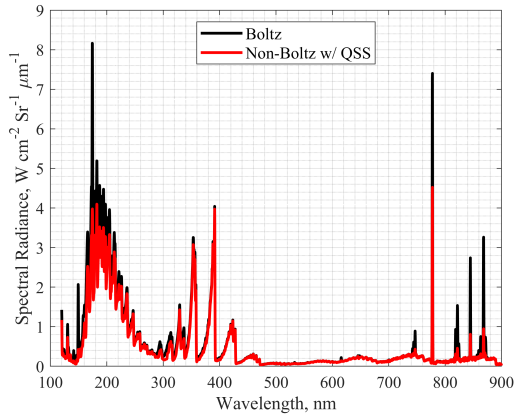
(c) N^+ (d) E^-

Fig. A.34 Results from applying constrained spectral fitting routine to artificial NESS-NEQAIR data with different spectral resolutions and wavelength regions. Results have been normalised against the NESS output values. A logarithmic x axis is used to aid readability of results near the shock front.

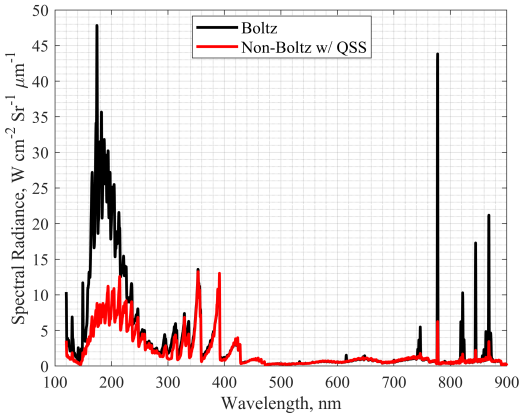
To conclude, the findings of this study therefore have indicated that T_{tr}, although it may be worth measuring in its own right, does not subsequently improve characterisation of the remaining parameters (as has been shown for E^-). Additionally, spectral data from a wider range of wavelength regions may be a means to improve the confidence in T_{tr}, though again, does not improve characterisation of the remaining species.

A.11 Radiation Model Dependency

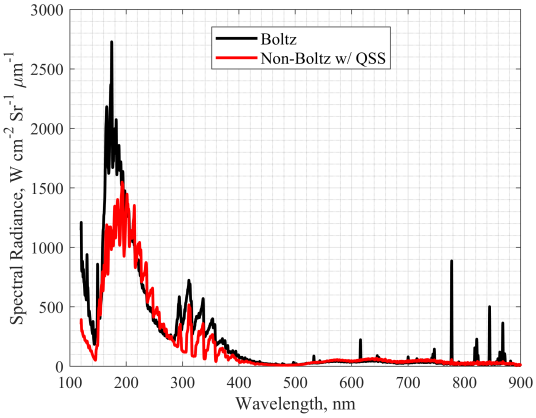
This section aims to briefly emphasise that all results of the constrained spectral fitting routine are dependent on the radiative modelling and chosen energy distributions. All spectral fitting performed in this thesis has assumed Boltzmann distributions within version 15.1 of the NASA's NEQAIR radiative transport code. Figure A.35 shows the results of performing NESS-NEQAIR simulations for a synthetic air test case at 7.3 km/s through a 33.3 Pa test mixture. This condition is equivalent to T6s484, which is spectrally fit in Chapter 7 and has been compared against NESS-NEQAIR simulations in the work of Clarke et al. [31].



(a) 110 mm post-shock



(b) 18 mm post-shock



(c) 0.8 mm post-shock

Fig. A.35 Spectral radiance predictions from a NESS simulation of 7.3 km/s 33.3 Pa synthetic air test case, with version 15.3 of NEQAIR at different points through the predicted test slug. Both Boltzmann and non-Boltzmann QSS model results are shown for comparison.

Here, the spectra have been generated from the latest version 15.3 of NEQAIR [42]. Additionally, the simulations have been performed for the case of assuming Boltzmann

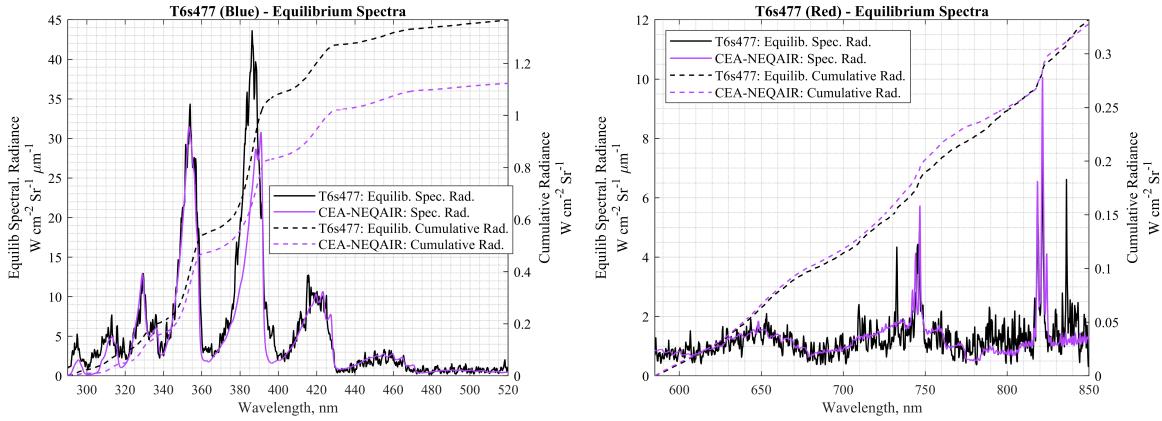
distributions and non-Boltzmann distributions, using the latest quasi-state-specific (QSS) modelling. These simulations are to provide an example of the dependency spectral predictions have on the chosen modelling method, especially in the lower wavelengths where NO dominates for air spectra. Therefore, as radiative models are updated in future works, the constrained spectral fitting should be repeated while incorporating these new models, to provide updated results.

Appendix B

Supplementary Content for Spectral Fitting of Pure Nitrogen Tests

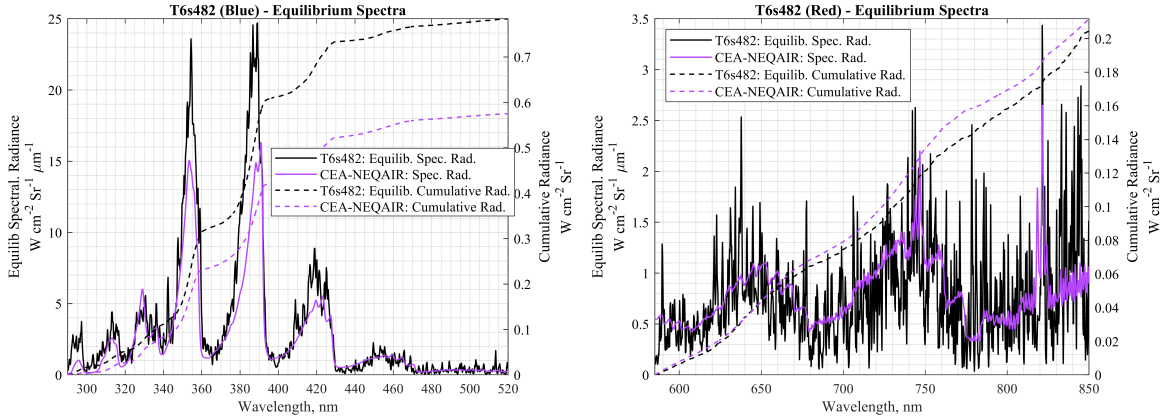
B.1 CEA-NEQAIR Spectral Radiance Comparisons

Comparisons between the CEA-NEQAIR equilibrium spectral radiance predictions and calibrated experimental data are given here. Good agreement between experimental radiance and radiative transport models in the equilibrium region is necessary to avoid skewing the results of a non-equilibrium analysis from any offsets. The steps taken to achieve improved agreement in the recent T6 AST low-speed campaign are documented in Chapter 4 of this thesis. The equilibrium spectral comparisons have thus been provided as evidence to justify the non-equilibrium thermochemical characterisation undertaken in this work. In the case of T6 AST data, equilibrium spectra are generated as far back as possible in the observed portion of the test slug, representing the closest measurements to a fully relaxed thermochemical equilibrium state. In the case of EAST data, spectra are generated from immediately after the non-equilibrium peak and before the radiance increases from shock deceleration effects. This gives both facilities their closest match to the equilibrium prediction. The CEA-NEQAIR simulations were run with a pure nitrogen mixture. Discrepancies due to contaminant species can be identified. The CN violet band emits strongly in the UV region, superimposing with the N_2^+ first negative band. Additionally, aluminium atomic lines contribute at 394 and 396 nm.



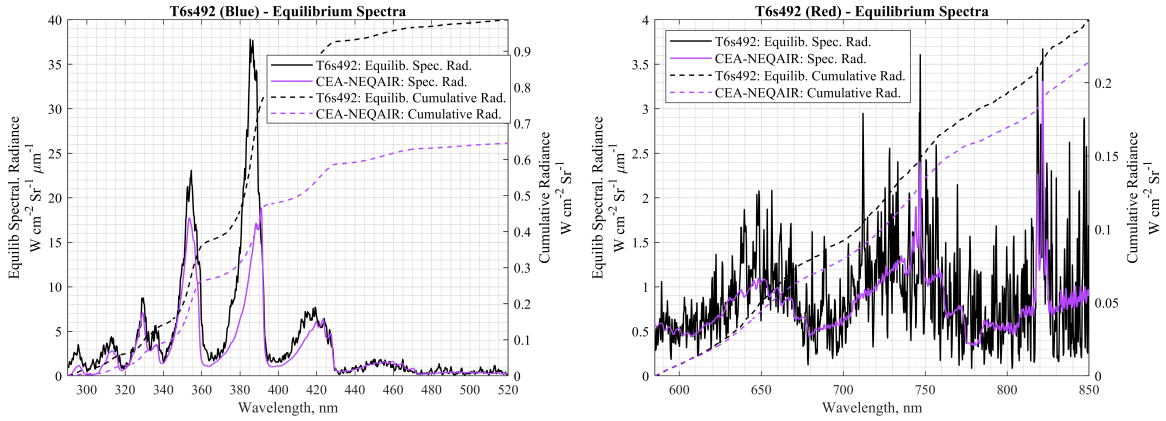
(a) 290 - 520 nm (b) 585 - 850 nm

Fig. B.1 T6s477 measured equilibrium spectral radiance traces compared to CEA-NEQAIR predictions convolved with experiment ILS.



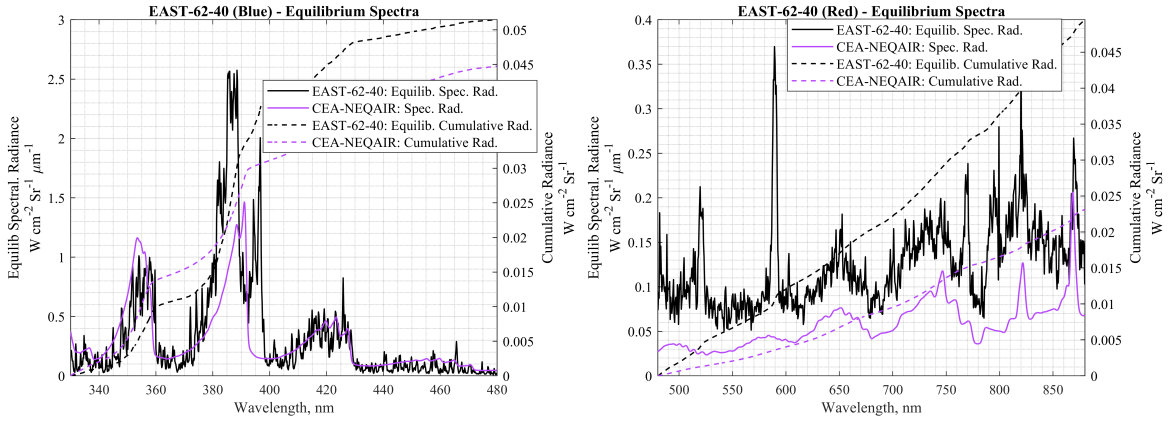
(a) 290 - 520 nm (b) 585 - 850 nm

Fig. B.2 T6s482 measured equilibrium spectral radiance traces compared to CEA-NEQAIR predictions convolved with experiment ILS.



(a) 290 - 520 nm (b) 585 - 850 nm

Fig. B.3 T6s492 measured equilibrium spectral radiance traces compared to CEA-NEQAIR predictions convolved with experiment ILS.



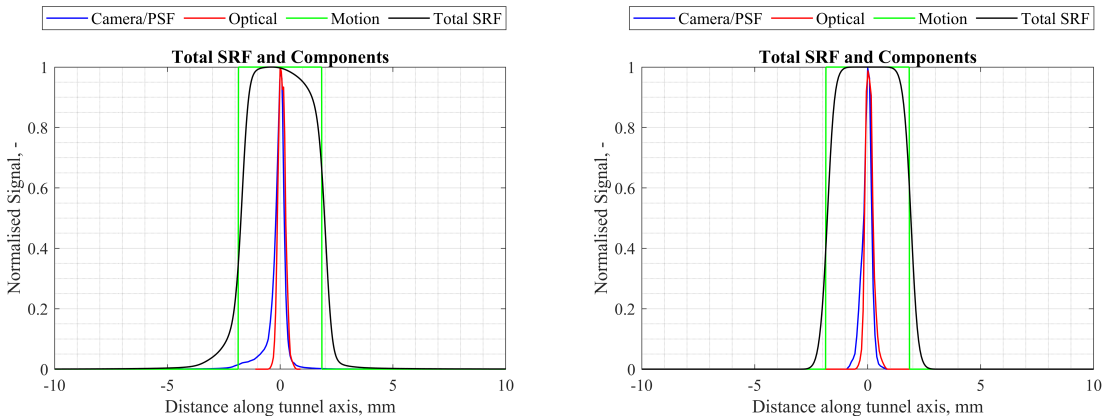
(a) 330 - 480 nm (b) 480 - 880 nm

Fig. B.4 EAST-62-40 measured equilibrium spectral radiance traces compared to CEA-NEQAIR predictions convolved with experiment ILS.

B.2 Spatial Resolution Functions

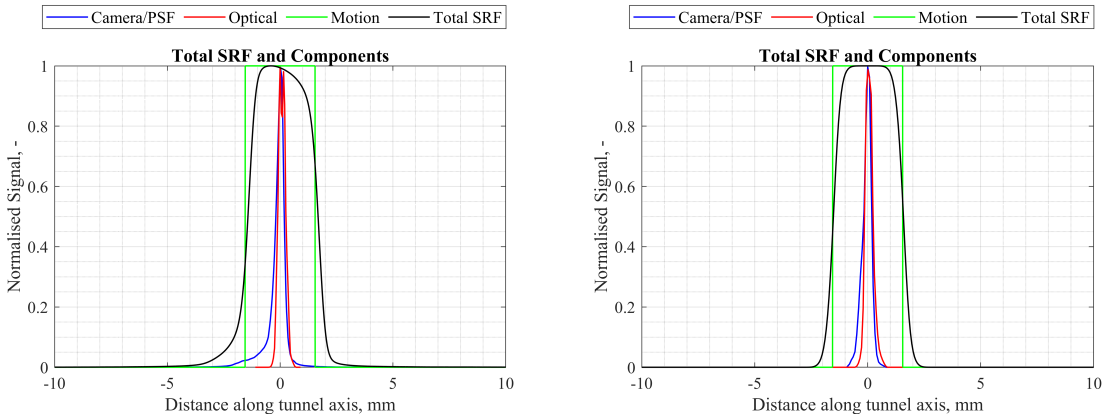
The SRF functions for each test and spectral channel are provided here. Generally, the largest smearing contribution is due to shock motion. A comprehensive explanation of each source can be found in the works of Cruden [41]. The measurement of the T6 smearing functions differs from this only for the camera component, where a Point Spread Function (PSF) measurement was taken. This involves a 50 μm pinhole light source on the tunnel centreline to project light through the optical system and onto an area smaller than one pixel

in the plane of the camera's sCMOS array. This is in contrast to differentiating the signal captured over a sharp edge and fitting with the square root of a Voigt function, as done with the EAST-62-40 SRF's.



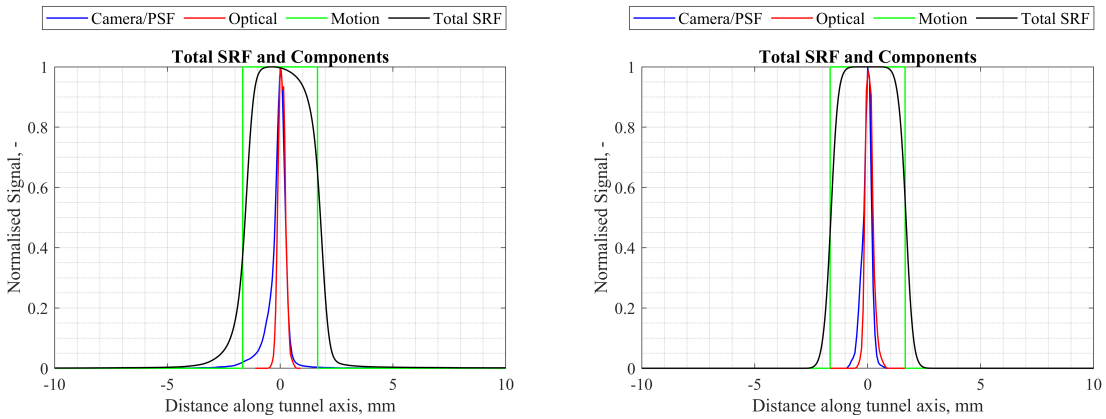
(a) Blue (b) Red

Fig. B.5 T6s477 total SRF's and constituent components.



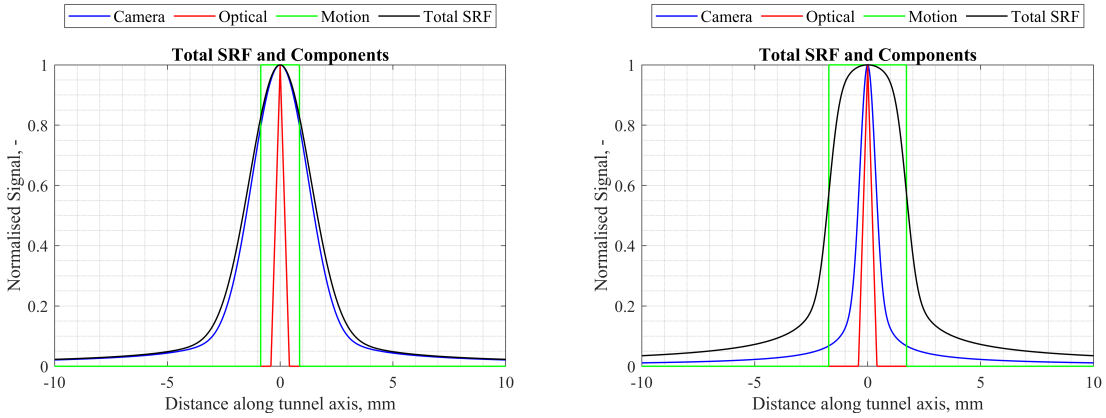
(a) Blue (b) Red

Fig. B.6 T6s482 total SRF's and constituent components.



(a) Blue (b) Red

Fig. B.7 T6s492 total SRF's and constituent components.



(a) Blue (b) Red

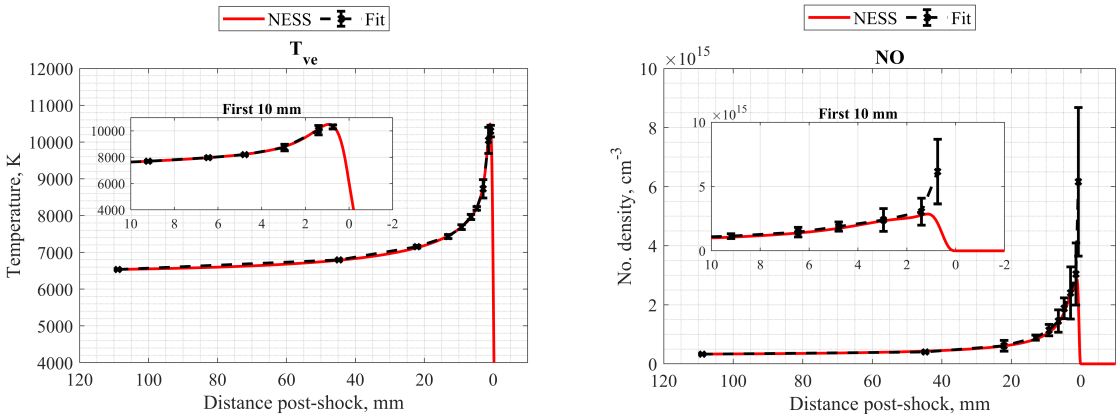
Fig. B.8 EAST-62-40 total SRF's and constituent components.

Appendix C

Supplementary Content for Spectral Fitting of Synthetic Air Tests

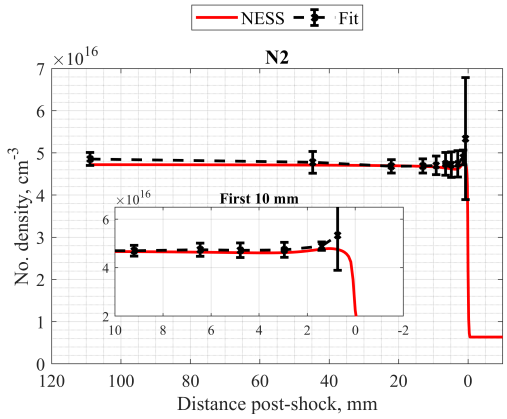
C.1 Synthetic Air Validation

The previous validation study conducted in Chapter 5 only showed successful characterisation of pure nitrogen data by the constrained spectral fitting routine. This section therefore briefly demonstrates the successful application to artificial synthetic air data, to justify its use for the selected tests in Chapter 7. The methodology is the same as used in the prior pure nitrogen validation, feeding the results of a one-dimensional Non-Equilibrium Shock Solver (NESS) simulation into NASA's NEQAIR v15.1 as a line of sight. This generates artificial radiance data, for which the corresponding temperature and number density profiles are known, to assess the performance of the fitting routine. The reader is directed to the previous validation works in Chapter 5 for a more detailed explanation of the process. Additionally, details of the NESS code may be found in the works of Clarke et al. [30]. The NESS simulation was based on T6s484, using a shock speed of 7.3 km/s in 33.3 Pa in synthetic air. Figure C.1 demonstrates successful extraction of T_{ve} and NO, N_2, N_2^+, N and O evolutions through the artificial test slug. It's highlighted that the same settings were used in the NEQAIR simulations to generate the artificial data, as is used in the spectra generated during the fitting process. This ensures a match between the two is theoretically possible. Finally, it's noted that increasing the number of species from a pure nitrogen to a synthetic air test gas increases the spectral fitting run time to typically $\sim$3 days. The error bars here represent the 95% confidence limits ($\pm$2 standard deviations) from a Monte Carlo analysis.

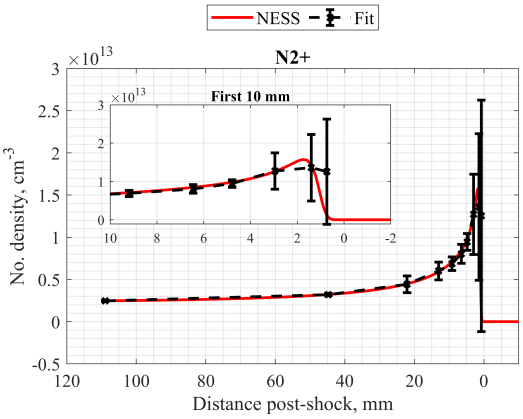


(a) T_{ve}

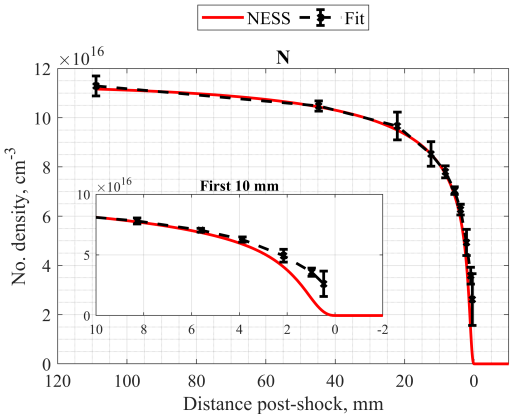
(b) NO



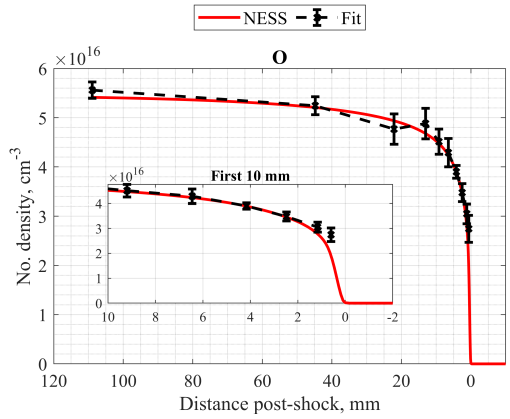
(c) N_2



(d) N_2^+



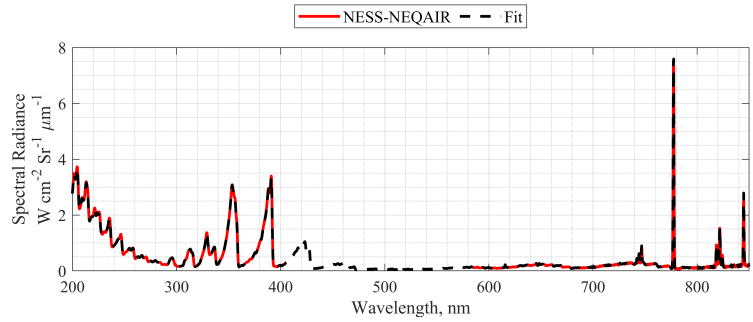
(e) N



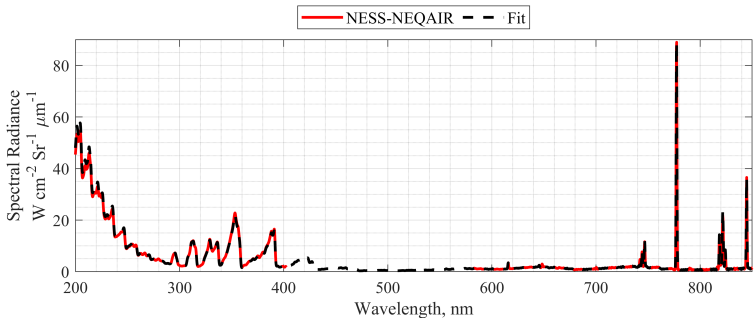
(f) O

Fig. C.1 Validation of constrained spectral fitting routine for NESS-NEQAIR artificial radiance data at 7.3 km/s in 33.3 Pa synthetic air. Selected parameters showed close agreement to original NESS results.

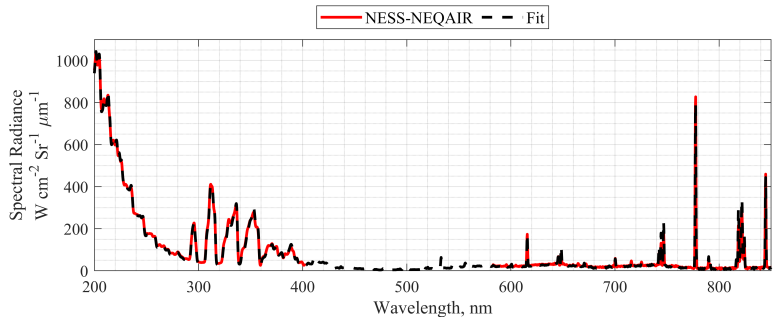
The associated spectral fits are given in Fig. C.2 through different stages of the post-shock relaxation. It's evident close fits are attained in all portions of the artificial test slug. These results justify the use of the constrained spectral fitting routine on real synthetic air datasets. Species included in the spectral fitting of real radiance data in Chapter 7 are: N_2, O_2, NO, N, O, N_2^+, O_2^+, NO^+, N^+, O^+, CN, NH and E^-. However, only results for T_{ve} and NO, N_2, N_2^+, N and O are shown, since they are the parameters shown to be extracted accurately.



(a) Equilibrium



(b) Relaxation

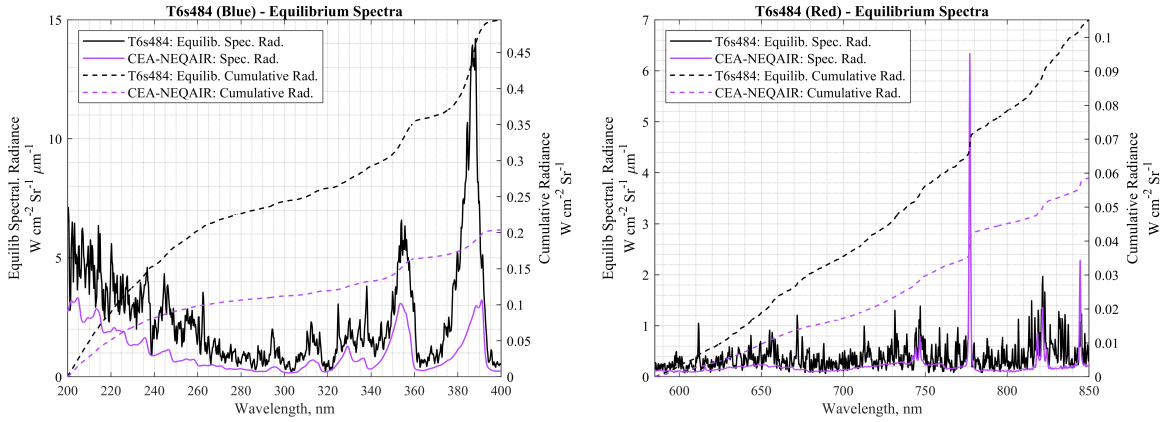


(c) Immediate post-shock

Fig. C.2 Spectral fit results in different portions of the test slug against the NESS-NEQAIR generated spectra for 7.3 km/s shock in 33.3 Pa synthetic air. Emission data from NESS-NEQAIR was only provided in the plotted spectral regions.

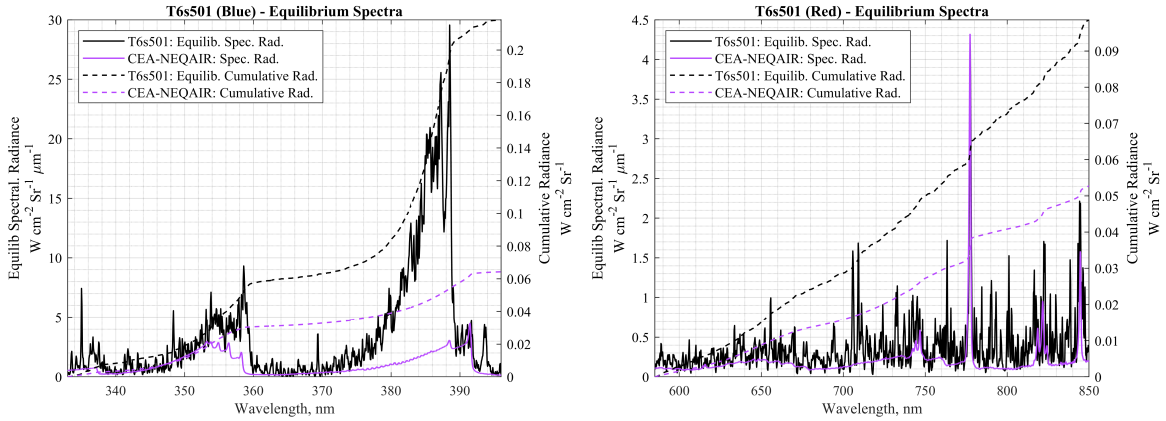
C.2 CEA-NEQAIR Spectral Radiance Comparisons

Comparisons between the CEA-NEQAIR equilibrium spectral radiance and experimental data are given here. Good agreement between experimental radiance and radiative transport models in the equilibrium region is necessary to avoid skewing the results of a non-equilibrium analysis from any calibration or radiative modelling errors. The steps taken to achieve improved agreement in the recent T6 AST low-speed campaign are documented in Chapter 4 of this thesis. The equilibrium spectral comparisons have thus been provided as evidence to justify the non-equilibrium thermochemical characterisation undertaken in this work. In the case of T6 AST data, spectra are generated as far back as possible in the observed portion of the test slug, representing the closest measurements to a fully relaxed thermochemical equilibrium state. In the case of EAST data, spectra are generated from immediately after the non-equilibrium peak and before the radiance increases from shock deceleration effects. This gives both facilities their closest match to the equilibrium prediction. The CEA-NEQAIR simulations were run with a 20.9% O_2/ 79.1% N_2 mixture by volume. Discrepancies due to the contaminant CN violet band can dominate the UV region, as seen in Fig. C.4a from the high resolution UV data of T6s501.



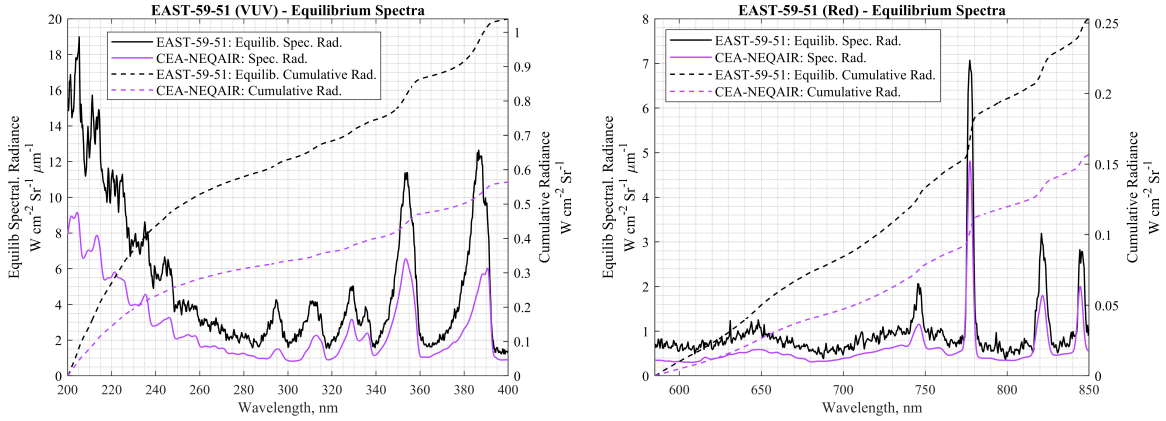
(a) 200 - 400 nm (b) 585 - 850 nm

Fig. C.3 T6s484 measured equilibrium spectral radiance traces compared to CEA-NEQAIR predictions convolved with experiment ILS.



(a) 200 - 400 nm (b) 585 - 850 nm

Fig. C.4 T6s501 measured equilibrium spectral radiance traces compared to CEA-NEQAIR predictions convolved with experiment ILS.



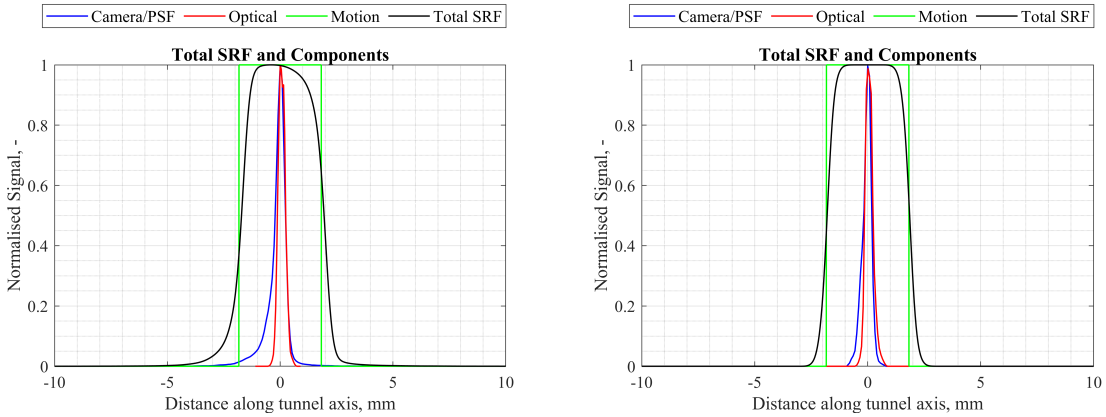
(a) 200 - 400 nm (b) 585 - 850 nm

Fig. C.5 EAST-59-51 measured equilibrium spectral radiance traces compared to CEA-NEQAIR predictions convolved with experiment ILS.

C.3 Spatial Resolution Functions

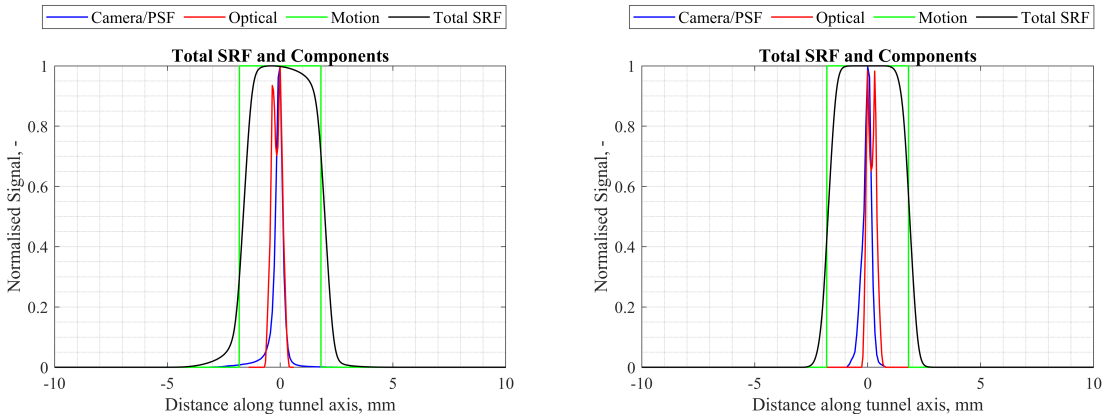
The SRF functions for each test selected for spectral fitting in Chapter 7 are provided here. Generally, the largest smearing contribution is due to shock motion. A comprehensive explanation of each source can be found in the works of Cruden [41]. The measurement of the T6 smearing functions differs from this only for the camera component, where a Point Spread Function (PSF) measurement was taken. This involves a 50 μm pinhole light source on the tunnel centreline to project light through the optical system and onto an area smaller

than one pixel in the plane of the camera's sCMOS array. This is in contrast to differentiating the signal captured over a sharp edge and fitting with the square root of a Voigt function, as done for the EAST-59-51 SRF's.



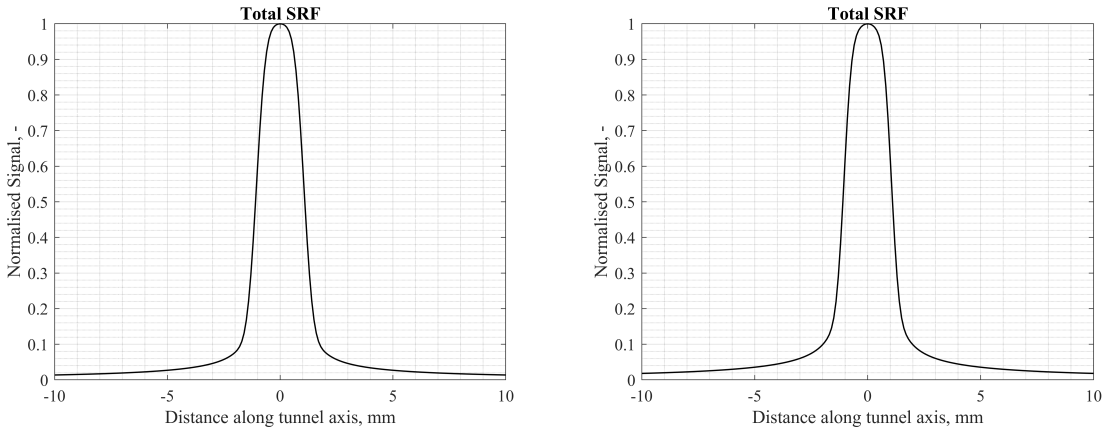
(a) Blue (b) Red

Fig. C.6 T6s484 total SRF's and constituent components.



(a) Blue (b) Red

Fig. C.7 T6s501 total SRF's and constituent components.



(a) VUV (b) Red

Fig. C.8 EAST-59-51 SRF's.